

Human Motion Control

Reader for Delft University course wb2407 and
Twente University course 115047

Revision: 2.1
Date: January 2008

Authors:
Herman van der Kooij
Bart Koopman
Frans C.T. van der Helm

Table of contents

1. INTRODUCTION TO HUMAN MOTION CONTROL	3
INTRODUCTION	3
1.1 <i>Introduction</i>	3
1.2 <i>Goal</i>	5
1.3 <i>The neuromusculoskeletal system</i>	5
1.4 <i>Contents of the course</i>	6
2. KINEMATICS	11
INTRODUCTION	11
2.1 <i>Joints</i>	12
2.3 <i>Motion recording and description</i>	30
REFERENCES.....	35
SUGGESTED FURTHER READING	35
APPENDIX A: ANATOMICAL FRAME DEFINITIONS FOR THE LOWER LEGS	36
APPENDIX B: ANATOMICAL FRAME DEFINITIONS AND EULER ANGLES OF THE DELFT SHOULDER MODEL	44
3. RIGID BODY DYNAMICS.....	47
INTRODUCTION	47
3.1 <i>Equations of motion</i>	47
4. MUSCLE DYNAMICS	63
INTRODUCTION	63
4.1 <i>Muscle morphology and physiology</i>	63
4.2 <i>Muscle models</i>	67
REFERENCES.....	86
5. OPTIMIZATION	87
INTRODUCTION	87
5.1 <i>Why optimization?</i>	87
5.2 <i>The optimization procedure</i>	89
5.3 <i>Linear and non-linear optimization criteria</i>	96
5.4 <i>Inverse and forward dynamic optimization</i>	102
5.5 <i>Validation</i>	105
6. HUMAN GAIT	107
INTRODUCTION	107
6.1 <i>Description of normal walking</i>	107
6.2 <i>Inverse dynamical analysis of gait</i>	111
6.3 <i>Forward dynamical simulation of gait</i>	114
7. HUMAN SENSES AND THEIR DYNAMICS.....	117
INTRODUCTION	117
7.1 <i>Introduction</i>	117
7.2 <i>The neural system</i>	118
7.3 <i>Classification of the human senses</i>	124

7.4	<i>Joint sensors</i>	127
7.5	<i>Muscle sensors</i>	127
7.6	<i>The hearing</i>	137
7.7	<i>Tactile senses</i>	141
7.8	<i>The visual system</i>	144
7.9	<i>The vestibular organ</i>	152
	REFERENCES.....	162
8.	STABILITY AND ADMITTANCE	163
	INTRODUCTION	163
8.1	<i>Introduction</i>	163
8.2	<i>The neuromusculoskeletal model</i>	164
8.3	<i>Linearization of the neuromusculoskeletal model</i>	167
8.4	<i>Experimental validation</i>	172
	REFERENCES.....	179
9.	(MODELS OF) HUMAN PERCEPTION	181
	INTRODUCTION	181
9.1	<i>Sensory interactions</i>	181
9.2	<i>An adaptive model of sensory integration in a dynamic environment (modified from van der Kooij et al., 2002)</i>	195
	REFERENCES.....	212
	APPENDIX A: TAPPED DELAY LINE AS PREDICTOR FOR TIME DELAYS	214
	APPENDIX B: SENSOR DYNAMICS.....	214
	APPENDIX C:	215
	APPENDIX D:	216

Introduction to human motion control

INTRODUCTION

Humans are well capable of performing a large number of different physical activities, ranging from standing, holding objects, walking, running, throwing to fine motor functions as writing, sewing, etc. It will take probably another century before a robot is developed which can execute the same variety of functions. In the class 'Human Motion Control' the focus will be on the way that humans are able to control their movements during all those activities. The role of individual parts of the neuromusculoskeletal system (skeleton, muscles, sensors, Central Nervous System) will be shown, and especially the integration of all parts which results in a wonderful mechanical system.

Knowledge of the mechanical and control behavior of the musculoskeletal system is necessary e.g. for the design of assistive devices like prostheses, orthoses and neuroprostheses in case that parts of the neuromusculoskeletal system fail.

OBJECTIVES

This chapter addresses:

- A short introduction in the field of biomechanics, especially focusing on motion biomechanics.
- The goal of the course on Human Motion Control.
- An overview of the topics in this course on Human Motion Control.
- A short introduction about the anatomical parts involved in the neuromusculoskeletal system.

1.1 Introduction

1.1.1 BIOMECHANICS

Biomechanics is a contraction of the words 'biology' and 'mechanics'. In Biomechanics the application of the laws of physics and especially the laws of mechanics, on biological systems is studied. Traditionally, the field of biomechanics can roughly be divided in three sectors: Fluid biomechanics, tissue biomechanics and motion biomechanics. In fluid biomechanics the focus is on the cardiovascular system, the way blood is transported through the vessels, and the effort of the heart to pump the blood around in the body. Tissue biomechanics deals with the mechanical behavior of various tissues in the human (and animal) body, ranging from cell biomechanics, organs, cartilage, bone, tendons, ligaments, etc. For the mechanical behavior especially the tissue deformations under mechanical loading are studied, with the accompanying strains and stresses in the material. It is e.g. attempted to predict what are the failure criteria and failure mechanisms, but also how the tissue may adapt to the loading. In motion biomechanics the motions of the neuromusculoskeletal system are analyzed, especially focusing on the role of joints, bones, muscles, sensors and the central and peripheral nervous system.

Biomechanics has a number of application fields. In clinical applications it is attempted to improve the diagnosis, treatment and prevention of disorders to the

musculoskeletal and cardiovascular system. In sport biomechanics the aim is to improve performance by a thorough understanding of the biomechanical principles of the movements. In ergonomic applications the behavior of human in interaction with the environment is studied, in order to prevent work-related diseases like RSI and to improve the performance.

Biomechanics is a multidisciplinary field of research, in which medical researchers (orthopedics, neurology, rehabilitation, morphology, physiology) collaborate with mechanical, electrical and control engineers, and with researchers of biophysics and human movement science. Each of these research disciplines has their valuable contribution, and it is challenging to communicate results to researchers with another background.

1.1.2 RELATED COURSES AND PREREQUISITES

The reader 'Human Motion Control' is used in lectures at Delft University of Technology and the University of Twente. Students at these universities have slightly different backgrounds and therefore related courses and prerequisites have been subdivided for the two universities. Both curricula result in a broad knowledge on biomechanics and related fields for students interested in Biomedical Engineering.

1.1.2.1 Delft University of Technology

Students are required to have sufficient understanding of dynamics and control engineering, like taught in the course 'Systems and Control 2' (wb2206). A background on human physiology can be acquired from the course 'Physiological systems' (wb2408). In some aspects the human can be approached as a control system. In this course motion is controlled; the course 'The Human Controller' (wb2306) addresses many control aspects and discusses human performance. More applied courses are 'Biomechatronics' (wb2432), primarily on prostheses and orthoses and 'Haptic system design', concerned with the design process of robotic systems in interaction with humans.

1.1.2.2 University of Twente

In the course 'Biomechanics' (nr. 115739) the emphasis is on fluid and tissue biomechanics. In the course 'Functionality of the Motion System (nr. 115745) a background on the functional anatomy of joints, ligaments and muscles is presented. Other, more applied courses will be presented on 'Design in Biomedical Engineering' (nr. 114733), 'Rehabilitation Engineering' (nr. 115744) and 'Biomechatronics' (nr. 117127). For a successful course in 'Human Motion Control' (nr. 115747) only 'Biomechanics' is a pre-requisite. Students are required to have reasonable knowledge in dynamics and in control engineering, like presented in the course 'System- and Control Engineering' (nr. 113143).

1.1.3 BACKGROUND

Since 1980 there has been research in tissue and motion biomechanics at the Departments of Mechanical Engineering of the University of Twente and Delft University of Technology. There is a traditional division in the field of motion biomechanics between the Universities of Twente and Delft, in which Twente focuses on the lower extremities and Delft focuses on the upper extremities. However, recently researchers in Delft have started to study bipedal locomotion

and researchers in Twente have begun to study arm movements, especially the training of hand and arm motions with the use Functional Electrical Stimulation (FES) and robotics. The motions under study for the lower extremity are standing, walking and running. The research has involved a combination of experiments with motion and force recordings, and the development of simple and complex models of the lower extremities.

Models are necessary to transform the theories on motion control into testable, quantitative hypotheses, which can subsequently be subjected to validation experiments. Models are also necessary to structure the knowledge, but only experiments can add new information to the existing body of knowledge.

1.2 Goal

The goals of the course on ‘Human Motion Control’ are that students

- Acquire fundamental knowledge about how humans control their motions.
- Get acquainted with methods and techniques to analyze the motions and control.

The course will be research-oriented, which means that not only information and ‘facts’ about human motions and control are presented, but also how this information is acquired by experiments and models, and how accurate this information and data are. Often competing theories will be presented, in order to show that more than one theory can explain at least part of the experimental results. Articles of scientific journals are part of the reading material for this course, in order to get a flavor of the state-of-the-art in this field.

1.3 The neuromusculoskeletal system

In Figure 1.1 a conceptual scheme of the neuromusculoskeletal system is shown, with a linkage system (body segments), actuators (muscles), sensors (proprioceptive and tactile sensors, visual and vestibular system) and the controller (*Central Nervous System, CNS*). The scheme shows a feedback control system, but later in this course also feedforward control schemes will be demonstrated. In a feedback control system, a (position) setpoint is generated somewhere in the brain. This setpoint is compared with the actual position of the limb, and the CNS will send a neural signal to the muscles. The muscles exert forces on the bones of the skeletal system, which will start moving if it is not constrained by the environment. The movements are detected by the sensors which are all over the body, e.g. in the muscles, joints, skin but also the visual and vestibular system. Using these sensory signals the actual position of the skeletal system can be reconstructed.

In the control scheme of Figure 1.1 two inputs can be discerned: The setpoint and a disturbance. Disturbance forces like wind or friction may act on the body, and the resulting position will deviate from the intended position. The transfer from the setpoint to the actual position is called the control or tracking behavior, i.e. how well can the system follow the intended setpoint. The transfer from the disturbance to the actual position is called the disturbance or compensatory behavior, i.e. how well can the system resist or compensate for the disturbance forces.

One of the main difficulties in biomechanical research is the recording of necessary variables in living subjects. Only the outside of the human body and a few inside signals can be measured, and the underlying mechanisms must be derived from this visible and measurable behavior. When the scheme in Figure 1.1 is considered, only the external motions and external forces can be

*Central Nervous
System (CNS)*

measured. Direct measurements of internal forces require highly invasive techniques, and are rarely done. Measurements of electrical signals in peripheral nerves (going towards muscles or coming from sensors) and inside the Central Nervous System are difficult to trace back to conceptual variables in a control scheme. Identification of model parameters using the input (set-point!) and output signal is impossible, e.g. due to the highly non-linear properties of the system. Therefore models are used to relate existing knowledge on subsystems, and predict the behavior of the whole system given a certain task. These predictions can be compared with measurements of the behavior, which may give insight if the assumptions in the model were reasonably correct.

1.4 Contents of the course

1.4.1 OVERVIEW

In the course on Human Motion Control the scheme in Figure 1.1 will be the basis for treating the various parts of the neuromusculoskeletal system. The scheme will be discussed ‘from right to left’, since only the outputs of the system can be measured. How further we proceed to the left of the block scheme, more and more modeling assumptions are needed.

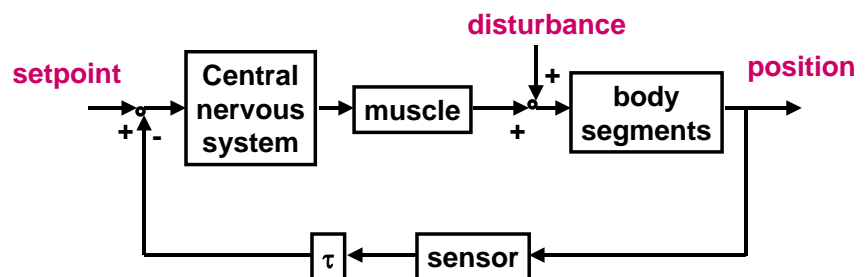


Figure 1.1: Conceptual scheme of the motion control of a musculoskeletal system, with a linkage system (body segments), actuators (muscles), sensors (proprioceptive and tactile sensors, visual and vestibular system) and the controller (Central Nervous System). τ represents the time-delays caused by transport and processing in the nervous system.

The following order in topics will be treated:

- To model the dynamics of body segments, one requires knowledge about how to describe motions of rigid bodies in space (Kinematics). Kinematics describe motion and external force recording (Kinematics, Chapter 2).
- Furthermore knowledge is required about how to describe and solve the equations of motion (Kinetics). Kinetics describe the calculation of net moments around joints (Rigid Body Dynamics, Chapter 3).
- Muscle dynamics are very complex and non-linear. The force generated by muscles depends on the muscles activation, length and velocity. Under some conditions muscles behave like springs and dampers. Various methods to model the muscle dynamics are available (Muscle models, Chapter 4).
- When the joint moments and movements are known it is possible to calculate the muscle forces that generated these moments by using optimization techniques (Optimization, Chapter 5).
- By applying the methods described in Chapters 2-5 it is possible to analyze (impeded gait) patterns. (Human gait, Chapter 6).

- For the control of movements the CNS utilize sensory information from multiple sensory systems that each has its own dynamical characteristics (Human Senses and their Dynamics, Chapter 7).
- The CNS can be considered as a feedback controller. In this view the CNS uses sensory information to obtain a desired posture. The desired posture is compared with the actual posture and the error is used to control and stabilize the musculoskeletal system. (Stability and Admittance, Chapter 8).

1.4.2 KINEMATICS

In Chapter 2 theory and application of a kinematic analysis of the human body is presented. In Figure 1.2 the kinematic part of the conceptual scheme is shown as the outcome of the motion equations. Kinematics only deals with motions, without considering any forces that generate the motions. Motions can be recorded with e.g. camera systems or electromagnetic devices. The passive skeletal system is presented, consisting of joints, bones and ligaments, resulting in the degrees-of-freedom (DOF) of the system. The motions of a body segment can be described with respect to another segment (knee angle is the angle between the thigh and shank segment), or with respect to a global (measurement) coordinate system. The parameterization of three-dimensional motions by Euler angles and helical axes will be shown. Finally, some measurement methods and data processing methods (filtering, differentiation, etc.) are presented.

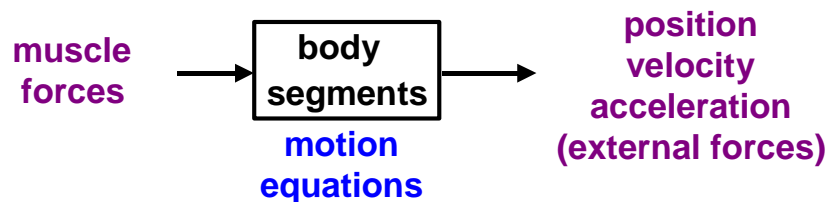


Figure 1.2: Motions of the body segments are the outcome of the motion equations.

1.4.3 RIGID BODY DYNAMICS

In Chapter 3 rigid body dynamics are presented, i.e. the equations of motion relating the motions of the body segments to the forces and moments that are causing those motions. Three different methods to derive the motion equations are discussed: Newton-Euler, Lagrangian or TMT. It is shown how the net joint moments are calculated from the recorded motions and external forces, using an inverse dynamic analysis (see Figure 1.3).

Important parameters for this segmental model are the joint rotation centers and inertial parameters like the segment mass, rotational inertia and the center-of-mass. It is shown how these parameters are recorded. Other parameters like geometrical parameters describing muscle and ligament attachments (and hence the muscle and ligament moment arms) and muscle dynamic parameters will be briefly discussed, since these parameters will be extensively used in the next chapters.

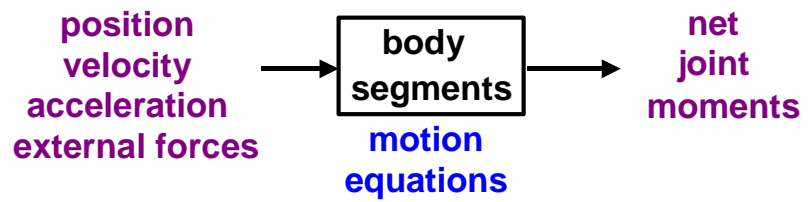


Figure 1.3: Inverse dynamics of the body segments.

1.4.4 MUSCLE DYNAMICS

Muscles are the actuators of the musculoskeletal system. A muscle is a complex biochemical plant, transforming chemical energy into mechanical energy, controlled by neural input from the CNS. Muscles have highly non-linear dynamic properties, e.g. the muscle force depends on the muscle length and contraction velocity. There are muscle models of varying complexity; depending on the detail the overall behavior of the musculoskeletal system must be described (see Figure 1.4). Two basic muscle models are described in Chapter 4. Hill-type muscle models contain describing functions of the most important non-linear and dynamic properties, though they are not very informative over the underlying biochemical processes. Huxley-type muscle models, or cross-bridge muscle models, are one step more detailed, in that they described the basic mechanism of muscle contraction, i.e. the force generation on micro-level by the so-called 'cross-bridges'.

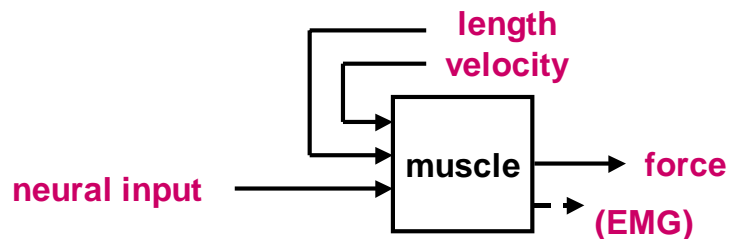


Figure 1.4: Representation of a basic muscle model.

1.4.5 OPTIMIZATION

The net joint moments as calculated in Chapter 3 are generated by the muscle forces, multiplied by the muscle moment arms. However, calculating the muscle forces from the net joint moments is not trivial. From a mathematical point of view, there are more muscles than motion equations, resulting in an underdetermined set of equations. Physically it means that the same motion can be generated using varying combinations of muscle forces. In order to derive a unique solution, another criterion must be taken into account, e.g. the solution that requires the least metabolic energy. In Chapter 5 some optimization criteria and search algorithms will be presented, for inverse (quasi-)static optimization and for inverse optimization using inverse muscle models. Finally, also forward dynamic optimization schemes will be presented (see Figure 1.5).

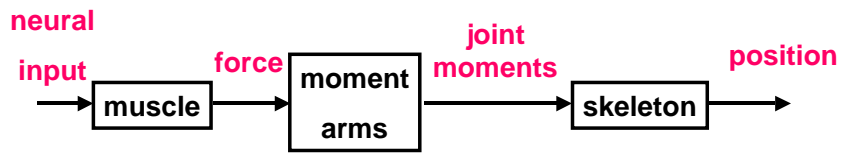


Figure 1.5: Forward dynamic optimization scheme of motion.

1.4.6 HUMAN GAIT

In the previous chapters some tools for the analysis of musculoskeletal systems have been presented, i.e. motion description, the motion equations for the skeletal system, and dynamic equations for the muscle behavior and optimization schemes for calculating muscle forces. These tools are currently the state of the art in gait analysis. In Chapter 6 these tools will be combined in order to describe an open-loop model (without sensory feedback) of walking. Gait parameters like cycle time, step length and walking velocity are presented, in combination with other events like toe-off and heel strike, single stance phase and double stance phase. The motions and net moments of the joints are described with respect to cycle time. Then, the power balance and energy expenditure during walking can be analyzed in order to determine where the most energy is generated and where it is dissipated.

1.4.7 HUMAN SENSES AND THEIR DYNAMICS

The human body is stuffed with sensors, ranging from tactile sensors in the skin, pressure and stretch sensors in capsule, length and velocity sensors in the muscle fibers, force sensors in muscle tendons, and on a more global level the visual and vestibular system. These sensors are indispensable for any motor control scheme. The sensors are part of the closed-loop transfer function; therefore the sensor dynamics are important for the overall dynamic behavior of the neuromusculoskeletal system. In Chapter 7 some basic dynamic features of length, contraction velocity and force sensors in the muscles are presented and their potential role in human motion control.

The CNS consists of the brain and the spinal cord. It contains about 10^{11} nerve cells (or neurons). With each neuron having an average of 10^4 connections, a total of 10^{15} connections are present. Given this huge complexity, any model attempting to understand the function of the CNS is only very simple. In Chapter 7 some basic characteristics of the CNS will be presented.

1.4.8 STABILITY AND ADMITTANCE

In Chapter 8 modeling and identification of postural dynamics will be discussed. The components of the neuromusculoskeletal system will be integrated in a block scheme, comprising muscles, the skeletal system (motion equations), sensors and some control action of the CNS. As shown in Figure 1.1, there are two inputs, which will result in motions of the neuromusculoskeletal system. Neural inputs from the CNS will initiate motions through muscle activation. This is called the control behavior or tracking behavior. External forces are injected into the system having a direct effect on the skeletal system. External force perturbations may cause the system to deviate from its desired position or trajectory. Humans will try to suppress the deviations. This is called disturbance behavior.

Some features of this neuromusculoskeletal model will be discussed like the stability and admittance of the system. The stability is defined as the ability of

the system to return to its original position or trajectory. A system is stable or instable. One way of looking at stability of a closed-loop system is by analysis of its open-loop transfer function, i.e. the combination of the forward and the backward path. The open-loop transfer function should have a positive phase margin (and hence a positive gain margin). For stable systems, the actual behavior is described by the admittance (the inverse of impedance). The admittance is the sensitivity of the neuromusculoskeletal system for force perturbations, i.e. what position deviations will occur for a certain force. For instance, a very compliant system will result in larger position deviations than a very stiff system. The admittance depends on the inertia, viscosity and stiffness of the neuromusculoskeletal system, but also on the feedback control properties of the CNS.

Kinematics

INTRODUCTION

In this chapter the theory and application of a kinematic analysis of the human body is presented. In Figure 1.2 the kinematic part of the conceptual scheme is shown as the outcome of the motion equations. Kinematics only deals with motions, without considering the forces which generate the motions. Motions can be recorded with e.g. camera systems or electromagnetic devices. The passive skeletal system is presented, consisting of joints, bones and ligaments, resulting in the degrees-of-freedom (DOF) of the system. The motions of a body segment can be described with respect to another segment (knee angle is the angle between the thigh and shank segment), or with respect to a global (measurement) coordinate system assuming that they are rigid and some local frame is fixed to them. Even then, there are different descriptions possible, ranging from definitions in medical science and anatomy to various technical definitions. In this chapter the parameterization of three-dimensional motions by Euler angles and helical axes are addressed. Finally, some measurement methods and data processing methods (filtering, differentiation) are presented. In Chapter 3 the motion equations will be derived, and used to calculate the net moments and/or muscle forces if the position, velocity, acceleration and external forces are known.

OBJECTIVES

This chapter addresses:

- The differences between medical and technical descriptions of movement.
- The general way to describe rigid body motion with a translation vector and a rotation matrix.
- Some alternatives in 3-D to derive rotation angles from the rotation matrix, e.g. Euler angles, Euler parameters and helical axes.
- The pitfalls of the different angle definitions.
- The protocol to derive a movement description from a set of measured positions.

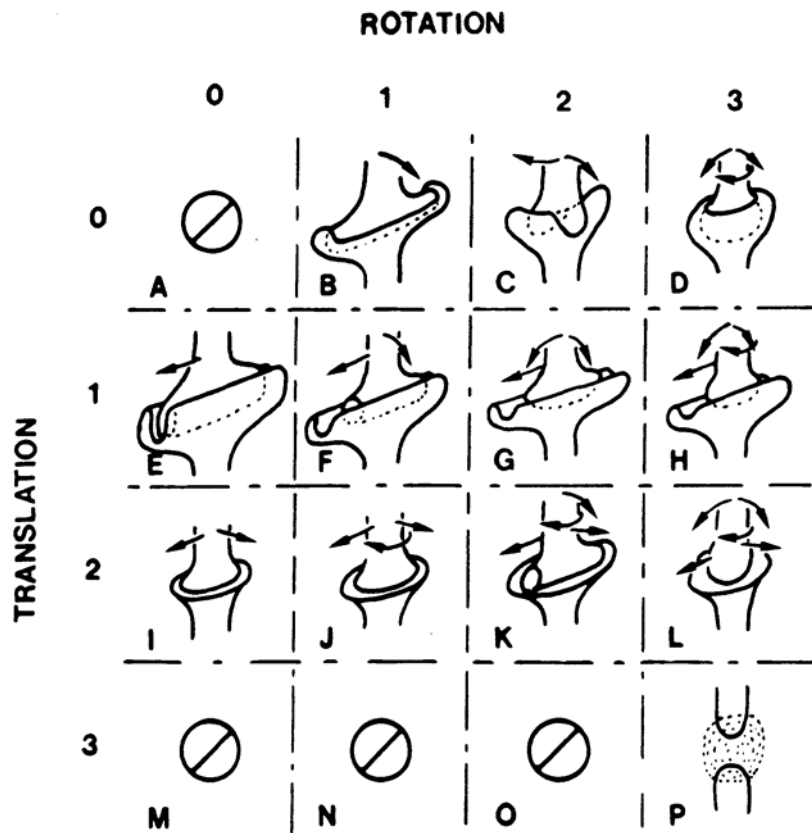


Figure 2.1: Combinations of constraints on rotational and translational degrees of freedom opposed by different types of joints. Many of the shown joints are hypothetical and are not found in the human body. Names of most common joints: A-Bracket; B-Hinge; C-Saddle; D-spherical; E-prismatic/slider; F-Cylindrical; J-planar.

2.1 Joints

Two bones can move with respect to each other by virtue of the joint in between. In the human body three types of joints are discerned:

1. *Junctura fibrosa*: Two bones are connected by connective tissue (collagen fibers). An example is the junction between the pubic bones in the pelvis.
2. *Junctura cartilaginea*: Two bones are connected by cartilage in between. An example is the junction between the ribs and the sternum, and the ribs and the spinal column.
3. *Junctura synovialis*: Two bones are connected by a synovial joint. Synovia is the fluid in the articular junction. These types of joints have cartilage at the articular surfaces and a capsule surrounding the joint, which contains the synovial fluid. Parts of the capsule are often strengthened by collagen fibers: intracapsular ligaments. It is sometimes difficult to discriminate the borders of the ligaments from the capsule.

Since the first two types of articulations do not permit much motion, in this course only the synovial joints (the most common, most moveable type of joint like the shoulder, knee and ankle joint), will be studied in more detail. In

Degrees-of-Freedom (DOF)

restraint

constraint

principle, a bone has six degrees-of-freedom (DOF) of motion with respect to the other bone: three rotations and three translations. The motions of the joint are limited by passive structures like the articular surfaces and the ligaments. These passive structures pose *restraints* to the joint motions: Though motions in the direction of the restraint are still possible, these motions will be very small. For example, cartilage can be compressed a few millimeters. Most of the time these small motions are neglected, and the motion is said to be *constrained*. For each *constraint* the number of DOF diminishes by one. As soon as constraints are coming into the picture, one has already started modeling the joint. In Figure 2.1 all combinations of (constrained) rotations and translations are shown. Many of them are merely hypothetical, and will not be found in the human body. Traditionally, joints have been studied (e.g. by Fick, 1911) by comparing them with standard revolute joints: Hinges, spherical joints, ellipsoidal joints, saddle joints (see Figure 2.2). In the human body, joints can be found, which motions quite resemble these standardized revolute joints. The shoulder joint and the hip joint behave approximately as spherical joints only permitting three rotational DOF. The elbow joint and finger joints can be regarded as hinge joints with one rotational DOF. The first thumb joint and the ankle joint resemble a saddle joint, having two non-intersecting rotational axes. But many times one can not derive the potential motions from the shape of the articular surfaces. For example, the knee joint shows a complex combination of translations and rotations, resulting from an interaction between the articular surfaces and the knee ligaments. The sternoclavicular joint between the sternum and the clavicle almost subluxates at the end of the arm elevation.

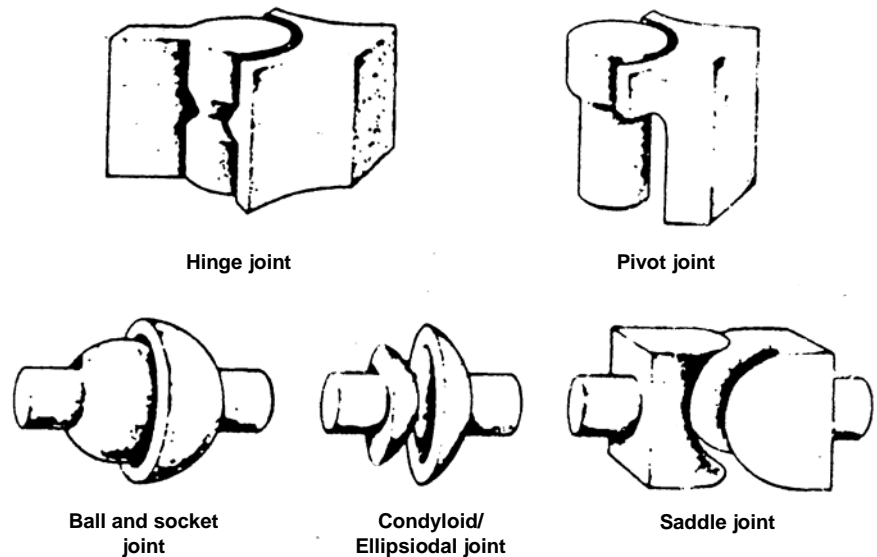


Figure 2.2: Examples of standard revolute joints (Fick, 1911).

2.2 Motion description

2.2.1 MEDICAL DEFINITIONS

Since physicians were the first to study joint motions, medical definitions still dominate the way joint motions are described. The medical definitions are to distinguish between pathological and normal motion and to evaluate the outcome of treatments: Is there improvement in the range of motion?

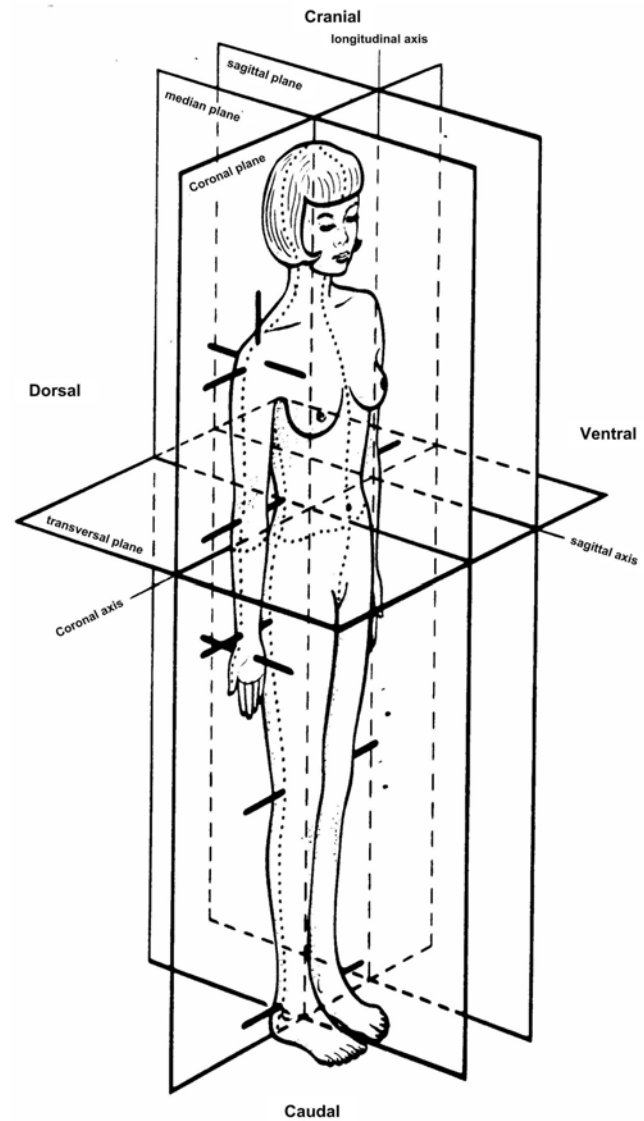


Figure 2.1: The anatomical position.

arthrokinematics
osteokinematics

anatomical
position

Motions are described in two ways: *arthrokinematics* and *osteokinematics*. In arthrokinematics the motions of the articular surfaces with respect to each other are described, like slip, roll and spin. In osteokinematics the motion of a bone with respect to the proximal (towards the center of the body) bone is described. As a starting position the *anatomical position* is used: a well-defined position of the human body¹ (Figure 2.3). From this position the motion is defined for each single rotation apart. For spherical joints the rotation axes are defined along the axis of the global coordinate system: a vertical axis and two horizontal axes, pointing backward-forward and medial-lateral (from the center of the body to the left or right outside). Often used terms are flexion-extension (bending and stretching a joint), abduction-adduction (rotations about a backward-forward axis outside and inside, respectively), anteflexion-retroflexion (rotations about a

¹ The anatomical position is officially defined in the Nomina Anatomica: A kind of dictionary of anatomical terms and concepts.

medial-lateral axis, forward and backward respectively), endorotation-exorotation (rotation about a vertical axis, towards and away from the body respectively). A problem occurs if the motion is not about just one of the standardized axis, but is a combination of rotations. The order of rotations is not defined and it is not clear whether the rotation axes move with the bone or not. This still results in much confusion about rotation angles, and makes the comparison between studies often impossible.

The ‘Codman-paradox’ is an example of one of the pitfalls encountered when you do not take into account the order of rotations. Start with your arm hanging down, with the palm of the hand facing forward. You should try the following:

1. Rotate the arm 90 degrees forward around a medial – lateral axis.
2. Subsequently rotate the arm 90 degrees sideward around a vertical axis.
3. Then rotate the arm 90 degrees downward around a ventral - dorsal axis.
4. Look where the palm of your hand is facing.

And see what happens if the rotation order is changed:

1. Rotate the arm 90 degrees sideward around a ventral - dorsal axis.
2. Subsequently rotate the arm 90 degrees towards the front of the body around a vertical axis.
3. Then rotate the arm 90 degrees downward around a medial - lateral axis.
4. Look where the palm of your hand is facing now!

2.2.2 TECHNICAL DEFINITIONS

2.2.2.1 Transformation matrices

Vectors do not change when shifting from one coordinate system to another. However their components do. A vector \underline{r} to a point P can be expressed in different coordinate systems (Figure 2.4). For example, we define a global reference system (G) defined by the axis $X1, Y1, Z1$, and a local reference system (L) defined by the axis $X2, Y2, Z2$. The origins of G and L coincide. Note that the names for the coordinate systems are arbitrary.

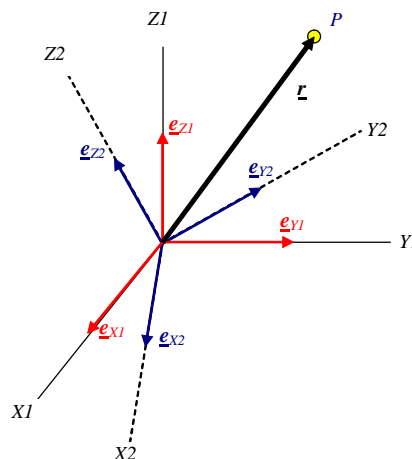


Figure 2.4: A vector \underline{r} can be expressed in various coordinate systems, for example in $X1, Y1, Z1$ or in $X2, Y2, Z2$. $\underline{e}_{x1}, \underline{e}_{y1}, \dots$ are the unit vectors along the axes of the coordinate systems.

First, a note on the conventions used in this reader: bold capitals are used to denote matrices, underlined lowercase bold characters are used to denote vectors. Vectors have a superscript prefix of the coordinate system in which

they are defined.

\underline{r} can be expanded in G and L as:

$$\underline{r} = r_{X1} \underline{e}_{X1} + r_{Y1} \underline{e}_{Y1} + r_{Z1} \underline{e}_{Z1} \quad (2.1)$$

and:

$$\underline{r} = r_{X2} \underline{e}_{X2} + r_{Y2} \underline{e}_{Y2} + r_{Z2} \underline{e}_{Z2} \quad (2.2)$$

where \underline{e}_{X1} , \underline{e}_{Y1} , \underline{e}_{Z1} , \underline{e}_{X2} , \underline{e}_{Y2} , \underline{e}_{Z2} are the unit vectors along the $X1$, $Y1$, $Z1$, $X2$, $Y2$, $Z2$ axis respectively. The vectors that define \underline{r} in both coordinate systems are defined as:

$${}^G \underline{r} \equiv [r_{X1} \quad r_{Y1} \quad r_{Z1}]$$

$${}^L \underline{r} \equiv [r_{X2} \quad r_{Y2} \quad r_{Z2}]$$

r_{X1} , r_{Y1} , r_{Z1} are the projections of \underline{r} on \underline{e}_{X1} , \underline{e}_{Y1} , \underline{e}_{Z1} :

$$\begin{aligned} r_{X1} &= {}^G \underline{r} \cdot {}^G \underline{e}_{X1} \\ r_{Y1} &= {}^G \underline{r} \cdot {}^G \underline{e}_{Y1} \quad , \\ r_{Z1} &= {}^G \underline{r} \cdot {}^G \underline{e}_{Z1} \end{aligned} \quad (2.3)$$

and r_{X2} , r_{Y2} , r_{Z2} are the projections (no vectors!) of \underline{r} on \underline{e}_{X2} , \underline{e}_{Y2} , \underline{e}_{Z2} :

$$\begin{aligned} r_{X2} &= {}^L \underline{r} \cdot {}^L \underline{e}_{X2} \\ r_{Y2} &= {}^L \underline{r} \cdot {}^L \underline{e}_{Y2} \\ r_{Z2} &= {}^L \underline{r} \cdot {}^L \underline{e}_{Z2} \end{aligned} \quad (2.4)$$

In Equations 2.3 and 2.4, the dot denotes the inner product. The vector \underline{r} defined in coordinate system G can be projected on the axis \underline{e}_{X2} , \underline{e}_{Y2} , \underline{e}_{Z2} , which are the unit vectors along the axis $X2$, $Y2$, $Z2$ of the coordinate system L :

$$\begin{aligned} r_{X2} &= {}^G \underline{r} \cdot {}^G \underline{e}_{X2} = (r_{X1} \underline{e}_{X1} + r_{Y1} \underline{e}_{Y1} + r_{Z1} \underline{e}_{Z1}) \cdot {}^G \underline{e}_{X2} \\ r_{X2} &= r_{X1} \underline{e}_{X1} \cdot {}^G \underline{e}_{X2} + r_{Y1} \underline{e}_{Y1} \cdot {}^G \underline{e}_{X2} + r_{Z1} \underline{e}_{Z1} \cdot {}^G \underline{e}_{X2} \\ r_{Y2} &= {}^G \underline{r} \cdot {}^G \underline{e}_{Y2} = (r_{X1} \underline{e}_{X1} + r_{Y1} \underline{e}_{Y1} + r_{Z1} \underline{e}_{Z1}) \cdot {}^G \underline{e}_{Y2} \\ r_{Y2} &= r_{X1} \underline{e}_{X1} \cdot {}^G \underline{e}_{Y2} + r_{Y1} \underline{e}_{Y1} \cdot {}^G \underline{e}_{Y2} + r_{Z1} \underline{e}_{Z1} \cdot {}^G \underline{e}_{Y2} \\ r_{Z2} &= {}^G \underline{r} \cdot {}^G \underline{e}_{Z2} = (r_{X1} \underline{e}_{X1} + r_{Y1} \underline{e}_{Y1} + r_{Z1} \underline{e}_{Z1}) \cdot {}^G \underline{e}_{Z2} \\ r_{Z2} &= r_{X1} \underline{e}_{X1} \cdot {}^G \underline{e}_{Z2} + r_{Y1} \underline{e}_{Y1} \cdot {}^G \underline{e}_{Z2} + r_{Z1} \underline{e}_{Z1} \cdot {}^G \underline{e}_{Z2} \end{aligned} \quad (2.5)$$

These equations can be written in matrix form as:

$${}^L \underline{r} = \begin{bmatrix} r_{X2} \\ r_{Y2} \\ r_{Z2} \end{bmatrix} = \begin{bmatrix} {}^G \underline{e}_{X1} \cdot {}^G \underline{e}_{X2} & {}^G \underline{e}_{Y1} \cdot {}^G \underline{e}_{X2} & {}^G \underline{e}_{Z1} \cdot {}^G \underline{e}_{X2} \\ {}^G \underline{e}_{X1} \cdot {}^G \underline{e}_{Y2} & {}^G \underline{e}_{Y1} \cdot {}^G \underline{e}_{Y2} & {}^G \underline{e}_{Z1} \cdot {}^G \underline{e}_{Y2} \\ {}^G \underline{e}_{X1} \cdot {}^G \underline{e}_{Z2} & {}^G \underline{e}_{Y1} \cdot {}^G \underline{e}_{Z2} & {}^G \underline{e}_{Z1} \cdot {}^G \underline{e}_{Z2} \end{bmatrix} \begin{bmatrix} r_{X1} \\ r_{Y1} \\ r_{Z1} \end{bmatrix} = {}^{LG} \mathbf{T}^G \underline{r}$$

(2.6)

In this equation the transformation matrix ${}^L G \mathbf{T}$ transforms the vector $\underline{\mathbf{r}}$ from coordinate system G into coordinate system L . Since the origins of both coordinate systems coincide, ${}^L G \mathbf{T}$ is called a rotation matrix. It describes the rotation from the local coordinate system L to the coordinate system G (the global coordinate system). The first prefix describes the coordinate system to which the vectors are rotated; the second prefix describes the coordinate system in which the vector is described. The rotation matrix ${}^L G \mathbf{T}$ can only rotate vectors described in coordinate system L .

The elements of the rotation matrix are the inner products of the unit vectors along the axis of both coordinate systems. The inner product between two vector can (by definition) also be expressed by the cosines of the angles between these vectors:

$${}^L G \mathbf{T} = \begin{bmatrix} \cos({}^G \underline{\mathbf{e}}_{X1}, {}^G \underline{\mathbf{e}}_{X2}) & \cos({}^G \underline{\mathbf{e}}_{Y1}, {}^G \underline{\mathbf{e}}_{X2}) & \cos({}^G \underline{\mathbf{e}}_{Z1}, {}^G \underline{\mathbf{e}}_{X2}) \\ \cos({}^G \underline{\mathbf{e}}_{X1}, {}^G \underline{\mathbf{e}}_{Y2}) & \cos({}^G \underline{\mathbf{e}}_{Y1}, {}^G \underline{\mathbf{e}}_{Y2}) & \cos({}^G \underline{\mathbf{e}}_{Z1}, {}^G \underline{\mathbf{e}}_{Y2}) \\ \cos({}^G \underline{\mathbf{e}}_{X1}, {}^G \underline{\mathbf{e}}_{Z2}) & \cos({}^G \underline{\mathbf{e}}_{Y1}, {}^G \underline{\mathbf{e}}_{Z2}) & \cos({}^G \underline{\mathbf{e}}_{Z1}, {}^G \underline{\mathbf{e}}_{Z2}) \end{bmatrix} \quad (2.7)$$

Defining a transformation in the other direction (from local to global) is done in exactly the same way, which yields:

$${}^G \underline{\mathbf{r}} = {}^G L \mathbf{T} {}^L \underline{\mathbf{r}} \quad (2.8)$$

Exercise

- 1) Show that ${}^G L \mathbf{T} = ({}^L G \mathbf{T})^T$
- 2) Determine in which cases $({}^G L \mathbf{T})^T \neq ({}^G L \mathbf{T})^{-1}$

Equation 2.8 can be used to express the unit base vectors of the local coordinate system defined in L into the global coordinate system:

$$\begin{aligned} {}^G \underline{\mathbf{e}}_{X2} &= {}^G L \mathbf{T} {}^L \underline{\mathbf{e}}_{X2} \\ {}^G \underline{\mathbf{e}}_{Y2} &= {}^G L \mathbf{T} {}^L \underline{\mathbf{e}}_{Y2} \\ {}^G \underline{\mathbf{e}}_{Z2} &= {}^G L \mathbf{T} {}^L \underline{\mathbf{e}}_{Z2} \end{aligned} \quad (2.9)$$

Since the unit vectors in coordinate system L (see Figure 2.4) were chosen as orthonormal unit vectors, they are expressed as:

$${}^L \underline{\mathbf{e}}_{X2} = \begin{bmatrix} 1 \\ 0 \\ 0 \end{bmatrix}, {}^L \underline{\mathbf{e}}_{Y2} = \begin{bmatrix} 0 \\ 1 \\ 0 \end{bmatrix}, {}^L \underline{\mathbf{e}}_{Z2} = \begin{bmatrix} 0 \\ 0 \\ 1 \end{bmatrix} \quad (2.10)$$

After the substitution of Equation 2.10 into Equation 2.9, a special property of this transformation can be shown:

$${}^G L \mathbf{T} = \begin{bmatrix} {}^G \underline{\mathbf{e}}_{X2} & {}^G \underline{\mathbf{e}}_{Y2} & {}^G \underline{\mathbf{e}}_{Z2} \end{bmatrix} \quad (2.11)$$

This equation shows that the rotation matrix from a local to a global coordinate

system can be obtained by calculating the orthonormal vectors of a local coordinate system in global coordinates. This expression will prove very useful in recording of (human) motion (see Section 2.3).

So in case the unit vectors \underline{e}_{x2} , \underline{e}_{y2} , \underline{e}_{z2} are orthogonal the columns of \mathbf{T} are orthogonal as well. Therefore, the transformation matrix has the property that:

$$({}^{GL}\mathbf{T})^T ({}^{GL}\mathbf{T}) = \mathbf{I} \quad (2.12)$$

This means that $\mathbf{T}^T = \mathbf{T}^{-1}$. This special property permits an easy inversion of Equation 2.8 to obtain:

$${}^L\underline{\mathbf{r}} = ({}^{GL}\mathbf{T})^T ({}^G\underline{\mathbf{r}}) \quad (2.13)$$

When the origins of two coordinate systems do not coincide the translations of the coordinate system must also be taken into account and the rotation matrix and transformation matrix are no longer the same.

Mathematically, the motion of a body with respect to another body can be described unambiguously by a [3x3] *rotation matrix* \mathbf{R} and a *translation vector* $\underline{\mathbf{t}}$ (see Figure 2.5):

$${}^G\underline{\mathbf{r}} = {}^G\underline{\mathbf{t}} + {}^{GL}\mathbf{R} {}^L\underline{\mathbf{r}} \quad (2.14)$$

rotation matrix
translation vector

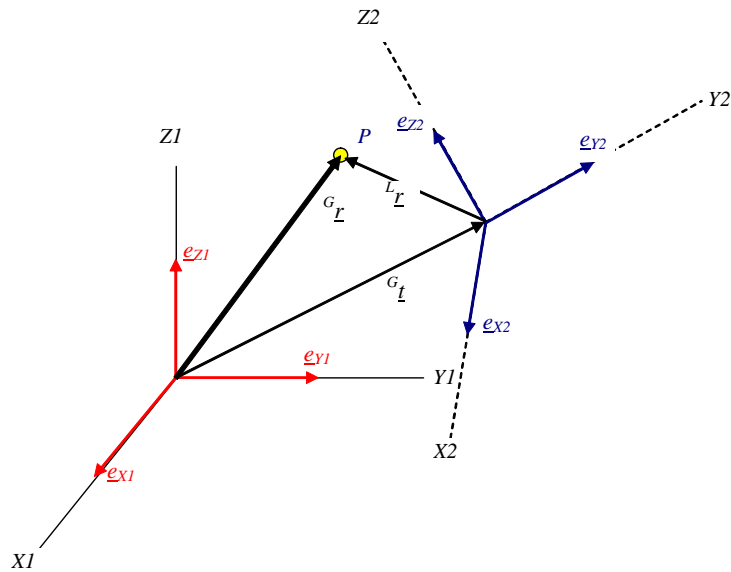


Figure 2.5: ${}^G\underline{\mathbf{r}}$ is the position vector of point P in the global coordinate system G; ${}^L\underline{\mathbf{r}}$ is the position vector of point P in the local coordinate system L; ${}^G\underline{\mathbf{t}}$ is the translation vector from the origin of A expressed in coordinate system G. A transformation of a vector $\underline{\mathbf{r}}$ from a local coordinate system L (X_2, Y_2, Z_2) into the global coordinate system G (X_1, Y_1, Z_1) can be described by the summation of the translation ${}^G\underline{\mathbf{t}}$ of the origin of the local coordinate system and a of the rotation of the local vector ${}^L\underline{\mathbf{r}}$ into global coordinates, resulting in the vector ${}^G\underline{\mathbf{r}}$.

An alternative form for Equation 2.14 is:

$$\begin{bmatrix} {}^G\underline{\mathbf{r}} \\ 1 \end{bmatrix} = \begin{bmatrix} {}^{GL}\mathbf{R} & | & {}^G\underline{\mathbf{t}} \\ \hline 0 & 0 & 0 & | & 1 \end{bmatrix} \begin{bmatrix} {}^L\underline{\mathbf{r}} \\ 1 \end{bmatrix} = {}^{GL}\mathbf{T} \begin{bmatrix} {}^L\underline{\mathbf{r}} \\ 1 \end{bmatrix} \quad (2.15)$$

In this form, the combination of a translation vector and a rotation matrix were combined to a newly defined transformation matrix ${}^{GL}T$. In the rotation matrix ${}^{GL}R$, nine directional cosines define the orientation of the $X1, Y1, Z1$ -axes relatively to the $X2, Y2, Z2$ -axes. However, these nine values are not independent. The reason for this is that the unit vectors of a coordinate system cannot move or rotate with respect to each other. Rotation around one unit vector also implies rotation of the other unit vectors. In formula form this is seen when substituting Equation 2.7 into Equation 2.12. It results in six constraint equations (three of the nine equations are repeated twice). Thus, only three directional cosines are independent. Although it is possible to adopt the directional cosines constraint to six constraints as rotational coordinates, this is neither practical nor convenient.

Exercise:

- Use Equations 2.7 and 2.12 to obtain three rotational coordinates that describe the orientation of two different orthonormal coordinate systems.

2.2.2.2 Axis Rotation Matrix

Rotation matrices of a single rotation about an axis of the coordinate system have a special structure. From Figure 2.6 it is easily seen that:

$$y_1 = y_2 \cos(\phi) - z_2 \sin(\phi) \tag{2.16}$$

$$z_1 = y_2 \sin(\phi) + z_2 \cos(\phi) \tag{2.17}$$

where y_1 and z_1 are the projections of the vector \underline{r} on the $Y1, Z1$ axes (coordinate system G) ; y_2 and z_2 are the projections on the $Y2, Z2$ axes (coordinate system A); ϕ is the angle of rotation around the shared X -axis of the coordinate systems.

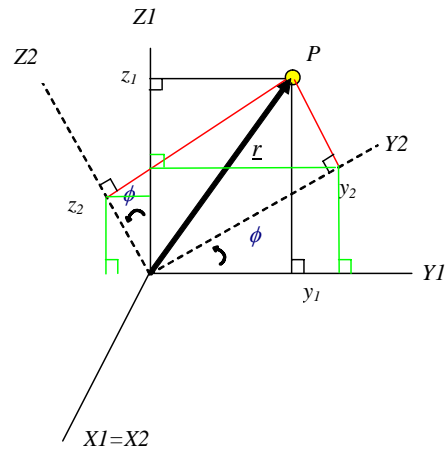


Figure 2.6: The projection of the vector \underline{r} changes when the coordinate system is rotated around the X axis with an angle ϕ .

When the global coordinate system G is defined by $X1, Y1, Z1$ and the coordinate system A by $X2, Y2, Z2$ it follows that the rotation matrix around the X -axis is:

$${}^{GA}\mathbf{R}_x(\phi) = \begin{bmatrix} 1 & 0 & 0 \\ 0 & c\phi & -s\phi \\ 0 & s\phi & c\phi \end{bmatrix} \quad (2.18)$$

c and s denote the cosine and sine functions respectively. In the same way the rotation matrix for rotations θ and ψ about the Y- or Z-axis can be derived:

$${}^{GA}\mathbf{R}_y(\theta) = \begin{bmatrix} c\theta & 0 & s\theta \\ 0 & 1 & 0 \\ -s\theta & 0 & c\theta \end{bmatrix} \quad (2.19)$$

$${}^{GA}\mathbf{R}_z(\psi) = \begin{bmatrix} c\psi & -s\psi & 0 \\ s\psi & c\psi & 0 \\ 0 & 0 & 1 \end{bmatrix} \quad (2.20)$$

The rotation matrices \mathbf{R}_x , \mathbf{R}_y and \mathbf{R}_z are called the axis-rotation matrices and will be used in the next paragraph.

Exercises

- Derive Equations 2.19 and 2.20 yourself.
- Equations 2.18-2.20 are valid for a right-handed coordinate system. How do the axis rotation matrices change when we have a left-handed coordinate system?

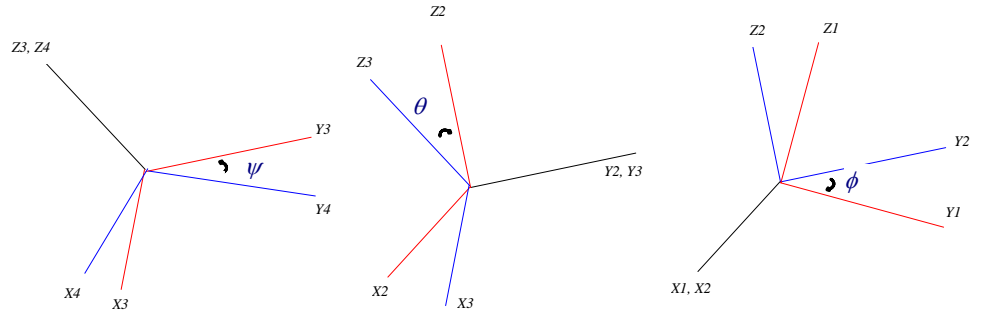
2.2.2.3 Orientation angles- Euler/ Cardanian Angles

The axis rotation matrices of the previous paragraph can be used to transform a vector from one reference to another by successive rotations around different axis. The sequence of the axis rotations can be chosen from a total of 12 different combinations (Table 2.1).

Table 2.1: Overview of sequences of axis rotations to describe the rotation from one coordinate system to another.

	Cardan systems $i \neq j \neq k$		Euler systems $i = k \neq j$	
Cyclic	XYZ		XYX	
	YZX	Cardan angles	YZY	Euler angles
	ZXY		ZXZ	
Anti cyclic	ZYX		ZYZ	
	XZY	Nautic angles	XZX	Euler angles
	YXZ		YXY	

It is important to understand that a former axis transformation determines the latter axis transformation (Figure 2.7): rotation around the first axis will change the orientation of the second and third axes, rotation around the second axis will change the orientation of the third axis, and rotation about the third axis will result in the desired orientation of the coordinate system.



Exercise:

- Sketch on a similar way as Figure 2.7 the successive rotations of the axes of a coordinate system using cardan angles for the case in which the second rotation is 90°. Explain what happens.
- Sketch on a similar way as Figure 2.7 the successive rotations of the axes of a coordinate system using Euler angles for the case in which the second rotation is 180°. Explain what happens.

When the local coordinate system L is defined by X4, Y4, Z4 and the global coordinate system G by X1, Y1, Z1 the three successive rotations ψ , θ and ϕ of Figure 2.7 result in:

$$\begin{aligned}
 {}^{GL}\mathbf{R} &= {}^{GL''}\mathbf{R}_x \cdot {}^{L''L'}\mathbf{R}_y \cdot {}^{L'L}\mathbf{R}_z = \\
 &= \begin{bmatrix} 1 & 0 & 0 \\ 0 & c\phi & -s\phi \\ 0 & s\phi & c\phi \end{bmatrix} \begin{bmatrix} c\theta & 0 & s\theta \\ 0 & 1 & 0 \\ -s\theta & 0 & c\theta \end{bmatrix} \begin{bmatrix} c\psi & -s\psi & 0 \\ s\psi & c\psi & 0 \\ 0 & 0 & 1 \end{bmatrix} = \\
 &= \begin{bmatrix} c\theta c\psi & -c\theta s\psi & s\theta \\ s\psi c\phi + s\theta c\psi s\phi & c\psi c\phi - s\theta s\psi s\phi & -c\theta s\phi \\ s\psi s\phi - s\theta c\psi c\phi & c\psi s\phi + s\theta s\psi c\phi & c\theta c\phi \end{bmatrix} \quad (2.21)
 \end{aligned}$$

Note that ${}^{L''L'}\mathbf{R}_y$ describes the rotation around the y-axis of the intermediate coordinate system L'. This axis coincides, because of the nature of the rotation, with the y-axis of intermediate coordinate system L''. Likewise, the z-axis of L' coincides with the z-axis of L and the x-axis of L'' coincides with the x-axis of G. Normally, the reverse of this operation will take place: A rotation matrix ${}^{GL}\mathbf{R}$ reconstructed from measurements (using Equation 2.11) will be decomposed into three rotation matrices with the accompanying Euler angles. From Equation 2.21 ϕ , θ and ψ can be found:

$$\begin{aligned}
 \theta &= \text{asin}({}^{GL}\mathbf{R}_{1,3}) \\
 \psi &= \text{atan2}(-{}^{GL}\mathbf{R}_{1,2} / {}^{GL}\mathbf{R}_{1,1}) \\
 \phi &= \text{atan2}(-{}^{GL}\mathbf{R}_{2,3} / {}^{GL}\mathbf{R}_{3,3})
 \end{aligned} \quad (2.22)$$

where atan2 is a special mathematical function, e.g. in Matlab, in which the arctangent is defined for the four quadrants. However, a second solution exists since $\sin(\theta) = \sin(\pi - \theta)$, and multiple values for ϕ and ψ can be found. Recently, it has been proposed in the standardization of joint rotations to choose the solution with θ between -90° and 90° .

Instead of the order x - y - z any other combination of these rotations could have been chosen. Since matrix multiplication is not a commutative operation (remember the Codman paradox!), each sequence of rotations will result in other values of ϕ , θ and ψ . Figure 2.8 demonstrates that reversing the order of rotation indeed results in a different position.

Other possible combinations of rotation have the first and third rotation about the same axis, though this axis is moved due to the second rotation, e.g. the order y - z - y . Here, it is advised to choose the solution in which the second rotation is between 0° and 180° .

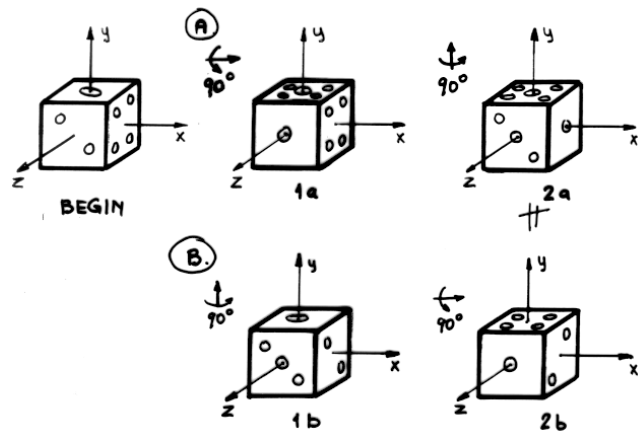


Figure 2.8: In situation A) the die is first rotated 90° about the x -axis and then 90° about the y -axis. In B) the first rotation is 90° about the y -axis and then 90° about the x -axis. Different orientations result.

gimbal lock

A pitfall of using Euler and Cardan angles is the *gimbal lock* position. The term 'gimbal lock' comes from the physical situation in which three consecutive orthogonal hinges (rotation axes) are present, for example in a gyroscope. Then, if the second hinge is rotated -90° or 90° , the first and third hinge coincide. All three hinges are located in one plane. If now a rotation is desired around an axis out of this plane, this can not be achieved: The system is 'locked' and the gyroscope can not take every desired orientation. Only a rotation around the second axis can 'unlock' the system.

In Cardan angle calculations this situation occurs if the second rotation is -90° or 90° . When in case of Euler angle calculations the second rotation is 0° or 180° , the first and third axis coincide and a singular position results.

Worse than the gimbal lock itself, near the gimbal lock position the calculated angles become very sensitive to measurement noise. For example, in case that $\phi = 30^\circ$, $\theta = 89^\circ$ and $\psi = 60^\circ$, the rotation matrix ${}^{GA}\mathbf{R}$ becomes:

$${}^{GA}\mathbf{R} = \begin{bmatrix} 0.0087 & -0.0151 & 0.9998 \\ 1.0000 & 0.0001 & -0.0087 \\ 0.0001 & 0.9999 & 0.0151 \end{bmatrix}$$

If noise is simulated on the elements of ${}^{GA}\mathbf{R}$, e.g. by adding a small noise matrix

N , ${}^G\mathbf{R}$ becomes:

$$N = \begin{bmatrix} 0.0022 & 0.0068 & 0.0052 \\ 0.0005 & 0.0093 & 0.0083 \\ 0.0068 & 0.0038 & 0.0003 \end{bmatrix} \quad {}^G\mathbf{R}' = \begin{bmatrix} 0.0109 & -0.0083 & 1.0050 \\ 1.0004 & 0.0094 & -0.0004 \\ 0.0069 & 1.0037 & 0.0155 \end{bmatrix}$$

Reconstruction of the angles with the noisy rotation matrix ${}^G\mathbf{R}'$, results in values of $\phi = 1.5^\circ$, $\theta = 89.1^\circ$ and $\psi = 37.3^\circ$. Within about 20° of the gimbal lock position, this noise amplification effect will be present.

Nothing can be done once the system is in a gimbal lock position. Therefore, the gimbal lock position should be avoided by a proper definition of the rotation order, such that the second rotation is not likely to become $90^\circ / -90^\circ$ or $0^\circ / 180^\circ$ for Cardan or Euler angles respectively.

Application of Euler angles for joint rotations

Euler angles can only be used to describe rotations. Any translations in the joints are neglected. Therefore, applications to spherical joints and hinge joints are most suited.

In *spherical joints* there are three rotational DOF. The rotation in the joint, with proximal (towards the center of the body) system A and distal (towards the outside of the body) system B , can be written as:

$$\begin{aligned} {}^G\mathbf{B} &= {}^G\mathbf{R} {}^A\mathbf{B} = {}^G\mathbf{R} {}^B\mathbf{B} = {}^G\mathbf{R} \Rightarrow \\ {}^A\mathbf{B} &= {}^A\mathbf{R} {}^G\mathbf{R} = {}^A\mathbf{B} \end{aligned} \quad (2.23)$$

where ${}^A\mathbf{B}$, the base of B expressed in coordinates of A (so ${}^B\mathbf{B}$ is the unit matrix), equals the relative (joint) rotation matrix ${}^A\mathbf{B}$ from B to A . This rotation matrix can be decomposed into Cardan angles to obtain a representation of the joint angles. A good choice of rotation order is to save the last rotation about the longitudinal axis (~axial rotation) of the distal bone. Then the first two rotations can be used to describe the orientation of the longitudinal axis with respect to the proximal bone.

In hinge joints the application of Euler angles is more difficult. There is only one DOF present, and it would be a pure coincidence if this rotation axis coincides with one of the rotation axes of the proximal local coordinate system. However, there always exist constant rotation matrices that project the axis of rotation on an axis (in coordinate system C) for which the rotation matrix is known, for example $\mathbf{R}_z(\psi)$ in Equation 2.20:

$${}^A\mathbf{B} = ({}^A\mathbf{R})({}^B\mathbf{B}) = {}^A\mathbf{B} = {}^A\mathbf{R} {}^C\mathbf{C}' \mathbf{R} {}^C'B = {}^A\mathbf{R} {}^C\mathbf{C}' \mathbf{R}_z(\psi) {}^C'B \quad (2.24)$$

This describes the single rotation ψ about the z -axis, where the orientation of the z -axis is defined by the constant rotations ${}^A\mathbf{R}$ and ${}^C'B$.

For application to joints with substantial translations, the Cardan angles must be combined with a translation vector from a point in the proximal local coordinate system to a point in the distal local coordinate system. The best choice would be the joint rotation center, in which both points in the proximal and distal local coordinate system would coincide in the initial position. The choice of this initial point will affect the calculated translation, since motion of the distal point will be partly due to translations, partly due to rotations. It is difficult to find a 'joint rotation center', since obviously it is not a fixed point whenever translations are present.

2.2.2.4 Helical axis

The sequence dependence of the Euler angles and the occurrence of gimbal lock positions resulted in a search for other parameterizations of the rotation matrix, like Euler parameters, quaternions and helical axis.

The motion of a rigid body from one position to another can be described as a combination of a rotation about an axis and a translation along the same axis. There is only one unique axis for which this is true. This axis is called the *helical axis* or *screw axis* (see Figure. 2.9). More precisely, this is called the Finite Helical Axis (FHA). In contrast, the Instantaneous Helical Axis (IHA) describes the angular velocity vector ω of the moving rigid body at a certain time t . If the time interval Δt between the two positions of the FHA approaches zero, the FHA will approach the IHA.

helical axis
screw axis

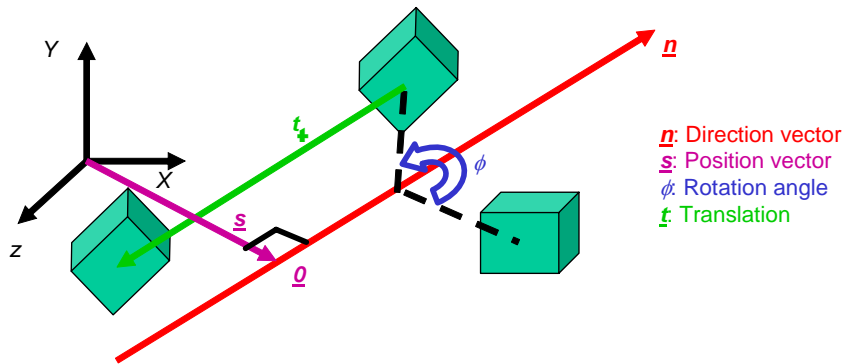


Figure 2.9: The motion of a rigid body from one position to another can be described by a rotation ϕ about the helical axis and a translation \underline{t} along this axis. The helical axis itself is described by position vector \underline{s} and direction vector \underline{n} .

The FHA is characterized by 6 independent parameters, and describes all 6 DOF of the motion between two positions of the distal bone with respect to the proximal bone. These 6 parameters are:

- The unit direction vector \underline{n} (two independent parameters since the length is given as in sphere coordinates),
- the position vector \underline{s} (two independent parameters since \underline{s} is defined perpendicular to \underline{n} , or by the projection of the center of gravity of the rigid body on the helical axis),
- rotation ϕ and
- translation \underline{t} .

Without further derivation, the helical axis parameters can be calculated from the rotation matrix ${}^{GL}\mathbf{R}$ and the translation vector ${}^G\underline{t}$ by

$$\sin(\phi) = 0.5\sqrt{({}^{GL}\mathbf{R}_{3,2} - {}^{GL}\mathbf{R}_{2,3})^2 + ({}^{GL}\mathbf{R}_{1,3} - {}^{GL}\mathbf{R}_{3,1})^2 + ({}^{GL}\mathbf{R}_{1,2} - {}^{GL}\mathbf{R}_{3,2})^2}$$

$$\cos(\phi) = 0.5({}^{GL}\mathbf{R}_{1,1} + {}^{GL}\mathbf{R}_{2,2} + \mathbf{R}_{3,3} - 1)$$

$$\underline{n} = \frac{1}{2 \sin(\phi)} \begin{bmatrix} {}^{GL}R_{3,2} - {}^{GL}R_{2,3} \\ {}^{GL}R_{1,3} - {}^{GL}R_{3,1} \\ {}^{GL}R_{2,1} - {}^{GL}R_{1,2} \end{bmatrix}$$

$$\underline{t} = \underline{n}^T \cdot {}^G \underline{t}$$

$$\underline{s} = -0.5 \underline{n} \times (\underline{n} \times {}^G \underline{t}) + \frac{\sin(\phi)}{2(1 - \cos \phi)} \underline{n} \times {}^G \underline{t}$$
(2.25)

helical angles

From the FHA the *helical angles* ϕ_x, ϕ_y, ϕ_z can be derived, which are defined by the 'vector' $\underline{\phi} = \phi \underline{n} = [\phi_x \phi_y \phi_z]^T$. Advantage of this description is the complete symmetry of the vector components. Disadvantage is the missing physical interpretation of $\underline{\phi}$ since it is defined in a non-linear vector space which does not permit vector addition.

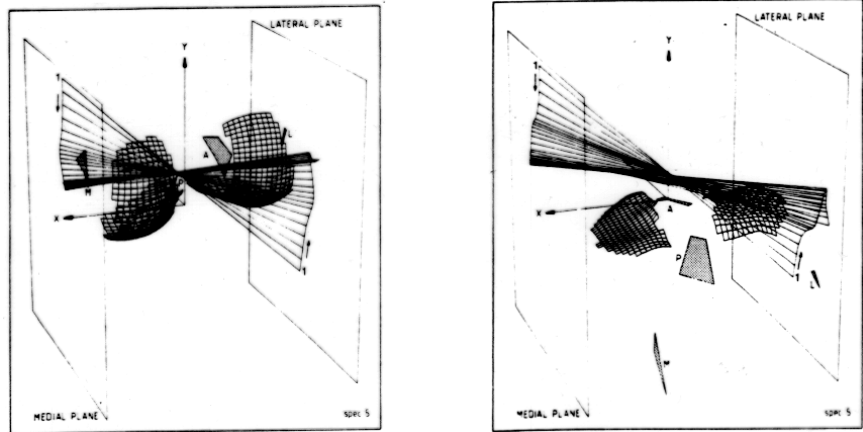


Figure 2.10: The Finite Helical Axis during motions of the knee. For clarity, the intersection points with vertical planes are shown (Blankevoort, 1991).

A clear advantage of the FHA is that it approaches the IHA (i.e. the true joint rotation axis) for small increments Δt . This is illustrated in Figure 2.10 in which the helical axis of a knee motion is shown. Disadvantages are the description and interpretation of the motions of the FHA itself. Another major disadvantage is the sensitivity to measurement errors. In case of very small rotations the orientation \underline{n} of the helical axis and its rotation ϕ are hard to assess. In general, the translation t and especially the position vector \underline{s} are very sensitive to errors in the marker recordings, which can result in quite large offsets of the helical axis. Therefore, the helical axis is most often used for describing rotations in cadaver joints. For measurements in vivo (which means in living subjects) the helical axis is hardly used.

2.2.2.5 Euler parameters

With four Euler parameters a rotation can also be unambiguously described without the disadvantages associated with Euler angles; i.e. the gimbal lock and the sequence dependency. Euler angles are often used in software packages for the forward simulation of the equations of motion; e.g. DADS or SPACAR. Euler's theorem states that the general displacement of a rigid body with one point fixed is a rotation about some axis.

Euler's theorem

As a consequence the coordinates that define the direction of this axis and the angle of rotation around this axis are sufficient to describe the relative orientation of two Cartesian coordinate with a common origin. These coordinates are the Euler Parameters and can be derived with simple vector algebra.

In Figure 2.11 the initial position of vector \underline{r} is denoted by \underline{OP} and the final position \underline{r}' is denoted by \underline{OP}' . The unit vector along the orientation axis of rotation is denoted by \underline{e} . The distance between O and N has the magnitude $\underline{e} \cdot \underline{r}$ so that the vector \underline{ON} can be written as $\underline{e}(\underline{e} \cdot \underline{r})$. In the plane normal to the axis of rotation lies the vector \underline{NP} that can be described as $\underline{r} - \underline{e}(\underline{e} \cdot \underline{r})$, and its magnitude equals that of the vectors \underline{NP}' and $\underline{r} \times \underline{e}$ that both lie in the same plane. Vector \underline{r} can be expressed as the sum of three vectors:

$$\underline{r}' = \underline{ON} + \underline{NQ} + \underline{QP}' \quad (2.26)$$

or

$$\underline{r}' = \underline{e}(\underline{e} \cdot \underline{r}) + ((\underline{r} - \underline{e}(\underline{e} \cdot \underline{r})) \cos(\phi) + (\underline{r} \times \underline{e}) \sin(\phi)) \quad (2.27)$$

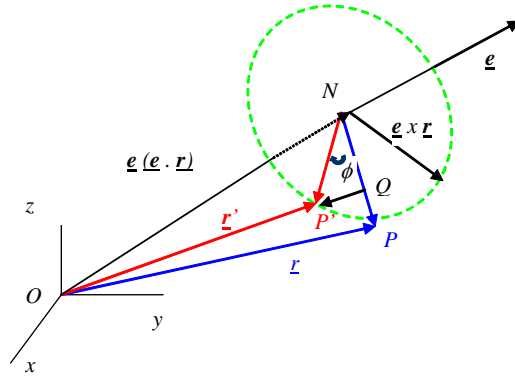


Figure 2.11: Vector diagram for derivation of the rotation formula

rotation formula

Arrangement of terms gives the rotation formula:

$$\underline{r}' = \underline{r} \cos(\phi) + \underline{e}(\underline{e} \cdot \underline{r})(1 - \cos(\phi)) + (\underline{r} \times \underline{e}) \sin(\phi) \quad (2.28)$$

Euler parameters

By introducing the Euler parameters,

$$\lambda_0 = \cos\left[\frac{\phi}{2}\right]$$

$$\underline{\lambda} = \underline{e} \sin\left[\frac{\phi}{2}\right]$$

after some goniometric manipulations (see Goldstein or Jonker) Equation 2.28 can be put into the form:

$$\underline{r}' = (2\lambda_0^2 - 1)\underline{r} + 2\underline{\lambda}(\underline{\lambda} \cdot \underline{r}) - 2\lambda_0(\underline{\lambda} \times \underline{r}) \quad (2.29)$$

From this equation it is apparent that the components of \underline{r}' are linear functions of \underline{r} and thus can be written in matrix notation:

$$\underline{r}' = \left[(2\lambda_0^2 - 1)\mathbf{I} + 2\underline{\lambda}\underline{\lambda}^T - 2\lambda_0\tilde{\underline{\lambda}} \right] \underline{r} \quad (2.30)$$

with

$$\begin{aligned}\underline{\lambda} &= [\lambda_1, \lambda_2, \lambda_3]^T \\ \tilde{\lambda} &= \begin{bmatrix} 0 & -\lambda_3 & \lambda_2 \\ \lambda_3 & 0 & -\lambda_1 \\ -\lambda_2 & \lambda_1 & 0 \end{bmatrix}\end{aligned}\quad (2.31)$$

The term in brackets in Equation 2.30 is the transformation matrix of $\underline{r}' = \mathbf{R}\underline{r}$:

$$\mathbf{R} = \left[(2\lambda_0^2 - 1)\mathbf{I} + 2\underline{\lambda}\underline{\lambda}^T - 2\lambda_0\tilde{\lambda} \right] \quad (2.32)$$

and thus

$$\mathbf{R}^T = \left[(2\lambda_0^2 - 1)\mathbf{I} + 2\underline{\lambda}\underline{\lambda}^T + 2\lambda_0\tilde{\lambda} \right] \quad (2.33)$$

Without further proof the determination of the Euler parameters from the transformation matrix \mathbf{R}^T is:

$$\lambda_0^2 = \frac{\text{trace } \mathbf{R}^T + 1}{4} \quad (2.34a)$$

$$\lambda_1^2 = \frac{1 + 2\mathbf{R}^T_{1,1} - \text{trace } \mathbf{R}^T}{4} \quad (2.34b)$$

$$\lambda_2^2 = \frac{1 + 2\mathbf{R}^T_{2,2} - \text{trace } \mathbf{R}^T}{4} \quad (2.34c)$$

$$\lambda_3^2 = \frac{1 + 2\mathbf{R}^T_{3,3} - \text{trace } \mathbf{R}^T}{4} \quad (2.34d)$$

Equation 2.34 only gives the magnitude of the Euler parameters, not their signs. The sign of λ_0 may be chosen arbitrarily after which the other Euler parameters can be calculated:

$$\lambda_1 = \frac{\mathbf{R}^T_{3,2} - \mathbf{R}^T_{2,3}}{4\lambda_0} \quad (2.35a)$$

$$\lambda_2 = \frac{\mathbf{R}^T_{1,3} - \mathbf{R}^T_{3,1}}{4\lambda_0} \quad (2.35b)$$

$$\lambda_3 = \frac{\mathbf{R}^T_{2,1} - \mathbf{R}^T_{1,2}}{4\lambda_0} \quad (2.35c)$$

Exercise:

- Derive Equation 2.34 (hint: first derive $\sum_{i=1}^4 \lambda_i^2$)
- Express the rotation matrix \mathbf{R} in Euler parameters
- Derive Equation 2.35
- What happens with the angle ϕ and the direction cosines (\underline{e}) associated with the Euler parameters if the sign of λ_0 is inverted?

2.2.2.6 Angular velocity vector

Imagine a point P on a body A . The body rotates with an angular velocity $\underline{\omega}_{A/G}$ relative to O (Figure 2.12). Since the velocity of a body is only defined with respect to another body, one should always use a notation in which this is clear.

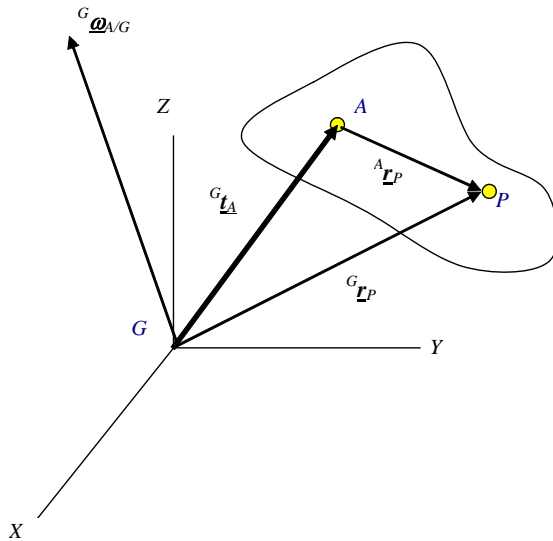


Figure 2.12: A point P on body A that rotates with an angular velocity $\underline{\omega}_{A/G}$

angular velocity vector

The angular velocity vector is defined by

$$\underline{\omega} dt \equiv d\phi \underline{e} \tag{2.36}$$

where $d\phi$ is an infinitely small rotation about the instantaneous axis of rotation defined by the directional cosines of \underline{e} (similar as in Figure 2.11). In magnitude $\underline{\omega}$ measures the instantaneous rate of rotation.

It is important to note that $\underline{\omega}$ is not the derivative of any vector and therefore integration of the angular velocity has no physical meaning!

The velocity of point P can be expressed in the global referenced frame by:

$${}^G \dot{\underline{r}}_P = {}^G \dot{\underline{r}}_A + {}^{GA} \mathbf{R} ({}^A \dot{\underline{r}}_P + {}^A \underline{\omega}_{A/O} \times {}^A \underline{r}_P) \tag{2.37}$$

or by differentiation of Equation 2.14

$${}^G \dot{\underline{r}}_P = {}^G \dot{\underline{r}}_A + {}^{GA} \dot{\mathbf{R}} {}^A \underline{r}_P + {}^{GA} \mathbf{R} {}^A \dot{\underline{r}}_P \tag{2.38}$$

When point P is fixed within body A and the origins of the global coordinate system and of body A coincide the velocity can also be expressed as:

$${}^G \dot{\underline{r}}_P = ({}^G \underline{\omega}_{A/L} \times {}^G \underline{r}_P) = {}^G \underline{\Omega} {}^G \underline{r}_P$$

$${}^G \underline{\Omega} = \begin{bmatrix} 0 & -{}^G \omega_z & {}^G \omega_y \\ {}^G \omega_z & 0 & -{}^G \omega_x \\ -{}^G \omega_y & {}^G \omega_x & 0 \end{bmatrix} \quad (2.39)$$

and

$${}^G \dot{\underline{r}}_P = {}^{GA} \dot{\underline{R}}^A \underline{r}_P = {}^{GA} \dot{\underline{R}} ({}^{GA} \underline{R}^T) {}^G \underline{r}_P \quad (2.40)$$

Comparison of Equations 2.39 and 2.40 results in:

$$\underline{\Omega} = {}^{GA} \dot{\underline{R}} ({}^{GA} \underline{R}^T) \quad (2.41)$$

The angular velocity of a local coordinate system relative to a global coordinate system can be expressed as the time derivatives of the orientation angles that define the orientation of the local coordinate system relative to the global coordinate system. Care should be taken to transform these independent velocity vectors into a common reference frame.

Assume a rotating local coordinate system L that is rotating with respect to a global reference system G (Figure 2.13). The angular velocity vector of L is a vector addition of the derivatives of orientation angles projected in a common reference frame. For example the angular velocity vector of L relative to G can be expressed in the global reference frame.

$${}^G \underline{\omega}_L = \begin{bmatrix} \dot{\phi} \\ 0 \\ 0 \end{bmatrix} + {}^{GA''} \underline{R}_x \begin{bmatrix} 0 \\ \dot{\theta} \\ 0 \end{bmatrix} + {}^{GA''} \underline{R}_x {}^{A''A'} \underline{R}_y \begin{bmatrix} 0 \\ 0 \\ \dot{\psi} \end{bmatrix}$$

$$= \begin{bmatrix} \dot{\phi} \\ 0 \\ 0 \end{bmatrix} + {}^{GA''} \begin{bmatrix} 1 & 0 & 0 \\ 0 & c\phi & -s\phi \\ 0 & s\phi & c\phi \end{bmatrix} \begin{bmatrix} 0 \\ \dot{\theta} \\ 0 \end{bmatrix} + \begin{bmatrix} 1 & 0 & 0 \\ 0 & c\phi & -s\phi \\ 0 & s\phi & c\phi \end{bmatrix} \begin{bmatrix} c\theta & 0 & s\theta \\ 0 & 1 & 0 \\ -s\theta & 0 & c\theta \end{bmatrix} \begin{bmatrix} 0 \\ 0 \\ \dot{\psi} \end{bmatrix}$$

$$= \begin{bmatrix} 1 & 0 & s\phi \\ 0 & c\phi & -s\phi c\theta \\ 0 & s\phi & c\phi c\theta \end{bmatrix} \begin{bmatrix} \dot{\phi} \\ \dot{\theta} \\ \dot{\psi} \end{bmatrix}$$

or in its own local coordinate system. (2.42)

$${}^L \underline{\omega}_{L/G} = \begin{bmatrix} 0 \\ 0 \\ \dot{\psi} \end{bmatrix} + {}^{A'L} \underline{R}_z^T \begin{bmatrix} 0 \\ \dot{\theta} \\ 0 \end{bmatrix} + {}^{A'L} \underline{R}_z^T {}^{A''A'} \underline{R}_y^T \begin{bmatrix} \dot{\phi} \\ 0 \\ 0 \end{bmatrix} \quad (2.43)$$

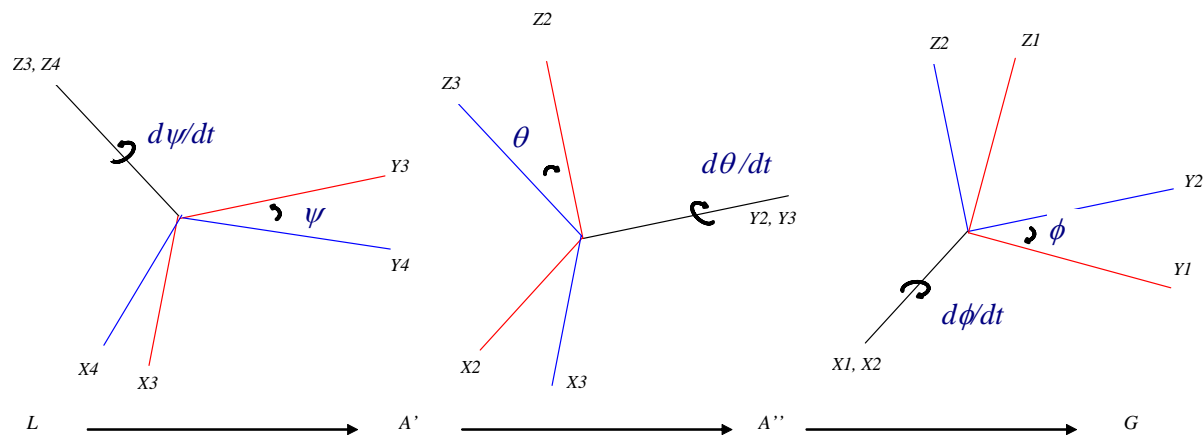


Figure 2.13: three successive rotations change the coordinate system from the local $X4, Y4, Z4$ system into the global $X1, Y1, Z1$ system. Note that the signs of ϕ and θ are negative since their associated rotations are anti clockwise. By taking the time-derivatives of the orientation angles three independent angular velocities are obtained around the $Z3=Z4$ axis, the $Y2=Y3$ axis, and the $X1=X2$ axis

2.3 Motion recording and description

In Section 2.2 it was shown how the position and orientation of a coordinate system can be expressed with respect to another coordinate system. Each segment of the body (e.g. trunk, upper arm, foot, etc.) can be attributed its own local coordinate system. By recording the motions of the segments, the position and orientation of the local coordinate systems are known, and the rotations can be expressed e.g. by Euler angles.

Recording human motions is quite different from motion recording in technical mechanical systems. In technical systems, joints have well-defined DOF, are reasonably easy to access for measurement devices and motions are reproducible. In humans, there are large intra- and inter-individual differences. The joints themselves are inaccessible, and measurements are noisy. Ideally, the system itself should not be affected by the measurement system. For human motion recordings this requirement is not always fulfilled. In this paragraph some measurement methods, a protocol for determining bone and joint rotations and some filtering methods are described.

2.3.1 MEASUREMENT METHODS

Measurement methods can be divided into two categories: Optical and non-optical. Examples of non-optical methods are:

- Goniometers. Attached to the proximal and distal link, goniometers record the angle between the links in one plane (or three planes if three goniometers are placed in succession with a common rotation center).
- Accelerometers. Accelerometers are sensitive to acceleration but also to gravity. Typically, two accelerometers rigidly attached on one link are needed to distinguish between accelerations and the orientation with respect to the gravity field. Velocities and positions can be derived by integration of the acceleration signal. However, this will often result in a static offset.
- Stereosonic. Using speakers, the position of microphones can be determined using the delay time due to the limited speed of sound as a

measure of the distance to each speaker.

- Electromagnetic devices. A magnetic field is generated by a transmitter, and the position and orientation of sensors can be derived by measuring the current in electric coils in the sensors. Obviously, this method is very sensitive to metallic objects interfering with the magnetic field.

Examples of optical methods are:

- (Stereo-)cinematography / (stereo-)photogrammetry. Markers are attached to the subject, and their positions are digitized from the film (manually!).
- Video-computer systems. Video-images are processed on-line to detect the marker positions.
- Röntgenphotogrammetry and röntgencinematography. Bony ridges are used as a reference to detect joint angles. In 3-D röntgen implanted markers are necessary for sufficient accuracy, which is currently not allowed in the Netherlands. Clear disadvantage of this method is the exposure of the subject to radiation. Maximal loads for experimentation are limited to a few photos or a few seconds of film. Photos have a better contrast. The contrast in films is amplified by fluorescence. The films have a very limited field-of-view.

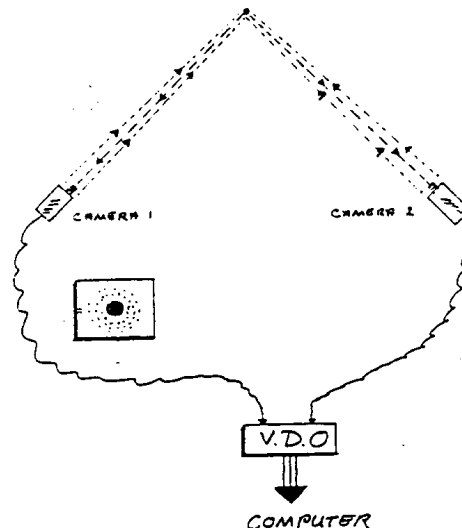


Figure 2.14: A marker is positioned on the intersection point of two lines through the focus point and image point of each camera.

Usually, markers are attached to the subjects which can be seen in the optical image. Markers can be reflexive (requiring usually additional spotlights) or 'active', i.e. they lit up and hence require a wire connection to a power source. The markers are placed approximately on the joint centers of rotation, and the segment is approximated by the line between the markers. A third marker is necessary to obtain the axial rotation around the line connecting the joint markers. An alternative method is to use 'marker trees' (usually 4 or 5 markers fixed with respect to each other, and fixed to the segment). Then, the location of the marker tree with respect to the local coordinate system (defined by bony landmarks) is measured by marking also the bony landmarks. The rotations can be calculated through the local coordinate systems.

For 3-D measurements at least two cameras are necessary, but usually 4 to 6 cameras are used in order to be sure to record each marker by at least two cameras. When a marker is 'seen' by a camera, its position is determined on a

marker trees

line from the focus point of the camera through the marker projection on the image plane (see Figure 2.14). The accuracy of the system is determined by the accuracy of the line (depending amongst others on the number of field lines, lens distortion, distance from the camera, etc.) and the accuracy with which the cameras are positioned with respect to each other. In video- and film systems, the camera positions are calibrated using a calibration frame with known marker positions.

Direct Linear Transfer (DLT)

Then, the Direct Linear Transfer (DLT) method is used to determine the transfer function from the image positions of both camera's (x_c, y_c) to the three-dimensional coordinates X, Y and Z :

$$\begin{aligned} x_c &= \frac{L_1 X + L_2 Y + L_3 Z + L_4}{L_9 X + L_{10} Y + L_{11} Z + 1} \\ y_c &= \frac{L_5 X + L_6 Y + L_7 Z + L_8}{L_9 X + L_{10} Y + L_{11} Z + 1} \end{aligned} \quad (2.44)$$

If a sufficient number of known markers are present, L_1 to L_{11} can be estimated for each camera. Then in reverse, X, Y and Z can be calculated as a least squares optimization from at least two camera images. The resulting accuracy depends on the distance from the cameras, the accuracy of the cameras and the field-of-view, and ranges typically from about 2 mm. (e.g. VICON systems) to less than 1 mm. (e.g. Optotrack systems). The calibration algorithm implicitly calculates the camera positions and orientations with respect to each other.

2.3.2 PROTOCOL

The goal of motion recording is to quantify human motions, either for clinical purposes (in which patients are compared with normal subjects) or for scientific purposes (e.g. to validate theories on human motion control). This protocol will describe a methodology for an optical method using markers attached to the skin. One of the problems to deal with is the motion of the skin (and the markers attached to it) with respect to the bone underneath. In order to determine the human motions (i.e. the joint rotations or the rotations of the segments) the following steps are necessary:

1. Definition of the local coordinate system of a bone with respect to well-defined bony landmarks.
2. Assessment of the position and rotation of the cluster reference frame (or coordinate system) with respect to the local coordinate system in initial position. This is called the static trial.
3. Recording of the orientation of the marker reference frame with relatively to the static trial in each time-step.
4. Calculation of the local coordinate system from 3 and 2.
5. Calculation of joint rotations (rotation with respect to the proximal bone) or bone rotations (with respect to the global coordinate system or a central body-oriented local coordinate system).
6. Decomposition of the rotation matrix into a defined sequence of Euler angles.

1) Definition of the local coordinate system of a bone with respect to well-defined bony landmarks.

No two bones are identical. Therefore, quantifying the absolute motion of segments somehow depends on the definition of the local coordinate system of the bone. The position and orientation of the local coordinate system is defined

with respect to at least three bony landmarks on the bone. In Appendix A and B definitions of local coordinate systems are shown for the lower and upper extremities, respectively using bony landmarks.

2) *Assessment of the position of a 'marker tree' with respect to the local coordinate system in a static trial.*

The next step in the protocol is measuring the standard position of the marker tree with respect to the bony landmarks in a static trial, so that the markers are clearly visible. From the bony landmarks the local coordinate system in initial position L^0 is calculated, e.g. according to Equation 2.8. The marker positions \underline{q}_i belonging to this static position of the local coordinate system are recorded.

3) *Estimation of the translation matrix of the marker reference frame in each time-step relative to the static trial.*

Subsequently, the markers at the bony landmarks can be removed if necessary.² These markers are no longer needed to determine the LCS, and only obscure the measurements. During the measurements, each time instant there will be a position recording \underline{p}_i of the marker tree. Using a non-linear least squares algorithm (Veldpaus et al., 1988) the rotation matrix and translation vector can be calculated by minimizing

$$J = \sum_{i=1}^N e_i^2 \quad (2.45)$$

$$e_i = \left\| \underline{q}_i - (\mathbf{R}(\underline{p}_i - \underline{a}) + \underline{a} + \underline{v}) \right\|$$

in which \underline{p}_i is the position of marker i in the static trial and \underline{q}_i the position of the marker during the measurement. \mathbf{R} is the rotation matrix from the static trial to the measured position, \underline{v} is the translation vector and \underline{a} is the center of the marker tree, computed as the average of the marker positions \underline{p}_i in the static trial. The vector \underline{a} is used to reduce the noise effects in estimating rotation matrix \mathbf{R} . The error e_i is the difference between the measured position \underline{q}_i and the estimated position of \underline{q}_i . Minimizing this error will give the best estimate for the rotation matrix \mathbf{R} and translation vector \underline{v} .

Alternatively \mathbf{R} can also be calculated by:

$$\mathbf{R}(t) = (\mathbf{M}^0)^T \mathbf{M}(t) \quad (2.46)$$

where \mathbf{M}^0 is the rotation matrix of the marker tree in initial position and $\mathbf{M}(t)$ is the rotation matrix of the marker tree at each time step. In case only three markers on each segment are attached \mathbf{M} can be easily obtained using simple vector algebra (see Appendix A and Equation 2.8). In case more than three markers are used on each segment (clusters of markers) other techniques can be used such as a singular value decomposition.

4) *Calculation of the local coordinate system in each time-step.*

Using the initial orientation of the local coordinate system L^0 , defined by the position of the bony landmarks (step 2), and the rotation matrix \mathbf{R} determined by the marker tree (step 3), the position of the local coordinate system can be calculated for each time-step t again, using:

$$\mathbf{R}(t)L^0 = L^i(t) \quad (2.47)$$

² One can define the orientation of a segment using three or more markers on each segment. It is also possible that two segments 'share' a marker by placing a marker on a joint axis.

5) *Calculation of joint rotations and bone rotations*

Joint rotations are defined as rotations of a local coordinate system with respect to the proximal bone. Bone rotations are defined as rotations with respect to the global coordinate system or a central body-oriented local coordinate system. The latter is useful e.g. to define the motion of the thorax with respect to the global coordinate system, or the motion of the upper arm with respect to the thorax. Joint rotations can be calculated as follows:

$$\mathbf{L}^P \cdot {}^{DP}\mathbf{R} = \mathbf{L}^D; \quad {}^{DP}\mathbf{R} = (\mathbf{L}^P)^T \cdot \mathbf{L}^D \quad (2.48)$$

where \mathbf{L}^P and \mathbf{L}^D are the local coordinate systems of the proximal and distal bone respectively, and ${}^{DP}\mathbf{R}$ is the rotation matrix defined as local rotations about the axes of the proximal coordinate system.

Bone rotations are calculated by:

$$\mathbf{L}^C \cdot {}^{DC}\mathbf{R} = \mathbf{L}^D; \quad {}^{DC}\mathbf{R} = (\mathbf{L}^C)^T \cdot \mathbf{L}^D \quad (2.49)$$

where \mathbf{L}^C is the central body-oriented local coordinate system, \mathbf{L}^D is the coordinate system of the bone in question, and ${}^{DC}\mathbf{R}$ the rotation matrix defined about the axes of the central body-oriented local coordinate system.

In the Appendix B, Tables B.1 and B.2 examples of the joint and bone rotations are given for the shoulder.

6) *Decomposition of the rotation matrix into a defined sequence of Euler angles.*

Once the rotation matrix is properly derived, it can be decomposed into Euler angles (see Equation 2.22). The choice of the order is subjective, though it is advisable that the last rotation is about the longitudinal axis of the bone, or a well-recognizable bony ridge. Then, the first two rotations can be interpreted as ‘polar’ angles to orient the longitudinal axis.

In Appendix B, Tables B.3 and B.4 an example is given of the definition of Euler angles for the shoulder.

2.3.3 NUMERICAL TECHNIQUES

When the motion is recorded, the position information is usually available as a time series. This is not sufficient to analyze the data; one usually needs velocity and acceleration information as well. A straightforward way to obtain these is to numerically differentiate the time series.

Suppose $x = \{\dots, x_{i-1}, x_i, x_{i+1}, \dots\}$ is a representation of some position parameter at times $t = \{\dots, t_{i-1}, t_i, t_{i+1}, \dots\}$. When x is measured at a constant rate, the time steps $\Delta t = t_i - t_{i-1} = \text{constant} = \Delta t$. In the simplest approach, the velocity and acceleration are then given by

$$\begin{aligned} \dot{x}_i &= \frac{x_{i+1} - x_{i-1}}{2\Delta t} \\ \ddot{x}_i &= \frac{x_{i+1} - 2x_i + x_{i-1}}{\Delta t^2} \end{aligned} \quad (2.50)$$

Note that a central differences scheme is chosen; otherwise a time shift of $\frac{1}{2}\Delta t$ would occur.

For an ideal recording without measuring errors this would be sufficient. However, as measuring inaccuracies are likely to occur, this scheme leads to a large amplification of the inaccuracies in the derivatives. Suppose the noise can be modeled as an error signal e with a frequency similar to the measuring frequency (typically 50 Hz), whereas the error-free signal x' has a typical

frequency of 1 Hz (for walking):

$$x = x' + e = x_0 \sin(2\pi t - \varphi_0) + e_0 \sin(50 \cdot 2\pi t - \varphi_e) \quad (2.51)$$

This would result in an acceleration signal of

$$\ddot{x} = \ddot{x}' + \ddot{e} = -x_0 4\pi^2 \sin(2\pi t - \varphi_0) - e_0 50^2 \cdot 4\pi^2 \sin(50 \cdot 2\pi t - \varphi_e) \quad (2.52)$$

For the position signal, the orders of magnitude are $x_0 \approx 1$ m and $e_0 \approx 0.001$ m, resulting in a signal to noise ratio of about 1000. For the acceleration, the signal to noise ratio reduces to 0.4, demonstrating that the error dominates the acceleration. Therefore, the measured signal has to be filtered or smoothed, at least when numerical differentiation is applied.

The numerical filter should have the characteristic of a low-pass filter, since the interesting part of the data is at the lower frequencies and the noisy part at the higher frequencies. This is demonstrated in Figure 2.10.

The problem is then to find the suitable cut-off frequency. One way to solve this is by applying a generalized cross-validation (GCV) (Woltring, 1995). In the GCV method the cut-off frequency is minimized under the constraint that the error signal (the difference between the measured signal and the filtered signal) only contains white noise. Standardized subroutines written in Matlab using this method (e.g. GCVSPL) are available on the internet.

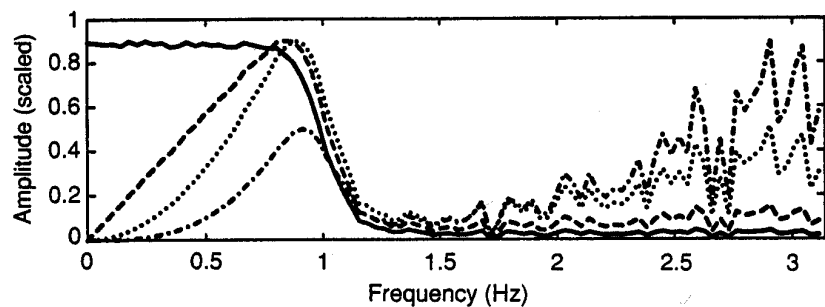


Figure 2.10: Example of a noisy signal spectrum (solid line) and the first (---), second (...) and third (-.-.-) derivatives.

REFERENCES

- Woltring, H.J. (1995): Smoothing and differentiation techniques applied to 3-D data. In: Allard, P., Stokes, Three-dimensional analysis of human motion. Human Kinetics, Champaign, IL

SUGGESTED FURTHER READING

- Goldstein H, Classical Mechanics, Chapter 4, ISBN 0-201-02969-3, Addison-Wesley Publishing company, 1950
- Jonker JB, Dynamics of Machines and Mechanisms: A finite element approach, dictaat 113130 UT, Enschede
- Murray MM, LI Z, Sastry SS, A Mathematical introduction to robotic manipulation, ISBN 0-8493-7981-4 CRC Press, London, 1994

APPENDIX A: ANATOMICAL FRAME DEFINITIONS FOR THE LOWER LEGS

To simulate motion with a segments model, the local frames of each segment have to be defined. Both position and orientation of anatomical frames are commonly defined using observable anatomical landmarks. These landmarks are chosen such that they are relatively easy to identify by palpation and determination is repeatable. According to Capozzo et al³, a segment anatomical frame should be based on points belonging to that segment only. This is not always the case as can be seen in the definitions by Koopman⁴. The motion data derived from the Analyse program written by Koopman is based on a different frame definition than the international standard proposed by Capozzo et al. Both definitions are discussed in this appendix.

Usually the movement between the separate bones of the pelvic girdle is considered negligible. In most cases the bones of the foot are also considered to be rigidly connected. The axes are defined for the right leg. It is indicated when the definition for the left leg is different from the one for the right leg.

Anatomical landmarks and frames

The identification of the local segment frames is based on the location of specific anatomical landmarks. For each segment these landmarks are described in table A1.

Table A1: Overview of bony landmarks used for definition of local axis of body segments used by Capozzo, Vakhum and Koopman. In the last column the abbreviations used in the figures are shown.

<i>Segment</i>	<i>Anatomical Landmark</i>	<i>Capozzo</i>	<i>Vakhum</i>	<i>Koopman</i>	<i>Figures</i>
<i>Pelvis</i>	<i>Anterior superior iliac spine</i>	<i>ASIS</i>	<i>asis</i>	<i>ASIS</i>	<i>asis</i>
	<i>Posterior superior iliac spine</i>	<i>PSIS</i>	<i>psis</i>	-	<i>psis</i>
	<i>Pubic tubercle</i>	-	-	<i>PUT</i>	<i>put</i>
	<i>Hip joint centre (centre of femoral head)</i>	<i>FH</i>	<i>fh</i>	<i>HIP</i>	<i>hf</i>
	<i>Centre of acetabulum</i>	<i>AC</i>	-	-	
<i>Femur</i>	<i>Top of greater trochanter</i>	<i>GT</i>	-	<i>TTM</i>	
	<i>Lateral epicondyle</i>	<i>LE</i>	<i>le</i>	<i>LEP</i>	<i>le</i>
	<i>Medial epicondyle</i>	<i>ME</i>	<i>me</i>	<i>MEP</i>	<i>me</i>
<i>Tibia/Fibula</i>	<i>Tibial tuberosity</i>	<i>TT</i>	<i>tt</i>	<i>TIT</i>	<i>tt</i>
	<i>Intercondylar eminence</i>	<i>IE</i>	-	-	
	<i>Apex of the head of the fibula</i>	<i>HF</i>	<i>hf</i>	-	<i>hf</i>

³ Capozzo A, et al., *Position and orientation in space of bones during movement: anatomical frame definition and determination*; 1995

⁴ Koopman H, *The Three-Dimensional Analysis and Prediction of Human Walking*, Ph.D. Thesis, The Netherlands: University of Twente, 1989.

	<i>Medial malleolus</i>	<i>MM</i>	<i>mm</i>	<i>MMA</i>	<i>mm</i>
	<i>Lateral malleolus</i>	<i>LM</i>	<i>lm</i>	<i>LMA</i>	<i>lm</i>
<i>Foot</i>	<i>Upper ridge of the calcaneus</i>		<i>ca</i>	-	<i>ca</i>
	<i>Dorsal aspect of first metatarsal head</i>	<i>FM</i>	<i>fm</i>	-	<i>fm</i>
	<i>Dorsal aspect of second metatarsal head</i>	<i>SM</i>	<i>sm</i>	-	<i>sm</i>
	<i>Dorsal aspect of fifth metatarsal head</i>	<i>VM</i>	<i>vm</i>	-	<i>vm</i>

Each definition is based on a number of landmarks, but not necessarily the same. In table A1 the abbreviations used in the definitions can be found.

Koopman

For each segment the anatomical landmarks are used to construct a right handed orthogonal local frame. The directions of the axis are defined by:

$$\underline{y}_i^0 = \underline{p}_1^0 - \underline{p}_2^0$$

$$\underline{x}_i^0 = \underline{y}_i^0 \times (\underline{p}_3^0 - \underline{p}_2^0)$$

$$\underline{z}_i^0 = \underline{x}_i^0 \times \underline{y}_i^0$$

where \underline{x}_i^0 , \underline{y}_i^0 and \underline{z}_i^0 are the axis directions of the local frame of segment i in coordinates of the global reference frame 0 .

PELVIC FRAME

The pelvic frame has its origin at the midpoint between the hip joint centers (\underline{p}_{rft}^0 and \underline{p}_{lft}^0).

$$\underline{O}_p^0 = \left(\frac{\underline{p}_{rft}^0 + \underline{p}_{lft}^0}{2} \right)$$

where (Figure A1),

$$\underline{p}_1^0 \text{ midpoint between } \underline{p}_{rasis} \text{ and } \underline{p}_{lasis}$$

$$\underline{p}_2^0 \text{ midpoint between } \underline{p}_{rput} \text{ and } \underline{p}_{lput}$$

$$\underline{p}_3^0 \underline{p}_{rasis}$$

FEMURAL FRAME

The origin of the femoral frame lies in the knee joint centre, the midpoint between \underline{p}_{rme} and \underline{p}_{rle} .

$$\underline{O}_f^0 = \left(\frac{\underline{p}_{rme}^0 + \underline{p}_{rle}^0}{2} \right)$$

where (Figure A1),

\underline{p}_1^0 Hip joint centre (\underline{p}_{fh})

\underline{p}_2^0 Knee joint centre (\underline{p}_{rkne})

\underline{p}_3^0 \underline{p}_{rle} (for left femur \underline{p}_{lme})

TIBIAL FRAME

The origin of the tibial frame lies at the ankle joint centre (\underline{p}_{rank}), which is the midpoint between \underline{p}_{rmm} and \underline{p}_{rlm} :

$$\underline{O}_t^0 = \left(\frac{\underline{p}_{rmm}^0 + \underline{p}_{rlm}^0}{2} \right)$$

where (Figure A1),

\underline{p}_1^0 Knee joint centre (\underline{p}_{rkne})

\underline{p}_2^0 Ankle joint centre (\underline{p}_{rank})

\underline{p}_3^0 \underline{p}_{rlm} (for left tibia \underline{p}_{lmm})

FOOT FRAME

The origin of the foot frame lies in the ankle joint centre (\underline{p}_{rank}). $\underline{O}_{fo}^0 = \underline{O}_t^0$ The axes are oriented in the same directions as the global reference frame for the body at rest.

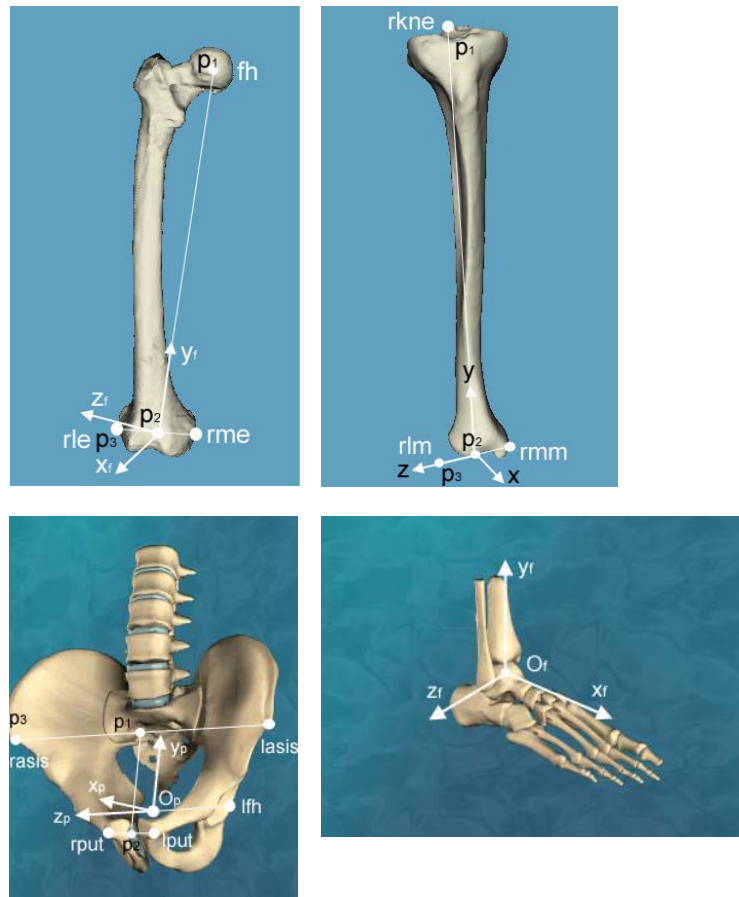


Figure A1: Definition of local axis by Koopman, from left to right: The Pelvic, the femoral, the tibial, and the foot frame

VAKHUM

Another definition can be found in the Virtual Animation of the Kinematics of the Human for Industrial, Educational and Research Purposes Project (VAKHUM).⁵

This definition is based on the standardized definition proposed by Capozzo et al., which will be discussed in the next paragraph (Figure A2).

PELVIC ANATOMICAL FRAME

- \underline{O}_a Origin of the anatomical frame $(\underline{x}_p, \underline{y}_p, \underline{z}_p)$ of the pelvic segment; midpoint between $\underline{p}_{\text{rasis}}$ and $\underline{p}_{\text{IASIS}}$
- \underline{z}_p oriented along the line passing through $\underline{p}_{\text{rasis}}$ and $\underline{p}_{\text{IASIS}}$, with the positive direction pointing right
- \underline{x}_p lies in the plane through $\underline{p}_{\text{rasis}}$, $\underline{p}_{\text{IASIS}}$, and the midpoint between $\underline{p}_{\text{rpsis}}$ and $\underline{p}_{\text{rpsis}}$ (\underline{O}_p), perpendicular to \underline{z}_p axis and positive in anterior direction
- \underline{y}_p Perpendicular to both \underline{x}_p and \underline{z}_p and pointing upwards

In formulas:

⁵ www.ulb.ac.be/project/vakhum/

$$\underline{O}_a^0 = \left(\frac{\underline{p}_{rasis}^0 + \underline{p}_{lasis}^0}{2} \right)$$

$$\underline{z}_p^0 = \underline{p}_{rasis}^0 - \underline{O}_a^0$$

$$\underline{y}_p^0 = \underline{z}_p^0 \times \left(\underline{O}_a^0 - \left(\frac{\underline{p}_{rpsis}^0 + \underline{p}_{lpsis}^0}{2} \right) \right)$$

$$\underline{x}_p^0 = \underline{y}_p^0 \times \underline{z}_p^0$$

FEMURAL ANATOMICAL FRAME

- \underline{O}_t Origin of the anatomical frame of the thigh segment ($\underline{x}_t, \underline{y}_t, \underline{z}_t$), midpoint between \underline{p}_{le} and \underline{p}_{me}
- \underline{y}_t Oriented along line passing through \underline{O}_t and \underline{p}_{fh} , positive direction upwards
- \underline{z}_t lies in plane through $\underline{p}_{me}, \underline{p}_{le}$ and \underline{p}_{fh} , perpendicular to \underline{y}_t and positive direction pointing right
- \underline{x}_t Perpendicular to both \underline{y}_t and \underline{z}_t pointing anterior

In formulas:

$$\underline{O}_t^0 = \left(\frac{\underline{p}_{le}^0 + \underline{p}_{me}^0}{2} \right)$$

$$\underline{y}_t^0 = \underline{p}_{fh}^0 - \underline{O}_t^0$$

$$\underline{x}_t^0 = \underline{y}_t^0 \times (\underline{p}_{le}^0 - \underline{O}_t^0)$$

$$\underline{z}_t^0 = \underline{x}_t^0 \times \underline{y}_t^0$$

TIBIAL/FIBULA ANATOMICAL FRAME

- \underline{O}_s Origin of the anatomical frame of the shank segment ($\underline{x}_s, \underline{y}_s, \underline{z}_s$), located at the midpoint of the line joining \underline{p}_{lm} and \underline{p}_{mm}
- \underline{y}_s Defined by the intersection between the plane through $\underline{p}_{hf}, \underline{p}_{lm}$ and \underline{O}_s and the plane orthogonal to that plane containing both \underline{O}_s and \underline{p}_{tr} , pointing upward
- \underline{z}_s Lies in the plane through $\underline{p}_{hf}, \underline{p}_{lm}$ and \underline{O}_s and is perpendicular to \underline{y}_s , pointing to the right
- \underline{x}_s Perpendicular to both \underline{y}_s and \underline{z}_s , pointing anterior

In formulas:

$$\underline{O}_s^0 = \left(\frac{\underline{p}_{lm}^0 + \underline{p}_{mm}^0}{2} \right)$$

$$\underline{x}_s^0 = (\underline{p}_{hf}^0 - \underline{O}_s^0) \times (\underline{p}_{lm}^0 - \underline{O}_s^0)$$

$$\underline{z}_s^0 = \underline{x}_s^0 \times (\underline{p}_{tt}^0 - \underline{O}_s^0)$$

$$\underline{y}_s^0 = \underline{z}_s^0 \times \underline{x}_s^0$$

FOOT ANATOMICAL FRAME

Foot quasi-transverse plane	defined by \underline{p}_{ca} , \underline{p}_{fm} , \underline{p}_{vm}
Foot quasi-sagittal plane	orthogonal to quasi transverse plane and through both \underline{p}_{ca} and \underline{p}_{sm}
Foot quasi-coronal plane	Perpendicular to both other planes

- \underline{O}_f Origin of the anatomical frame of the foot segment ($\underline{x}_f \underline{y}_f \underline{z}_f$), in point \underline{p}_{ca}
- \underline{y}_f Defined by the intersection between quasi-coronal and quasi-sagittal plane, pointing upwards
- \underline{z}_f Lies in the quasi-transverse plane perpendicular to the \underline{y}_f axis, pointing right
- \underline{x}_f Perpendicular to both \underline{y}_f and \underline{z}_f , pointing anterior

In formulas:

$$\underline{O}_f^0 = \underline{p}_{ca}^0$$

$$\underline{y}_f^0 = (\underline{p}_{vm}^0 - \underline{O}_f^0) \times (\underline{p}_{fm}^0 - \underline{O}_f^0)$$

$$\underline{z}_f^0 = (\underline{p}_{sm}^0 - \underline{O}_f^0) \times \underline{y}_f^0$$

$$\underline{x}_f^0 = \underline{y}_f^0 \times \underline{z}_f^0$$

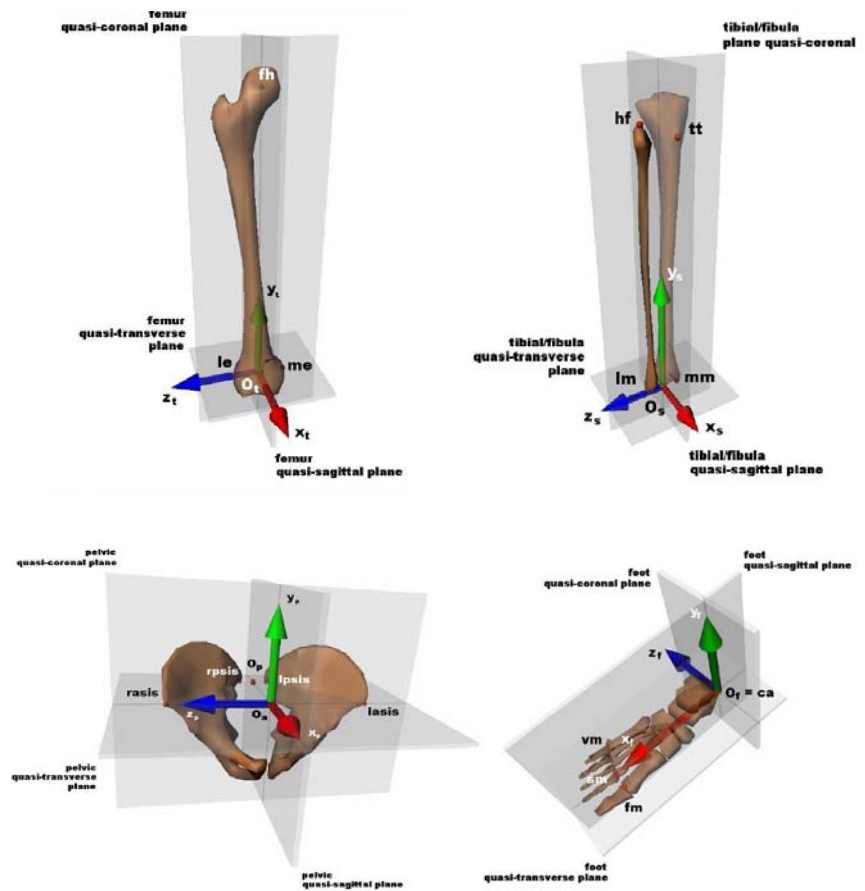


Figure A2: Definition of local axis in the VAKHUM project, from left to right: The pelvic, the femoral, the tibial, and the foot frame

Capozzo

Capozzo aims to standardize the definition of anatomical landmarks and frames in order to make data sharing in movement analysis more effective and databanks possible. End results will be the same irrespective of the specific experimental technique used (for instance marker placement) and therefore be directly comparable.

This definition can be seen as the international standard for anatomical frame conventions.

Since the definitions in the VAKHUM project were based on the standardized definitions proposed by Capozzo, there is no need to describe these frames again. However there is one difference, the axes in the foot frame are defined differently. Therefore they will be discussed below (Figure A3).

FOOT FRAME

- O_f Origin is located at the calcaneus landmark p_{ca}
- y_f Defined by the intersection between quasi-transverse and quasi-sagittal plane, pointing proximal
- z_f Lies in the quasi-transverse plane perpendicular to the y_f axis, pointing right

\underline{x}_f Orthogonal the \underline{y}_f - \underline{z}_f -plane, positive direction is dorsal.

$$\underline{O}_f^0 = \underline{p}_{ca}^0$$

$$\underline{x}_f^0 = (\underline{p}_{vm}^0 - \underline{O}_f^0) \times (\underline{p}_{fm}^0 - \underline{O}_f^0)$$

$$\underline{z}_f^0 = (\underline{p}_{sm}^0 - \underline{O}_f^0) \times \underline{x}_f^0$$

$$\underline{y}_f^0 = \underline{z}_f^0 \times \underline{x}_f^0$$

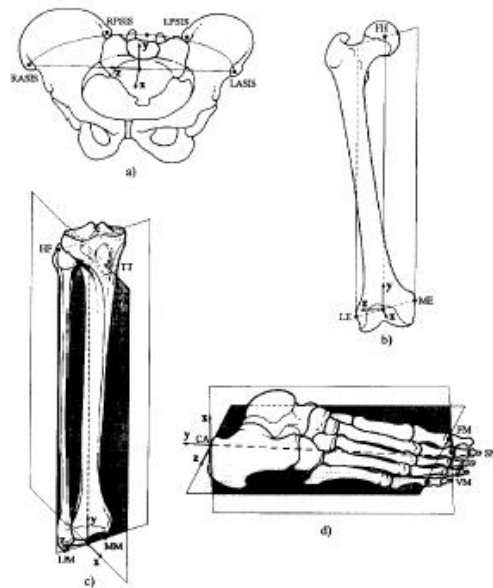


Figure A3: Frame definitions by Capozzo.

References

- ISB recommendation on definitions of joint coordinate system of various joints for the reporting of human joint motion-part I: ankle, hip and spine. 2002
- Capozzo A, Catani F, DellaCroce U, Leardini A, *Position and orientation in space of bones during movement: anatomical frame definition and determination*; Clinical Biomechanics, Vol.10(4) 1995;171-178
- Koopman H, *The Three-Dimensional Analysis and Prediction of Human Walking*, Ph.D. Thesis, The Netherlands: University of Twente, 1989. ISBN 90 9003075 1.
- VAKHUM, *Technical report on data collection procedure annex I* IST-1999-10954, www.ulb.ac.be/project/vakhum/

APPENDIX B: ANATOMICAL FRAME DEFINITIONS AND EULER ANGLES OF THE DELFT SHOULDER MODEL

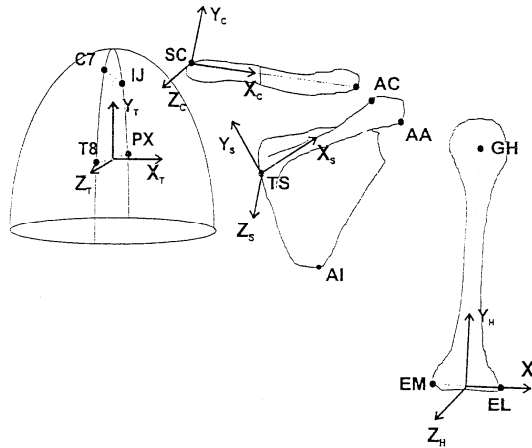
The local coordinate systems are defined as in Figure B1. For example, the medial epicondyle (\underline{EM}), the lateral epicondyle (\underline{EL}) and the rotation center of the glenohumeral joint (\underline{GH}) are bony landmarks of the humerus (see Figure B2). The \underline{y}_H -axis is from the midpoint between \underline{EM} and \underline{EL} to \underline{GH} , the \underline{z}_H -axis is perpendicular to the plane through \underline{EM} , \underline{EL} and \underline{GH} , pointing backward and the \underline{x}_H -axis is perpendicular to the \underline{y}_H - and \underline{z}_H -axis:

$$\underline{y}'_H = \underline{GH} - (\underline{EM} + \underline{EL}) / 2; \quad \underline{y}_H = \frac{\underline{y}'_H}{|\underline{y}'_H|}$$

$$\underline{z}'_H = (\underline{EL} - \underline{EM}) \times \underline{y}_H; \quad \underline{z}_H = \frac{\underline{z}'_H}{|\underline{z}'_H|}$$

$$\underline{x}_H = \underline{y}_H \times \underline{z}_H; \quad {}^G\mathbf{H} = [\underline{x}_H \quad \underline{y}_H \quad \underline{z}_H]$$

in which \underline{GH} is the local coordinate system of the humerus.



Bone segment	Bony landmr	Description
Thorax	IJ	Incisura Jugularis (suprasternal notch)
	PX	Processus Xiphoideus, most caudal point on sternum
	C7	Processus Spinosus of 7th cervical vertebra
	T8	Processus Spinosus of 8th cervical vertebra
Clavicle	SC	Most ventral point on Sternoclavicular joint
	AC	Most dorsal point on Acromioclavicular joint
Scapula	AC	Most dorsal point on Acromioclavicular joint
	TS	Trigonum Spinae, point on medial border in line with the scapular spine
	AI	Angulus Inferior, most caudal point of scapula
	AA	Angulus Acromialis, most latero-dorsal point of scapula
humerus	PC	Most ventral point of processus coracoideus
	GH	Glenohumeral rotation center, estimated by regression
	EM	Most caudal point on Medial Epicondyle
	EL	Most caudal point on Lateral Epicondyle

Figure B1: Definition of the local coordinate system of the Thorax, Clavicle, Scapula, and Humerus. For example, the scapula is defined by three bony landmarks: Trigonum Spinae (TS), acromioclavicular joint (AC) and Angulus Inferior (AI).

Table B.1: Calculation of rotation matrices for joint rotations.

	Joint	Rotation matrix
Clavicle w.r.t. Thorax	Sternoclavicular joint	${}^G T \cdot R_{C_i} = {}^G C \Rightarrow R_{C_i} = {}^G T^T \cdot {}^G C$
Scapula w.r.t. Clavicle	Acromioclavicular joint	${}^G C \cdot R_{S_i} = {}^G S \Rightarrow R_{S_i} = {}^G C^T \cdot {}^G S$
Humerus w.r.t. Scapula	Glenohumeral joint	${}^G S \cdot R_{H_i} = {}^G H \Rightarrow R_{H_i} = {}^G S^T \cdot {}^G H$

Table B.2: Calculation of rotation matrices for bone rotations.

	Rotation matrix
Thorax w.r.t. Global C.S.	${}^G \cdot R_{t_i} = {}^G T \Rightarrow R_{t_i} = {}^G T \cdot {}^G T$
Clavicle w.r.t. Thorax	${}^G T \cdot R_{C_i} = {}^G C \Rightarrow R_{C_i} = {}^G T^T \cdot {}^G C$
Scapula w.r.t. Thorax	${}^G T \cdot R_{S_i} = {}^G S \Rightarrow R_{S_i} = {}^G T^T \cdot {}^G S$
Humerus w.r.t. Thorax	${}^G T \cdot R_{H_i} = {}^G H \Rightarrow R_{H_i} = {}^G T^T \cdot {}^G H$

Table B.3: Definition of rotation order of the SC-, AC- and GH-joint rotations. Axes denoted with single and double quotes are rotated with respect to the initial aligned orientation of the local coordinate systems.

	Rotation order	Description
Sternoclavicular joint	Y	Pro/retraction about the <i>thoracic</i> ${}^G\mathbf{y}_t$ axis
	Z'	elevation/depression about the local \mathbf{z}_c axis
	X''	axial rotation about the local \mathbf{x}_c (longitudinal axis)
Acromioclavicular joint	Y	Pro/retraction about the <i>clavicular</i> ${}^G\mathbf{y}_c$ axis
	Z'	lateral/medial rotation about the local \mathbf{z}_s axis perpendicular to the scapular plane
	X''	tipping forward/backward about the local \mathbf{x}_s axis through the scapular spine
Glenohumeral joint	Y	Plane of elevation with respect to the <i>scapular</i> ${}^G\mathbf{y}_s$ axis
	Z'	Elevation/depression about the local \mathbf{y}_h axis
	Y''	axial rotation about the local \mathbf{y}_h axis

Table B.4: Definition of rotation order of the thorax, clavicle, scapula and humerus rotations. Axes denoted with single and double quotes are rotated with respect to the initial aligned orientation of the local coordinate systems.

	Rotation order	Description
Thorax	X	Forward/backward rotation about the <i>global</i> \mathbf{y}_G axis
	Z'	Lateral flexion about the local ${}^G\mathbf{z}_t$ axis
	Y''	Torsion about the local ${}^G\mathbf{y}_t$ axis
Clavicle	Y	Pro/retraction about the <i>thoracic</i> ${}^G\mathbf{y}_t$ axis
	Z'	elevation/depression about the local \mathbf{z}_c axis
	X''	axial rotation about the local \mathbf{x}_c (longitudinal axis)
Scapula	Y	Pro/retraction about the <i>thoracic</i> ${}^G\mathbf{y}_t$ axis
	Z'	lateral/medial rotation about the local \mathbf{z}_s axis perpendicular to the scapular plane
	X''	tipping forward/backward about the local \mathbf{x}_s axis through the scapular spine
Humerus	Y	Plane of elevation with respect to the <i>thoracic</i> ${}^G\mathbf{y}_s$ axis
	Z'	Elevation/depression about the local \mathbf{y}_h axis
	Y''	axial rotation about the local \mathbf{y}_h axis

Rigid body dynamics

INTRODUCTION

The next step after defining the movement of rigid bodies is to apply the equations of motion. This results, depending on the application, in either an inverse dynamics or a direct dynamics formulation of the system, derived in most cases with a Newton-Euler approach or a Lagrange approach, or with the TMT combination method. The application of the equations of motion to human movement requires the human body to be described as a linked system of rigid bodies, the so-called segments model. This chapter deals with the properties of the segments model (how to relate it to the properties of the human body) and how to define the dynamics of the system in either a forward simulation or an inverse analysis of a measured movement.

In 3D the derivation of the equations of motion are much more complex since rotations in 3D do not commute and the time integral of the angular velocity vector does not have a physical meaning as was shown in the previous chapter.

OBJECTIVES

This chapter addresses:

- The derivation of the equations of motion of multiple linked rigid body system using the TMT combination method.
- The main differences between the Lagrange, the Newton-Euler, and the TMT combination method.
- Numerical integration of the equations of motion.

3.1 Equations of motion

3.1.1 NEWTON-EULER EQUATIONS FOR A SINGLE RIGID BODY

Newton formulated the equations of motion for systems of mass particles. Euler recognized that a rigid body is a special case for such a system: The positions of the particles are constrained with respect to each other. This leads to the notion that the internal forces (the forces acting between the particles) do not perform work and do not contribute to the equations of motion for the entire system, the rigid body. Since a rigid body has six *degrees of freedom (DOF)*, there must be six equations describing the relation between forces and motion. This leads to the formulation of the Newton-Euler equations of motion⁶:

$$\begin{aligned}\underline{\mathbf{F}}_{CoM} &= \dot{\underline{\mathbf{p}}}_{CoM} = m\ddot{\underline{\mathbf{r}}}_{CoM} \\ \underline{\mathbf{M}} &= \dot{\underline{\mathbf{h}}} = \frac{\mathbf{d}(\mathbf{J}_{CoM}\boldsymbol{\omega})}{\mathbf{d}t}\end{aligned}\quad (3.1)$$

Where $\underline{\mathbf{F}}_{CoM}$ is the resulting external force acting on the *center of mass (CoM)* of the rigid body, $\underline{\mathbf{p}}_{CoM}$ is the momentum of *CoM*, which equals (with a constant mass

⁶ The bottom equation in Equation 3.1, in somewhat different form, is usually referred to as the Euler equation of motion.

degrees of freedom (DOF)

center of mass (CoM)

m) the product of mass and velocity of CoM . Any force, acting on the rigid body, can be divided in a force, acting on CoM , and a moment of force \underline{M} . When no moments of force act on the rigid body the angular momentum \underline{h} is conserved. \underline{h} is the product of the rotation inertia tensor \underline{J}_{CoM} and the angular velocity vector $\underline{\omega}$. Unlike the mass m , \underline{J}_{CoM} is in general not constant in each coordinate system. This leads to considerable complications in 3-D; in 2-D \underline{J}_{CoM} reduces to a single constant component. However, since the body is rigid, \underline{J}_{CoM} expressed in local body coordinates must be a constant tensor. In global coordinates, \underline{J}_{CoM} depends on time (see Equation 3.12). Also, $\underline{\omega}$ does not behave like a regular velocity vector: The time integral of $\underline{\omega}$ does not have a physical meaning. As is shown in Chapter 2, rotations cannot be considered as a vector since they do not commute. For this reason, $\underline{\omega}$ is often called a non-holonomic vector. Consider a single rigid body A on which an external force \underline{F}_P and an external moment of force \underline{M}_P act in point P . The center of mass of A is located in point A (see Figure 3.1). The Newton-Euler equations of motion for this system are:

$$\begin{aligned} \underline{F}_P + m\underline{g} &= m\underline{\ddot{r}}_A \\ \underline{M}_P + \underline{r}_{AP} \times \underline{F}_P &= \frac{d(\underline{J}_A \underline{\omega})}{dt} \end{aligned} \quad (3.2)$$

It is assumed that a volume or gravity force $\underline{F}_g = m\underline{g}$ (reflecting the weight of the body) is present. The position vector \underline{r}_{AP} points from center of gravity A to P . Note that these equations are coordinate-free, i.e. no decision is yet made in which coordinate frame the equation is expressed. However, the equations of motion are only valid in an inertial system (frame), which is a frame attached to the ‘solid’ world. If the reference frame is not an inertial frame then some ‘dummy’ forces (often related to well-known inertial forces) have to be introduced to make the system obey the basic laws of Newton.

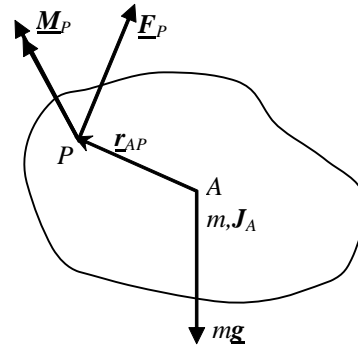


Figure 3.1: Free body diagram of a rigid body with the CoM in point A and external force and moment of force in point P .

To obtain the scalar equations of motion from Equation 3.2, some choices still have to be made (see also Figure 3.2):

- The orientation and position of the inertial (global) frame G .
- The orientation and position of the local (attached to the rigid body) frame A .
- The generalized coordinates, i.e. the variables to express the equations of motion in.

1. The orientation and position of G

In most applications it is convenient (but not necessary) to choose one of the

axes in the direction of the vertical. In this case, the gravity forces occur only in one of the three force equations. The position of the global frame is not important; one inertial frame differs a constant position vector from another. Because of the differentiation in Equation 3.2, this constant does not affect the resulting equations of motion. However, in a laboratory setup there may be other arguments as well, for example to define the position of the force-plates in a standardized way.

Together with the definition of the global frame the signs of the force components are defined. Usually, force components are taken positive in the directions of the global frame axes, and moment of force components are taken positive in the axes directions with the right-hand rule. For the gravity force in Figure 3.2 this results in:

$$m\mathbf{g} = -mg \begin{bmatrix} 0 & 1 & 0 \end{bmatrix}^T \quad (3.3)$$

With g the gravitational acceleration constant, $g \approx 9.81 \text{ m/s}^2$.

2. The orientation and position of A

Also here, it is often convenient (but not necessary) to choose direction of the local frame axes along the principal axes of the body: In this case, the off-diagonal components of the moment of inertia tensor \mathbf{J} are zero. In biomechanics, the orientation of a local body frame is mostly based on the position of some bony landmarks (Chapter 2) instead of based on the moment of inertia tensor. It is then often assumed that the thus defined frame coincides with the principal axes. Strictly spoken, this is not correct. However, when the local frame is defined with enough common sense, the off-diagonal components only have a small contribution to the equations of motion, especially when compared to the errors present in the measured or estimated moment of inertia tensor.

It does matter where the local frame is attached to the body. In one option, the local frame is attached to the *CoM* of the body (Figure 3.2a), in another option this may be the position of a joint or the position where the external forces apply (Figure 3.2b). This is important because the generalized coordinates depend on it: The translation vector of the rigid body is defined as the position of the origin of A with respect to G.

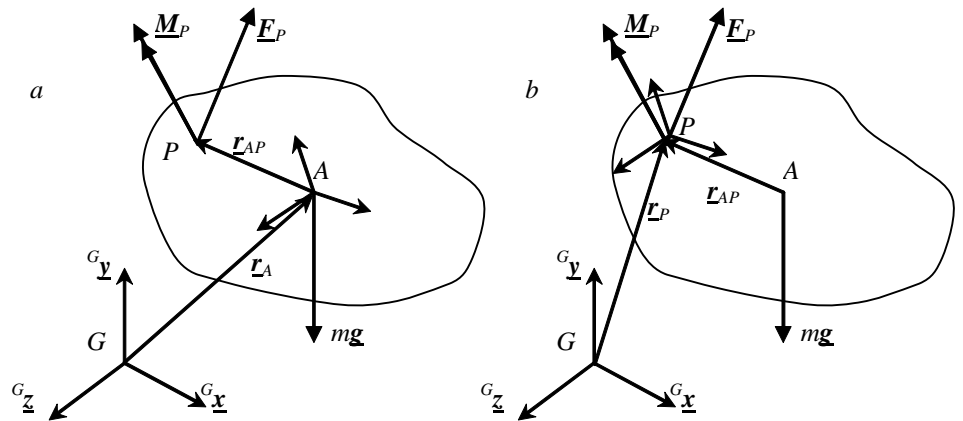


Figure 3.2: Free body diagram of a rigid body with different positions for the local frame of A. a) The translation vector is defined by the position of CoM ${}^G\mathbf{r}_A$. b) The translation vector is defined by ${}^G\mathbf{r}_P$. Both definitions result in different (but equivalent) equations of motion since the generalized coordinates are different.

3. The generalized coordinates

The difficulty in 3-D is what to do with the rotations since they introduce some non-linearities because they do not commute. Also, one may choose the position of the local frame freely. The only restriction on the generalized coordinates is that they are able to describe each position of the rigid body uniquely. There may be more generalized coordinates than DOF (the generalized coordinates are not independent then), but in this case also some constraint equations should be included with the equations of motion. One may express the equations of motion with helical axis parameters, which leads to rather complex equations. It is more convenient to derive the equations based on Euler angles and the translation vector.

Figure 3.2 shows two different definitions of the position of the local frame, which means that the generalized coordinates describing the translation are different. In Figure 3.2a (origin A in CoM), the force-part of the equations of motion will evaluate to:

$$\begin{bmatrix} {}^G F_{Px} \\ {}^G F_{Py} - mg \\ {}^G F_{Pz} \end{bmatrix} = m \begin{bmatrix} {}^G \ddot{r}_{Ax} \\ {}^G \ddot{r}_{Ay} \\ {}^G \ddot{r}_{Az} \end{bmatrix} \quad (3.4)$$

In Figure 3.2b (origin A in point P), the acceleration of point A has to be expressed in the acceleration of point P . The derivative of any vector quantity \underline{v} is given in coordinate-free notation by (see Chapter 2)

$$\dot{\underline{v}} \equiv \left(\frac{d\underline{v}}{dt} \right)_G = \left(\frac{d\underline{v}}{dt} \right)_A + {}^G \underline{\omega}_{A/G} \times {}^G \underline{v} \quad (3.5)$$

Where $(d\underline{v}/dt)_G$ is the derivative in the global frame G , $(d\underline{v}/dt)_A$ is the derivative in the local frame A and ${}^G \underline{\omega}_{A/G} \times {}^G \underline{v}$ is the contribution of the relative rotation of the local frame with respect to the global frame. In local coordinates, Equation 3.5 becomes (see Chapter 2):

$${}^G \dot{\underline{v}} = {}^{GA} \mathbf{R} \left({}^A \dot{\underline{v}} + {}^A \underline{\omega}_{A/G} \times {}^A \underline{v} \right) \quad (3.6)$$

rotation matrix

Where ${}^{GA} \mathbf{R}$ is the rotation matrix. The acceleration of point P is now written as:

$$\begin{aligned} {}^G \underline{r}_P &= {}^G \underline{r}_A + {}^{GA} \mathbf{R} {}^A \underline{r}_{AP} \\ {}^G \dot{\underline{r}}_P &= {}^G \dot{\underline{r}}_A + {}^{GA} \mathbf{R} \left({}^A \dot{\underline{r}}_{AP} + {}^A \underline{\omega} \times {}^A \underline{r}_{AP} \right) \\ {}^G \ddot{\underline{r}}_P &= {}^G \ddot{\underline{r}}_A + {}^{GA} \mathbf{R} \left({}^A \ddot{\underline{r}}_{AP} + 2 {}^A \underline{\omega} \times {}^A \dot{\underline{r}}_{AP} + {}^A \dot{\underline{\omega}} \times {}^A \underline{r}_{AP} + {}^A \underline{\omega} \times {}^A \underline{\omega} \times {}^A \underline{r}_{AP} \right) \end{aligned} \quad (3.7)$$

And the force-part of the equations of motion will evaluate to (note that ${}^A \underline{r}_{AP}$ is a constant vector):

$${}^G \underline{F}_P + m \left({}^G \underline{g} + {}^{GA} \mathbf{R} {}^A \underline{\omega} \times {}^A \underline{\omega} \times {}^A \underline{r}_{AP} \right) = m \left({}^G \ddot{\underline{r}}_P - {}^{GA} \mathbf{R} {}^A \dot{\underline{\omega}} \times {}^A \underline{r}_{AP} \right) \quad (3.8)$$

Note that Equation 3.8 is equivalent to Equation 3.4; the equations of motion are only expressed in a different set of parameters. However, Equation 3.8 is more complicated, since it depends on the generalized coordinates describing the rotation as well. For this reason, the local body frame is usually attached to the center of mass so that ${}^A \underline{r}_{AP} = \underline{0}$.

For the moment of force equation, similar reasoning can be followed in deriving the scalar expression. To avoid large complexity, only the scalar equations for the system in Figure 3.2a are derived (origin A in CoM). The equation in global

coordinates is:

$${}^G \underline{\mathbf{M}}_P + {}^G (\underline{\mathbf{r}}_{AP} \times \underline{\mathbf{F}}_P) = \left(\frac{d({}^G \underline{\mathbf{J}}_A \underline{\boldsymbol{\omega}})}{dt} \right)_G \quad (3.9)$$

Multiplying with ${}^A \mathbf{R}$ to transform the entire equation to local coordinates, using Equation 3.6, and with the notion that \mathbf{J}_A is a constant tensor in local coordinates, this reduces to:

$${}^A \underline{\mathbf{M}}_P + {}^A \underline{\mathbf{r}}_{AP} \times {}^A \underline{\mathbf{F}}_P = {}^A \mathbf{J}_A {}^A \dot{\underline{\boldsymbol{\omega}}} + {}^A \underline{\boldsymbol{\omega}} \times {}^A \mathbf{J}_A {}^A \underline{\boldsymbol{\omega}} \quad (3.10)$$

When the local frame A is defined along the principal axes of the rigid body, this evaluates to the original Euler equation of motion:

$${}^A \underline{\mathbf{M}}_P + {}^A \underline{\mathbf{r}}_{AP} \times {}^A \underline{\mathbf{F}}_P = \begin{bmatrix} J_{xx} \dot{\omega}_x - (J_{yy} - J_{zz}) \omega_y \omega_z \\ J_{yy} \dot{\omega}_y - (J_{zz} - J_{xx}) \omega_z \omega_x \\ J_{zz} \dot{\omega}_z - (J_{xx} - J_{yy}) \omega_x \omega_y \end{bmatrix} \quad (3.11)$$

As demonstrated in Chapter 2 it can be shown that when the Euler angles in the z - y - x convention (see Section 2.2.2.3), are used to represent the generalized coordinates of the rotation, the components of $\underline{\boldsymbol{\omega}}$ can be expressed in the Euler angles ϕ , θ and ψ (where $c\theta$ equals $\cos(\theta)$, etc.):

$${}^A \underline{\boldsymbol{\omega}} = \begin{bmatrix} \dot{\phi} c \theta c \psi + \dot{\theta} s \psi \\ -\dot{\phi} c \theta s \psi + \dot{\theta} c \psi \\ \dot{\phi} s \theta + \dot{\psi} \end{bmatrix} \quad (3.12)$$

$${}^A \dot{\underline{\boldsymbol{\omega}}} = \begin{bmatrix} \ddot{\phi} c \theta c \psi - \dot{\phi} \dot{\theta} s \theta c \psi - \dot{\phi} \dot{\psi} c \theta s \psi + \ddot{\theta} s \psi + \dot{\theta} \dot{\psi} c \psi \\ -\ddot{\phi} c \theta s \psi + \dot{\phi} \dot{\theta} s \theta s \psi - \dot{\phi} \dot{\psi} c \theta c \psi + \ddot{\theta} c \psi - \dot{\theta} \dot{\psi} s \psi \\ \ddot{\phi} s \theta + \dot{\phi} \dot{\theta} c \theta + \ddot{\psi} \end{bmatrix}$$

Equations (3.4), (3.11) and (3.12) finally result in six scalar equations in the generalized coordinates ${}^G r_{Ax}$, ${}^G r_{Ay}$, ${}^G r_{Az}$, ϕ , θ and ψ that represent the equations of motion for a single rigid body. These equations may either be used in a *direct dynamics* approach where the equations are integrated (with known external forces) to obtain the movement, or in an *inverse dynamics* approach where the movement is known and the forces are calculated. However, in a strict inverse dynamics approach, the above calculations are often too cumbersome. For a measured movement, the rotation matrix is often a direct result from the data, as well as the position of the center of mass in global coordinates ${}^G \underline{\mathbf{r}}_A$. The acceleration and angular velocity vectors are obtained with numerical differentiation. In this case, the external forces and moments of force are calculated with

$${}^G \underline{\mathbf{F}}_P = m({}^G \ddot{\underline{\mathbf{r}}}_A - {}^G \underline{\mathbf{g}}) \quad (3.13)$$

$${}^G \underline{\mathbf{M}}_P = \frac{d({}^G \mathbf{R}^A \mathbf{J}_A {}^A \mathbf{R}^G \underline{\boldsymbol{\omega}})}{dt} - ({}^G \mathbf{R}^A \underline{\mathbf{r}}_{AP}) \times {}^G \underline{\mathbf{F}}_P$$

This requires numerical differentiation of the angular momentum. Note that the rotation inertia tensor in global coordinates ${}^G \mathbf{J}_A = {}^G \mathbf{R}^A \mathbf{J}_A {}^A \mathbf{R}^G$ depends on time. In principal, it is possible but not advisable to use these equations in a direct dynamics approach: The nine unknown components of ${}^A \mathbf{R}$ (that can be

direct dynamics

inverse dynamics

considered as dependent generalized coordinates) require six additional constraint equations to be included, so the total number of equations will be twelve. In the inverse approach, the constraints are automatically fulfilled when the rotation matrix is derived correctly.

3.1.2 NEWTON-EULER EQUATIONS FOR LINKED RIGID BODY SYSTEMS

Usually a rigid body is not moving freely in space, in general, there is some interaction with the inertial world or with other rigid bodies. These connections are expressed in constraint equations with the following general formulation:

$$\underline{c}(\underline{q}, \underline{\dot{q}}, t) = \underline{0} \tag{3.14}$$

\underline{c} is the vector of m constraint equations for the vector \underline{q} of n generalized coordinates. For example, if in Figure 3.2a the position P is fixed in the global frame, the three constraint equations are

$$\underline{c}(\underline{q}) = {}^G \underline{r}_A + {}^{GA} \mathbf{R} \cdot {}^A \underline{r}_{AP} - {}^G \underline{r}_P = \underline{0} \tag{3.15}$$

The constraint equations are added to the equations of motion, so in total a set of $n+m$ equations is needed to describe the dynamics of a single rigid body. Alternatively, there are techniques to incorporate the constraints in the equations of motion and thus to reduce the set to a minimum of $n-m$ equations. For *holonomic constraints*, i.e. constraints depending on the generalized coordinates only, as well as for *non-holonomic constraints* that depend on the generalized velocities and coordinates only, this is always possible. It should be noted that when these techniques are applied the constraint forces would also disappear from the equations; these cannot be calculated anymore.

holonomic constraints
non-holonomic constraints

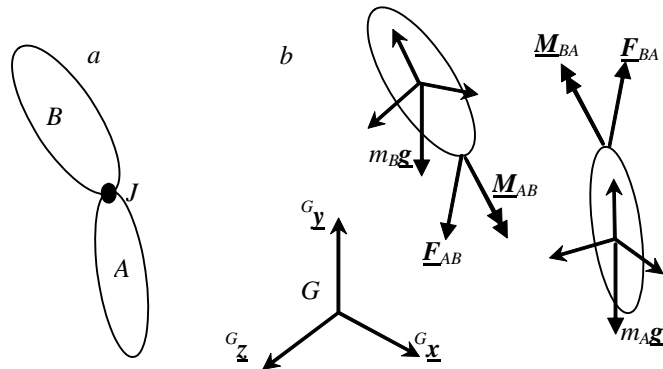


Figure 3.3: a) Linked system of two rigid bodies. b) Free body diagram of each separate rigid body. The constraint forces that each body act on the other have to be included.

In summary, for the linked systems of rigid bodies (Figure 3.3a) the following analysis sequence is followed:

1. Define the global frame and a local frame in each rigid body.
2. Define the free body diagram for each rigid body (Figure 3.3b) with constraint forces at the joints.
3. Choose the set of generalized coordinates to express the movement in.
4. Formulate the equations of motion for each segment.
5. Implement the force constraint equations directly in the equations of motion. These are simply (according to Newton's third law):

$$\begin{aligned}\underline{\mathbf{F}}_{BA} &= -\underline{\mathbf{F}}_{AB} \\ \underline{\mathbf{M}}_{BA} &= -\underline{\mathbf{M}}_{AB}\end{aligned}\quad (3.16)$$

6. Define the constraint equations. For example, when joint J is a spherical joint, the constraint equations looks like

$${}^G \underline{\mathbf{r}}_J = {}^G \underline{\mathbf{r}}_A + {}^{GA} \mathbf{R} \cdot {}^A \underline{\mathbf{r}}_{AJ} = {}^G \underline{\mathbf{r}}_B + {}^{GB} \mathbf{R} \cdot {}^B \underline{\mathbf{r}}_{BJ} \quad (3.17)$$

For the above system, a set of in total 15 ($2n+m$) equations describes the dynamics of the linked rigid bodies. However, for a measured movement in an inverse dynamics approach, it is possible to construct the movement such that the constraint equations are automatically fulfilled. In this case the constraints need not be considered in describing the dynamics of the system.

3.1.3 LAGRANGE EQUATIONS FOR LINKED RIGID BODY SYSTEMS

The Lagrange equations of motion can be derived from the Newton-Euler equations or the principle of d'Alembert: The virtual work done on the system by external forces must lead to a similar increase of the system's kinetic or potential energy. The main difference is that usually only kinematically admissible virtual displacements (i.e. infinitesimal or first-order displacements of the system that satisfy all constraints on the system's generalized coordinates). This means that the constraints are automatically fulfilled. When the generalized coordinates are independent, the number of equations that describe the dynamics of the system is minimal and equals the number of DOF. A drawback, however, is that the constraint forces do not appear in the equations, unless the related dependent generalized coordinates are included. Because of these properties, the Lagrange equations are suitable for direct dynamics problems: The minimal set of equations that need to be integrated assures relatively small numerical computation times. On the other hand, the Lagrange equations are not very suitable for inverse dynamics problems: The constraint forces are not calculated and the derivation of the equations will be very time consuming for larger systems.

The derivation of the Lagrange equations requires the following steps to be taken:

1. Define the global frame and a local frame in each rigid body.
2. Define the free body diagram for each rigid body with constraint forces at the joints.
3. Define the Lagrangian from the system's kinetic and potential energy.
4. Choose the set of generalized coordinates to express the movement in.
5. Express the Lagrangian in the generalized coordinates and velocities.
6. Determine the generalized forces from the external forces on each rigid body that perform (virtual) work.
7. Derive the Lagrange equations.

As an example, the 2-link system of Figure 3.4 will be considered.

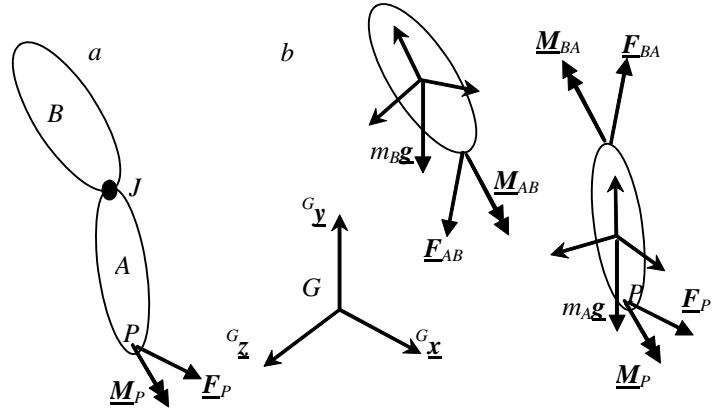


Figure 3.4: a) Linked system of two rigid bodies, with external force and moment of force acting in point P. b) Free body diagram of each separate rigid body. The bodies are connected with a spherical joint J.

1. Define the global frame and a local frame in each rigid body

The considerations here are the same as for the Newton-Euler equations: The global frame must be an inertial frame and the choice of each local frame depends on the choice of generalized coordinates and the orientation of the rotation inertia tensor.

2. Define the free body diagram for each rigid body

See Figure 3.4: The constraint forces at the joints must be included.

3. Define the Lagrangian from the system's kinetic and potential energy

The kinetic energy T_A of a rigid body A is composed of the translational and rotational kinetic energy:

$$T_A = \frac{1}{2} \dot{\underline{r}}_A^T \cdot \underline{p}_A + \frac{1}{2} \underline{\omega}_A^T \cdot \underline{h}_A = \frac{1}{2} m_A \dot{\underline{r}}_A^T \cdot \dot{\underline{r}}_A + \frac{1}{2} \underline{\omega}_A^T \cdot \underline{J}_A \cdot \underline{\omega}_A \quad (3.18)$$

Note that T_A is a scalar; it does not matter whether the vectors are expressed in local or global coordinates, as long as these are not mixed within each term. In most applications, it is useful to derive the translational kinetic energy in global coordinates for a simple relation with generalized coordinates and the rotational kinetic energy in local coordinates because \underline{J}_A is a constant tensor then.

The potential energy V_A may include all contributions from forces that can be derived from a potential, such as gravitational forces, spring forces etc.

However, this is not a necessity, since in principal these forces may also be included in the generalized forces, as long as these are not included twice. The gravitational potential energy is defined as:

$$V_A = -m_A \underline{r}_A^T \cdot \underline{g} = m_A g^G r_{Ay} \quad (3.19)$$

By definition, the Lagrangian L for the system in Figure 3.4 equals:

$$\begin{aligned} L &= T - V; \\ T &= T_A + T_B; \quad V = V_A + V_B \end{aligned} \quad (3.20)$$

4. Choose the set of generalized coordinates

Again, the same considerations as for the Newton-Euler equations apply. To

obtain a minimal set of equations, the number of generalized coordinates equals the number of DOF. The restriction is that the generalized coordinates must be able to describe any kinematically admissible movement.

The system in Figure 3.4 has nine DOF. A reasonable choice for the generalized coordinates is: 1) the components of the translation vector of body A, i.e. ${}^G\mathbf{r}_A$. 2) the Euler angles defined by the rotation matrix ${}^G\mathbf{A} = {}^{GA}\mathbf{R}$. 3) The Euler angles defined by the rotation matrix ${}^G\mathbf{B} = {}^{GB}\mathbf{R}$. As an alternative to 3), also the joint rotation defined by ${}^A\mathbf{B} = {}^{AB}\mathbf{R}$ could be chosen.

The generalized coordinates are usually expressed as a vector \mathbf{q} with length n :

$$\mathbf{q} = [q_1 \quad q_2 \quad \dots \quad q_n]^T \quad (3.21)$$

In this case, n equals 9.

5. Express the Lagrangian in the generalized coordinates and velocities

This step usually requires a lot of attention; mistakes are easily made. With the angular velocity vector given in Equation 3.11, the kinetic and potential energy for body A are already in generalized coordinates or velocities. For body B, the position and velocity of the center of mass have to be expressed in generalized coordinates:

$$\begin{aligned} {}^G\mathbf{r}_B &= {}^G\mathbf{r}_A + {}^{GA}\mathbf{R} \cdot {}^A\mathbf{r}_{AJ} + {}^{GB}\mathbf{R} \cdot {}^B\mathbf{r}_{BJ} \\ {}^G\dot{\mathbf{r}}_B &= {}^G\dot{\mathbf{r}}_A + {}^{GA}\mathbf{R} \cdot \left({}^A\dot{\mathbf{r}}_{AJ} + {}^A\boldsymbol{\omega} \times {}^A\mathbf{r}_{AJ} \right) + {}^{GB}\mathbf{R} \cdot \left({}^B\dot{\mathbf{r}}_{BJ} + {}^B\boldsymbol{\omega} \times {}^B\mathbf{r}_{BJ} \right) \end{aligned} \quad (3.22)$$

6. Determine the generalized forces

The generalized forces can be calculated from the virtual work of each of the external forces that are not derivable from a potential (see Figure 3.4b). The virtual work of the constraint forces equals

$$\delta W_J = (\mathbf{F}_{BA}^T + \mathbf{F}_{AB}^T) \cdot \delta \mathbf{r}_J = 0 \quad (3.23)$$

This shows that the constraint forces do not appear in the generalized forces. For the virtual displacement connected to external force \mathbf{F}_P we can write (see Equation 3.7):

$$\begin{aligned} {}^G\dot{\mathbf{r}}_P &= {}^G\dot{\mathbf{r}}_A + {}^{GA}\mathbf{R} \cdot {}^A\boldsymbol{\omega} \times {}^A\mathbf{r}_{AP} = \mathbf{D}_P(\mathbf{q}) \cdot \dot{\mathbf{q}} \Rightarrow \\ \delta \mathbf{r}_P &= \mathbf{D}_P(\mathbf{q}) \cdot \delta \mathbf{q} \end{aligned} \quad (3.24)$$

Where $\mathbf{D}_P(\mathbf{q})$ is a $[3 \times n]$ matrix. Likewise, we can write for the virtual rotations (see Equation 3.11):

$$\begin{aligned} \boldsymbol{\omega} &= \mathbf{E}(\mathbf{q}) \cdot \dot{\mathbf{q}} \Rightarrow \\ \delta \boldsymbol{\pi} &= \mathbf{E}(\mathbf{q}) \cdot \delta \mathbf{q} \end{aligned} \quad (3.25)$$

Where $\mathbf{E}(\mathbf{q})$ is a $[3 \times n]$ matrix. Note that the virtual rotation, like an infinitesimal rotation, is correctly considered as a vector. From the virtual work done on the system of Figure 3.4b, the n generalized forces \mathbf{Q} follow:

$$\delta W = \mathbf{F}_P^T \cdot \delta \mathbf{r}_P + (\mathbf{M}_P^T + \mathbf{M}_{BA}^T) \cdot \delta \boldsymbol{\pi}_A + \mathbf{M}_{AB}^T \cdot \delta \boldsymbol{\pi}_B = \mathbf{Q}^T \cdot \delta \mathbf{q} \quad (3.26)$$

Since this is true for any virtual displacement $\delta \mathbf{q}$, with Equations (3.24) and (3.25) this results in:

$$\underline{Q} = \mathbf{D}_P^T(\underline{q}) \cdot \underline{F}_P + \mathbf{E}_A^T(\underline{q}) \cdot (\underline{M}_P + \underline{M}_{BA}) + \mathbf{E}_B^T(\underline{q}) \cdot \underline{M}_{AB} \quad (3.27)$$

7. Derive the Lagrange equations

For each of the generalized coordinates q_i , an equation of motion is now derived according to:

$$\frac{d}{dt} \left(\frac{\partial L}{\partial \dot{q}_i} \right) - \frac{\partial L}{\partial q_i} = Q_i; \quad i = 1, \dots, n \quad (3.28)$$

3.1.4 TMT COMBINATION METHOD

In general, the number of degrees of freedom (independent coordinates) of a rigid body moving in three-dimensional space will be less than the maximum of six. Via the principles of virtual work and D'Alembert, the equations of motion as stated by Newton in his Second Law can be expressed in this minimal set of independent coordinates. Obviously, this facilitates computation because the number of equations to be solved is reduced to a minimum. Lagrange used this as a basis for his well known equations, in which he converted the set of equations to an expression that depends only on the kinetic and potential energy of a system. This expression makes it a lot easier to solve many common dynamical problems by hand. As mentioned in Section 3.1.3, the major drawback of this method is that the constraint forces are not known explicitly. With the advent of computers, it is no longer necessary to take the sidetrack Lagrange took in his days. The equations of motion that follow from the principles of virtual work (or virtual power), which is no more than an alternative statement of static equilibrium and that of D'Alembert, which makes the principle of virtual work (or power) applicable to dynamics as well, can directly be numerically integrated. Moreover, this method takes the constraint forces into account and is not sensitive to the numerical errors associated with directly integrating the Newton-Euler equations of motion. This is because the constraint forces are implicitly incorporated in the transformation to independent coordinates. This method, although it represents no more than a straightforward mathematical reduction of a set of equations, has come to be known as *Kane's method* or *TMT-method* (among others), depending on whether the velocity or the position vector is used in deriving the transformation.

In the following a short derivation of Kane's equations of motion is given, focusing on the movement of linked rigid bodies. In the example at the end it is used to analyze the movement of a model of a human arm consisting of two interconnected rigid bodies moving in three (rotational) degrees of freedom.

3.1.4.1 Deriving the equations of motion using the TMT-method, for a system of linked rigid bodies.

For clarity, we will use the separate Newton and Euler equations (translation and rotation for rigid bodies) in this derivation. The equations are written in index-notation according to Einstein's summation-convention (see appendix A or Van der Linden, 2002).

Making use of the principle of D'Alembert to rewrite the Newton-Euler equations of motion, we can extend the principle of virtual power to the dynamical case (Meirovitch, 1986):

$$\begin{aligned}\delta \dot{x}_i \left\{ f_i - \frac{d}{dt} (M_{ij} \dot{x}_j) \right\} &= 0 \\ \delta \omega_i \left\{ m_i - \frac{d}{dt} (J_{ij} \omega_j) \right\} &= 0\end{aligned}\quad (3.29)$$

With x_j the position vector of the center(s) of mass, ω_j the angular velocity vector, M_{ij} and J_{ij} the matrices of inertia, f_i the vector stating the sum of forces (at a given point) and m_i the vector of moments (around the given point). $\delta \dot{x}_i$ is the virtual velocity at the point of application of f_i and the components of $\delta \omega_i$ are the virtual (angular) velocities in the direction of the corresponding components of m_i .

Next step is transforming the coordinates \dot{x}_j and ω_j to one set of k independent generalized coordinates (q_1, q_2, \dots, q_k). This will introduce transformation matrix T , which expresses the global coordinates in the generalized coordinates.

$$\begin{aligned}\dot{x}_j &= T_{j,k} \dot{q}_k \\ \ddot{x}_j &= T_{j,k} \ddot{q}_k + \frac{\partial T_{j,k}}{\partial t} \dot{q}_k = T_{j,k} \ddot{q}_k + \frac{\partial T_{j,k}}{\partial q_m} \frac{dq_m}{dt} \dot{q}_k = T_{j,k} \ddot{q}_k + T_{j,km} \dot{q}_k \cdot \dot{q}_m\end{aligned}\quad (3.30)$$

$$\begin{aligned}\omega_j &= S_{j,k} \dot{q}_k \\ \dot{\omega}_j &= S_{j,k} \ddot{q}_k + S_{j,km} \dot{q}_k \cdot \dot{q}_m\end{aligned}\quad (3.31)$$

By stating the coordinate transformation this way, the equations can be used for systems having both holonomic and non-holonomic, first-order constraints.

Where ω_j is a non-holonomic vector by nature, \dot{x}_j can be both holonomic as non-holonomic. If the constraints for \dot{x}_j are holonomic (' \dot{x}_j is integrable'), it is most convenient to first express x_j in q_k and differentiate this expression. This is used in the example below.

As mentioned in previous paragraphs, it is most convenient to express rotation in the local coordinate systems, resulting in a constant tensor J_{ij} . When these local coordinate systems are also chosen along the principal axes of the rigid bodies, J_{ij} becomes a diagonal matrix, just like M_{ij} .

The result is the following:

$$\begin{aligned}T_{i,k} \delta \dot{q}_k \left\{ f_i - M_{ij} (T_{j,k} \ddot{q}_k + T_{j,km} \dot{q}_k \dot{q}_m) \right\} &= 0 \\ S_{i,k} \delta \dot{q}_k \left\{ m_i - J_{i,j} (S_{j,k} \ddot{q}_k + S_{j,km} \dot{q}_k \dot{q}_m) \right\} &= 0\end{aligned}\quad (3.32)$$

This should hold for all virtual velocities compatible with the system constraints, so $\delta \dot{q}_k$ can be eliminated from the equations above. The two equations are in exactly the same form, so we might as well incorporate them in one set of equations to conclude this derivation:

$$\begin{aligned}
& \{T_{i,k}, S_{i,k}\} \cdot \begin{bmatrix} M_{ij} & \mathbf{0}_{ij} \\ \mathbf{0}_{ij} & J_{ij} \end{bmatrix} \cdot \begin{Bmatrix} T_{j,k} \\ S_{j,k} \end{Bmatrix} \cdot \ddot{q}_k = \\
& = \{T_{i,k}, S_{i,k}\} \cdot \begin{Bmatrix} f_i \\ m_i \end{Bmatrix} + \{T_{i,k}, S_{i,k}\} \cdot \begin{bmatrix} M_{ij} & \mathbf{0}_{ij} \\ \mathbf{0}_{ij} & J_{ij} \end{bmatrix} \cdot \begin{Bmatrix} T_{j,lm} \\ S_{j,lm} \end{Bmatrix} \cdot \dot{q}_l \cdot \dot{q}_m
\end{aligned} \tag{3.33}$$

This way, the equations are represented most conveniently for further (numerical) calculations, e.g. with Matlab's Symbolic Toolbox. In case the generalized coordinates represent rotation angles (as in the following example) and there are no external moments acting on the elements, there is no need to transform moments m_i from the global coordinates to the generalized coordinates. The net joint moments always act around the joint axes and are thus already in the generalized coordinate frame. Therefore, in this example the above can be simplified by replacing $S_{ik} \cdot m_i$ with a vector containing these joint moments.

3.1.4.2 AN EXAMPLE: USING THE TMT-METHOD TO SIMULATE MOTION OF A HUMAN ARM MODEL.

In this example the human arm is modeled by two interconnected rigid bodies, representing the forearm (F) and the upper arm (U) (Figure 3.5).

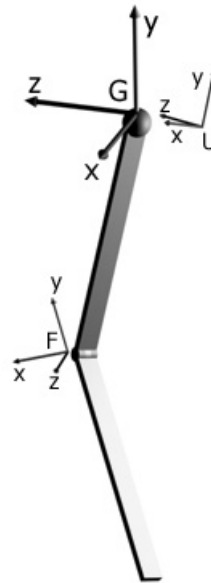


Figure 3.5: 3D model of human arm

Each rigid body has a local coordinate system (U and F). Both U and F have their axes oriented parallel to their principal axes. The origin of U lies in the center of the shoulder, the origin of F lies in the center of the elbow. The global coordinate system (G) is defined as having its origin in the center of the shoulder, and its orientation as follows (for a human facing forward): the global z -axis from front to back, the x -axis from left to right and the y -axis from down to up.

The length of the upper arm is $2 \cdot L_U$ and the length of the forearm is $2 \cdot L_F$.

The arm muscles generate moments of force and resulting rotations around the

${}^G z$ -axis (abduction-adduction, α), the ${}^U x$ -axis (anteflexion-retroflexion, β) and the ${}^F x$ -axis (elbow flexion-extension, γ). The origin of G is assumed fixed. These angles (α, β, γ) will conveniently be used as generalized coordinates, and will be regarded as Euler angles by taking the z - y - x rotation order into account. Aside from gravity in the negative ${}^G y$ -direction, no further external forces are taken into account in this example.

The following coordinates will be used in expressing the equations of motion:

$$x_j = \begin{Bmatrix} {}^G(C_U)_k \\ {}^G(C_F)_k \end{Bmatrix} = \begin{Bmatrix} {}^G(C_U)_x \\ {}^G(C_U)_y \\ {}^G(C_U)_z \\ {}^G(C_F)_x \\ {}^G(C_F)_y \\ {}^G(C_F)_z \end{Bmatrix} \omega_j = \begin{Bmatrix} {}^U(\omega_U)_x \\ {}^U(\omega_U)_y \\ {}^U(\omega_U)_z \\ {}^F(\omega_F)_x \\ {}^F(\omega_F)_y \\ {}^F(\omega_F)_z \end{Bmatrix} q_k = \begin{Bmatrix} \alpha \\ \beta \\ \gamma \end{Bmatrix}$$

with ${}^G(C_U)_k$ the position vector of the center of mass of the upper arm in the global coordinate system, ${}^U(\omega_U)_x$ the scalar component in x -direction of the angular velocity vector of the upper arm in its local coordinate system, q_k the vector of generalized coordinates. ($j = 1..6, k = 1..3$)

To solve Equation 3.32, we have to find expressions for the coordinate transformations $T_j(q_k)$ and $S_i(q_k)$ first.

In the expressions below, U' , F'' and F' are intermediate coordinate systems. Note that U' and F'' , and U and F' only differ in the position of their origin.

$$\begin{aligned}
 {}^G(C_U)_k &= {}^{GU'} \mathbf{R}_z(\alpha) \cdot {}^{U'U} \mathbf{R}_x(\beta) \cdot {}^U(C_U)_k \\
 &= \begin{bmatrix} \cos(\alpha) & -\sin(\alpha) & 0 \\ \sin(\alpha) & \cos(\alpha) & 0 \\ 0 & 0 & 1 \end{bmatrix} \cdot \begin{bmatrix} 1 & 0 & 0 \\ 0 & \cos(\beta) & -\sin(\beta) \\ 0 & \sin(\beta) & \cos(\beta) \end{bmatrix} \cdot \begin{Bmatrix} 0 \\ -L_U \\ 0 \end{Bmatrix}
 \end{aligned}$$

$$\begin{aligned}
 {}^G(C_F)_k &= 2 \cdot {}^G(C_U)_k + {}^{GF''} \mathbf{R}_z(\alpha) \cdot {}^{F''F'} \mathbf{R}_x(\beta) \cdot {}^{F'F} \mathbf{R}_x(\gamma) \cdot {}^F(C_F)_k \\
 &= \begin{Bmatrix} \sin(\alpha) \cdot \cos(\beta) \cdot 2L_U \\ \cos(\alpha) \cdot \cos(\beta) \cdot 2L_U \\ \sin(\beta) \cdot 2L_U \end{Bmatrix} + \begin{bmatrix} \cos(\alpha) & -\sin(\alpha) & 0 \\ \sin(\alpha) & \cos(\alpha) & 0 \\ 0 & 0 & 1 \end{bmatrix} \cdot \begin{bmatrix} 1 & 0 & 0 \\ 0 & \cos(\beta + \gamma) & -\sin(\beta + \gamma) \\ 0 & \sin(\beta + \gamma) & \cos(\beta + \gamma) \end{bmatrix} \cdot \begin{Bmatrix} 0 \\ -L_F \\ 0 \end{Bmatrix}
 \end{aligned}$$

After evaluation of the equation we have a transformation from generalized

coordinates to Cartesian coordinates, $\mathbb{T}_j(q_k) = \begin{Bmatrix} {}^G(C_U)_k \\ {}^G(C_F)_k \end{Bmatrix}$ and its derivatives

follow from Equation 3.29.

(Note that in this example \tilde{T}_j is a 1D-matrix, $T_{jk} = \overline{T}_{j,k}$ a 2D-matrix and $T_{jl,m}$ a 3D-matrix, with sizes 6x1, 6x3 and 6x3x3 respectively.)

The problems associated with adding rotation angle vectors (not being commutative), do not apply to angular velocity vectors or infinitesimal angular displacements in general (Meriam & Kraige, 1993). Therefore, we can use the same rotation matrices and vector addition as we did in the translational case. Three angular velocity vectors are known, in one or more coordinate systems. These are the scalar derivatives of the Euler angles $(\dot{\alpha}, \dot{\beta}, \dot{\gamma})$, expressed along an axis in the corresponding (intermediate) coordinate system(s):

$$\begin{Bmatrix} 0 \\ 0 \\ \dot{\alpha} \end{Bmatrix} \text{ in } G, U' \text{ and } F'',$$

$$\begin{Bmatrix} \dot{\beta} \\ 0 \\ 0 \end{Bmatrix} \text{ in } U', U, F'' \text{ and } F',$$

$$\begin{Bmatrix} \dot{\gamma} \\ 0 \\ 0 \end{Bmatrix} \text{ in } F' \text{ and } F.$$

These three vectors have a resultant that can be expressed in any desired coordinate system. The third vector above only applies to the forearm and will hence not be used in deriving the angular velocity of the upper arm. Notice for example, that the angular velocity of the upper arm expressed in U' is simply $\{\dot{\beta}, 0, \dot{\alpha}\}^T$.

$\underline{\omega}_j$ follows from (k=1..3):

$$\begin{aligned} {}^U(\omega_U)_k &= \begin{Bmatrix} \dot{\beta} \\ 0 \\ 0 \end{Bmatrix} + {}^{UU'}(\mathbf{R}_x(\beta)^{-1}) \begin{Bmatrix} 0 \\ 0 \\ \dot{\alpha} \end{Bmatrix} \\ {}^F(\omega_F)_k &= \begin{Bmatrix} \dot{\gamma} \\ 0 \\ 0 \end{Bmatrix} + {}^{FF'}(\mathbf{R}_x(\gamma)^{-1}) \begin{Bmatrix} \dot{\beta} \\ 0 \\ 0 \end{Bmatrix} + {}^{FF''}(\mathbf{R}_x(\gamma)^{-1} \mathbf{R}_x(\beta)^{-1}) \begin{Bmatrix} 0 \\ 0 \\ \dot{\alpha} \end{Bmatrix} \end{aligned}$$

and equals:

$$\omega_j = \begin{Bmatrix} \dot{\beta} \\ \sin(\beta) \cdot \dot{\alpha} \\ \cos(\beta) \cdot \dot{\alpha} \\ \dot{\beta} + \dot{\gamma} \\ \sin(\beta + \gamma) \cdot \dot{\alpha} \\ \cos(\beta + \gamma) \cdot \dot{\alpha} \end{Bmatrix} = \begin{bmatrix} 0 & 1 & 0 \\ \sin(\beta) & 0 & 0 \\ \cos(\beta) & 0 & 0 \\ 0 & 1 & 1 \\ \sin(\beta + \gamma) & 0 & 0 \\ \cos(\beta + \gamma) & 0 & 0 \end{bmatrix} \cdot \begin{Bmatrix} \dot{\alpha} \\ \dot{\beta} \\ \dot{\gamma} \end{Bmatrix} = S_{jk} \cdot \dot{q}_k$$

The derivative of ω_j again follows from Equation 3.30.

Next step is the quite straightforward task of determining the inertia matrices M_{ij} and J_{ij} . These are diagonal 6x6 matrices in this example, with diagonal elements the inertia in the corresponding degree of freedom (global for linear displacements and local for angular displacements):

$$M_{ij} = \text{diag}(m_U, m_U, m_U, m_F, m_F, m_F)$$

$$J_{ij} = \text{diag}(J_{Ux}, J_{Uy}, J_{Uz}, J_{Fx}, J_{Fy}, J_{Fz})$$

When deriving the values of J_{ij} , be aware that the origins of the local coordinate systems are not taken in the centers of mass. Gravity is the only external force in this example:

$$f_i = \{0, -m_U g, 0, 0, -m_F g, 0\}^T$$

Strictly speaking, (3.32) can now be solved. Remember that $(S_{ik} \cdot m_i)$ represents the vector with the muscle moments of force that initiate movement in the generalized coordinates. Because these are exactly the (muscle) moments we want to work with, $(S_{ik} \cdot m_i)$ is replaced

$$\text{by } \{m_\alpha, m_\beta, m_\gamma\}^T.$$

3.1.4.3 TMT-METHOD EXERCISES

Explain the physical meaning of the two terms in the expressions for $\dot{\omega}_j$:

$$(S_{jk} \cdot \ddot{q}_k) \text{ and } (S_{jl,m} \cdot \dot{q}_l \cdot \dot{q}_m).$$

To get acquainted with the different methods to derive the equations of motion it is suggested to perform the following exercises. It is recommended to use the Matlab symbolic toolbox or similar software.

- Try to make the example yourself using the Matlab symbolic toolbox.
- Try to find the equations of motion by expressing the angular momentum in global coordinated instead of in the local coordinate systems as in the example.
- Obtain the equations of motion without ignoring the constraint forces that act between the upper arm and forearm. What happens with the constraint forces?
- Try to find the equations of motion using the Lagrange method.
- Try to find the equations of motion using the Newton-Euler method.

REFERENCES

- Meirovitch, L., *Elements of vibrational analysis*, McGraw-Hill, 1986
 Meriam, J.L. and Kraige, L.G., *Dynamics*, John Wiley & Sons, 1993
 Jonker, J.B., *Dynamics of Machines and Mechanisms: a Finite Element Approach*, Universiteit Twente, 2001
 Van der Linde, R.Q., *Multibody Dynamica B*, Technische Universiteit Delft, 2002

APPENDIX A: THE INDEX-NOTATION

The index-notation is an alternative way to describe vector algebra. A few examples to make it clear:

- f_i : a one-dimensional vector with i elements (matrix-notation: \underline{f})
- A_{ij} : a two-dimensional matrix with $i \times j$ elements (matrix-notation: \mathbf{A})
- $y_i = A_{ij}x_j$: matrix-multiplication (matrix-notation: $\underline{y}=\mathbf{A}\underline{x}$). In vector algebra $\mathbf{A}\underline{x}$ is essentially a vector with sums of element-products (see for yourself). This summation is denoted in index-notation by using ‘free’ indices, in this case j . It is called a free index because it will not appear in the resulting vector (y_i) and can therefore be substituted with any other index except i .
- For example, when $i=1..3$ and $j=1..3$: $y_1 = A_{11}x_1 + A_{12}x_2 + A_{13}x_3$
- $T_{i,k}$: a two-dimensional matrix holding the partial differentials of T_i with respect to the elements of a vector with index k (Jacobian matrix). The comma indicates this partial differentiation. ($\frac{\partial T_i}{\partial q_k} = T_{i,k}$).

Muscle dynamics

INTRODUCTION

Muscles are the actuators of the skeletal system. Models are needed to identify how a neural input to the muscle finally results in a mechanical output, i.e. a contraction force, possibly combined with a displacement at the muscle ends. The complex structure of a muscle is not easily captured in a model; a lot of assumptions and simplifications are needed. This chapter shows how the structure of a muscle relates to its functional properties and how these properties are modeled. In Section 4.1 the muscle morphology and physiology are described. In Section 4.2.1 Hill type muscles are discussed and in 4.2.2 cross-bridge models.

OBJECTIVES

This chapter addresses:

- Basic morphological and physiological aspects of muscles.
- How these aspects relate to muscle function and properties.
- Various techniques to model muscle properties and function and their differences.
- The derivation of the differential equation of a Hill-type muscle model.
- Linearization of a Hill-type muscle model and linear analysis around the operating point.

4.1 Muscle morphology and physiology

There are three kinds of muscles: skeletal, heart and smooth muscles. Skeletal muscles are striated and make up a major part of the body; they are the prime mover of locomotion and are controlled by the nerves. When stimulated at a sufficiently high frequency, it can generate a maximal tension, which remains (about) constant in time. In this case, the muscle is tetanized: The activity of the contracting mechanism is thought to be maximal.

Heart muscle is also striated like skeletal muscle, but is never tetanized in its normal function. Instead, it functions in single twitches. Each electrical stimulation evokes one twitch. Until a certain refraction period is passed, another electric stimulation will not evoke a response.

Smooth muscles are not striated, and are not controlled by voluntary nerves. There are many kinds of smooth muscles, for example surrounding blood vessels.

We will focus on skeletal muscles since this course is concerned with motion control. Since a resting skeletal muscle has quite ordinary visco-elastic properties, the interesting part is the contraction. Muscles exert force when activated by stimuli from a nerve or artificially by an electrode (Functional Electrical Stimulation, FES). These stimuli start a chain reaction of chemical processes that initiate a connection between the actin filament and opposite myosin filament. Such a connection is addressed as a cross-bridge. The myofilaments, actin and myosin, are together the smallest functional unit of a muscle, the *sarcomere* (Figure 4.1). In a muscle fiber a large number of sarcomeres are arranged in series. The alignment of sarcomeres in series

sarcomere

observed in parallel arranged fibers attributes to the name of striated muscle. Movement is initiated when the myo-filaments slide past one another. A large number of muscle fibers arranged in parallel form a muscle belly. Through aponeuroses (tendon-sheets) and tendons, the muscle fibers are attached to the bone structure at origin and insertion. An aponeurosis is made of tendinous tissue at which fibers are attached at an angle. At one end an aponeurosis turns into a tendon.

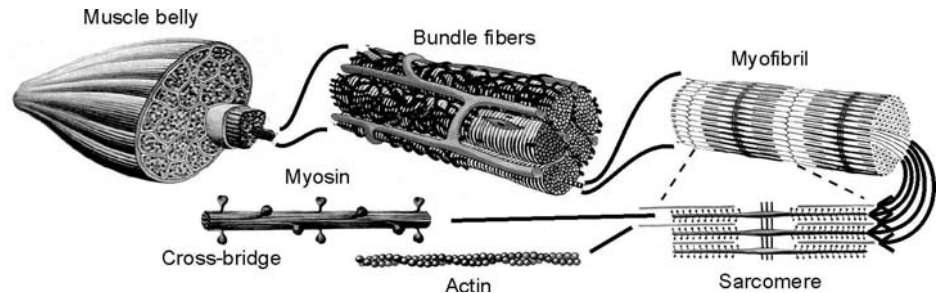


Figure 4.1: Muscle anatomy. Adapted from Gray's anatomy (Warwic and Willems, 1973).

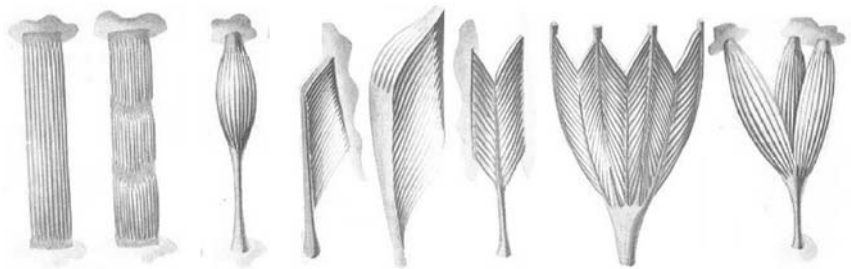


Figure 4.2: Variety of muscle architectures. Adapted from Gray's anatomy (Warwic and Willems, 1973).

muscle architecture

The orientation of the muscle fibers with respect to the direction of force of the whole muscle defines the *muscle architecture*. A schematic representation of a classification in architectural characteristics is given in Figure 4.2. The most common muscle architectures are the parallel fibered and the pennate muscles. In parallel fibered muscle is assumed that fibers are arranged along the direction of force in the muscle. In pennate muscle fibers are relatively short compared to the muscle length and have an angle of operation with respect to the direction of force in the whole muscle. That so many different muscle architectures exist suggests a relation with the function of the muscle. It can be shown that a pennate muscle, with the same fiber length and volume as a parallel fibered muscle, can exert a larger force at the cost of a smaller contraction velocity.

The active components of a muscle cannot function without the presence of passive mechanical structures. The fibers are arranged in a network of connective tissue, the endomysium (Figure 4.3). The muscle is organized in bundles of fibers, each bundle containing over a hundred fibers and surrounded by the perimysium. Finally, the outer surface of the muscle is shielded by the epimysium. Together with tendon and aponeurosis, the epimysium, perimysium and endomysium make up the passive, visco-elastic properties of the muscle. Other structures in the muscle, such as blood and lymph vessels, motor and sensor nerves, are not considered as contributing to the mechanical behavior.

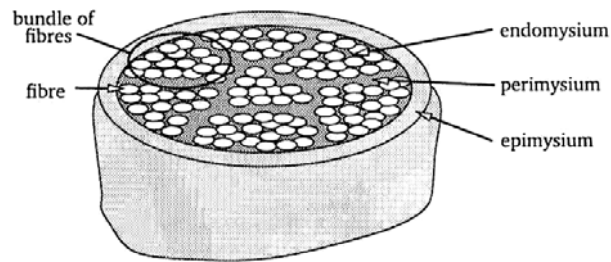


Figure 4.3: Location of the connective tissues epimysium, perimysium and endomysium (adapted from Gielen, 1998)

muscle fiber

A *muscle fiber* is a single cell (Figure 4.4), ranging in length from a few millimeters to several centimeters, and in diameter from 10 to 100 μm . Unlike other cells, it has multiple nuclei, resulting from a fusion of myoblasts in the embryonic phase.

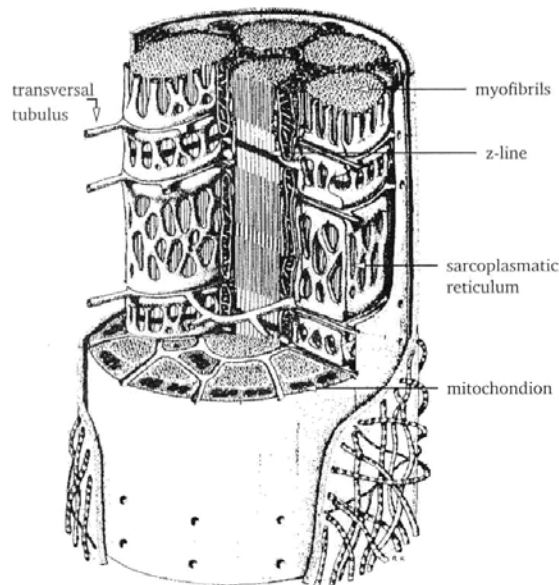


Figure 4.4: Structure of the muscle fiber or cell. Adapted from Ganong (1981).

myofibrils

The cytoplasm of the fiber contains *myofibrils* that convert chemical (metabolic) energy into mechanical energy, and a sarcotubular system needed for the release of Ca^{2+} ions into the muscle cell (Figure 4.4). The sarcoplasmic reticulum buffers the Ca^{2+} ions and the transversal tubuli (two for each sarcomere) provide the transmission of the action potential from the cell membrane to the sarcoplasmic reticulum surrounding the myofibrils. A large number of mitochondrions provide the required energy.

actin, myosin

The chemical reaction that performs the contraction of muscle takes place between the actin and myosin molecules of a sarcomere. The energy is provided by ATP (adenosinetriphosphate) and controlled by Ca^{2+} ions. The Ca^{2+} ions act as a catalyser: without them, the reaction would be very slow at body temperature.

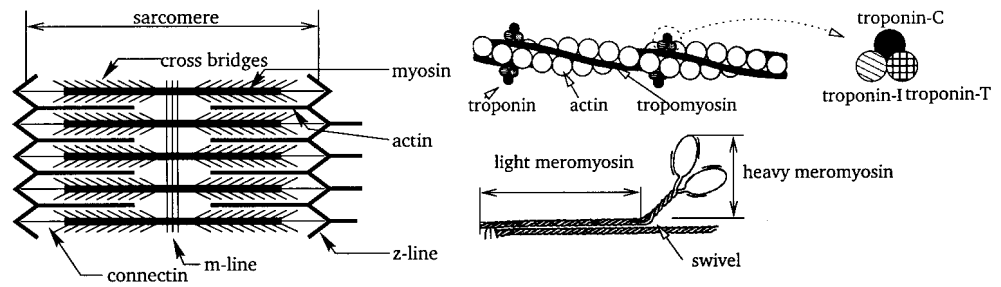


Figure 4.5: Structure of a sarcomere. The heads of the myosin (bottom right) may bind to the troponin sites on the actin filament (top right) to form cross-bridges.

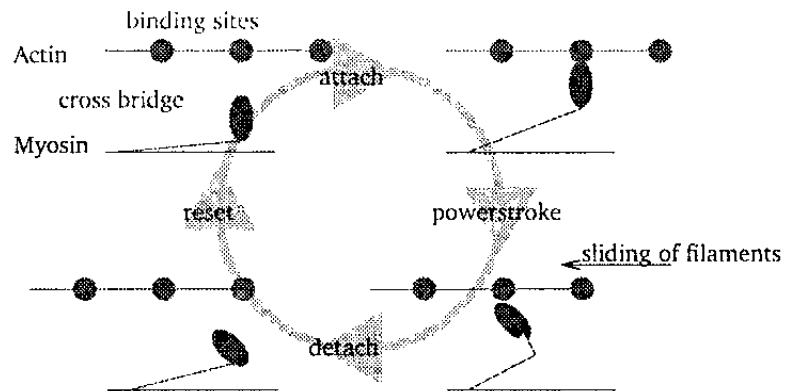


Figure 4.6: Sliding filament model. When the troponin molecules are activated by the Ca^{2+} ions, the myosin can attach to the actin. The myosin head swivels, producing a power stroke. When detached, the myosin is reset for the next

troponin

Under influence of Ca^{2+} , the heads of the myosin attach to the *troponin* sites of the actin molecule to form cross-bridges (Figures 4.5 and 4.6). The myosin head then rotates about 45° : Force is generated or, in the absence of an external force, the filaments will slide along each other. With ATP the connection is detached, and the myosin head is reset in its original position. This detachment costs energy. The myosin head is then ready for the next cycle.

The force output of a sarcomere is regulated by the Ca^{2+} -concentration. An action potential (moving electrical impulse that locally depolarizes the cell membrane) arrives from the nervous system and moves along the fiber membrane with a speed of 1 to 5 m/s. The tubular system transports the action potential into the muscle fiber and depolarizes the sarcoplasmic reticulum. This has the effect that the sarcoplasmic reticulum becomes permeable for Ca^{2+} , the Ca^{2+} is released into the fibrils. The Ca^{2+} is continuously pumped back into the sarcoplasmic reticulum. So, the action potential results in a short increase of Ca^{2+} -concentration, depending on the fiber type (Figure 4.7). For fast fibers this twitch lasts shorter than for slow fibers. When the frequency of the action potentials increases, single twitches are added until no ripple is visible anymore. The constant Ca^{2+} -concentration in the so-called tetanized state results in a constant force output.

motor units

When looking at a more macroscopical level, the muscle fibers are organized in so called *motor units* with about 100 fibers which are distributed (not clustered) over the muscle volume. When a low force output is required, the small motor units, containing a relatively small number of slow fibers, are

excited first. At larger force levels, larger motor units are excited as well, until finally the largest motor units containing the fastest fibers are used. This mechanism is called the size principle and reduces fatigue in natural contractions. Fatigue is also minimized by motor unit rotation: After a certain stimulation time, an activated motor unit is allowed some rest and replaced by another motor unit. So, muscle force output can be increased by increasing the activation frequency and by increasing the number of active motor units.

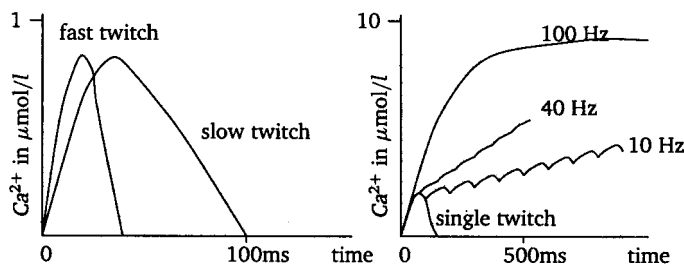


Figure 4.7: Ca^{2+} -concentration for a single action potential (left) and for a pulse train at different frequencies (right).

4.2 Muscle models⁷

Numerous models are developed to describe aspects of muscle functioning, with the purpose to describe or predict how a muscle behaves under certain conditions. As the knowledge of muscles and the numerical capacities increase, these models tend to increase in complexity as well. However, it is often more fruitful to apply as simple as possible models for each specific problem to develop a clear insight in the underlying mechanisms. For example, to study the effect of the pennation angle on muscle force, planimetric models seem appropriate (Huijing and Woittiez, 1984). To describe the relation between neural activation and the resulting joint rotation, the model should at least describe the force-length and force-velocity characteristics (Winters and Stark, 1985). When the shape of the muscle or the interaction between fibers is considered, finite element-like models are unavoidable (van der Linden, 1998).

There are basically two different models developed: a Hill-type muscle model that describes muscle function on a macroscopic level, based on empirical relations and a cross-bridge model that explains muscle behavior on a microscopic level.

4.2.1 HILL-TYPE MUSCLE MODELS

The original model developed by Hill is shown in Figure 4.8. The muscle is considered as a large sarcomere, the *contractile element (CE)*, with some additional passive visco-elastic properties to contribute for the tendon and aponeuroses, the *series element (SE)*, and connective tissues epimysium, perimysium and endomysium, the *parallel element (PE)*.

First some experiments with muscles will be discussed briefly in Section

contractile element (CE), series element (SE), parallel element (PE)

⁷ For this paragraph we used large parts of Chapter 5, written by Jack M. Winters, of Multiple muscle systems (ISBN 0-387-97307-9). This chapter is highly recommended since it discusses the background and many details of muscle modeling.

4.2.1.1. These experiments are used in the identification of the properties of the CE (Section 4.2.1.2.) and in identification of the properties of the connective (passive) tissues (Section 4.2.1.3) represented by the SE and PE in Hill type models (see Figure 4.8). Next variations on the original Hill model are discussed in Section 4.2.1.4. In Section 4.2.1.5 some critical remarks are made about the validity of Hill-type muscle models.

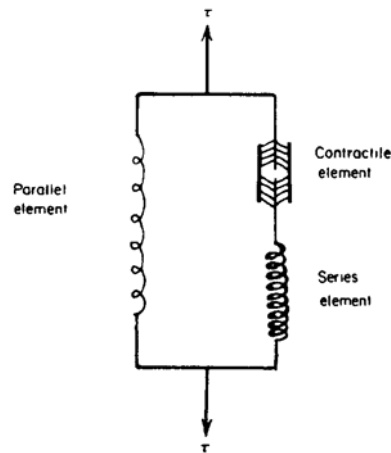


Figure 4.8: Hill-type muscle model with active properties in the contractile element and passive lightly damped elastic properties in the series and parallel element.

4.2.1.1 Modeling foundations

It is important to notice that Hill type models are phenomenologically based lumped parameter models that are based on interpretations of input-output relations obtained from controlled experiments. There are three potential ‘inputs’ to a muscle: muscle load, muscle length, and muscle stimulation. The traditional experimental approach has been to specify the input sequence for neural stimulation and:

- 1) specify and control the muscle force while measuring the muscle length/velocity or;
- 2) specify and control the length/velocity of the measuring while measuring the developed muscle force

Typically one input is held constant while the other is varied as an impulse, a step, ramp, sinusoid, or a ‘white noise’ (random) signal. Notice that many combinations are possible, and, as seen in Figure 4.9 many of the classic combinations have been given specific names.

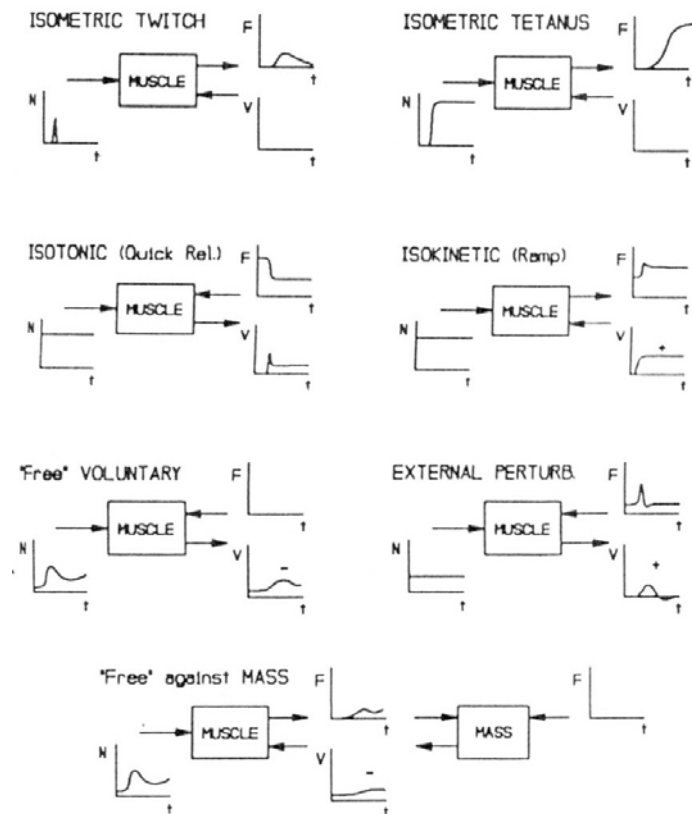


Figure 4.9: Input-output combinations for skeletal muscle. In each case the neural input (N) is on the left and the mechanical variable pair, force (F) and velocity (v) is on the right. Notice that in each case there are two input sequences and one output trajectory to be measured. An ‘impulse’ is an input of short time duration relative to the system response –the area under the curve determines the intensity. A ‘step’ is a change in level that, relative to the overall system response, is rapid. A ‘ramp’ is the integral of a step. (Source Winters, 1990)

4.2.1.2 Identification of model structure: Contractile element (CE)

Hill published his famous paper in 1938 which formally identified a lightly damped passive elastic element in series with a nonlinear contractile element (CE). This contractile element is the only element in the model that can generate energy. The other muscle elements are all passive in nature and are only able to generate or dissipate energy. The force generation of CE depends on its velocity, on its length and on its activation. The relation of the muscle force to these three variables are discussed next.

The force-velocity relation

For maximal activation, the generated force was found to decrease non-linearly with shortening velocity. The CE force velocity behavior could be described by a hyperbolic equation:

$$(v + b)(F + a) = b(F_0 + a) \tag{4.1}$$

Where F is the muscle force, v is muscle shortening velocity, and a , b and F_0

are constants. Roughly, if we ignore the constants a and b on the left-hand side, Equation 4.1 states that the rate of work done, or the rate of energy conversion from chemical reaction, is a constant.

The empirical equation is based on an energy balance:

$$E = A + S + W \quad (4.2)$$

Where E is the rate of energy release, A is the activation or maintenance heat per unit of time, $W=Fv$ is the mechanical power output and S is the shortening heat, needed for change of muscle shape.

Hill measured the energy balance of a frog sartorius muscle by keeping it fixed at a certain length and with maximal stimulation resulting in a tetanic force F_0 . By keeping the muscle isometric and measuring the heat production he could identify the value of A in Equation 4.2. Then, he quickly released one of the fixations and allowed the muscle to contract against a smaller force F , resulting in a muscle speed v (Figure 4.10). He empirically identified the additional heat production as

$$S + W = b(F_0 - F) \quad (4.3)$$

He asserts further that empirically:

$$S = av \quad (4.4)$$

Substituting S and W in to Equation 4.3 results in Equation 4.1.

In an alternative equation for the force-velocity relation, the sarcomere is a force-generating element in parallel with a non-linear damper:

$$F = F_0 - \frac{F_0 + a}{v + b} v = F_0 - k(v)v \quad (4.5)$$

The damping k is maximal at low contraction velocities and minimal (but not zero) at large velocities.

Usually, the force-velocity equation is put in a dimensionless form $g(v)$:

$$\begin{aligned} F &= F_0 \frac{1 - (v/v_0)}{1 + c(v/v_0)} = F_0 \cdot g(v) \\ c &= F_0 / a \\ v_0 &= b \cdot c \end{aligned} \quad (4.6)$$

Where c is a shape factor and v_0 the maximal contraction velocity of the sarcomere when not loaded. It is often assumed that c and v_0 are constant for a certain muscle, only depending on the fiber type and rest-length l_r . For fast fibers, $c=0.1$ and $v_0=8l_r$ per second, for slow fibers $c=1$ and $v_0=2l_r$ per second. However, in Equation 4.6 is shown that c and v_0 both depend on the tetanic force F_0 .

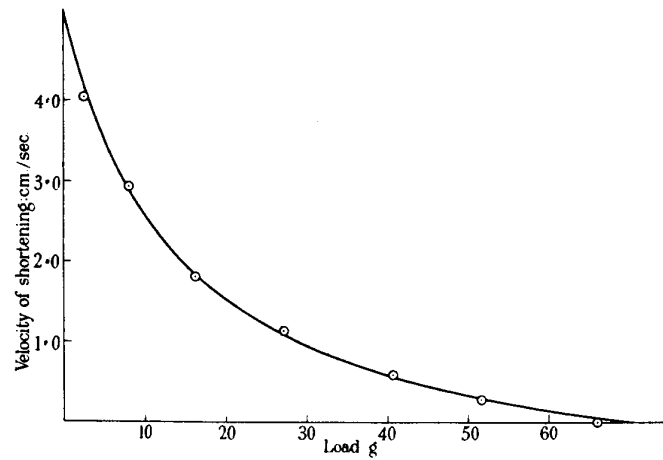


Figure 4.10: Force-velocity curve: Experimental data from Hill (1938) with the fitted Equation 4.1.

The force-velocity relation $g(v)$ is extended to account for all muscle loading situations: The original relation derived by Hill is valid for concentric contractions (i.e. shortening muscle, the muscle generates mechanical energy) only. For eccentric contractions (i.e. lengthening muscle, the muscle dissipates energy) it is found that the muscle force can be 1.2 to 1.8 times larger than the isometric force (Figure 4.11). The actual shape of the force-velocity relation is defined by a number of muscle-dependent parameters.

It is obvious that the mechanical power output has an optimal value between zero and maximal velocity. At zero velocity (isometric contraction) the mechanical power output is zero. This does not mean that no chemical energy is required, as can easily be verified by carrying a weight.

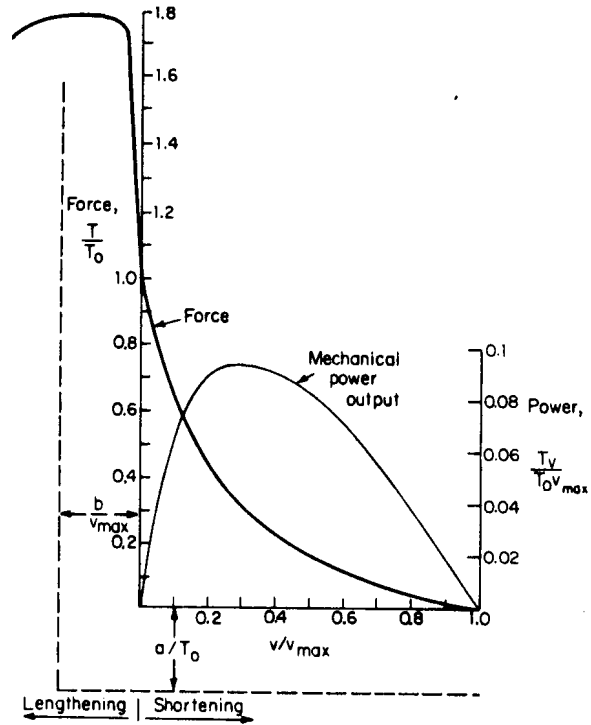


Figure 4.11: The muscle force velocity relation and mechanical power output. From McMahon (1984)

An expression for this extended force-velocity relation is given by (Winter and Stark, 1995):

$$g(v_{ce}) = \begin{cases} 0 & v_{ce} \leq -v_{max} \\ \frac{V_{sh} v_{max} + V_{sh} v_{ce}}{V_{sh} v_{max} - v_{ce}} & -v_{max} < v_{ce} \leq 0 \\ \frac{V_{sh} V_{shl} v_{max} + V_{ml} v_{ce}}{V_{sh} V_{shl} v_{max} + v_{ce}} & v_{ce} > 0 \end{cases} \quad (4.7)$$

$$v_{max} = V_{vm} (1 - V_{er} (1 - q(t))(f(l_{ce})))$$

with:

- V_{sh} determining the concavity of the Hill curve during shortening;
- V_{shl} determining the concavity during lengthening,
- V_{ml} determining the maximum relative force during eccentric contraction,
- V_{vm} the maximum velocity during concentric contraction
- V_{er} determining the dependence of the maximum velocity on the active state and length of the muscle
- $f(l_{ce})$ the force-length relation of the CE (Equation 4.10)
- $q(t)$ the active state function (Equation 4.11)

Note that the maximum contraction velocity is dependent on the length and the activation of the sarcomeres.

The force-length relation

The force the contractile element delivers depends not only on the contraction velocity but also on its length. The force that can be developed depends on the number of cross-bridges that can be formed, which is related to the amount of overlap of the actin and myosin filaments (Figure 4.12). Therefore, the force F_0 in Equation 4.6 depends on the length of the sarcomere. The maximum overlap occurs between B and C in Figure 4.12. The part between O and B is called the ascending limb and between C and D the descending limb of the force-length curve. The force-length relation is usually expressed as a dimensionless function $f(l_{ce})$:

$$F_0 = F_{\max} \cdot f(l_{ce}) \tag{4.8}$$

Where F_{\max} is the maximal isometric force at optimum sarcomere length and l_{ce} is the actual sarcomere length. F_{\max} is considered proportional to the fiber cross-area with a constant fiber stress (estimated by different authors between 10 and 100 N/cm²).

The total force output of the sarcomere is then:

$$F_{CE} = F_{\max} \cdot f(l_{ce}) \cdot g(v_{ce}) \tag{4.9}$$

Note that this equation is valid for a tetanized fiber only and it is assumed that the length and contraction velocity of the sarcomere are independent (see Equation 4.6), which is not necessarily true.

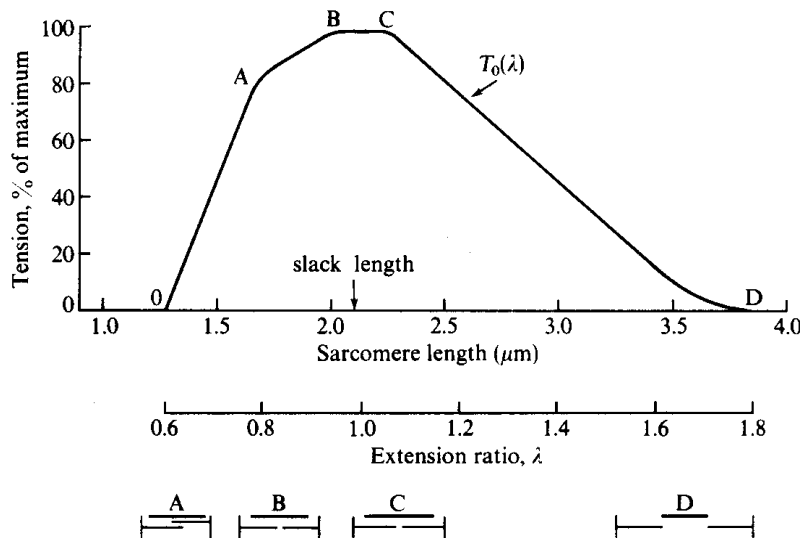


Figure 4.12: The (isometric) force-length curve for frog skeletal muscle fibers. The relative positions of the actin and myosin filaments for A to D are shown at the bottom. From Gordon et al. (1966).

The total muscle force is measured for a fully tetanized muscle under isometric conditions (otherwise the force-velocity relation would also contribute). From the total and the passive curve the active force-length relation is determined. In principle, this is not a correct procedure, since the passive properties may depend on the activation of the muscle: The muscle geometry in both states is

different. The active force is smoother than for a single sarcomere (compare Figure 4.12 with 4.16) because the local effects of numerous sarcomeres are averaged for the entire muscle. The active force-length relation is often described by a set of polynomials or an exponential function such as:

$$f(l_{ce}) = \exp\left(-\left(\frac{L_{ce} - L_{ce0}}{L_{cesh}}\right)^2\right) \quad (4.10)$$

where L_{cesh} is a shape parameter determining the width of the force-length relationship, L_{ce} is the actual fiber length and L_{ce0} is the optimum fiber length (~ optimum CE length).

Active state function

In the previous two sections only a fully tetanized (maximally activated) muscle was considered. One needs the active state function to describe muscles other than fully tetanized. It relates the neural input $u(t)$ to the muscle activation $q(t)$ and is normalized between zero and one. The most simple relation would be linear: $q(t)=u(t)$. A force output of half the maximal force would then require a neural input of 0.5. This implicitly assumes that at each force level the muscle is tetanized, which is of course not correct. In addition, a single twitch could not be modeled with it (see also Figure 4.13).

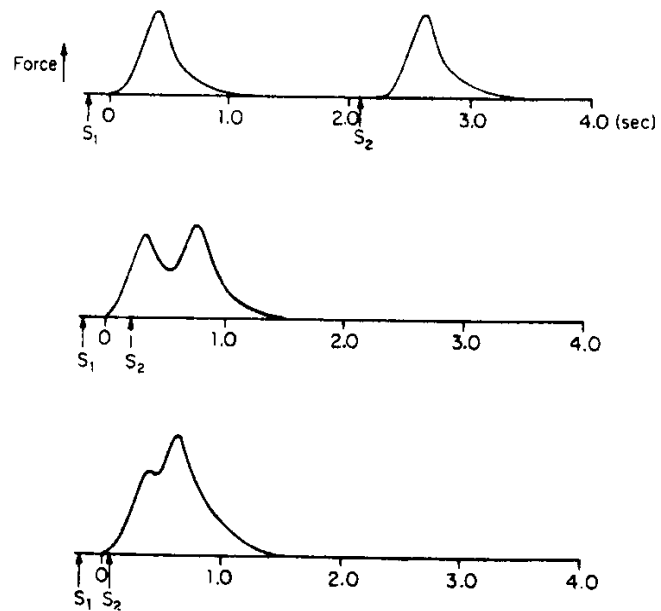


Figure 4.13: Superposition of two twitches with decreasing time-intervals. Note the time delays for excitation and the Ca^{2+} -concentration.

Winters and Stark (1985) proposed to model the active state with two first-order differential equations:

$$\begin{aligned}
\tau_1 \frac{dN_a}{dt} + N_a &= u(t); \\
\tau_{a/d} \frac{d\psi}{dt} + \psi &= N_a; \\
q(t) &= h(\psi)
\end{aligned} \tag{4.11}$$

The first equation describes the excitation dynamics: The relation from the neural input to the excitation N_a of the sarcoplasmic reticulum. The time delay τ_1 of this process is about 30 ms and is shown in Figure 4.13 as the time difference between S_1 and the start of the twitch. The second equation describes the Ca^{2+} -concentration in the sarcomere ψ as a function of the excitation. As it takes more time to pump the Ca^{2+} back into the sarcoplasmic reticulum than to insert it into the sarcomere, the time constant for activation τ_a is shorter than for deactivation τ_d , with magnitudes of about 10 and 50 ms respectively (see Figure 4.13). The last equation describes how the Ca^{2+} -concentration relates to the force output of the fiber. It is often assumed that this is a linear relation.

Exercise

- Implement Equation 4.11 into Matlab Simulink and use as input different pulse trains of different frequencies and try to obtain results similar as in Figure 4.13.

Summarizing, the force of the contractile element can be expressed as:

$$F_{CE} = F_{\max} \cdot q(t) \cdot f(l_{ce}) \cdot g(v_{ce}) \tag{4.12}$$

4.2.1.3 Identification of model structure: Connective tissues (Winters, 1990)

Since the contractile element is connected both in series and parallel with visco-elastic structures (Figure 4.8), it is appropriate to develop an understanding of the basic properties of such tissues. Passive connective tissues, ranging from tendon, to skin to blood vessel, tend to have quasi-static mechanical properties such as shown in Figure 4.14b in which the stiffness increase fairly linearly with force over the primary operating range (Fung, 1967). This can be described mathematically:

$$\frac{dF}{dx} = K_1 F + K_2 \tag{4.13}$$

where F is force, x is extension, and K_i are constants. Solving this equation and applying boundary conditions, we arrive at the classic exponential relationship for connective tissues (e.g. Fung, 1969; Hatze, 1974):

$$F = K_3 \exp(K_1 \Delta x - 1) \tag{4.14}$$

where Δx is the extension relative to the rest (i.e. zero force) length.

For most tissues this behavior is due to wavy collagen fibers (which vary in number and orientation between tissues) gradually straightening out and bearing load (e.g. Fung, 1981). Thus, the overall curve could be exponential shaped even if linear collagen properties are assumed (Figure 4.14c-d). This relation can be reformulated to possess a more convenient set of parameters (Hatze, 1981; Winters and Stark, 1985):

$$F = \left(\frac{F^*}{\exp(K_{sh} - 1)} \right) (\exp(K_{sh} / \Delta x^*) \Delta x - 1) \quad (4.15)$$

where the describing parameters are now very intuitive: a point on the curve (here F^* and Δx^*) and dimensionless shape parameter (Figure 4.14d). If desired, an exponential-shaped toe region can easily be connected to a linear region, with the shape parameter set by the constraint of no discontinuity in slope (i.e. stiffness), as shown in Figure 4.14e.

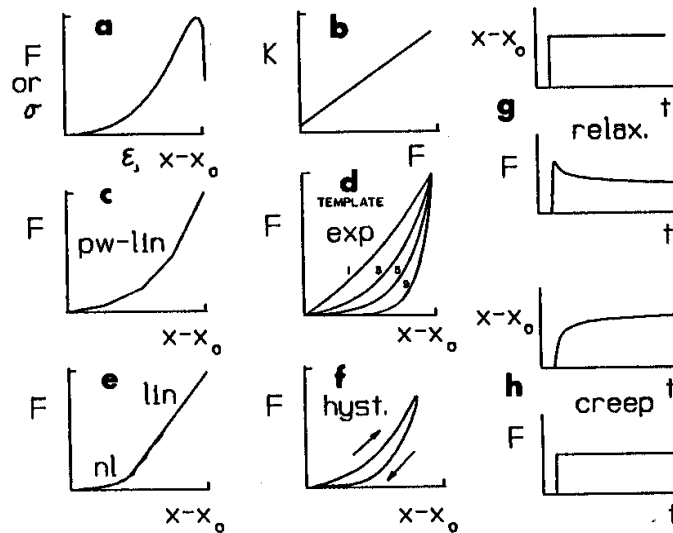


Figure 4.14: Classical mechanical properties of biological soft connective tissue.

a) Typical quasi static-static stress-strain or force-extension curves $\sigma = \mathbf{F}/(\text{cross-sectional area } A)$ $\varepsilon = \Delta x/\text{rest length } L_0$. **b)** Classic stiffness-force relation, which results in the exponential force-extension of **d**. **c)** Concept of linear collagen fibers, of different initial orientation, starting to stretch at different extensions ('piecewise linear'). **d)** Exponential fit via 'intuitive' parameters: a dimensionless 'shape' parameters K_{sh} and point on the curve (conveniently F_{max} and Δ_{max}). **e)** 'hybrid' curve: exponential 'toe' segment followed by linear region. **f)** Hysteresis due to visco-elasticity for tissues under cyclic loading (constant stretch velocity followed by release). **g)** Force 'relaxation' output trajectory due to a length step input. **h)** length 'creep' output trajectory due to a step change in force. (Source Winters, 1990)

Biological connective tissues are also inherently visco-elastic, i.e. they exhibit hysteresis during cyclic loading (Figure 4.14f), force relaxation when held at a constant length (Figure 4.14g) and length creep when held at a constant force (Figure 5.4h). Of note is that visco-elastic properties are evident within both short (milliseconds) and long (minute or hours) time periods. Thus, the amount of hysteresis (measure of energy loss) varies with both the speed of ongoing extension and the history of recent extensions. Most of the time these viscous effects are not considered in Hill-type models. However one must keep these (neglected) passive properties in mind especially for experiments that unfold over very fast (order of milliseconds) or very slow (man second time) intervals.

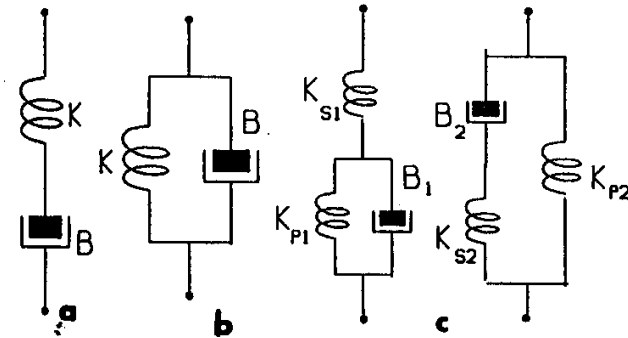


Figure 4.15: Classic models for describing visco-elastic properties. In each case the constitutive relation for the spring is $F=f(\Delta x)$, the dashpot is $F=f(\Delta v)$. **a)** “Maxwell” series model. **b)** “Voigt” parallel model. **c)** “Kelvin” or “standard” models. (Source Winters, 1990).

The effect of the connective tissues can be clearly seen in the force-length characteristic of the whole muscle (Figure 4.16). Besides the amount of overlap of actine and myosin filaments the force-length relation of the whole muscle depends on the deformation of passive visco-elastic structures that surround the muscle fibers (the parallel element in Figure 4.8).

In the force-length relation of the full muscle the following two contributions can be identified (Figure 4.16): the passive behavior from the parallel element and the active behavior from the contractile element. The total muscle force is the summation of the two. The passive muscle force is measured by stretching the inactive muscle. Above a certain length, usually the rest length of the muscle, a force is developed. Below the rest length the muscle does not resist compression. The passive force may depend on the stretching velocity (i.e. visco-elastic instead of elastic), although this is not always included in the model. It should be noted that the relative contribution of the passive force to the total force might depend on the geometry of the muscle (Figure 4.16).

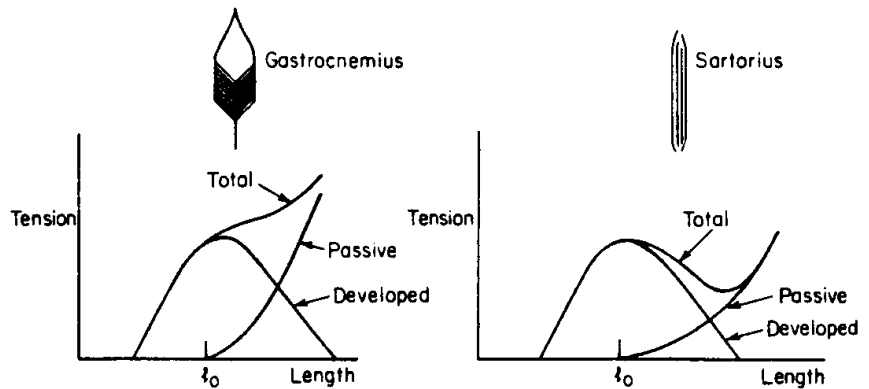


Figure 4.16 Force-length relation for two muscles under isometric conditions. From McMahon (1984).

4.2.1.4 Structural extensions of the Hill-type muscle model (Winters, 1990)

Model structures for musculotendinous systems that have been commonly used are shown in Figure 4.8 and 4.17. Essentially, the difference between these models is the arrangement of passive spring and dashpot elements. In both of these figures, springs with lower stiffness are shown smaller. Model *d* is a better approximation of the physical reality. However, is the accuracy increase worth the cost of the added complexity? If dash-pots are assumed negligible (as is common), it turns out that some of the springs are not mathematically independent of each other. This can be seen by using methods such as bond graphs to identify independent storage elements. When this is the case, models can be reduced without any loss of dynamic performance, and in fact, extra springs may confound interpretation and make modeling computationally less efficient. However, if an internal node location, such as node *d* in Figure 4.17 happens to be of special interest (e.g. for sensory feedback of muscle length), then the added structure is worthwhile.

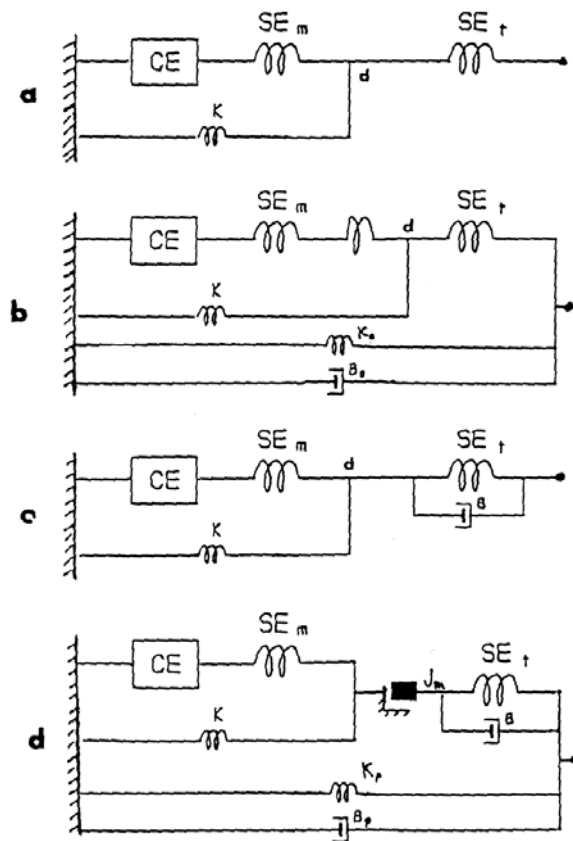


Figure 4.17: Common elaborate musculoskeletal structures (beyond Figure 4.8). *a*) tendon in series with classic muscle structures. *b*) combined muscle-tendon models with additional springs (see Hatze, 1981 for details). *c*) simple model structure with a 'lumped' SE visco-elastic element. *d*) 'complex' model which includes an internal node for muscle mass (the usual convention is to lump mass with the limb segment). (Source Winters, 1990)

4.2.1.5 Discussion

Hill-type models are very useful to make a link between the neural system and a resulting force production on and movement of a body segment. The drawback is it is difficult to assess the validity of these models. The model is based on well-defined, but only few experiments; therefore there may be discrepancies with real muscles. Some points require attention:

- It is implicitly assumed that $f(l_{ce})$ and $g(v_{ce})$ are independent of time. Most likely they are not. It is known that the force output is contraction history dependent (Meijer, 1998) and effects like fatigue are not considered.
- The equations for the different elements of the muscle are dependent on a large number of parameters, such as maximal force, maximal contraction velocity, and optimal muscle length. The parameters are mostly based on animal experiments and are not well known yet for human muscles. In addition, an isolated muscle (*in vitro*) may behave different from the same muscle *in vivo*.
- In reality the parameters are not constant, otherwise it would be useless to exercise and train. Muscle is living tissue that adapts to the required performance.
- Hill-type models are not linked to the microscopic mechanisms within a muscle; they are the result of experimental curve fitting, it is a descriptive model and can not be used to estimate e.g. the muscle metabolism.
- The descending limb of the force-length relation can show a negative slope. This relates to a destabilizing negative stiffness in a model. In real life this negative stiffness is unlikely to occur. One should keep in mind that the force-length relation is the result of a large number of *isometric* experiments. For the purpose of modeling, these separate points are fitted with a curve.

4.2.2 COMPUTER SIMULATION WITH A HILL-TYPE MUSCLE MODEL

4.2.2.1 Introduction

In previous paragraph the characteristics of the various muscle structures were discussed. We are now able to derive a dynamic model of muscle, i.e. differential equations that can be integrated numerical with for example Matlab Simulink. An important choice is the choice of model structure. The following dynamic muscle model is based on the work of Winters & Stark (1985, 1987), adapted by Happee (1992). The muscle model has three input variables, i.e. neural input u , muscle length l and muscle velocity v , and one output variable, i.e. muscle force. Often muscle velocity is not used as an separate input variable, but is it rather calculated inside the muscle model as the derivative of muscle length. The change of muscle force due to the neural input is the control behaviour of the muscle. The change of muscle force due to length input (and velocity input) results in the visco-elastic properties of the muscle, i.e. the muscle stiffness (dF/dl) and muscle viscosity (dF/dv). In Hill-type muscle models the muscle stiffness and viscosity are effectively the derivative of the force-length and force-velocity curves at the operating point.

In Figure 4.18 a block scheme of the muscle model in combination with an external linkage system is shown. The output of a muscle is force, and not position. What happens to the position of the muscle after it received neural input depends on the environment the linkage system is attached to. If the environment is a free mass, the muscle force will result in an acceleration of the mass and the muscle will shorten: *concentric contraction*. If the linkage system is fixed, the muscle will not shorten and an isometric contraction will result. If

*concentric
contraction*

*eccentric
contraction*

an external force is applied on the linkage system, the muscle might actually be lengthened in the opposite direction of its own force: *eccentric contraction*.

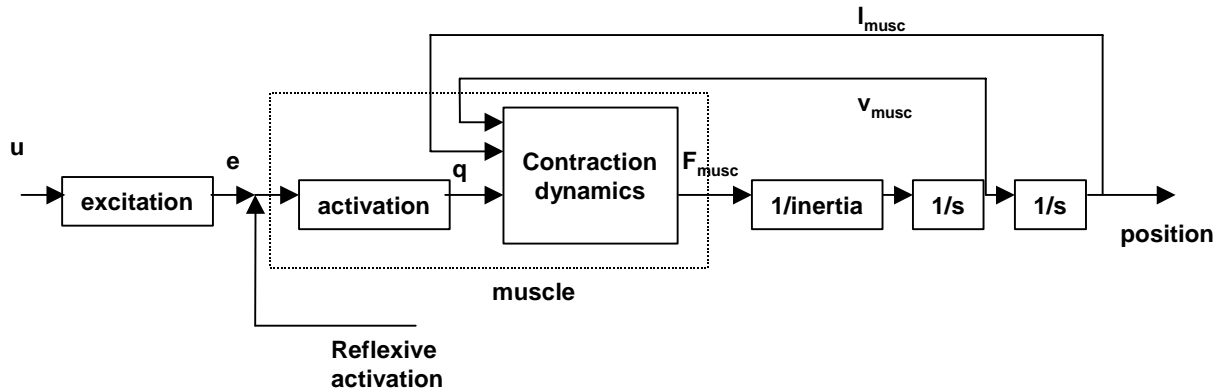


Figure 4.18: A block scheme of a muscle model in connection to a linkage system (inertia). The model consists of three dynamic blocks, i.e. excitation, activation and contraction dynamics. Input to the muscle is neural input u , muscle length l_{musc} and contraction velocity v_{musc} . Output is muscle force.

The length and velocity dependency of the muscle is shown in Figure 4.18 as a feedback loop. In Chapter 8 it will be shown that these feedback loops constitute the joint stiffness and viscosity, which is called the intrinsic component of joint dynamics. This intrinsic component can be added to the reflexive feedback loops (reflexive component), and together with the joint inertia they constitute the total joint impedance.

4.2.2.2 Muscle model

The muscle model is a third order model, consisting of a linear first-order model of excitation dynamics, a non-linear first order model for activation dynamics and a non-linear first-order model for the force-velocity relationship of the contractile element, which represents the muscle fiber. In the contractile element the active muscle force is generated. In addition, the muscle model contains a non-linear force-length relationship, a non-linear series-elastic element, representing the tendon but also the cross-bridge stiffness, and a non-linear parallel-elastic element, representing the passive muscle properties. Input to the model is neural input with an infinite bandwidth, bounded between zero (no input) and one (maximal input). Another input is muscle length, which is fed back from the motions of the skeletal (inertial) system. Output of the muscle model (and input of the skeletal system) is muscle force.

In state equations:

$$\begin{aligned}\dot{x} &= f(x, u) \\ F_{\text{mus}} &= g(x)\end{aligned}\tag{4.16}$$

in which the vector of state variables $x = [e \ q \ L_{ce}]^T$ are the excitation, active state and length of the contractile element, respectively. The derivatives of the state vector are $\dot{x} = [\dot{e} \ \dot{q} \ V_{ce}]^T$, in which V_{ce} is the contraction velocity of the contractile element. If we are able to find the function $f(x, u)$, Equation 4.16 can be

integrated as a function of input u in time, and muscle force F_{mus} is calculated at each time instant. From the empirical relations as discussed in Section 4.2.1, the functions f and g can be derived as shown in the following sections.

4.2.2.3 Excitation dynamics

The excitation dynamics describe the relation between a hypothetical neural input and the excitation of the muscle. The neural input can be thought of as a motor program of infinite bandwidth, i.e. this can be a pure step. The excitation can be thought of as the neural signal which arrives at the muscle membrane. The latter can be compared with the EMG signal. It should be noted that the puls-type neural spikes are represented by a continuous signal, which can be interpreted as spikes/second. The excitation dynamics are a low-pass filter, representing the fact that the change of neural input has a limited frequency.

Neural input due to reflexive feedback does only contain low frequencies, because it has been low-pass filtered by the inertia of the linkage system. These signals are assumed to be direct input to the activation dynamics (see Figure 4.18).

The excitation dynamics are captured by the linear first-order system with input u and output e :

$$e(s) = \frac{1}{1 + \tau_{ne} \cdot s} u(s) \quad (4.17)$$

or after inverse Laplace transformation in state equation form

$$\dot{e}(t) = \frac{u(t) - e(t)}{\tau_{ne}} \quad (4.18)$$

where e is excitation, u is neural input and τ_{ne} is the time-constant for neural excitation.

4.2.2.4 Activation dynamics

The activation dynamics describe the relation between muscle excitation e and muscle activation q , and can be interpreted as the calcium flow through the muscle membrane. Since calcium inflow is a much faster process than calcium outflow, the first-order system can be described with two time-constants:

$$q(s) = \frac{1}{1 + \tau_{ac} \cdot s} e(s) \quad (4.19)$$

$$q(s) = \frac{1}{1 + \tau_{da} \cdot s} e(s) \quad (4.20)$$

or after inverse Laplace transformation in state equation form

$$\dot{q}(t) = \frac{e(t) - a(t)}{\tau_{ac}} \quad (4.21)$$

$$\dot{q}(t) = \frac{e(t) - q(t)}{\tau_{da}} \quad (4.22)$$

where q is activation, and τ_{ac} is the time-constant for increased muscle activation ($e > q$) and τ_{da} is the time-constant for decreasing muscle activation. Note that

Equations 4.17-4.22 are not similar to Equation 4.11. In the latter the neural input u was considered as a spike rate (in spikes per second), while in this paragraph the neural input is considered to be a normalized continuous signal (range 0..1).

4.2.2.5 Contraction dynamics

The actual muscle part of the muscle model is modeled with a contractile element, in series with a non-linear passive series-elastic element. This chain is in parallel with a non-linear passive parallel-elastic element. The configuration of the active and passive elements is shown in Figure 4.19. The contractile element is an active element, in which force development is a function of the non-linear force-length and force-velocity relationships. In this part of the muscle model, activation q and muscle length L_{mus} are input, and muscle force is output.

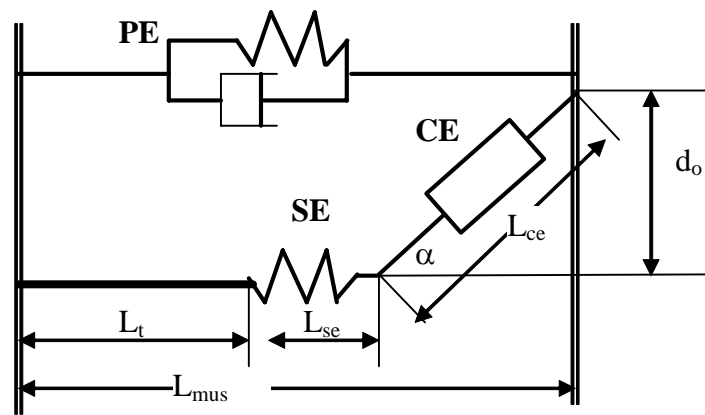


Figure 4.19: Muscle model

Force-length relation

To relate muscle length to fiber length, first the effects of pennation angle and tendon length must be taken into account:

$$d_0 = \sin(\alpha_0) \cdot L_{ce0} \quad (4.23)$$

$$\alpha = \arcsin\left(\frac{d_0}{L_{ce}}\right) \quad (4.24)$$

where d_0 is the width of the muscle due to pennation. It is assumed that the muscle is bi-pennate (or multi-pennate), and that the width of the muscle does not change, i.e. d_0 is constant. α_0 is the initial pennation angle, and L_{ce0} is the optimum fiber length (\sim optimum length contractile element). α is the actual pennation angle, and can be calculated from the actual fiber length L_{ce} .

Hence, the length of the SE can be calculated (see Figure 4.19):

$$L_{se} = L_{mus} - \cos(\alpha) \cdot L_{ce} - L_t \quad (4.25)$$

in which L_{se} is the length of SE, L_{mus} is the normalized muscle length and L_t is the length of the tendon. It should be noted that L_{ce} , L_{se} , L_t are all normalized with respect to optimum muscle length. The normalized force-length relation $f(l_{ce})$ of the CE can be described with Equation 4.10.

Series-elastic element

The force (F_{se}) in the series-elastic element can be described by a function such as Equation 4.15.

Since by virtue of the structure of the muscle model, the force in the SE should be equal to the component of the force in the CE along the axis of SE the force-velocity relation $g(v_{ce})$ can be expressed in the length of SE and of CE (using Equation 4.12).

$$F_{se}(l_{se}) = \cos(\alpha) F_{max} q(t) f(l_{ce}) g(v_{ce}) \Leftrightarrow$$

$$g(v_{ce}) = \frac{F_{se}(l_{se})}{\cos(\alpha) F_{max} q(t) f(l_{ce})} = g^* \quad (4.26)$$

Inverted force-velocity relationship

By inverting the force-velocity relation of the CE (Equation 4.7), v_{ce} can be expressed in the outcome (g^*) of Equation 4.26:

$$v_{CE} = \dot{l}_{CE} = \begin{cases} \frac{V_{sh} v_{max} (g^* - 1)}{g^* + V_{sh}} & \text{if } 0 \leq g^* \leq 1 \\ \frac{-V_{shl} V_{sh} v_{max} (g^* - 1)}{g^* + (-1 - (1 + V_{sh} V_{shl})(V_{ml} - 1))} & \text{if } 1 < g^* \leq V_{ml} \end{cases} \quad (4.27)$$

Parallel visco-elastic element

The force-length relation of the parallel element F_{pe} can be modeled by for example Equation 4.15. For the force-velocity relation a simple linear relation:

$$F_{pve} = p_v \cdot v_{mus} \cdot F_{max} + F_{pe} \quad (4.28)$$

is used where p_v is a constant, and v_{mus} is the normalized muscle velocity.

Total muscle force

The output of the muscle model is the total muscle force F_s :

$$F_{mus} = F_{se} + F_{pve} \quad (4.29)$$

State variables

We now have three differential equations (Equation 4.18, 4.21 or 4.22, and 4.27). The state variables in the muscle model are excitation e , activation q and length of the contractile element L_{ce} . These states can be integrated numerically using the state derivatives, of which contraction velocity is the derivative of muscle fiber length

Exercises

- 1) Implement this muscle model in Matlab Simulink.
- 2) Perform simulations with this muscle model similar to the ones in Figure 4.9.
- 3) Linearize the model for different equilibrium positions (different lengths and activation patterns, take care that the length of the CE is smaller than its optimum length).
- 4) Make Bode-diagrams for different equilibrium positions.
- 5) How can different muscle structures be recognized in the Bode-

- diagram?
- 6) Make a block diagram of the linearized model with u as input and f as output. Define the force-length relation and the force-velocity relation in control theory terminology?
 - 7) For high levels of co-contraction the muscle activation increases. What is the effect of co-contraction?

4.2.3 CROSS-BRIDGE MODELS

Huxley (1957) developed the first cross-bridge model to explain on a molecular level how a muscle produces force. The cross-bridge model is in fact a replacement for the contractile element in Figure 4.8. It assumes that the cross-bridge can be in one of two different states (Figure 4.20): attached or detached⁸. A function $f(x)$ describes the rate with which detached cross-bridges can attach, a function $g(x)$ describes the rate of the reverse process. As this is a cyclic process, these rates are equivalent to the probabilities that cross-bridges attach or detach.

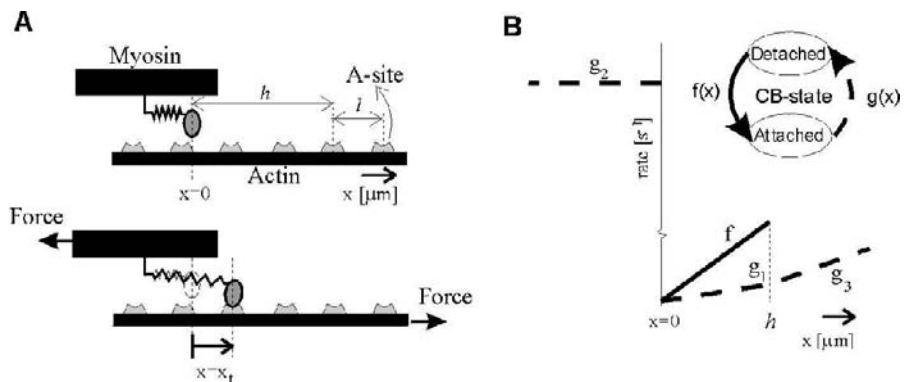


Figure 4.20: Cross-bridge model with the molecular mechanism (a) and cross-bridge states (b).

The functions f and g depend on a distance x , which is the distance that a myosin molecule is stretched. The myosin head may attach to the troponin sites on the actin filament (see also Figure 4.5). It is assumed that a certain range of stretch lengths is available ($0 < x < h$) for attachment at unoccupied troponin sites, and with increasing x the probability of an attachment f increases. Outside this range the cross-bridges can only detach. For a negative x , i.e. a compressed myosin filament, the probability of detachment g is so large that almost immediately detachment occurs. The force a single cross-bridge can deliver is assumed proportional with stretch length x .

Suppose N is the total number of available cross-bridges, and n is the number of attached cross-bridges with stretching length x and at time t . Alternatively, $n(x,t)$ can be viewed as the distribution (over x) of attached cross-bridges at time t .

The rate of change of $n(x,t)$ in time is proportional to the attachment rate times the number of detached cross-bridges minus the detachment rate times the number of attached cross-bridges:

⁸ Later models included more intermediate states to explain more aspects of muscle behavior.

$$\frac{dn(x,t)}{dt} = \frac{\partial n}{\partial t} + v \frac{\partial n}{\partial x} = f(x)\{N - n(x,t)\} - g(x)n(x,t) \quad (4.30)$$

Where v equals the contraction velocity of the sarcomere. All cross-bridges are acting in parallel, so the total sarcomere force equals the sum of all cross-bridge forces:

$$F_{CE} = k \int_{-\infty}^{\infty} x \cdot n(x,t) \cdot dx \quad (4.31)$$

Where k is the stiffness modulus of a single cross-bridge. With known sarcomere dimensions and initial conditions the partial differential equation as indicated in Equation 4.30 can be integrated, although this requires considerable numerical effort. The cross-bridge model predicts the force-velocity curve well: For eccentric contractions, a relatively large number of cross-bridges is at a large stretch length x , thus increasing the force. For concentric contractions x is relatively small, resulting in a lower force.

4.2.3.1 Distribution moments approach of Huxley's model

Zahalak (1981) proposed a method to rewrite the partial differential equation (Equation 4.30) as an (infinite) set of ordinary differential equations. The essence of the method is that the spatial distribution of n can be approximated by a set of orthogonal functionals, in this case polynomials. The same is done in, for example, Taylor series expansions or the approximation of a cyclic function with a Fourier series. The spatial part of the equation can then be integrated, resulting in an (infinite) set of differential equations in time. By substituting a known spatial distribution, the integration constants are obtained and the ordinary differential equations can be solved.

Zahalak introduced the distribution moments $Q_\lambda(t)$:

$$Q_\lambda(t) = \int_{-\infty}^{\infty} x^\lambda \cdot n(x,t) \cdot dx \quad (4.32)$$

It can be shown easily that the cross-bridge stiffness is proportional to Q_0 , the force F_{CE} equal to kQ_1 and the elastic energy of the active part proportional to Q_2 . Clever substitution in Equation 4.16 results in the ordinary differential equation:

$$\frac{dQ_\lambda(t)}{dt} = h(t) + \lambda \cdot v \cdot Q_{\lambda-1}(t) \quad \lambda = 1, 2, 3, \dots \quad (4.33)$$

Where $h(t)$ is a time function depending on some integrals of f , g and $n(x,t)$. By assuming a Gaussian distribution function for $n(x,t)$, this set of equations can be approximated with the first three of them only. Evidently, this approach yields different solutions for $n(x,t)$ than the original model. However, the muscle force and stiffness is approximated well. Also, the numerical integration time is reduced significantly, which makes it possible to apply this approach in large-scale muscle models.

4.2.3.2 Discussion

Although the cross-bridge models explain how muscle force is developed, they are rather complex for application in large-scale muscle models. Simulation times would be very large. It should also be noted that the shape of the functions f and g is rather arbitrary, other functions could be found that behave equally

well. The model explains the force-velocity relation; the force-length relation has to be added more or less artificially. Also, the activation dynamics that has to be added is more complex. On the other hand, the method can be extended in a natural way to include the chemical (metabolic) energy release.

REFERENCES

- Ganong, WF (1981): Review of medical physiology. LANGE Medical Publications, Los Altos, California, 10th edition.
- Gielen, S (1998): A continuum approach to the mechanics of contracting skeletal muscle. PhD-thesis, Technical University of Eindhoven, Eindhoven.
- Gordon AM, AF Huxley and FJ Julian (1966): The variation in isometric tension with sarcomere length in vertebrate muscle fibers. *J Physiol*, 415:299-327
- Happee, R (1992): The control of shoulder muscles during goal directed movements. PhD-thesis, Delft University of Technology, the Netherlands
- Hill, AV (1938) The heat of shortening and the dynamic constants of muscle. *Proc R Soc Lond B*, 126:136-195
- Huijing, PA and RD Woittiez (1984). The effect of architecture on skeletal muscle performance: A simple planimetric model. *Neth J Zool*, 34:21-32
- Linden, BJJJ van der (1998): Mechanical modeling of skeletal muscle functioning. PhD-thesis, University of Twente, Enschede.
- McMahon, TA (1984): Muscles, reflexes and locomotion. Princeton University press, Princeton, New Jersey.
- Meijer, K (1998): Muscle mechanics. The effect of stretch and shortening on skeletal muscle force. PhD-thesis, University of Twente, Enschede.
- Warwick, R and PL Willems (editors) (1973): Gray's anatomy, 35th edition, Longman Group Ltd, Edinburgh
- Winters, JM and L Stark (1985): Analysis of fundamental human movement patterns through the use of in-depth antagonistic muscle models. *IEEE Trans Biomed Eng*, 32(10):826-839
- Winters, JM and L Stark (1987): Muscle models: what is gained and what is lost by varying model complexity. *Biol Cybern*, 55:403-420
- Zahalak, GI (1981): A distribution-moment approximation for kinetic theories of muscular contraction. *Math Biosc*, 55:89-114.

Optimization

INTRODUCTION

Muscle forces are one of the major sources of loading in the human body, i.e. they determine the joint loading, ligament forces, bone loading, etc. In general it is impossible to measure the muscle forces directly, and they must be calculated indirectly from the motion recordings. The joint moments are calculated from the recorded motions and external forces (Chapter 3). In the human body there are many more muscles present than degrees of freedom at the joint. Multiple combinations of muscle forces can result in the same net moments around the joint. However, EMG recordings show that the muscle activation patterns are very reproducible for the same motion. It is likely that an optimal pattern is being used to generate the motion. It is currently unknown what the optimization criterion is that is being used in the body, but generally it is assumed that energy consumption is one of the factors. By applying the appropriate optimization criterion, the muscle forces can be calculated from the net moments.

OBJECTIVES

This chapter addresses:

- The optimization procedure and the role of the optimization criterion and constraints.
- The effect of linear and non-linear optimization criteria.
- Task performance criteria and load sharing criteria.
- Inverse static, inverse dynamic including inverse muscle models, and forward dynamic optimization.
- Optimization algorithms like gradient methods, genetic methods and random search methods and discusses advantages and disadvantages.
- Validation methods of muscle force calculations using EMG and Near-InfraRed-Spectroscopy.

5.1 Why optimization?

In general there are many more muscles present in the human body than 'strictly' necessary. This means that multiple combinations of muscle forces will result in the same net joint moment, and hence in the same motion. In Figure 5.1 an elbow is shown with two flexor muscles. If a certain weight is held in the hand, any of these muscles could counterbalance the weight, or a number of combinations of muscle forces. If also the antagonistic (extensor) muscle is included, even more combinations of muscle forces resulting in the same net moment could result.

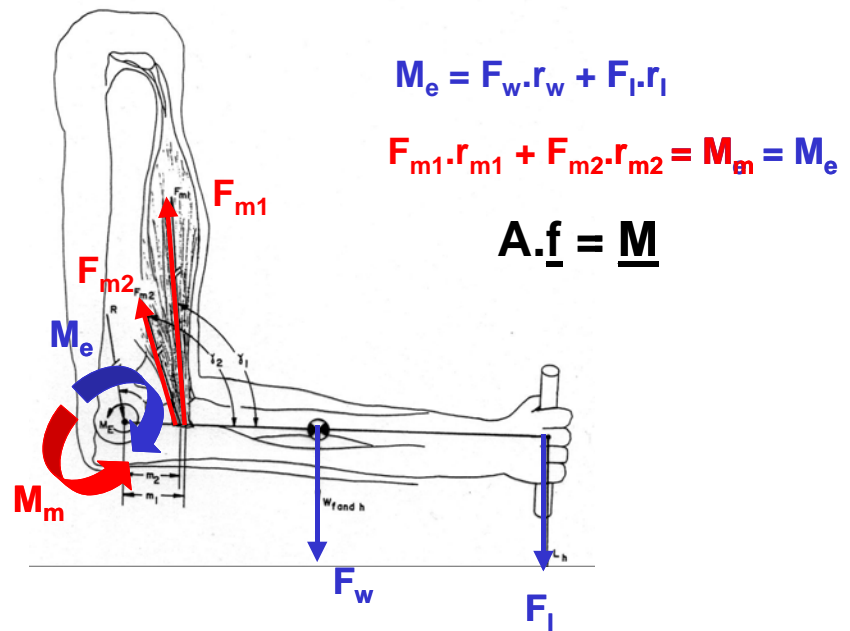


Figure 5.1: Simple model of the static equilibrium around the elbow joint. The two muscle forces F_{m1} and F_{m2} (resulting in muscle moment M_m) are in equilibrium with the external forces due to the weight of the forearm F_w and the load in the hand F_l , resulting in external torque M_e .

If the muscle forces could be measured, there would be no problem: By adding the muscle forces multiplied by their moment arms (= muscle moments), the net moment could be calculated. Unfortunately it is in general impossible to measure the muscle forces directly. In a few studies a buckle force transducer has been surgically placed on the Achilles tendon of living subjects, enabling the measurement of muscle forces during walking. In animal studies strain gauges have been sutured at the tendons. During some time, muscle forces in these animals could be recorded. After sacrificing the animals, the strain gauges could be calibrated. Except for these rare cases, muscle forces can not be measured directly, and they must be calculated indirectly from the recorded motions.

In Figure 5.1 the net moment M_e can be calculated from the weight of the forearm F_w and external load F_l and their moment arms (and from inertial terms in dynamic cases):

$$M_e = r_w \cdot F_w + r_l \cdot F_l \quad (5.1)$$

The net moment M_e is equal to the moment M_m generated by the muscles:

$$M_m = M_e \quad (5.2)$$

From a strict mathematical viewpoint, the system in Figure 5.1 is indeterminate. There is one equation of motion and two unknown variables (muscle forces F_{m1} and F_{m2}):

$$M_m = r_{m1} \cdot F_{m1} + r_{m2} \cdot F_{m2} \quad (5.3)$$

From this equation it is impossible to calculate unambiguously the muscle forces. Therefore, optimization methods are being used in order to enforce a

unique solution to this equation.

5.2 The optimization procedure

5.2.1 OPTIMIZATION, PARAMETER ESTIMATION AND OPTIMAL CONTROL

*optimization
criterion*

Optimization is necessary if there are more unknown variables than linear and non-linear equations (not inequalities). The procedures in optimization resemble very much the procedures in parameter estimation, though there are some important differences. In parameter estimation ('fitting of parameters') there are more equations than unknowns. Hence, it is usually not possible to exactly match each equation, and an error will remain. In parameter estimation, the error will be minimized. The *optimization criterion* will be a function of the error, e.g. in a Least Squares Error method the criterion will be $J = \Sigma e^2$. In optimization, the equations can be fulfilled with multiple combinations of the variables. The criterion is based on a function of the variables, e.g. $J = \Sigma F^2$, or $J = \Sigma (F/PCSA)^2$. In this chapter the optimization problem will be described: The muscle forces will be calculated for an *open-loop* musculoskeletal system without proprioceptive feedback.

5.2.2 INVERSE AND FORWARD DYNAMIC OPTIMIZATION

*inverse dynamic
optimization*

The equations in Figure 5.1 are valid for an *inverse dynamic optimization* problem. Since the accelerations and velocities are known in an inverse dynamic model, the differential motion equations reduce to algebraic equations. The advantage of algebraic equations is that the optimization problem is independent for each time sample. For each time sample the optimization criterion can be calculated, and the muscle forces can be estimated. E.g. if a motion is recorded for 5 seconds with a sampling frequency of 100 Hz, the optimization procedure must be repeated 500 times, but each repetition is independent from the other optimizations.

*forward dynamic
optimization*

In a *forward dynamic optimization* problem, the muscle force at one time sample affects the motion of the mechanism, and hence the force at the next time sample is likely to result in another moment. The whole motion will be different. The optimization problem becomes much more complex than the inverse dynamic optimization problem, since the variables are not independent from each other in time. The whole motion must be optimized in one large optimization procedure. E.g. if the model simulation produces output variables with a sample frequency of 100 Hz for 5 seconds, the number of unknown variables become 500 x the number of unknown muscle forces. The optimization criterion will be a function of the large number of unknown muscle forces. In addition, the forward dynamic simulation by integration of the motion equations requires much more computational effort than the inverse dynamic calculations. In biomechanics, most optimization problems are inverse dynamic optimization problems, and seldom forward dynamic optimization problems. In this chapter, the optimization procedure will be explained for an inverse dynamic optimization problem. The forward dynamic optimization problem is also described. In the last section, an efficient procedure is described which combines the advantages of the inverse dynamic optimization (low computational costs) with the advantages of forward dynamic optimization (better to investigate the sensitivity of the simulated motion with respect to the parameters).

5.2.3 OPTIMIZATION CRITERION

A general description of the problem as shown in Section 5.1 is found in the equation:

$$\underline{A} \cdot \underline{F} = \underline{M} \quad (5.4)$$

in which A is a $m \times n$ matrix with the moment arms of n muscles with respect to m DOF at the joints, \underline{F} ($F_1 \dots F_n$) is a $n \times 1$ vector with the muscle forces, and \underline{M} is a $m \times 1$ vector with net joint moments. If $n = m$, one unique solution would exist. This is never the case in the human body, where at least two antagonistic muscles must be present to move a joint in one direction and back. Therefore, in **any** musculoskeletal model $n > m$, and no unique solution can be found for muscle force vector \underline{F} . In case of a simple 1-DOF musculoskeletal model with two antagonistic muscles, both muscles could co-contract, resulting in high muscle forces but no net muscle moment.

Additional requirements are needed in order to arrive at a unique solution. Such requirements are implemented in an optimization criterion. If the optimization criterion is minimized (or maximized), a unique solution will result. An example of such an optimization criterion J is:

$$J = \sum_i \left(\frac{F_i}{PCSA_i} \right)^2 \quad (5.5)$$

in which F_i is the force of the i^{th} muscle, and $PCSA_i$ is the Physiological Cross-Sectional Area of the muscle, i.e. the area of the cross-section perpendicular to the muscle fibers. Since the muscle stress has a maximum σ_{max} (between 40-60 N/cm²), the $PCSA$ determines the maximal muscle force. If the actual muscle force is divided by the $PCSA$, the muscle stress (σ) results. Muscle stress is related to the energy consumption of the muscle. The higher the muscle stress, the more energy will be used by the muscle. Hence, minimizing the presented criterion will minimize the sum of squared muscle stresses in the musculoskeletal model, and a unique solution for the variables F_i will be found.

5.2.4 CONSTRAINTS

In addition to the optimization criterion, there are also a number of constraints which should be fulfilled by the variables F_i , otherwise a very trivial solution to the minimization problem would be that all muscle forces would be zero (indeed a very energy efficient solution!). The first set of constraints to be fulfilled are the moment equations: a set of *linear equality constraints*.

In a musculoskeletal system muscles would very often rotate a joint beyond its limits, if the joint was not restrained by ligaments. The force in the ligament is a function of the muscle forces loading the ligaments. A loaded ligament will act as a constraint in an inverse dynamic analysis. The constraint is expressed by the equation:

$$\underline{A}_{lig} \cdot \underline{F} = \underline{C}_{lig} \quad (5.6)$$

in which the $k \times n$ matrix \underline{A}_{lig} describes the sensitivity of k ligaments for a linear combination of specific muscle forces, and \underline{C}_{lig} ($k \times 1$ vector) describes offset terms.

However, in a ligament only tensile forces can occur, no compressive forces. So the ligament will function as a constraint to the system if the combination of muscle forces is loading the ligament. If the combination of muscle forces is larger than zero, tensile forces occur. If the combination is zero, no ligament forces occur and if the combination is less than zero, compression forces in the ligament would occur. Since no compression forces can exist in a ligament, the combination should be constrained to zero or larger than zero. This uni-directional constraint can be represented by a *linear inequality constraint*:

linear equality constraints

linear inequality constraint

$$\begin{aligned} \underline{\mathbf{A}}_{\text{lig}} \cdot \underline{\mathbf{F}} - \underline{\mathbf{C}}_{\text{lig}} &\geq \mathbf{0}, \quad \text{or} \\ \underline{\mathbf{A}}_{\text{lig}} \cdot \underline{\mathbf{F}} &\geq \underline{\mathbf{C}}_{\text{lig}} \end{aligned} \quad (5.7)$$

Another set of linear inequality constraints is formed by the restrictions that muscle forces themselves can only be tensile forces. The muscle forces are limited to the maximal muscle force, which can be calculated by the PCSA:

$$\frac{\sigma_{\max}}{F_{\max}} = \sigma_{\max} \cdot PCSA \quad (5.8)$$

The value of σ_{\max} is only approximately known. Muscle physiology studies with electrical stimulation showed that σ_{\max} is about 40 N/cm². However, most musculoskeletal models underestimate the maximal joint moment if this value would be used. In addition, most data for musculoskeletal models have been acquired at cadavers of old persons. Especially the *PCSA* values (or the σ_{\max}) should be scaled up to be representative for younger persons. Therefore, in musculoskeletal models values for σ_{\max} between 60 and 100 N/cm² are being used.

Hence, the following linear inequality constraints are added:

$$\begin{aligned} F_i &\geq 0, \quad \forall F_i \\ F_i &\leq PCSA_i \cdot \sigma_{\max}, \quad \forall F_i \end{aligned} \quad (5.9)$$

Another constraint might be that the coordination between muscles is such that dislocation of the joints is prevented, even without stressing the ligaments. This happens when the two articular surfaces of the joint are compressed onto each other, and hence the joint reaction vector intersects both articular surfaces. If this would not be the case, no equilibrium between 'action forces' from the one bone on the other and 'reaction forces' of the other bone on the first one could occur (Newton's second law), and the bones would move (dislocate) with respect to each other. The joint reaction force vector is a linear summation of the muscle forces (and other forces acting on the bone). Since only the direction of the joint reaction vector is constrained and not the magnitude, this imposes a *non-linear inequality constraint*:

$$f(\underline{\mathbf{F}}) \leq \underline{\mathbf{C}}_{\text{joint}} \quad (5.10)$$

in which $f(\underline{\mathbf{F}})$ represent the non-linear function of muscle force vector $\underline{\mathbf{F}}$, and $\underline{\mathbf{C}}_{\text{joint}}$ is the constraint, very often expressed in polar coordinates.

Summarizing, in an optimization procedure an optimization criterion is minimized with the restriction that the calculated muscle forces must obey to linear equality constraints (motion equations), linear inequality constraints (ligament constraints and minimal and maximal muscle forces) and non-linear inequality constraints.

5.2.5 FINDING A SOLUTION TO THE OPTIMIZATION PROBLEM

The optimization criterion and the linear and non-linear equality and inequality constraints must be solved simultaneously. One way to achieve this is to write the constraints as part of the optimization criterion to be minimized:

*non-linear
inequality
constraint*

$$J^* = \sum_i \left(\frac{F_i}{PCSA_i} \right)^2 + \lambda_{le} \cdot (\mathbf{A} \cdot \underline{\mathbf{f}} - \underline{\mathbf{M}}) + \lambda_{li} \cdot (\mathbf{A}_{lig} \cdot \underline{\mathbf{f}} - \underline{\mathbf{C}}_{lig} + s_{lig}) + \lambda_{ni} \cdot (f(\underline{\mathbf{f}}) - \underline{\mathbf{C}}_{joint} + s_{joint}) \quad (5.11)$$

In this equation, λ_{le} , λ_{li} , and λ_{ni} represent the so-called Lagrange multipliers for the linear equality, linear inequality and non-linear inequality constraints. The variables s_{lig} and s_{joint} are slack variables which can get any positive value. The minimum solution is reached if the derivatives of the optimization criterion J_{tot} with respect to the muscle forces are zero:

$$\frac{\partial J^*}{\partial F_i} = 0, \quad \forall F_i \quad (5.12)$$

which results in n equations!:

$$\frac{\partial J^*}{\partial \underline{\mathbf{f}}} = \frac{2}{PCSA^2} \cdot \underline{\mathbf{f}} + \lambda_{le} \cdot \mathbf{A} + \lambda_{li} \cdot \mathbf{A}_{lig} + \lambda_{ni} \cdot \frac{\partial f(\underline{\mathbf{f}})}{\partial \underline{\mathbf{f}}} = \underline{\mathbf{0}} \quad (5.13)$$

Also the derivative of J^* with respect to the Lagrange multipliers should be zero for any value of the multipliers:

$$\frac{\partial J^*}{\partial \lambda} = 0, \quad \forall \lambda_{le}, \forall \lambda_{li}, \forall \lambda_{ni} \quad (5.14)$$

resulting in a number of equations which is equal to the number of constraints:

$$\begin{aligned} \mathbf{A} \cdot \underline{\mathbf{f}} - \underline{\mathbf{M}} &= \underline{\mathbf{0}} \\ \mathbf{A}_{lig} \cdot \underline{\mathbf{f}} - \underline{\mathbf{C}}_{lig} + s_{lig} &= \underline{\mathbf{0}} \\ f(\underline{\mathbf{f}}) - \underline{\mathbf{C}}_{joint} + s_{joint} &= \underline{\mathbf{0}} \end{aligned} \quad (5.15)$$

Initially the Lagrange multipliers are relatively small, and fulfillment of the constraints is only weakly enforced. At the end of the iterative optimization procedure, the Lagrange multipliers are very large and the constraint is strictly enforced. The use of Lagrange multipliers enhances the convergence of the optimization procedure.

Summarizing, the procedure started with a undetermined set of equations less than the number of variables (= number of unknown muscle forces). An optimization criterion has been defined, and the constraint equations have been included in the optimization criterion. By taking the partial derivatives of the optimization criterion with respect to each muscle force and Lagrange multiplier, there are as many equations as unknowns, and a unique solution can be found.

5.2.6 OPTIMIZATION METHODS

Theoretically, the final set of equations derived in the previous section, with the unknown muscle forces and Lagrange multipliers, can be analytically solved by substitution of variables. In practice, this is likely to be an enormous endeavor, prone to errors. Usually, this kind of optimization procedures are being solved by numerical approximations of the optimal solution. In this chapter, four types of numerical approximations or search methods will be described:

- Grid search

- Gradient search
- Random search
- Genetic algorithms

5.2.6.1 Grid search

Basically, there is a function $J^*(\underline{F})$ of which we are searching for the minimal value in the parameter space of the vector $\underline{F} = \{F_1, F_2, \dots, F_n\}$. A brute force method is to fill in all possible values of \underline{F} and calculate the value of J^* . This method is called the ‘grid search’. A grid is drawn in parameter space with spacing between the possible values of each of the unknowns. For each node in the grid the value of J^* is calculated. This can result in an enormous amount of calculations. For example, if we have 20 unknown muscle forces, and we specify for each muscle force 100 possible values, then 100^{20} combinations must be calculated to check for the minimum value of J^* , and to check if the constraints are fulfilled.

The search for the minimal value of J^* can be compared to the problem to find the lowest point of Switzerland. If the grid search would be used to solve this problem, it would be equivalent to check every meter (or kilometer, depending on the spacing!) and measure the altitude. It would require quite some traveling to find the lowest point!

In practice, the grid search method is seldom used. Only for a small number of unknowns this method is feasible. Sometimes the grid search method is used to find a feasible point in parameter space, i.e. a point where all the constraint equations are fulfilled. Starting from a feasible point, more efficient search methods can be used.

5.2.6.2 Gradient search

As the name already indicates, the ‘gradient search’ method uses gradient information to search for the minimum of the function $J^*(\underline{F})$. At the minimal value of J^* all the partial derivatives (~gradients) are zero. From an initial feasible point in the parameter space, the optimum can be found by moving along the gradient towards the minimum of J^* , iteratively obtaining a better approximation of \underline{F} from iteration k to iteration $k+1$:

$$\underline{F}_{k+1} = \underline{F}_k - \alpha \cdot \frac{\partial J^k}{\partial \underline{F}_k} \quad (5.16)$$

In which J^k is the value of the optimization criterion using the parameter vector \underline{F}_k . This method is called the ‘steepest descent’ method, since it will move in parameter space in the direction of the steepest descent of the gradient. The coefficient α determines the step size. Only for an infinitesimal small step size α it is guaranteed that the gradient will result in a smaller value of J . The value of α is a trade-off between convergence (steadily moving towards the optimum) and speed of the algorithm.

A more advanced method is in the family of Newtonian gradient algorithms, of which the Gauss-Newton method is the most well-known. In the Newtonian methods, the second derivative (also called the *Hessian* $H(\underline{F}_k)$) is being used:

Hessian

$$\begin{aligned}\underline{\mathbf{F}}_{k+1} &= \underline{\mathbf{F}}_k - \alpha \cdot \mathbf{H}(\underline{\mathbf{F}}_k)^{-1} \cdot \frac{\partial J^k}{\partial \underline{\mathbf{F}}_k} \\ \mathbf{H}(\underline{\mathbf{F}}_k) &= \frac{\partial^2 J^k}{\partial \underline{\mathbf{F}}_k \cdot \partial \underline{\mathbf{F}}_k} \approx \left(\frac{\partial J^k}{\partial \underline{\mathbf{F}}_k} \right)^T \cdot \left(\frac{\partial J^k}{\partial \underline{\mathbf{F}}_k} \right)\end{aligned}\quad (5.17)$$

The latter equation is a good approximation of the Hessian near the optimum, and can be calculated at little extra cost. Especially in optimization problems with much interaction between the unknowns, the use of the Hessian will improve the convergence.

local minimum

A drawback of the gradient methods is that the optimization algorithm might get stuck in a ‘local minimum’ (see Figure 5.2). If the initial starting point is not in the same valley as the global minimum (the true minimal value of J^*), the gradient algorithm will never reach the global minimum. The risk of local minima is unavoidable in gradient search methods. It is a wise procedure to repeat the optimization procedure using a number of different starting points. If the same minimum is repeatedly obtained, one can be more certain that it might be the true global minimum.

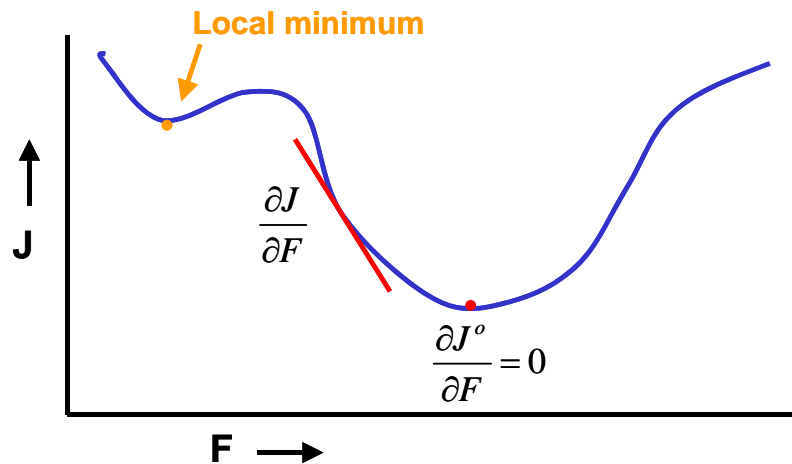


Figure 5.2: In a gradient method there is always the risk that the search algorithm ends in a local minimum.

In the analogy of reaching the lowest point of Switzerland, the gradient method can be compared to a blind-folded person stepping around. This person will feel with his/her feet in which direction the slope is. Then, a step will be made in this direction and again the slope will be tested. The larger the step, the sooner the lowest point will be reached. But there is always the possibility that the step is too large and that the other side of the valley is reached, of which the altitude might even be higher and no progress is made. Gradient methods use only local information to find the (global) minimum.

The gradient itself is usually calculated numerically, since analytical derivatives might be difficult to obtain:

$$\frac{\partial J}{\partial F_i} \approx \frac{J(\underline{\mathbf{F}} + \Delta F_i) - J(\underline{\mathbf{F}})}{\Delta F_i} \quad (5.18)$$

The i^{th} element of the parameter vector $\underline{\mathbf{F}}$ is increased by a very small value ΔF_i ,

and the criterion value $J(\underline{F} + \Delta F_i)$ is calculated. The gradient is approximated by the difference between $J(\underline{F} + \Delta F_i)$ and the original (current) value of $J(\underline{F})$, divided by ΔF_i . Calculating the numerical derivatives usually takes about 95% of the computing time in the gradient algorithms, and even then it is only very local information and must be repeated in the next iteration. Nevertheless, gradient algorithms are the most widely used optimization methods.

5.2.6.3 Random search

A special type of optimization methods are the ‘random search’ methods. Some examples are a blind random search and a localized random search. A blind random search uses a probability distribution to select parameter values and a localized random search uses a probability distribution around the best parameter values from the previous iteration. In the random search method, the search direction is chosen truly at random. Subsequently, the result is evaluated. If the criterion value decreases in that particular direction, the search is continued in that direction. If not, a next search direction is chosen at random:

$$\underline{F}_{k+1} = \underline{F}_k - \alpha \cdot \underline{v} \quad (5.19)$$

in which \underline{v} is the random search direction and α is the step size. One example of a more advanced random search method is the ‘Bremermann’-procedure. In this method, four points along the search direction \underline{v} are taken, two at each side of the current feasible point. A 4th order polynomial is fitted through the five points in parameter space, and the lowest point along this polynomial but between the outside points can be calculated analytically. If one of the outside points is the lowest point, the procedure is repeated in this direction. Otherwise a new random search direction is chosen.

The advantage of the random search methods is that no effort is spent on calculating the derivatives, and therefore many search directions can be tested. In the neighborhood of the minimum the random method is very inefficient, and it is better switched to a gradient search method. But how do you know that you are in the neighborhood of the minimum? Random search methods are also prone to end in a local minimum if the initial feasible point is not in the right valley.

Although it is tricky to make any general statements about random search methods, the efficiency relative to gradient search methods becomes better with larger number of parameters, since a larger number of parameters require more effort to calculate the gradients. Random search methods are seldom used in optimization problems.

5.2.6.4 Genetic algorithms

A relatively new branch to the tree of optimization algorithms are the genetic algorithms. Since the evolution seems to be a successful method to produce optimally adapted species, similar procedures have been incorporated in the genetic algorithms. Similar rules as in Nature are used: Survival of the fittest, reproduction, selection and mutation.

Starting with an initial population of parameter vectors \underline{F} , e.g. 30 or 40 vectors, the following steps are repeatedly performed:

- a. Calculate the criterion value $J(\underline{F})$ for each parameter vector
- b. Select solutions of $J(\underline{F})$, by attributing the best solutions the largest probability to be chosen.
- c. Generate children (new population vectors \underline{F}) from the selected parameter vectors (~parents):
 - Combine parent vectors \underline{F} : Cross-over of part of vector \underline{F} (intermediate

solutions: local)

- Mutation of children vector \underline{F} (scatter solutions over workspace: global), typically about 3 – 5 %

d. Go back to step a.

The advantage of genetic algorithms is that the starting population will be scattered all over the parameter space, thereby reducing the chance of a local minimum. Also the mutated children can be anywhere in parameter space. If the mutations are not successful, they are likely to be eliminated in the next iteration. However, successful mutations can start a new family of solutions, and start breeding intermediate solutions with the old successful families. The mutation results in a more global search pattern. The combination of parent vectors results in local search for a minimum, since the children vectors will always be more or less look-a-likes of the parent vectors.

Genetic algorithms are much slower than gradient algorithms. Especially near the optimum it is better to switch to a gradient algorithm. But the major advantage of genetic algorithm is that the risk of local minima is reduced. Genetic algorithms are more and more used in optimization procedures. One computational advantage is that the genetic algorithms lend themselves very good for parallel computers, like supercomputers with multiple processors or networks of PCs: The calculation of the criterion value $J(\underline{F})$ can be done in parallel, since it is an independent process. Only the combination and mutation is a central process.

5.3 Linear and non-linear optimization criteria

5.3.1 OVERVIEW

The optimization procedure is done in order to obtain a unique solution for the parameter vector \underline{F} . However, which unique solution is obtained depends on the optimization criterion chosen. The optimization criterion J usually consists of two parts, the performance criterion J_{pc} and the load sharing criterion J_{ls} , and a weighing factor W to determine the relative importance of each part:

$$J = J_{pc} + W \cdot J_{ls} \quad (5.20)$$

Performance criterion

The *performance criterion* specifies the objective of the motion, e.g.

- The goal to be reached (or rather the error between the final position and the goal position)
- Minimal time (as fast as possible)
- Maximal height (e.g. in jumping)
- Etc.

Load sharing criterion

The *load sharing criterion* specifies the effort which is being used, e.g.

- Minimal energy consumption (difficult to calculate)
- Energy related measures (easier to calculate), such as
 - Sum of squared muscle forces
 - Sum of squared muscle stresses
 - Maximal muscle stress needed
- Minimum fatigue (~maximum endurance)
- Minimum loading of the articular surfaces
- Pain
- Etc.

maximal effort

If the performance criterion requires *maximal effort*, e.g. as fast as possible (minimal time) or as high as possible, there will be only one unique solution of

Sub-maximal performance

muscle forces to obtain that maximal effort. Then there is no need for a load sharing criterion. A load sharing criterion is only needed if there is a *sub-maximal performance*. Then there are multiple ways to obtain that performance, and it is likely that a set of muscle forces is chosen that requires the minimum of energy consumption. Generally there is always a weighing between performance and effort in optimal control problems. If a little less performance requires much less effort, human beings will choose that option. But in general it is unknown which criterion humans choose in sub-maximal tasks. Many criterion have been proposed; it has been speculated that it is minimum fatigue (using muscles which have a larger supply of oxygen and less waste products like lactate), minimum joint loading (e.g. to avoid low back pain), and even minimum pain (which can easily be recognized in patients showing motion patterns avoiding painful positions). Warm-blooded species like mammals need a minimum amount of energy consumption to maintain their body temperature. Since the use of muscles is the only way to convert chemical energy into mechanical energy and heat, the requirement of minimal energy consumption might not be a major concern for very light tasks.

The load sharing criterion should be expressed as a function of muscle force, or as a function of muscle activation which will result in muscle force. When simple muscle models, like Hill-type models, are used, it is difficult to get an accurate approximation of the energy consumption. And also for fatigue or pain the direct relation with muscle force is difficult. But presumably more than 99% of the daily life performance are sub-maximal tasks, so it is very important to have at least a rough approximation of the true criterion used.

In forward dynamic simulations, the performance criterion is known, but not the actual motion to achieve the performance criterion. The time course of the muscle forces (# muscle forces x # time instants) are the unknown parameters to be found in the optimization process. As a result of the muscle forces, the motion can be calculated by integrating the equations of motion. Then, the performance criterion value is determined, and also the load sharing criterion value in case of a sub-maximal performance criterion.

In inverse dynamic optimization, the recorded motion is input of the optimization process. The performance criterion is not used, because the performance depends on the motion which does not change. Therefore, in inverse dynamic optimization, only the load sharing criterion J_{ls} is being used.

5.3.2 LINEAR CRITERIA

The optimization criterion can be a linear function of the muscle forces, or a non-linear function of the muscle forces. Examples of linear functions of muscle forces are:

- Sum of muscle forces: $J_{ls} = \sum_i F_i$ (5.21)

- Sum of muscle stresses: $J_{ls} = \sum_i \frac{F_i}{PCSA_i}$ (5.22)

- Minimum loading of the articular surfaces

In order to evaluate the effect of the different optimization criteria on the calculated muscle forces, an example presented by Dul (1984) is very illustrative. A knee model with three muscles was used (see Figure 5.3). The blue muscle (nr. 1) has the largest moment arm, followed by the red muscle (nr.

2) and the green muscle (nr. 3). The single motion equation is:

$$a_1 \cdot F_1 + a_2 \cdot F_2 + a_3 \cdot F_3 = M \quad (5.23)$$

If the sum of muscle forces is minimized, it is obvious that it is most advantageous to use only muscle 1 to generate the joint moment M . If muscle 1 is at its maximal force, muscle 2 is being activated, and muscle 3 is the last muscle to be activated (see Figure 5.4, upper left panel). If the sum of muscle stresses is optimized, the equation can be rephrased as:

$$a_1 \cdot PCSA_1 \cdot \frac{F_1}{PCSA_1} + a_2 \cdot PCSA_2 \cdot \frac{F_2}{PCSA_2} + a_3 \cdot PCSA_3 \cdot \frac{F_3}{PCSA_3} = M \quad (5.24)$$

The lowest value for muscle stress is obtained for the muscle with the largest product of moment arm x PCSA, in this particular case muscle 1. In Figure 5.4 it is seen that muscle 3 and muscle 2 switch their recruiting order, obviously because muscle 3 has a larger PCSA than muscle 2.

The use of linear optimization criteria result in recruitment of muscles: The muscles are activated the one after the other. This is in contrast with EMG measurements (electrical activity of the muscles), which show that all muscles with a advantageous moment arm are recruited simultaneously. Hence, linear optimization criteria do not result in realistic predictions about muscle forces. Minimization of the joint loading is an often used linear criterion value: The joint reaction force is equal to the sum of muscle force vectors. Obviously, minimizing the joint loading is not the (only) objective of the human body.

5.3.3 NON-LINEAR CRITERIA

5.3.3.1 Introduction

Linear optimization criteria do not always result in feasible solutions; then non-linear criteria may do better. Various criteria have been formulated in literature:

- Minimal energy consumption
- Energy related measures (easier to calculate), such as

○ Sum of squared muscle forces: $J_{ls} = \sum_i F_i^2 \quad (5.25)$

○ Sum of squared muscle stresses: $J_{ls} = \sum_i \left(\frac{F_i}{PCSA_i} \right)^2 \quad (5.26)$

○ Maximal muscle stress needed: $J_{ls} = \max_i \sigma_{\max} \quad (5.27)$

- Minimum fatigue (~maximum endurance)
- Pain
- Etc.

5.3.3.2 Muscle energy consumption

It is difficult to calculate the muscle energy consumption. The optimization criterion is

$$J_{ls} = \sum_{i=1}^n \dot{E}_i \quad (5.28)$$

in which \dot{E}_i represents the muscle energy consumption for the i^{th} muscle and is based on the two major energy-consuming processes in the muscle:

1. Unbinding of cross-bridges
2. Re-uptake of calcium

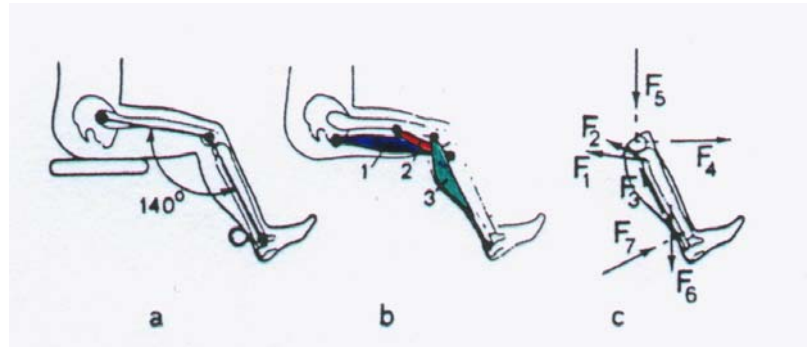


Figure 5.3: A simple knee model with three muscles is being optimized. Muscles 1 (blue), 2 (red) and 3 (green) generate a moment around the knee, which is in equilibrium with the force F_7 at the bar behind the ankle, and the weight of the shank and foot F_6 .

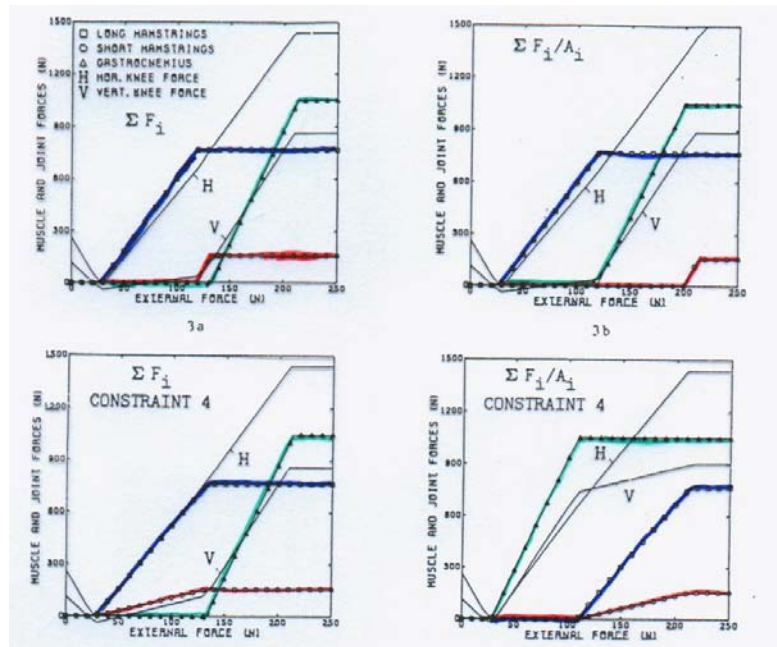


Figure 5.4: The effect of linear optimization criteria on the calculated muscle forces. In the upper left panel the sum of muscle forces is optimized. First the blue muscle with the largest moment arm is recruited, then the red muscle and the green muscle. In the upper right panel the sum of muscle stresses is optimized. First the blue muscle with the largest product of moment arm \times PCSA is recruited. Then the green muscle is recruited, which has a smaller moment arm than the red muscle (see the upper left panel) but a larger PCSA.

Under isometric conditions the number of bonded cross-bridges is linearly related to the muscle force (Huxley, 1957). When the same muscle force (F_m) is maintained with longer muscle fibers, more sarcomeres are in series and more cross-bridges are attached. Therefore the energy consumption rate for unbinding (\dot{E}_f) must be scaled by muscle fiber length (l_f):

$$\dot{E}_f \sim l_f \cdot F_m \quad (5.29)$$

Equation (5.28) can be rewritten:

$$\dot{E}_f \sim l_f \cdot F_m = V \cdot \frac{F_m}{PCSA_m} = \frac{m}{\rho} \cdot \frac{F_m}{PCSA_m} \quad (5.30)$$

in which V is muscle volume, m is the muscle mass and ρ is muscle density ($= m/V$).

This relation between energy consumption and muscle force can be any linear or non-linear relation multiplied by muscle length l_m , and is approximated by a Taylor series expansion:

$$\begin{aligned} \dot{E}_f &= f(F_m) = \\ &= a_0 + a_1 \cdot m \cdot \frac{F_m}{PCSA} + a_2 \cdot m \cdot \frac{F_m^2}{PCSA} + \dots \end{aligned} \quad (5.31)$$

\dot{E}_f is related to the distribution of bonded cross-bridges over the muscle length (Huxley, 1957). Under isometric conditions this distribution does not change, and is only affected by the number of bonded cross-bridges, i.e. the magnitude of force. Under dynamic conditions the distribution can be fairly accurately approximated with a normal distribution (Zahalak, 1981). Therefore the quadratic and higher order terms in Equation (5.31) can be neglected.

The second energy consuming process in the muscle is the re-uptake of calcium in the sarcoplasmic reticulum by an active calcium 'pump'. The energy (\dot{E}_a) is related to the active state a of the muscle, which is related to the calcium concentration ($[Ca^{2+}]$). The active state is represented by the fraction between muscle force F_m and maximal muscle force F_{max} , which depends on the force-length $f_l(l_m)$ and force-velocity $f_v(v_m)$ relations.

$$\dot{E}_a \sim V \cdot a = \frac{m}{\rho} \cdot \frac{F_m}{F_{max0} \cdot f_l(l_m) \cdot f_v(v_m)} \quad (5.32)$$

in which F_{max0} is the maximal muscle force at optimum muscle length and zero contraction velocity, and related to PCSA and maximal muscle stress (σ_{max}). During isometric contractions $f_v(v_m)$ is equal to one, and can be omitted. Then, a Taylor series expansion of \dot{E}_a :

$$\dot{E}_a = f(F_m) = b_0 + b_1 \cdot m \cdot \frac{F_m}{PCSA \cdot \sigma_{max} \cdot f_l(l_m)} + b_2 \cdot m \cdot \left(\frac{F_m}{PCSA \cdot \sigma_{max} \cdot f_l(l_m)} \right)^2 + \dots \quad (5.33)$$

Experimentally, linear and quadratic relations have been found between activation and energy consumption. Therefore, cubic and higher order terms are neglected.

The total energy consumption of the muscle (\dot{E}_m) is composed of terms derived in Equations 5.31 and 5.33. Omitting constants and incorporating constant muscle density ρ in the coefficients, the following equation can be derived:

$$\dot{E}_m = \dot{E}_f + \dot{E}_a = m \cdot \left\{ a_1 \cdot \frac{F_m}{PCSA} + b_1 \cdot \frac{F_m}{PCSA \cdot \sigma_{max} \cdot f_l(l_m)} + b_2 \cdot \left(\frac{F_m}{PCSA \cdot \sigma_{max} \cdot f_l(l_m)} \right)^2 \right\} \quad (5.34)$$

5.3.3.4 Energy related measures

For an accurate estimation of the energy consumption of the muscles, it is necessary to obtain many data about the muscle, i.e. mass (\sim volume), force-length relation (\sim optimum length), force – velocity relation, fiber type, etc. These data must be obtained in cadaver studies, which is difficult. Today, there is only one complete data set for the shoulder and elbow (Klein Breteler et al., 1999). None exist for the lower extremities or other joint systems. Data for other musculoskeletal systems are composed of multiple experiments done in different laboratories and on different specimen.

Since it is quite difficult to obtain direct estimates of the energy consumption of the muscles, most often a measure related to energy consumption is used. Such energy related measures should be a non-linear function of muscle forces, in order to obtain synergism between the muscles:

- Sum of squared muscle forces: $J_{ls} = \sum_i F_i^2$ (5.25)

- Sum of squared muscle stresses: $J_{ls} = \sum_i \left(\frac{F_i}{PCSA_i} \right)^2$ (5.26)

- Maximal muscle stress needed: $J_{ls} = \max_i \sigma_{\max}$ (5.27)

The reasoning is that if the muscle force or muscle stress increases, the energy consumption of the muscle also increases. It should be noted that neither of these criteria are weighed with the volume of the muscle. The stress of a muscle with long fibers is equally weighed as the stress in a muscle with small fibers. But in case of long fibers, the muscle force must be generated over the whole fiber length, resulting in a higher energy consumption.

The actual force distribution between the muscles depends on the criterion chosen. The experience has learned that minimization of the sum of squared muscle stresses provides the most stable and accurate results. The other criteria give other results if the muscle is divided in 2, 4 or more muscle lines of action.

5.4 Inverse and forward dynamic optimization

5.4.1 THE EFFECT OF MUSCLE DYNAMICS

In Section 5.3, in the inverse dynamic approach, the effect of muscle dynamics is neglected. Solutions may result in zero muscle force in one sample, and in maximal muscle force in the next sample. Obviously this is not possible, because due to the activation dynamics and contraction dynamics, it takes about 100 msec for a muscle to obtain maximal muscle force.

In forward dynamic simulations (and optimizations), muscle dynamics is automatically taken into account, if a muscle model is used. In inverse dynamic optimization, it is necessary to add additional constraints to the minimal muscle forces (if the activation drops to zero) or maximal muscle force (if the activation increases to maximal).

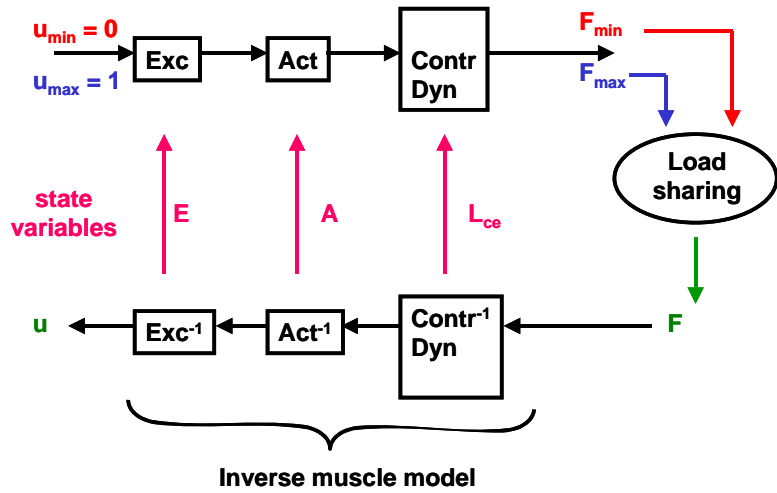


Figure 5.5: In a forward dynamic muscle model, the minimal and maximal feasible muscle force is calculated for the next time step, using neural input zero and one. After the optimization process (load sharing), the actual neural input is calculated backwards using an inverse muscle model. The states of the inverse muscle model are used in the next iteration cycle.

5.4.2 INVERSE/FORWARD DYNAMIC OPTIMIZATION

An important aspect of the optimization of muscle forces is that the constraints of muscular dynamics should be taken into account. Muscle force cannot drop instantaneously to zero or increase to maximal. In order to calculate the minimal and maximal muscle force for the next time step, a forward muscle model is needed to include the muscle dynamics. Then, an inverse model is needed to calculate back from the muscle force which was calculated in the optimization, to retrieve the muscle states and neural input, in order to be able for the next time step to calculate again the minimal and maximal values (see Figure 5.5). Following the terminology suggested by Winters (1991), this approach to sharing criterion. A load sharing criterion is only needed if there is a *sub-maximal performance*. Then there are multiple ways to obtain that performance, inverse-dynamic analysis is called *Inverse/Forward Dynamical Optimization (IFDO)* to distinguish it from *Inverse Dynamical Optimization (IDO)*, which is optimization without the constraints imposed by muscle dynamics. To start the inverse-dynamic optimization, the net joint moments are calculated at each time step I (see Figure 5.6). The discretization step size Δt between two time steps is determined by the sample frequency of the motion recording. Also, the muscle length $l_{mc,i}$ and moment arms are known at time step i . In IFDO, both an inverse muscle model and a forward muscle model are required in order to account for the effect of muscle dynamics in an inverse-dynamic optimization. In the forward-dynamic muscle model starting from the state of the muscle dynamics at time step $i-2$, a minimal ($u_{i-2} = 0$) and maximal ($u_{i-2} = 1$) input signal for the neural activation is used in a forward-dynamic simulation involving two discrete time steps in order to calculate the minimal ($F_{e,min,i}$) and maximal ($F_{e,max,i}$) muscle force for the time step i . The minimal and maximal values for muscle force can be incorporated into the optimization procedure to solve the load-sharing problem. In the optimization procedure, the muscle force $F_{e,i}$ is calculated. In the inverse muscle model, the neural activation u_{i-2} can be

*Inverse/Forward
Dynamical
Optimization
(IFDO), Inverse
Dynamical
Optimization
(IDO)*

calculated from $F_{e,i}$, and the states of the muscle model at time steps i and $i-1$ (i.e. $l_{ce,i}$ and e_{i-1}) can be updated.

5.4.3 INVERSE/FORWARD DYNAMIC OPTIMIZATION WITH FEEDBACK CONTROL

Applying a forward-dynamic model using the neural input calculated from the inverse-dynamic model will in general not result in exactly the same motion as the recorded motion that was input into the inverse-dynamic model, due to the discretization of the input, numerical inaccuracies and possibly instabilities. If the studied motion is unstable, e.g. a walking motion or an arm raised above shoulder level, large deviations can occur. A feedback control algorithm has been applied in the optimization process to generate a forward-dynamic solution which results in exactly the same motion as used in the inverse-dynamic model. This algorithm is called Inverse/Forward Dynamical Optimization with Controller (IFDOC), see Figure 5.7. In IFDOC, the calculated neural input u_i is used in a forward-dynamic musculoskeletal model (which is identical to the inverse musculoskeletal model). The difference in position and velocity of the recorded motion and the predicted motion from the forward-dynamic model will be fed back to the inverse-dynamic model. A controller will adjust the neural input signal in the next time step. Hence, a forward-dynamic simulation will be obtained which should result in exactly the same motion as the recorded motion (see Figure 5.8).

*Inverse/Forward
Dynamical
Optimization with
Controller
(IFDOC)*

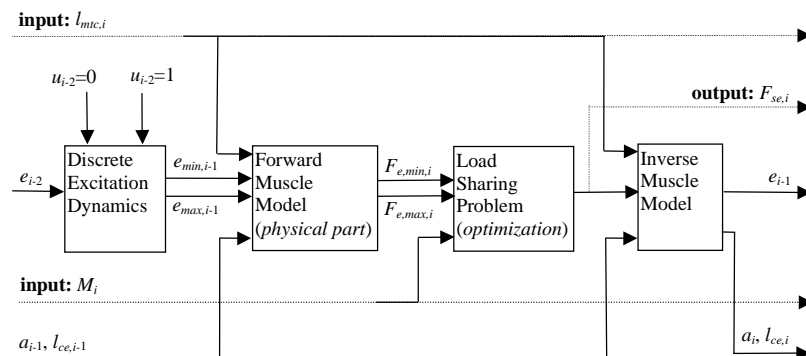


Figure 5.6: Inverse/Forward dynamic optimization (IFDO) at time step i .

The load sharing problem is solved for the net joint moments M_i by optimization. The upper and lower bound on e_{i-1} are calculated with a discrete time approximation of the excitation dynamics (equation 1) for maximum ($=1$) and minimum ($=0$) values of the hypothetical input u , respectively. A forward muscle model is used to compute the dynamic force boundaries ($F_{e,max,i}$ and $F_{e,min,i}$). From the optimized muscle forces $F_{se,i}$ the state variables $l_{ce,i}$ and a_i , and the constant excitation e_{i-1} are computed with the inverse muscle model. In the same way, the state variables $l_{ce,i-1}$, a_{i-1} and neural excitation e_{i-2} were computed from muscle force $F_{se,i-1}$ (at time step $i-1$). The secondary input (muscle length l_{mc}) of the inverse and forward muscle model is dependent on joint angles alone. The input time-series (dashed arrows) of M and l_{mc} are obtained in kinetic and kinematic analysis of the movement of interest, respectively.

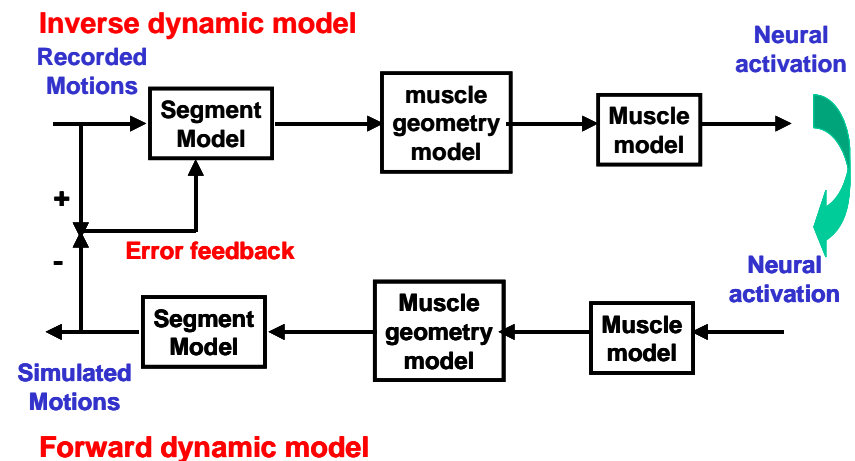


Figure 5.7: Usually, the neural input calculated in an inverse dynamic model will not result in the same motion in the forward dynamic model. In the IFDOC algorithm, an error feedback controller is added to adjust the neural activation pattern so that the simulated motions after the forward dynamic model will be the same as the recorded motions.

5.5 Validation

5.5.1 ELECTROMYOGRAPHY (EMG)

Traditionally, EMG (the electrical activity of muscles) have been used to validate muscle forces. EMG is recorded using surface electrodes attached to the skin, or wire electrodes inserted in muscles. The EMG signal is in the order of 1–2 mV. Hence, the signal must be amplified. Subsequent data processing involves rectifying and applying a low pass filter.

EMG can be compared with the excitation signal entering the calcium dynamics part of the Hill-type muscle model. Hence, there are additional dynamic systems (activation dynamics and contraction dynamics) between EMG and force. This will result in ‘time-delays’ between the peak of muscle force and EMG.

Therefore, it is better to compare EMG with the excitation signal predicted by an inverse muscle model, or IFDO/IFDOC optimization procedure.

In Figure 5.9 an example is given of the comparison of an EMG signal recorded during wheelchair propulsion, with the predicted muscle forces, using a large scale model of the shoulder and elbow (Van der Helm et al., 1998). It can be seen that the time patterns can pretty accurately be predicted. However, the amplitude of the muscle force cannot be compared with the amplitude of the EMG signal directly.

5.5.2 NEAR INFRA RED SPECTROSCOPY

Near InfraRed Spectroscopy (NIRS) is a non-invasive method from which information can be obtained about the oxygenation of a biological tissue, such as muscle tissue. Near Infrared light is transmitted through the muscle tissue at three different wavelengths (770, 850 and 905 nm). The absorption of the light depends on the amount of oxygen that is present in the tissue. Absorption changes can be measured and converted into changes in concentration of oxyhaemoglobin (O_2Hb) and deoxyhaemoglobin (HHb) by means of the Lambert-Beer law Colier et al., 1995. The Lambert-Beer equation, modified for light scattering media, describes the relationship between the concentration of a

chromophore and recovered light:

$$OD_\lambda = \varepsilon_\lambda \cdot c \cdot L \cdot B + OD_{r,\lambda} \quad (5.35)$$

where OD_λ (optical density) is the absorption of the light, ε_λ is the extinction coefficient of the chromophore, c is the concentration of the chromophore, L is the distance between the optodes, DPF (Differential Pathlength Factor) accounts for the increase in optical path length due to scattering in the tissue and $OD_{r,\lambda}$ represents the oxygen independent light losses due to scattering in the tissue.

When measurements are done during arterial occlusion and the DPF is known it is possible to quantify muscle oxygen consumption. The blood supply to the muscle ceases due to the occlusion, therefore the decrease of $[O_2Hb]$ reflects the oxygen consumption of the muscle. From the gradient of the $[O_2Hb]$ decrease, the oxygen consumption per unit of time ($\dot{V}O_2$) can be calculated. The DPF values for several muscles have been measured in previous studies (Ferrari et al., 1992; Van der Zee et al., 1992; Duncan et al., 1995).

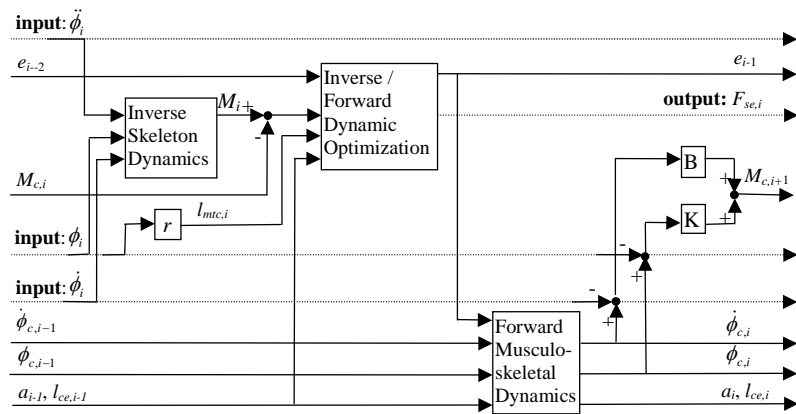


Figure 5.8: The IFDOC Algorithm at time-step i . The box labeled *Inverse/Forward Dynamic Optimization* represents figure 1. As in figure 1, dashed lines represent input time-series (kinematics) and output time-series (muscle forces $F_{se,i}$). The input time-series are used to calculate net joint moments M_i with inverse skeleton dynamics. The calculated excitation e_{i-1} is used for reproduction of joint angle and angular velocity with forward musculoskeletal dynamics. From the errors in position and velocity the correction term ($M_{c,i+1}$) is calculated (see Appendix III for details).

NIRS has been used in order to validate the predicted energy consumed by each individual muscle (Praagman et al., 2003). The load sharing part of the optimization criterion is an approximation of the consumed energy. In a comparison of many different energy related criteria, it was concluded that the muscle energy as calculated in Section 5.3.3.2 was the most accurate prediction.

Human Gait

INTRODUCTION

Bipedal walking is a complex movement, a balancing performance against the constant pull of gravity. A lot of definitions of walking are made, such as: “*In bipedal locomotion, man is continuously preventing to fall by placing one foot in front of the other.*” and “*The two basic requisites of walking are the continuing ground reaction forces that support the body and the periodic movement of each foot from one position of support to the next in the direction of progression.*”.

Apart from these formulations, walking can be quantified with a number of parameters. These are shown in Section 6.1: The step-parameters to describe the timing of the movement; kinematics for the movement itself (the joint rotations); dynamics to describe the forces and moments of force to make this movement possible and energetics for the metabolic cost.

The two ways to apply the equations of motion are usually referred to as the inverse dynamics and the direct (or forward) dynamics approach. In the inverse dynamics approach, the movement is assumed to be known and the forces and moments of force, needed to bring about that movement, are calculated (e.g. Koopman, 1989). Inverse dynamics is applied in gait analysis (Section 6.2), the equations of motion are usually derived with the Newton-Euler formulation. The estimated internal forces can be further processed in muscle models to estimate the distribution of muscle forces, which allows for a validation with measured EMG patterns (Chapter 5).

In the direct dynamics approach, the movements of the segments are calculated by integrating the equations of motion, usually based on a Lagrangian formulation. This is only possible when the joint moments of force are known or assumed to be zero. The latter is the case in ballistic walking (McMahon, 1984). The joint moments of force can be found by trial and error such that a normal walking pattern results (Pandy and Berme, 1988), from estimations of the muscle forces (e.g. Olney and Winter, 1985), as the result of an inverse dynamics model (Chapter 5) or by optimization techniques (Section 6.3).

OBJECTIVES

This chapter addresses:

- Human gait.
- Data interpretation of (impeded) gait pattern
- Reconstruction of kinetic data from a measured gait pattern through inverse dynamical models.
- Prediction of gait pattern through forward dynamical models.

6.1 Description of normal walking

6.1.1 STEP-PARAMETERS

The step-parameters are used for a general characterization of the walking pattern. They are determined by the points of heel contact (HC) and toe-off (TO) of the left and right foot. For a walking cycle beginning with left heel

contact (HCL), this is followed by right toe-off (TOR), right heel contact (HCR) and left toe-off (TOL). A cycle is completed with HCL again (Figure 6.1).

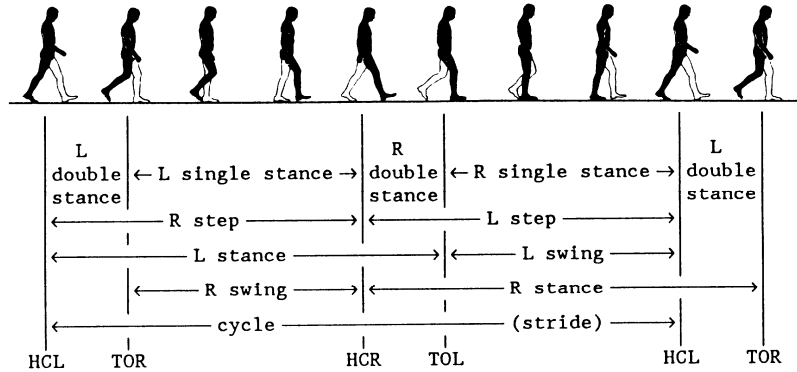


Figure 6.1: The walking cycle

These points divide the walking cycle in four different phases. For the left leg, the stance phase is from HCL to TOL and the swing phase (or the single stance phase of the right leg) is from TOL to HCL. There are two double stance phases where both feet are on the floor. The left double stance phase is from HCL to TOR. One stride consists of two steps: the left step is usually defined from HCR to HCL.

For the step-parameters, a distinction is made between the time-parameters and the distance-parameters. The time parameters relate to the time durations of the phases, sometimes normalized with the cycle or stride time T . For example, the right step time is defined as the time difference between the points of right and left heel contact, e.g. $t_{stR} = t_{HCR} - t_{HCL}$. Likewise, the distance parameters relate to the distance traveled in one phase, sometimes normalized with the stride length S . The stride length equals the sum of the left and right step lengths, i.e.

$$s_{stR} + s_{stL} = S.$$

The average forward velocity (v) and the step ratio (r) can be derived from the step length (S) and step time (T). These important parameters are calculated from:

$$v = \frac{S}{T} \quad (6.1)$$

$$r = \frac{1}{4} S \cdot T \quad (6.2)$$

The step ratio is usually defined as the step length divided by the step frequency. The reason for introducing the step ratio is that this parameter is shown to be reasonably constant for a wide range of walking velocities and for different human subjects (e.g. Rozendal, 1968). For normal walking, r ranges from 0.39 to 0.44 m·s for men and from 0.34 to 0.40 m·s for women (Waters et al., 1988; Inman et al., 1981). Other step-parameters that are found in the literature, such as the step frequency and the swing phase time, follow naturally from the step-parameters as defined above.

6.1.2 KINEMATICS

A more detailed description of the walking movement is obtained when the joint rotations are measured at each point in time of the walking cycle. The hip, knee and ankle flexion are well documented in the literature, so measured data can be compared with "standard" data. As an example, the rotations that are shown in Figure 6.2 are average values for normal walking, measured by Winter (1987).

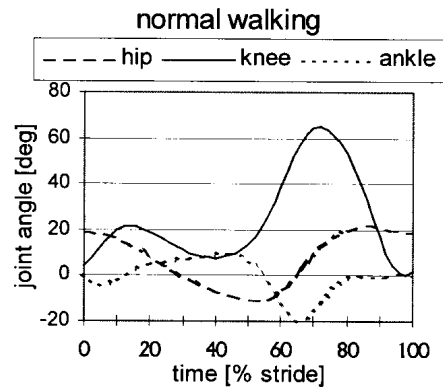


Figure 6.2: Joint rotations in the sagittal plane for a cycle beginning with heel contact (in deg). Hip flexion, knee flexion and ankle dorsiflexion; average values for 19 subjects. From Winter (1987).

The other rotations that also contribute to the walking movement (e.g. hip adduction, pelvic rotations) are less well documented; for these rotations generally accepted average values have not yet been established.

The kinematics of the walking movement could also be described with the displacements of the joints as time functions or with a combination of displacements and rotations. The choice for one of these possibilities mostly depends on the measuring and analysis system that is available (see also Chapter 2).

6.1.3 KINETICS

Besides kinematic terms human gait is also described in kinetic terms: the internal and external forces and moments of force, acting on the body segments. Of these forces only the ground reaction forces can be measured directly. The average ground reaction forces, as measured by Winter (1987), are shown in Figure 6.3.

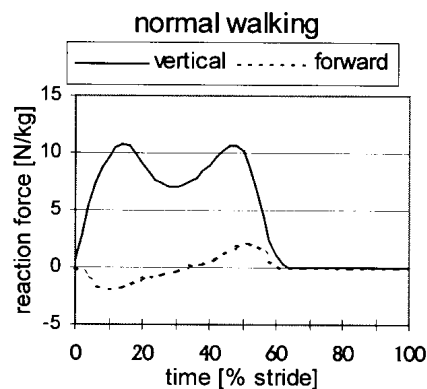


Figure 6.3: Forward (solid line) and vertical (dashed line) ground reaction forces, normalized with body mass, ensemble average from 19 subjects. Obtained from Winter (1987).

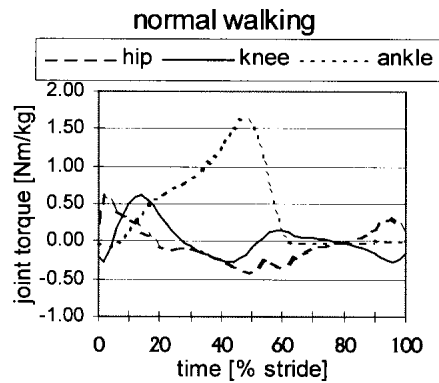


Figure 6.4: Joint moments of force in the sagittal plane (in Nm/kg). Average values for 19 subjects. From Winter (1987).

The joint moments of force can only be determined by analyzing and modeling the measured movement. This implies that in this case always some assumptions, concerning the properties of the human body, have to be made (Section 6.2). The joint moments of force are then computed from the measured ground reaction forces and the movement parameters (Chapter 3). The variation in the ground reaction forces between different subjects is reasonably small, which is not the case for the joint moments of force. Figure 6.4 shows some of the joint moments of force, as determined by Winter (1987). The joint moments of force can be viewed as the net result of all muscular, ligament and friction forces acting on the joint. For some applications, the muscular forces can be related to electromyographic (EMG) signals that can be measured.

6.1.4 ENERGY EXPENDITURE

By knowing the kinematics and kinetics it is possible to calculate the generated and absorbed energy on joint and segment level (Section 6.2.2). However, this mechanical energy on joint or segment level is not uniquely related to the energy absorption and generation at muscular level. The energy expenditure on muscular level determines how much energy is needed by the human. Another word for the latter energy expenditure is metabolic expenditure, which can be measured experimentally. In contrast, the mechanical energy can only be determined by modeling since the needed kinetic data is reconstructed by using modeling techniques.

The metabolic energy expenditure is measured with the oxygen uptake during walking and is usually expressed in energy per unit time (E_w) or energy per unit distance walked (E_m). Ralston (1958) first showed that E_w is proportional to the square of the walking velocity:

$$E_w = a + bv^2 \quad (6.3)$$

This relation is confirmed by various investigators (Inman et al., 1981). When E_w is expressed in Watt per kg body mass and v is in m/s, the experimental values for the constants a and b are $a=2.24$ W/kg and $b=1.26$ Hz. E_m is defined by

$$E_m = \frac{E_w}{v} = \frac{a}{v} + b \cdot v \quad (6.4)$$

E_w and E_m are shown in Figure 6.5.

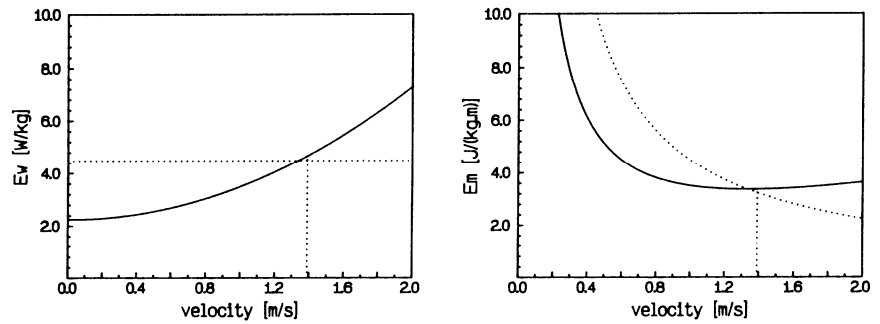


Figure 6.5: Metabolic energy expenditures E_w and E_m for normal walking at different velocities. The dotted lines indicate the optimal velocity that is defined as the walking velocity where the energy expenditure per walking distance (E_m) is minimal.

The optimal velocity v_{opt} (dotted lines in Figure 6.5) is defined as the velocity where E_m is minimal. Differentiating Equation 6.4 with respect to v and equating to zero yields $v_{opt}=1.33$ m/s. The comfortable walking velocity v_{comf} is the velocity a person tends to adopt in a natural walk. v_{comf} is found to have an average value of 1.39 m/s (Inman et al., 1981), which differs from v_{opt} by only 4%. Inman et al. called this an example of a fundamental feature of human motor behavior: "In freely chosen rate of activity, a rate is chosen that represents minimal energy expenditure per unit task". In the case of walking, a speed is adopted with a specific stride length S and cycle period T , such that each meter is covered as efficient as possible.

6.2 Inverse dynamical analysis of gait

In this paragraph it will be shown how the kinetic data and the energy flows on joint and segmental level can be calculated using inverse dynamical models of gait.

6.2.1 SEGMENTS MODELS

All models to simulate human movement are developed from segments models. These are coupled systems of rigid bodies, with dimensions and inertial properties that are deduced from the dimensions and inertial properties of the human body. Initially, these segments models were used to dimension the dummies used in experiments (e.g. Clauser, McConville and Young, 1969) and were therefore based on averaged data of human bodies. With the introduction of the segments models to computer simulations, a wider variety became possible. The segments models were scaled, with inertial properties usually depending on local segment dimensions and total body weight. In this way, the segments model could be matched to fit each individual (e.g. Chandler et al., 1975).

The choice of the number of segments should be large enough to simulate the movement adequately. Too large a number of segments, however, would lead to unnecessary complexity and large computation times. To simulate walking, segments models varying from 3 segments (McMahon, 1984) up to 17 segments (Hatze, 1981a) have been proposed. Besides the number of segments the complexity can be reduced by assuming symmetry between right and left leg (e.g. Brand et al., 1982) and restricting the movement to the sagittal plane only. In the model for normal walking there are segments for the upper legs, lower legs and feet. The head, arms and trunk (HAT) and the pelvis are modeled as

two separate segments. The segments are connected to each other in the joints (Figure 6.6). Although it is possible to have more than two joints on a segment (e.g. the pelvis), each joint is connecting exactly two segments. The point of contact between foot and floor is modeled as if it were a joint. In this view, the floor is a segment with zero velocity and infinite mass. The advantage of this view is that the ground reaction forces are treated in the same way as the joint forces. Notice that the position of the joint between the foot and the floor is not fixed but moves in general from the back to the front of the foot during the rollover of the foot.

To define the position of the segments in space, an absolute or reference frame is attached to the floor, with the x-axis pointing in the walking direction, the y-axis pointing upward and the z-axis perpendicular to the xy-plane in the lateral direction. Figure 6.6 shows the 8-segmental model that is used here, with the numbering of the segments and the joints and the definition of the reference frame. It should be noted that the shape of the segments is of no importance as long as the positions of the joints and the mass properties are well defined. The segments model includes the following definitions, that are dependent on individual characteristics: the dimensions and positions of the segments in space, the mass properties of the segments, the ranges of motion of the joints and the maximal joint angular accelerations, the maximal moments of force that can be exerted in the joints, and the models to define the muscle attachments in the segments and the muscle properties.

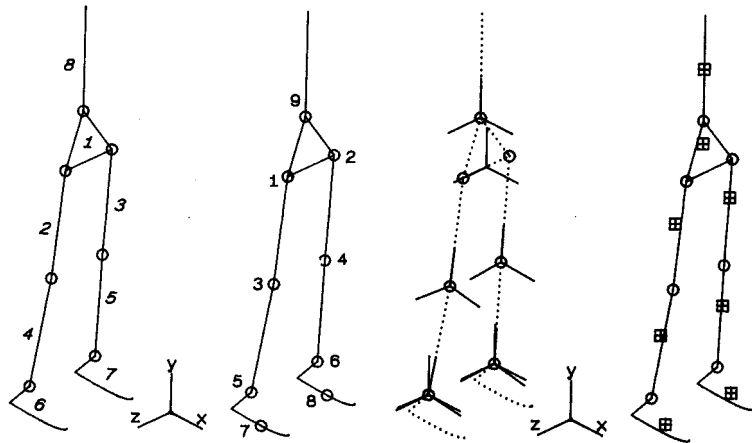


Figure 6.6: The segments model for the body at rest: numbering of segments and joints, definition of the reference frame, definition of local frames and positions of the centers of mass.

The segments model is the basis for a sound technical description of the walking movement. As explained in Chapter 2, the movement is defined as the displacements and orientations of the local frames relative to the reference frame. The joint rotations described in Section 6.1.2 implicitly assume that some kind of segments model is defined, otherwise the joint rotations have no unique meaning. As the offset position for the segments model, i.e. the position where the rotations are defined to be zero, usually the anatomical position is taken.

6.2.2 WORK BALANCE

By applying the equations of motion to the moving segments model in an inverse dynamics approach (Chapter 3), the internal forces and moments of force are calculated. In Section 6.1.3 the joint moments of force are shown. One should keep in mind that these are joint moments of force, acting on the

segments model that is made to move as a human subject. Without a segments model, these torques could never be estimated, and all deviations between segments model and human subject affect the outcome. It is very difficult to estimate the error involved, often an over-all error of 10% in the joint moments of force is assumed.

The vector product of the joint moment of force and the angular velocity equals the power output at the joint (Figure 6.7). A positive power reflects energy generation; a negative power reflects energy dissipation at the joint. On a muscular level, this is comparable to concentric and eccentric muscle contraction respectively. The joint powers have to go somewhere. These powers finally result in an increase (or decrease) of the mechanical energy (kinetic or potential) of the segments. However, since walking is a cyclic movement, the total power output of all the joints together in one cycle must equal zero for level walking. If for example the power output of one cycle would be positive, than the total mechanical energy of the segments model would be increased during one cycle. An increase of kinetic energy or walking speed is contradictory to the assumption of a cyclical movement; an increase of potential energy is possible for walking stairs or uphill.

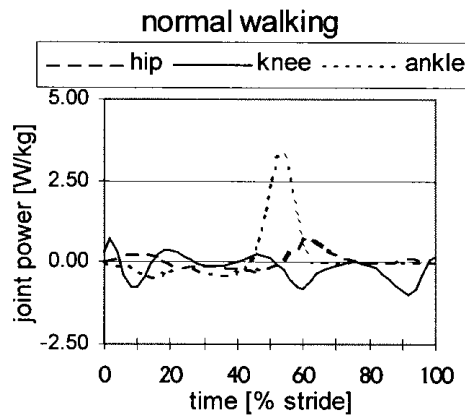


Figure 6.7: Joint powers (in W/kg). Average values for 19 subjects. Obtained from Winter (1987).

To be able to tell something about the work done at the joints, usually a distinction is made between the positive and the negative work (W_j^+ and W_j^-) at joint j with power P_j :

$$\begin{aligned}
 W_j^+ &= \int_0^T P_j^+ dt; & P_j^+ &= \begin{cases} P_j & (P_j > 0) \\ 0 & (P_j \leq 0) \end{cases} \\
 W_j^- &= \int_0^T P_j^- dt; & P_j^- &= \begin{cases} 0 & (P_j \geq 0) \\ P_j & (P_j < 0) \end{cases}
 \end{aligned} \tag{6.5}$$

This definition results in a work balance as shown in Table 6.1. From the table it is obvious which joints in general generate energy and which joints dissipate energy. In most cases, the hip joints generate as much as they dissipate, the knee joints are mainly dissipaters (in the beginning of the stance phase to accept body weight) and the ankle joints are mainly generators (at the end of the stance phase to push off). The total work for all joints during one cycle should equal zero. In table 1, the total $W_j^+ + W_j^-$ equals -2 J/cycle. This value reflects some inaccuracies of the calculation. Especially the fact that the properties of the segments model do not perfectly match the properties of the human body results in this unbalance.

Table 6.1: Typical work balance for normal level walking

joint j	normal walking [J/cycle]			
	W_j^+	W_j^-	$W_j^+ + W_j^-$	$W_j^+ - W_j^-$
R hip	18	-14	-4	32
L hip	18	-14	-4	32
R knee	17	-32	-15	49
L knee	17	-32	-15	49
R ankle	13	-3	10	16
L ankle	13	-3	10	16
Total	96	-98	-2	194

The last column shows the absolute amount of mechanical work done. When it is assumed that mono-articular muscles do all the work, no energy is stored in passive structures, and the efficiency equals 1 for concentric contractions and -1 for eccentric contractions, this number can be related to the metabolic energy consumption. The metabolic energy consumption for a person of 80 kg with a stride length of 1.5 m/cycle is about $3.4 \times 80 \times 1.5 = 408$ J/cycle (see Figure 6.5). About half this amount is needed for basal metabolism, the energy consumption at zero velocity. This leaves about 200 J/cycle that is spend on walking alone. This value is close to the estimated mechanical work (Table 6.1).

However, if more realistic values for the efficiencies are assumed (i.e. 0.3 and -1.0 for concentric and eccentric contractions respectively, see McMahon, 1984), the total mechanical work predicts a metabolic energy consumption of 418 J/cycle. This implies that energy transfer between joints through biarticular muscles and energy storage in passive structure are important mechanisms to reduce the over-all metabolic energy consumption.

The work balances are useful when analyzing situations that deviate from normal. An example is shown in Table 6.2, where the balance of a subject with a left above knee prosthesis is shown. The prosthetic joints are passive and do not contribute to the work balance. This has to be compensated in the other joints. The right ankle shows a stronger push-off, whereas the sound knee shows more dissipation. However, the largest compensatory effects are visible at the hip joints. In this case it could be shown that the hip abductors generated a large amount of work to lift the body weight and thus allowing the prosthetic leg to swing freely. Although the prosthetic joints do not contribute to the work balance, the total work is much larger than for normal walking.

Table 6.2: Typical work balance for prosthetic level walking

Joint	prosthetic walking [J/cycle]			
	W_j^+	W_j^-	$W_j^+ + W_j^-$	$W_j^+ - W_j^-$
R hip	78	-38	40	116
L hip	33	-50	-17	83
R knee	15	-49	-34	64
L knee	0	0	0	0
R ankle	21	-4	17	25
L ankle	0	0	0	0
Total	147	-141	-6	288

6.3 Forward dynamical simulation of gait

The synthesis or prediction of bipedal gait is a topic of interest in robotics as well as in biomechanics. The last decades several approaches have been

published and different 'bipedal walkers' have been constructed trying to predict or mimic human gait. Most 'predictive' models are complex, contain many parameters, demand tremendous computational effort, have poor stability properties, and do not give much additional insight in the control objectives needed to generate cyclic gait (e.g. Pandy et al., 1999; Yamaguchi, 1989, Van de Belt, 1997). In the field of robotics, most bipedal walkers require complex control schemes and consume much more energy than humans. Moreover, most bipedal walkers do not walk very 'natural' (see for overview bipedal walkers Sardain et al., 1998). Different approaches to synthesize bipedal gait, can roughly be categorized in:

1. Open loop control. In this approach one tries to find the control-input patterns (joint moments, muscle forces, muscle activation) or joint trajectories that will result in cyclic gait. Since information of the current system states is not fed back into the controller, the found solutions are unstable. This approach is widely used in biomechanical computer simulations (e.g. Pandy et al., 1999, Koopman et al., 1995; Yamaguchi 1989, Van de Belt, 1997). This approach is characterized by difficulties in finding feasible solutions and immense computation times (Anderson et al., 1995; Yamaguchi, 1990).
2. Closed loop trajectory control. In this approach every joint trajectory during the cycle is prescribed. An important issue within this approach is trajectory planning. Sometimes these trajectories are derived from human walking (e.g. Yang, 1997), from kinematic constraints (e.g. Lum et al., 1999), from coherent parameters characterizing human gait (Hurmuzlu, 1993), or they are obtained using learning algorithms (e.g. Benbrahim et al., 1997; Salatian et al., 1997). Stability is guaranteed about operation point (joint angles) utilizing feedback schemes. However, to ensure stability of walking, stability should not only be addressed with respect to prescribed trajectories. From our experience as humans we all know that it is sometimes necessary to take smaller or larger steps when we are subject to sudden perturbations, like a push or stumble. A 'trajectory tracking' strategy is then not the best-suited strategy to prevent falling.
3. End-point control. Instead of specifying all joint trajectories as a function of time one can specify only the values at the end of the step. Using linear state feedback and specifying the configuration of the biped at the end of the swing phase as set-point biped locomotion was realized (Mita et al., 1984). The biped could only make small steps. For larger steps the difference between the biped's configuration at begin and end of the swing phase will be too large, and the linear feedback controller will be unstable. For the built biped, the Center of Mass (CoM) motion during swing phase was (indirectly) controlled. However, when CoM position is relative high and the feet relative small - as in humans -, control of CoM motion is severely limited by the constraint that the feet should be flat on the ground (Kuo and Zajac, 1993)
4. Non linear dynamical system/Ballistic walking approach. In this approach, a cyclic gait pattern is the result of dynamical system properties (joint impedance, segment inertia) interacting with the environment. Ballistic walking down a slope is an old and well-known example of this system approach (e.g. McMahon, 1984; McGeer, 1990). The ballistic walking concept can be extended by including adjustable springs (Van der Linde, 1999) or 'passivity-mimicking' control laws (Goswami et al., 1997). Taga (1995) also demonstrated the capabilities of such a system approach. By entrainment of neural oscillators, the environment, and body mechanics, stable gait emerges. In the system approach, the system is structural stable for small disturbances. However, stability for larger disturbances is not

guaranteed and not explicitly addressed.

Human senses and their dynamics

INTRODUCTION

The musculoskeletal system is a mechanical system with muscles as actuators. Too often, the feedback system is ignored when the behavior of the system is studied. In comparison, one can not imagine a robot without feedback control. The properties of a physiological feedback system are besides the controller setting and the dynamics of muscles and the segmental dynamics determined by sensory dynamics. Several sensory systems are considered in this chapter: Visual, vestibular, tactile, muscle spindles and Golgi Tendon Organs (GTO). Some pathways in the Central Nervous System are described. In the next chapter, the contribution of length, velocity and force feedback to position control of the neuromusculoskeletal system will be described.

OBJECTIVES

This chapter addresses:

- Physiological sensors and neurons
- Dynamic properties of muscle spindles
- Dynamic properties of the visual system
- Dynamic properties of the vestibular system
- Dynamic properties of the tactile system
- Dynamic properties of the Golgi Tendon Organ
- Central Nervous System
- Reflex loops
- Reciprocal inhibition

7.1 Introduction

In Figure 7.1A, an open loop musculoskeletal system is shown. The Central Nervous System (CNS) generates a neural input (α -activation) to the muscles, which results in a muscle force that accelerates the skeletal system. The acceleration is twice integrated in order to obtain the position. If the neural input is fine-tuned, a desired position can be reached. However, in presence of (force) disturbances the desired position will presumably not be reached, since there is no way that information about the disturbance is used to adapt the neural input. However, strictly spoken the effect of the force disturbance will be attenuated by the length and velocity dependence of the muscular contraction dynamics, i.e. the muscular visco-elasticity.

In Figure 7.1B, a closed loop musculoskeletal system is shown. A number of sensors is present in the human body, which provide information about the state of the musculoskeletal system. Some sensors provide information about the whereabouts of the human body with respect to the outside world (exteroceptors), other sensors give information about the state of the inside of the human body (interoceptors). Important exteroceptors are the vestibular system and the visual system. Interoceptors are sensory organs in the joint capsule, muscles and tendon. In the joint ligaments and capsule sensors are present which can detect the position of the joint, i.e. the joint angle. However, since most ligaments are only stretched at the utmost joint angles, there is no

neural signal proportional with the joint angle, and it is unlikely that joint sensors have an important role in the direct control of the joint position.

Muscle spindles are sensors attached to the muscle fibers, which provide information about the length and contraction velocity of the muscle fibers. Golgi Tendon Organs are found in the muscle tendons, and result in neural signals proportional to the muscle force. Muscle spindles and GTOs give continuous signals, and it is very likely that the joint position can be reconstructed from this signal at any time.

Tactile sensors in the skin are a special category of interoreceptors, since they are excited by stimuli from outside the body.

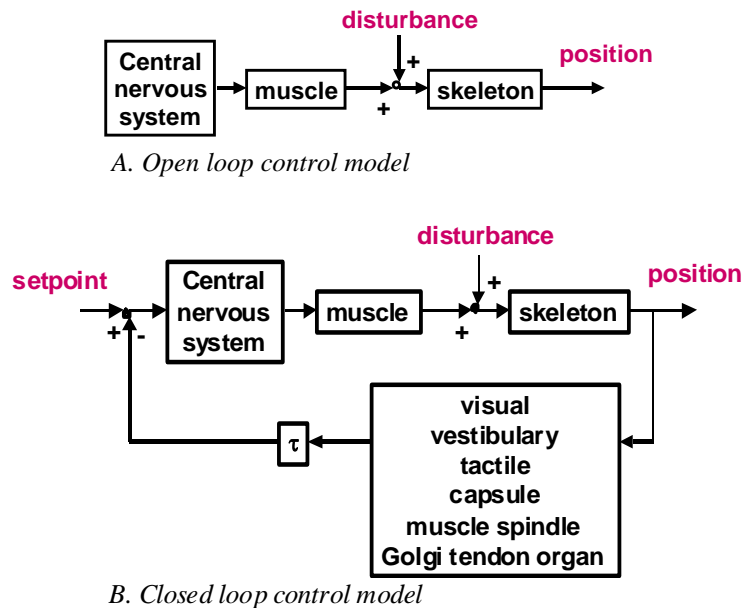


Figure 7.1: A: In the open loop control model, the Central Nervous System generates commands to generate motions of the musculoskeletal system. If disturbances are present, their effect on the position can not be compensated. B: In the closed loop control model the Central Nervous System acts as controller. Information from the sensory organs about the position of the musculoskeletal system is compared with the desired position (setpoint, also generated inside the CNS), and compensatory signals are sent to the muscles.

7.2 The neural system

7.2.1 NEURONS

The Central Nervous System consists of the brain inside of the skull, and the spinal cord inside the spinal column. The peripheral nervous system consists of afferent nerve fibers, transporting information from sensors towards the CNS, and efferent nerve fibers, transporting information from the CNS towards the muscles. In addition, there is the autonomous neural system that innervates organs like the bladder or the intestines. A typical nerve fiber (or neuron) has dendrites through which signals from other neurons or sensors are received, and axons that stimulate other neurons or muscle fibers (Figure 7.2). A signal is transmitted from a stimulating neuron to a receiving neuron through a synapse

(see Figure 7.3). When a neural signal arrives at a synapse, some neurotransmitter is released inside the synapse gap. The neurotransmitter is taken up through the membrane of the receiving neuron. There are excitatory and inhibitory neurons. The neurotransmitters of excitatory neurons will result in an increase of the potential of the receiving neuron. On the contrary, the neurotransmitters of inhibitory neurons will result in a decrease of the potential of the receiving neuron. If the potential of the receiving neuron exceeds a certain threshold, the neuron will start firing.

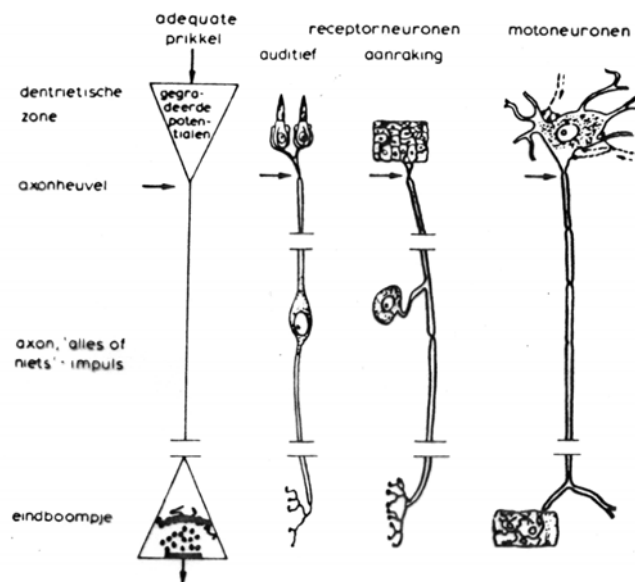


Figure 7.2: Neurons consists of dendrites, a nucleus and axons. The dendrites are stimulated e.g. by other neurons or by sensory organ. If the neuron is activated, nerve pulses are transmitted along the axon towards the end node. Here, another neuron or e.g. a muscle can be stimulated.

Efferent neurons, i.e. the motor neurons, are activated in the spinal cord and will transmit the information to the muscles. These cells can be longer than 1 m! Between the motor neuron and the muscle, there is also a synapse, the motor endplate. Here, a potential at the muscle membrane is generated which will propagate along the muscle fibers. Ultimately, this muscle potential will stimulate the calcium release from the sarcoplasmic reticulum, and the muscle will start to contract.

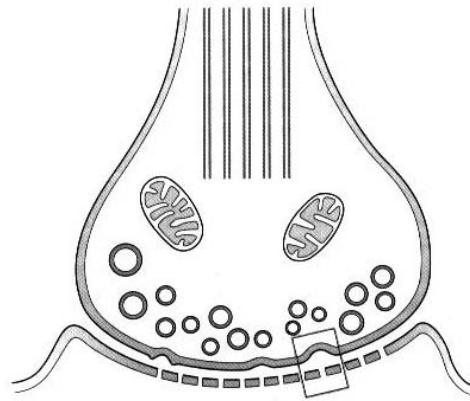


Figure 7.3: In a synapse gap between two neurons, neurotransmitter is released by a particle that passes the cell membrane. The neurotransmitter passes through the membrane of the receiving neuron, and increases (excitatory synapse) or decreases (inhibitory synapse) the cell potential.

Afferent neurons, i.e. the sensory neurons are stimulated when the sensor at the peripheral end of the neuron is triggered by a specific trigger to that sensor. The signal is transported towards the CNS, and will be transmitted through synapses to other neurons in the CNS. Also the sensory neurons are one big nerve cell between sensor and CNS. The cell nucleus of sensory neurons is located just outside the spinal cord, whereas the cell nucleus of motor neurons is located inside the spinal cord. When a peripheral nerve is dissected, the sensory neurons can not be distinguished from the motor neurons. However, inside the vertebral column, very near to the spinal cord, the nerve splits into a motor part which enters the spinal cord at the frontal side, and a sensory part which enters the spinal cord at the back side. Here it is possible to denervate solely the sensory nerves, which is done in case of animal experiments or for patients with spastic paralysis or severe pain complaints.

Interneurons are stimulated by neurons, and themselves stimulate other neurons through synapses. Interneurons are only found in the CNS: All sensory signals from the periphery are first transported to the CNS, processed and motor signals are sent back to the periphery. It is estimated that there are 10^{11} interneurons in the human CNS. On average each interneuron has about 10000 synapses with other interneurons, so in total there are 10^{15} synapses. In comparison, massive parallel computer systems have 'only' up to 128000 parallel chips! Very much in contrast to a computer chip, the information processing is parallel and asynchronous processed. One can imagine the enormous computing potential of the human brain, in many ways unequalled by the current computer systems. Any model of the CNS is just a very big simplification of the complex structure and function of the CNS.

7.2.2 SIGNAL TRANSMISSION ALONG THE NERVES

In the resting situation, there is a potential of -70 mV between the interior of the neuron and the exterior. If this potential decreases to -50 mV, e.g. due to excitation by another neuron or triggering of a sensor, a transport mechanism becomes active, which transports K^+ , Na^+ and Cl^- ions through the membrane, resulting in a reversal of the cell potential to $+20$ mV. Shortly after this depolarization the resting situation will be restored. This is called a twitch or a spike at the neuron. After the spike there is a short refractory period, in which the cell potential is even below -70 mV, and the neuron is more difficult to

stimulate. This limits the number of spikes that can pass to about 400 spikes/sec. At a higher potential at the dendrites, more spikes will be generated. The information is so to say frequency encoded: The number of spikes per second is an indication of the activation of the dendrites. Neural spikes have a very discontinuous character. For calculations, mostly the quantity 'spikes/sec' is used as a continuous variable to describe the activation. The number of spikes per second can be calculated from the interval between two spikes.

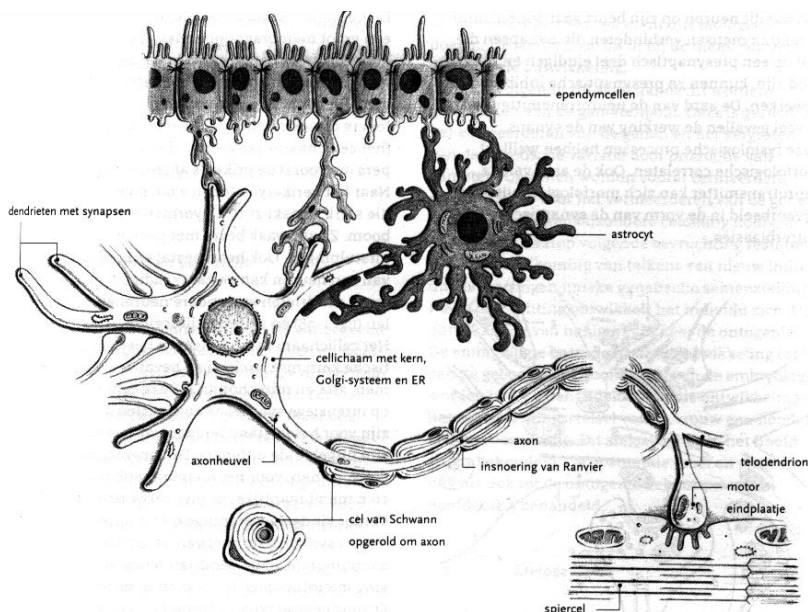


Figure 7.4: Motor nerve cell with dendrites receiving stimuli from other neurons. The spikes are transmitted along the long axon, isolated by myelin for faster transmission speeds. The myelin sheaths show the typical Nodes of Ranvier, through which small current loops come into existence.

A depolarization at a certain point at the nerve cell membrane will result in a change of the potential nearby, which will also result in a depolarization. In this way, the spike will propagate along the nerve cell. This is a relatively slow mechanism, about 2-4 m/sec. There is another mechanism to increase the transmission speed. The nerve cells are 'isolated' by myelin sheaths. At certain distances the myelin sheaths are interrupted by the so-called 'nodes of Ranvier' (see Figure 7.4). The myelin sheaths help to prevent potential leakage from the cell interior to the cell exterior, and an electrical current can pass through the cell interior, with a certain drop of potential. However, if at the next node of Ranvier the potential is still above the threshold potential of -50 mV, then an active depolarization will take place, and the cell potential is actively amplified! This can increase the transmission speed up to about 100 m/sec. If the myelin sheaths are larger (i.e. the nerve is thicker), there will be less leakage and the nodes of Ranvier can be at greater distances of each other. Hence, thicker nerves have larger transmission speeds. However, the maximal transmission speed of 100 m/sec is still a factor three slower than the speed of sound, and we will see in the remainder of this chapter that the time-delays due to the neural transmission speed, and also neural processing, play an important role in the control of motion. For larger animals, this limited transmission speed may become a real hassle for motor control. Therefore, it is thought that e.g. dinosaurs had a second brain located at the down end of the spinal cord, at the pelvic girdle.

7.2.3 ORGANIZATION OF THE HUMAN CENTRAL NERVOUS SYSTEM

The human CNS can be divided in four areas, the cerebrum (major brain), the cerebellum (minor brain), brain stem and the spinal cord. In the CNS, the axons show up as white material and the cell nucleus with the dendrites is gray matter. In the spinal cord, there are many pathways in vertical direction, transporting information up and down. These pathways are located in the central part of the spinal cord. Around these central areas, gray matter is located, made up by interneurons that can process information at this level. For instance, reflexes are generated at the spinal level. The pathways in the spinal cord can go up straight to parts of the cerebellum, or via indirect pathways with additional processing e.g. at the cerebrum or at the thalamus. Unraveling all these pathways is an enormous task, and one can imagine that only very small parts of the brain are analyzed in detail. Deriving the functional role of these pathways is even more difficult, since a working brain can not be dissected, and a dissected brain does not function any more. Most information is obtain by scanning the electrical signals at the skull (EEG) or the blood flow to certain brain areas using magnetic fields (PET scans). However, this information is about larger clusters of neurons.

In the brain stem, many upward and downward pathways have connections with the interneurons. It is thought that the brain stem has an important role in the generation of motion on a functional level. The Purkinje cells in the cerebellum have an enormous amount of dendrites and axons, and are thought to have a key role in comparing sensory and motor information, in order to adapt the motor output, but presumably also in order to learn from the proprioceptive information.

In the cerebrum and cerebellum by far the most interneurons are located. The sensory and motor part of the brain is located about halfway between the front and backside of the brain, and is more or less topographically organized according to the part of the body that it is connected to. In the cerebellum, intentions are generated which can be transformed into motions. Functions are located in a distributed manner, i.e. a certain function will be performed by the elicitation of a part of the brain which may also be (partly) active when another function is performed. So it is impossible to say that one neuron has one function.

There are many philosophical and religious theories about the nature of the human consciousness and 'soul'. From a mechanistic point of view, everything that happens boils down to signals transported along neurons and passed trough excitatory and inhibitory synapses. One can wonder how information is stored in the brain, e.g. how does the memory work or how is information retrieved. Since there is no 'hold-circuit' in which electrical or magnetic information is stored, the information must be stored in the structure of the system, i.e. the connectivity between the interneurons and the strength of the synapses. The strength of a synapse determines how much the potential of the receiving neuron is raised or lowered due to one spike of the stimulating neuron. It has been shown that the strength of synapses can change very rapidly, in the order of seconds, which will alter the function of the whole system.

7.2.4 PERIPHERAL NERVOUS SYSTEM

The peripheral nervous system consists of nerves outside the central nervous system, going to and from muscles, sensors and organs. The autonomous nervous system innervates the internal organs like the bladder, arteries, etc., and will not be discussed further in this chapter. Afferent nerves transport

information from the peripheral sensors towards the CNS, and efferent nerves transport information from the CNS to the muscles. Efferent nerves leave the CNS at the ventral side (front side) of the spinal cord; afferent nerves enter the CNS at the dorsal side (backside) of the spinal cord. A few centimeters from the spinal cord the efferent and afferent nerves merge and can not be distinguished from each other. The peripheral nerves pass through small openings in the spinal columns. At this stage, they are called the nerve roots. Spinal roots are named after the vertebrae between they leave the spinal column. There are 8 cervical roots (C1 - C8), 12 thoracic roots (T1 - T12), 5 lumbar roots (L1 - L5) and 5 sacral roots (S1 - S5). Spinal roots innervate more or less sensors and muscles in 'horizontal' segments if one assumes the arms and legs stretched out horizontally (which is obviously difficult for the legs!). Especially at the arm and leg segments, many sensors and muscles are innervated. At these segments the spinal roots enter a nerve network (the plexus brachialis and plexus lumbosacralis, respectively). At the distal side peripheral nerves leave the plexus. The peripheral nerves consist of motor and sensory neurons that originate at several spinal roots. The peripheral nerves split into branches that innervate individual muscles and e.g. parts of the skin. The neurons innervating muscles most often originate from multiple spinal roots. In general, one can state that the proximal muscles (closer to the center of the body) originate from higher spinal roots than more distal muscles (further away from the center of the body). For instance, the shoulder muscles are innervated by spinal roots C5 and C6, the elbow muscles by C6 and C7, the forearm and hand muscles by C7 to T1.

7.2.5 NERVE LESIONS

As stated before, motor and sensory neurons are very large cells, which run from the spinal cord to the peripheral structures. In case of lesions of the nerve cells, the part that is not connected any more with the cell nucleus will die. The cell nuclei of the motor neurons are located in the ventral part of the spinal cord; the cell nuclei of the sensory neurons are located in small 'bags' (ganglions) just *outside* the spinal column.

Most often nerve lesions are due to stretch trauma (fast elongation, e.g. after a fall on the arm) and more seldom due to direct trauma as cuts or shot wounds. The severity of nerve lesions can be different, because of the magnitude of the impact. In case of an edema due to an impact, the signal transmission is blocked while the nerve itself is intact. Function will return after a few days when the edema is away. If the axon is interrupted, the peripheral part that is not in connection with the cell nucleus will die. If the myelin sheaths are intact, the nerve will start to grow from the central part. The growing speed is about 1 mm per day. So to innervate the upper arm muscles again after a trauma near the neck, it takes almost a year before any function will return. The myelin sheaths will guide the axons to the muscles and sensors that were innervated by the same neurons before. A proper return of function is then expected. If the myelin sheaths are also interrupted but the collagen fibers around the nerve fibers are intact, the axons may also start to grow, but motor neurons might end at sensors, and sensory nerves at the muscles, which will not result in any function. On average 25% of the nerves will be connected to a proper site. For instance, motor neurons will innervate a great deal more muscle fibers after the trauma (giant motor units). The coordination after such a trauma can sometimes be very difficult and only part of the function will return (e.g. 'weak' muscles).

Due to the speed of nerve growth (1 mm per day), it may take up to two years after trauma to restore function. If after two years no function did return, it is very unlikely that it will ever return. Then, surgical action or conservative

treatment is indicated. Conservative treatment will aim at the improvement of function through orthotic and prosthetic devices, or through training and physical therapy. Surgical treatment can consist of orthopedic surgery, e.g. tendon transfers, or neurosurgery, aiming to reconnect the nerves. A dilemma is that the best time for neurosurgery is about 2 months after trauma. After six months, post-trauma neurosurgery does not provide very good results any more. However, after two months natural recovery might still occur! Hence, a good diagnosis is essential, and often surgery is attempted to see if any reconstruction can be made.

When the nerve is not in continuity any more after trauma, or scar tissue prevents nerve growth, no return of function is to be expected. Then, neurosurgery is indicated. During neurosurgery bad parts with scar tissue of the nerves will be removed, and replaced by nerve grafts. A nerve graft is a part of a nerve taken away from another part of the body. Usually sensory nerves innervating skin areas in the lower leg are used as nerve grafts. The nerve grafts is sutured to the healthy central part of the nerve, and to the peripheral part. The nerve graft functions as a tubing system, guiding axons towards the peripheral part of the nerve. As before, only 25% of the nerves is expected to end at a proper site. The return of function depends on the length of the graft (which can be up to 10 cm.), the distance between the central part and the muscle or sensor (hand function will seldom return), and the quality of the connection between the original nerve parts and the graft.

Spinal cord lesions occur after severe trauma, often fractures, of the spinal column. These are mostly stretch injuries. Very often, the cause of the nerve injury itself is due to the edema, which can cause a great pressure inside the spinal column. Complete and partial lesions can occur after trauma. Partial lesions might improve over time, and complete lesions can turn out to be partial lesion. However, if the nerves are not continuous no return of function is to be expected, since nerve growth passed the lesion site has never been detected in spinal cord lesions. If after a few months after trauma no return of function is seen, further improvement due to nerve recovery is unlikely. Neurosurgical repair of spinal cord lesions has been unsuccessful until now.

7.3 Classification of the human senses

A human constantly interacts with his environment: he perceives events, processes this information, and manipulates his environment by his actions. Subsequently, these actions are perceived and, if necessary, adjusted. This ongoing coupling between perception and action is essential to optimally exploit the environment, in order to survive.

In Figure 7.5 the interaction between a human and his environment is schematically shown. An external physical signal, e.g. light or sound, is sensed by one of the sensory systems. This sensor converts the physical signal to nerve pulses that are conducted to the Central Nervous System (CNS). In the CNS the signal goes through a first process: by pattern recognition (comparison to earlier received, stored information) the information is "classified". Next, the information that has been received from different sensory systems is integrated. Many of these processes are unconscious, however, when special attention will be paid to particular processes some of them can occur consciously. The received information is integrated with present information and knowledge, to finally take action.

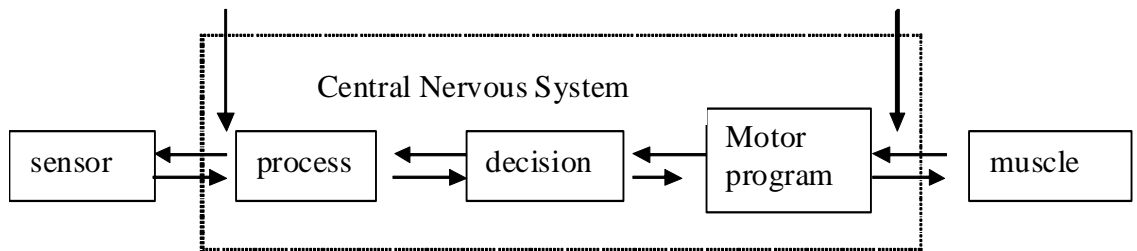


Figure 7.5: The interaction between the human and the environment.

Table 7.1: Overview of sensory systems

Homeostasis	Receptors for pressure, pO ₂ , pH, etc. in vegetative systems	-
Proprioception	Muscle spindles	Section 7.5.2
	Force sensors in tendons	Section 7.5.1
	Position sensors in joints	Section 7.4
	Vesibular organ	Section 7.9
Exteroreceptors	Skin: pressure, pain, cold, vibration	Section 7.7
	Taste	-
	Smell	-
	Hearing	Section 7.6
	View	Section 7.8

All organs that supply the CNS with information through nerve fibers are called sensors. The nerves from the sensory systems to the CNS are called afferent and/or sensoric nerves, while the nerves from the CNS to the muscles are called efferent and/or motor nerves. The sensors are classified according to their function. There are sensors for the control of internal functions of the body (homeostasis), to perceive posture and movement of the body (interoreceptors) and to perceive the environmental conditions (exteroreceptors, the well-known senses: vision, hearing, tactile sense, taste, smell). In Table 7.1 an overview is given of the most important sensors.

In the vegetative system local sensors exist that serve to maintain homeostasis. These sensors give information about the internal state of the human, for example the pH in the stomach, such that by means of internal control loops action can be taken if the internal state deviates from the optimum. There are other sensors that provide information about the position and movement of the body parts in space or with respect to each other. The perception of the position and movement of the body parts is called proprioception (= self-perception). Close to the ear the vestibular organ is situated, which provides information about the gravitational and inertial forces acting on the head and the angular velocity of the head. Joint receptors provide information about the position of the segments in relation to each other. In this way someone is constantly conscious of the posture of his body. Muscle spindles are situated in the muscles and provide information about the muscle length and velocity. Golgi tendon organs are sensitive to the force and are located in the tendons.

The exteroreceptors are taste, smell, the skin, the eye and the ear. In this course only the last three of these will be discussed since these contribute to motor control. In various (complex) sensory motor tasks multiple sensory information is used; e.g. posture, walking, head-eye coordination.

7.3.1 PERCEPTION WINDOWS

The sensitivity of a sensory system can be considered as a kind of “perception window”, through which a human perceives only a part of the physical reality by means of sensory input (Figure 7.6). In general, a sensory system is not sensitive to static signals but to changing signals. The perception window is determined by window-width, window-height and window-depth. The window-width is defined by the minimal and maximal frequency that can be perceived (for example 20-20,000 Hz. for the hearing, 380 – 720 nm for the visual system). The window-height is defined by the intensity of the signal (energy content). A minimal energy-exchange (threshold value) is necessary to let the sensor send a nerve-pulse to the CNS. The top of the window-height is defined by the intensity of the signal that would cause damage to the sensory system (in case the pain-limit is crossed). Examples of such conditions are an explosion or bright sunlight. The depth of the window is defined by the minimal stimulus duration to perceive a signal and the maximal duration for which damage of the sensory system occurs.

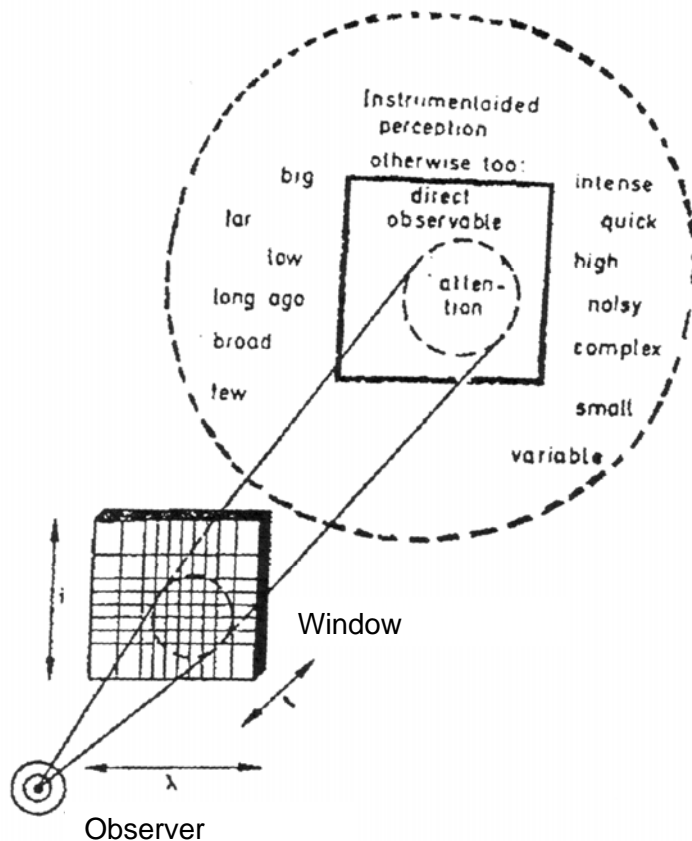


Figure 7.6: The perception window

Perception thresholds are often defined as those stimulus conditions for which 50% of the signals are just detected. The upper boundaries are more difficult to determine since there is a risk that organs will be damaged while exceeding the upper limits.

7.4 Joint sensors

The range of motion of a joint is determined by the capsule and ligaments, in which stretch and pressure sensors are located. The ligaments are strings of connective tissue strengthening the joint capsule. Often, only at the end of the range of motion the ligaments are stretched. Hence, these sensors are not firing at the mid range of motion; therefore it is not likely that they play a major role in the control of movement. On the other hand, information about the boundaries of the joint motion is necessary to learn to move within these boundaries, in order to prevent damage.

7.5 Muscle sensors

Inside each muscle two types of sensors are present: muscle spindles provide information about muscle length and contraction velocity, and Golgi tendon organs give information about the force transmitted through the muscle tendon.

7.5.1 GOLGI TENDON ORGANS

The Golgi tendon organs (GTO) are located in the muscle tendons. About 50 GTOs are located in a major tendon. The GTOs consist of nerve endings that are intertwined with the collagen fibers of the tendon (Figure 7.7). When the tendon is stretched, the nerve endings are 'squeezed'. The denervation of these nerve endings results in a spike train along the afferent nerve to the CNS. This afferent nerve is called the Ib afferent nerve fiber. The deformation of the tendon is in accordance with the muscle force exerted along the tendon. Therefore, the Golgi tendon organs provide information about the muscle force.

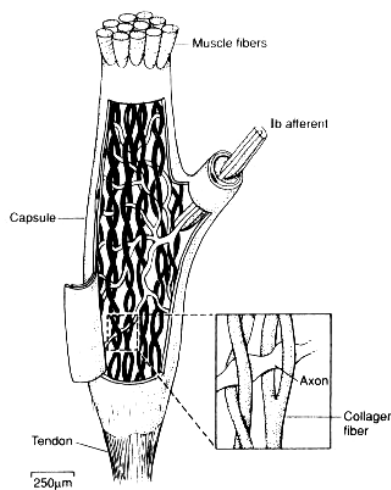


Figure 7.7: The Golgi tendon organ consists of a nerve ending intertwined with the tendon fibers. The Golgi tendon organ is sensitive to the muscle force exerted through the tendon.

In the earlier days, experiments in which the whole muscle was stretched resulted in little activity of the GTO. Therefore, it was thought that the function of the GTO was not in the fine motor control, but merely to detect large forces in the tendons and protect the tendon against damage. This theory was also in

accordance with the fact that the GTO are connected to the α -motor neuron through an inhibitory interneuron, i.e. when the tendon was stretched, the GTO caused the α -motor neuron to cease firing. However, this theory has been abandoned for two reasons. In the first place, if the α -motor neurons cease firing while the large external force is still stretching the muscle, the muscle will be stretched rapidly, and presumably the muscle fibers will be damaged. Secondly, more recent experiments showed that the Golgi tendon organs are especially sensitive to the forces exerted by the *active* muscle fibers, more than to the passive forces transmitted through endomysium and perimysium (the connective tissue around the muscle fibers).

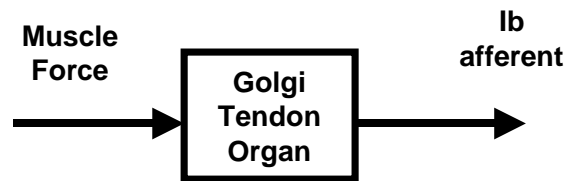


Figure 7.8: Block scheme of a Golgi tendon organ. The only input is muscle force, and the Ib afferent nerve signal is output which has a static and linear relation with the muscle force.

The GTO is a sensor inside a force feedback loop, in which the muscle force is fed back to the CNS. Forces down to a few μN can be sensed by the GTO. In addition, the Ib afferent fibers are among the fastest transmitting sensory fibers in the peripheral nervous system. It will be shown in the next chapter that the force feedback loop is an important inner loop of the velocity and position feedback loops. Inside the GTO, there are no dynamic effects, i.e. the Ib afferent nerve output is always proportional to the muscle force. Hence, there is a static (no time-history) and linear relation between the muscle force and the afferent nerve (Figure 7.8).

7.5.2 MUSCLE SPINDLES

In contrast to the Golgi tendon organs, muscle spindles are very complex sensory units. A muscle spindle is a unit consisting of about 3-5 nuclear chain fibers, and 1-2 nuclear bag fibers (Figure 7.9). A muscle spindle has a length of about 8 mm and is located parallel to the muscle fibers. The muscle spindle endings are attached to the muscle fibers, and hence the spindles are lengthened and shortened together with the muscle fibers. Hence, the length and velocity of a muscle spindle are always proportional to the length and contraction velocity of the muscle fibers.

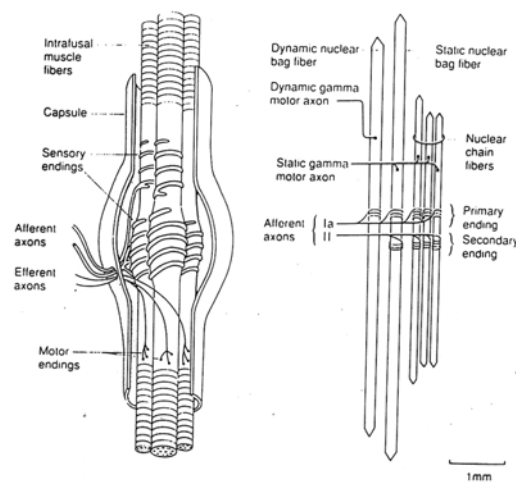


Figure 7.9: A muscle spindle unit consists of 3-5 nuclear chain fibers and 1-2 nuclear bag fibers.



Figure 7.10: Photo of the sensory part of the muscle spindle, in which the nerve ending is wrapped around the nuclear chain and nuclear bag fibers. In addition, the emergence of the sensory nerve towards the CNS can be seen at the left side.

The nuclear bag and nuclear chain fibers contain multiple cell nuclei. As the naming suggest, in the nuclear bag fibers the cell nuclei are located in a bag-formed area in the middle of the fiber, and in the nuclear chain fiber the nuclei are located in a chain along the whole length of the fiber. Both the nuclear chain and nuclear bag fibers consists of two small muscles at the endings, and a sensory part in the middle. A nerve ending is wrapped around the sensory part, and essentially is sensitive to the stretch of the sensory part (Figure 7.10). The small muscles inside the muscle spindle are called 'intrafusal' muscles (intrafusal means 'inside the spindle'). Hence, the normal muscle fibers outside the muscle spindle are called the extrafusal muscle fibers. The intrafusal muscle spindles are innervated by a separate motor neuron, the γ -motor neuron, which is an *efferent* innervation to the muscle spindle (carrying signals from the CNS to the periphery).

The nuclear bag fibers are sensitive to the stretch velocity, and the nuclear chain fibers are sensitive to the stretch length. There are two types of *afferent* nerves, Ia and II sensory nerves. The Ia sensory nerve receives branches from the sensors of both the nuclear bag and nuclear chain fibers, and thus contains length and velocity information. The II sensory nerve receives only branches from the nuclear chain fibers, and contains only length information. According to the specific sensitivity of the nuclear bag and nuclear chain fibers, the innervating γ -motor neurons are called γ_d (dynamic) and γ_s (static) motor

neurons. In Figure 7.11 all efferent and afferent nerves connected to the muscle spindle are shown.

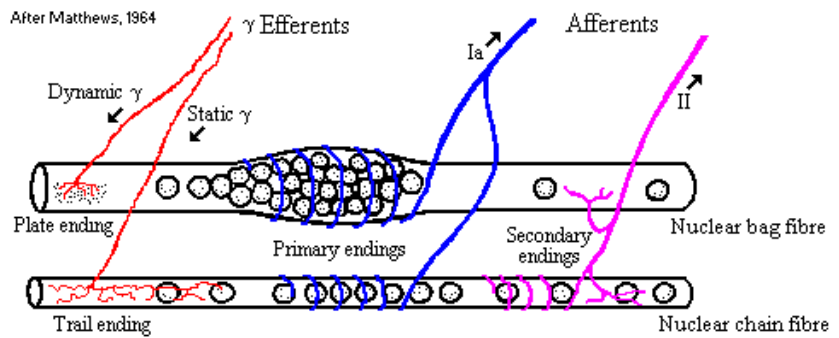


Figure 7.11: A muscle spindle has two efferent nerve inputs (γ_d to the nuclear bag muscle fiber and γ_s to the nuclear chain muscle fiber) and two afferent nerve outputs (Ia from both the nuclear bag and nuclear chain sensory parts, and II mainly from the nuclear chain sensory part).



Figure 7.12: A block scheme showing the two mechanical inputs (length and velocity) and two neural inputs (γ_a and γ_s motor neurons), and two neural outputs (Ia and II afferent nerves) of the muscle spindle.

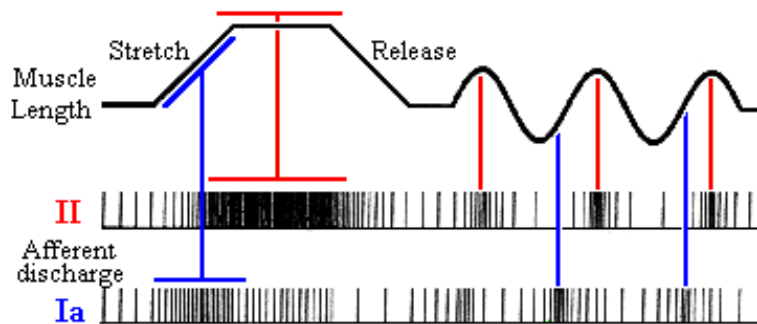


Figure 7.13: Response of the muscle spindle to a regime of stretch and release. From the spike trains in the afferent nerves it can be seen that the II afferent nerve is mainly sensitive to length, and the Ia afferent nerve is sensitive to lengthening velocity. During release, the Ia afferent nerve is almost silent.

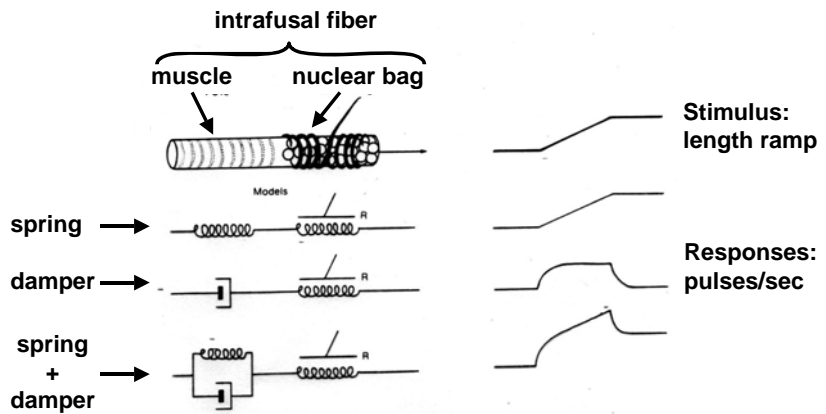


Figure 7.14: The stretch of the sensory part, and hence the afferent neural output, depends on the visco-elastic properties of the intrafusal muscle fibers.

Figure 7.12 contains a block scheme in which all inputs and outputs of the muscle spindle are depicted. The muscle spindle has two mechanical inputs (length and contraction velocity) and two neural inputs (γ_d and γ_s motor neurons), and two neural outputs (Ia and II sensory nerves). Hence, the muscle spindle is a multi-variable system in which there is a non-linear interaction between the inputs.

As stated before, the muscle spindle is sensitive to length and contraction velocity. The resulting spike trains in the Ia and II afferent nerves are shown in Figure 7.13. The figure shows that the muscle spindle is primarily sensitive to muscle stretch and stretching velocity (note that the stretch of the muscle spindle is proportional to the stretch of the extrafusal muscle fibers). During the release, the spike trains almost disappear, especially in the Ia afferent fibers. The II afferent fibers are mainly length dependent, and show their highest activity at the length peaks (shown with red lines). The Ia afferent fibers have their highest activity at the highest lengthening velocity.

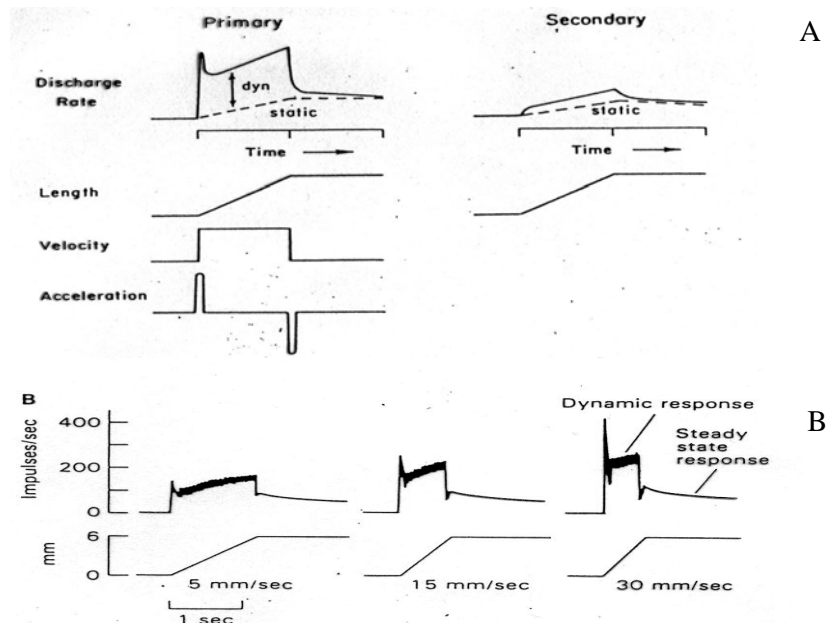


Figure 7.15: A: Theoretical response showing the length, velocity and acceleration contribution. B: Actual experimental results showing the dynamical response. The absence of a peak during release shows that the latest dynamic effect is due to stiction, instead of an acceleration effect.

The response of the muscle spindle to stretch depends also on the visco-elastic properties of the intrafusal muscle fibers. In Figure 7.14 can be seen that if the intrafusal muscle fibers would have only elastic properties, the sensor is a length sensor. If the intrafusal muscle fibers would have only viscous properties, the sensor is a velocity sensor. If the intrafusal muscle fibers combine elastic and viscous properties, the sensor is sensitive to both length and velocity. In Figure 7.15A the theoretical response of an Ia afferent nerve to a length ramp is shown, decomposed in a length, a velocity and an acceleration contribution. In Figure 7.15B the actual response is shown, showing the summation of the length and velocity input. The peak at the start of the lengthening ramp would suggest that also accelerations could be detected. However, experiments have shown that this peak is due to a stiction property in the intrafusal muscle fibers. If the spindle is stretched, the crossbridges in the intrafusal muscle fibers take up the majority of the force for being stretched. Only when the stretch is larger than 1 mm (equivalent to about 5 degrees of joint rotations!), the crossbridges are released and a new equilibrium results. The initial stiction of the crossbridges results that most of the stretch is taken up by the sensory part, which shows a huge initial peak. The fact that there is no peak at the end of the lengthening ramp shows that it is indeed stiction and no effect of acceleration.

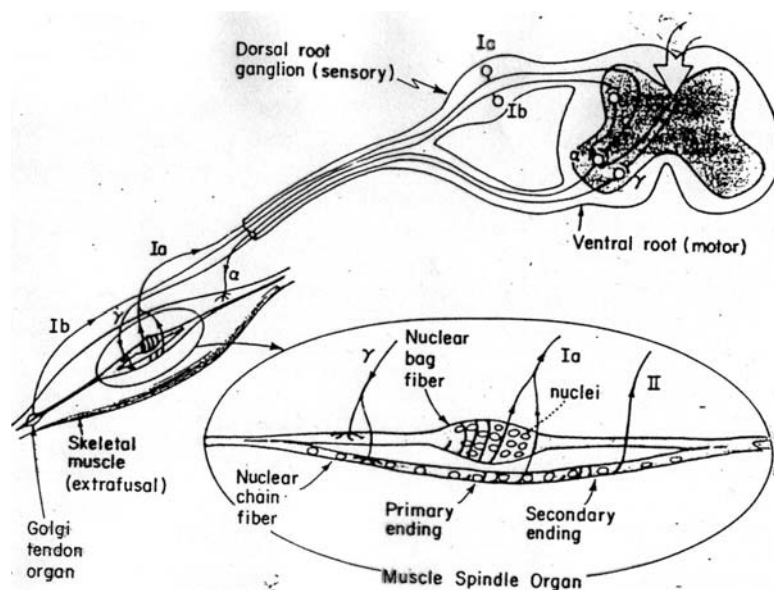


Figure 7.16: The Ia and II sensory nerves are directly connected through a excitatory to the α -motor neuron. The Ib sensory nerve is connected through an inhibitory interneuron to the α -motor neuron.

The visco-elastic properties of the intrafusal muscle fibers are further elaborated in Figure 7.16. If the ratio of stiffness and viscosity is the same for the sensory part as for the muscle part, then a proportional part of the lengthening will be taken up by the sensory part, and the muscle spindle acts as a position sensor. This is the case for the nuclear chain fibers. The intrafusal muscle fibers in the nuclear bags have very high viscous properties. Hence, if the lengthening velocity becomes higher, the sensory part is stretched more and a higher sensory output results.

The visco-elastic properties of the intrafusal muscle fibers as well as the neural output are changed when the muscle fibers are activated by the γ -motor neurons. As a direct effect when the intrafusal muscle force increases, the sensory part is stretched. As a secondary effect the stiffness and viscosity increases and the sensor becomes more sensitive: a relatively more compliant sensory part means that more of the stretch is taken up by the sensory part. Here, an important role of the γ -motor neurons arises: they keep the muscle spindle in the most sensitive region even for the extreme range of lengthening and shortening of the muscle. However, it also implies that for the correct interpretation of the afferent output in terms of length and velocity, also the efferent input to the muscle spindle must be known.

Some theories about the function of the γ -motor neurons state that they function as a set point for the muscle length, since the afferent neural output of the muscle spindles is directly connected to the α -motor neuron activity through a monosynaptic connection in the spinal cord. Because of the increased sensory output, the α -motor neuron activity increases and the muscle shortens. Then, the muscle and proprioceptive feedback would function like a servo-unit. However, it is easily shown that this theory cannot be true, since the afferent neural output will never cease firing when the γ -motor neurons are active, because γ -motor neurons results in a force (not a length!), and a force will always stretch the sensory part.

It is more logical to assume that the γ -motor neuron activation has a two-fold

function: Maintaining the muscle spindle in the most sensitive region, and adjusting the gain of the muscle spindle and thereby affecting the loop gain of the length and velocity feedback. The gain of the muscle spindle is the magnitude of sensory output compared to the length or velocity input. In that respect, increasing the spindle sensitivity and the spindle gain is the same action, though functionally interpreted in a different way.

The transmission speed of the sensory nerves depends on the thickness of the myelin sheaths. In Table 7.2, it can be seen that the tactile sensors and free nerve endings have a very slow transmission. The fastest transmission speeds are found for the Ia and Ib afferents. These sensory nerves are part of the inner loop of a feedback system. A pure time-delay causes a phase lag in the open-loop transfer function, which limits the bandwidth of the system. Especially the inner loops (force and velocity) need to be very fast, in order to enable higher feedback gains in the outer loop (position feedback). For a position-controlled system, a higher loop gain will result in a lower admittance, i.e. less sensitivity to force perturbations.

Table 7.2: Diameter and transmission speed of some of the proprioceptive sensors in the body

	Diameter (μm)	Transmission speed (m/s)	Type of sensor	Stimulus
Ia	12 - 20	70 - 100	Muscle spindle	Length & velocity
Ib	12 - 20	70 - 100	GTO	Force
II	6 - 12	35 - 70	Muscle spindle	Length
	2 - 5	12 - 30	Pacini corpuscle	Pressure
	0.5 - 2	3 - 12	Free nerve ending	Nociceptive

A typical non-linear phenomenon occurs in the Ia afferent nerve at the junction of the branch originating from the nuclear bag fiber, and the branch from the nuclear chain fiber. The spike trains from both nerve branches do not simply add, and continue with the summed spike frequency. Whenever a spike arrives at the junction, it will split into two directions: Towards the CNS but also in the opposite direction along the other branch. Whenever another spike is met at this branch, both spikes will extinct each other. Hence, the spike train with the highest frequency will completely extinct all spikes from the other branch: The winner takes all principle, or a max-operation between length and velocity. Only when the spike trains have about the same frequency they will enforce each other and the summed frequency will be about 110% of the original common frequency. In other words, when the velocity signal is dominant over the length signal, i.e. during movements, the CNS receives only velocity information. When the length signal is dominant over the velocity information, i.e. during postural tasks, the CNS receives only length information. Apparently, the CNS can cope with this phenomenon that it does not know whether the afferent information contains length or velocity information. The function and implications of this phenomenon is not known yet.

7.5.3 MODELS OF MUSCLE SPINDLES

A transfer function of muscle spindles can be obtained by deriving a mechanical model of a muscle filament in combination with muscle spindles. In literature normally a distinction is made between the primary and secondary endings. An example of a mechanical model is given in Figure 7.17. The $X(t)$ gives the extension of the filament. The model has a purely elastic part, and a visco-

elastic part. Assumed is that the displacements $\lambda(t)$ and $\alpha(t)$ stimulate the two different endings.

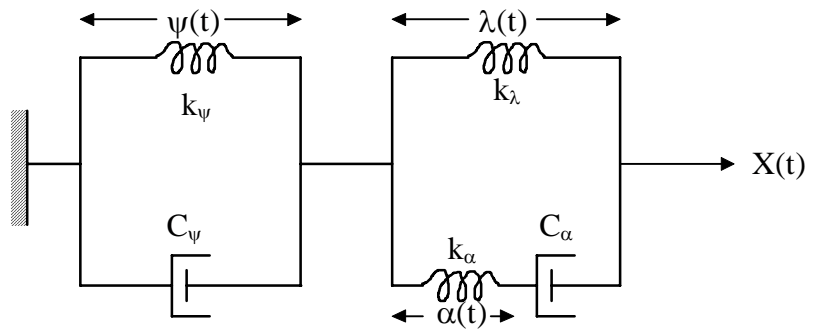


Figure 7.17: Mechanical model of a muscle filament

The output of the muscle spindle for the primary and the secondary endings can be presented in a function as follows:

$$H_1(s) = \frac{\lambda(s)}{X(s)} + \mu_\alpha \cdot \frac{\alpha(s)}{X(s)} \quad (7.1)$$

$$H_2(s) = \mu_\lambda \cdot \frac{\lambda(s)}{X(s)} \quad (7.2)$$

With the aid of the mechanical model it can be extended. Measurements on the filament of a cat (Poppele and Bowman) provided for example the following (Laplace) transfer functions.

$$H_1 = K \cdot \frac{s(s+44)}{s+0.04} \cdot H_t$$

$$H_2 = K_2 \cdot H_t \quad (7.3)$$

$$\text{With } H_t = \frac{(s+0.44)(s+11.3)}{s+0.816}$$

In here the constants have the values $K_1=10 \mu\text{m/sec}$ and $K_2=100 \mu\text{m/s}$.

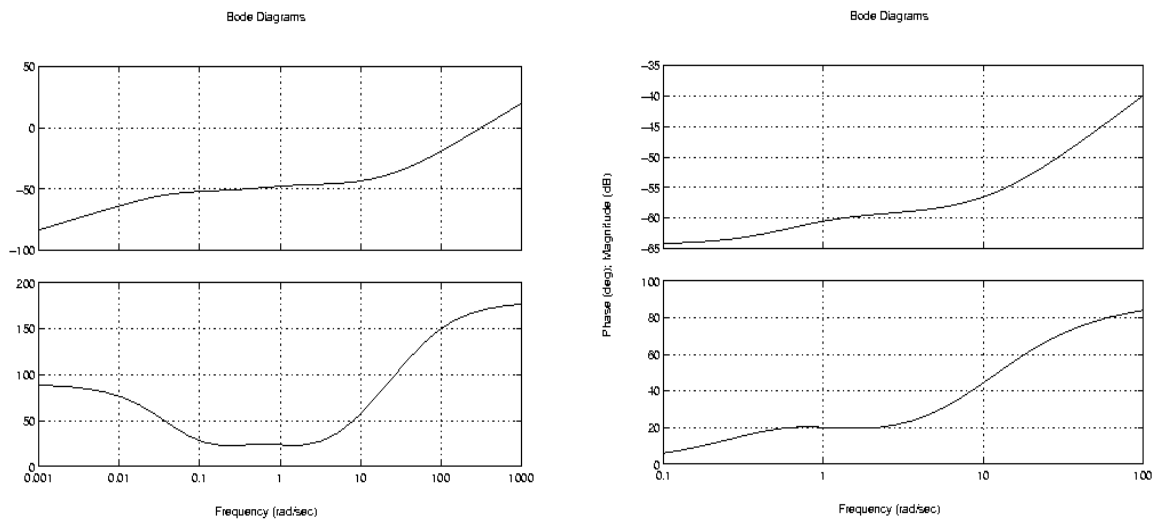


Figure 7.18: Bode plots for the muscle spindle transfer functions. The figure on the left is for the primary endings; on the right the bode plot for the secondary endings is given.

For an integrated model, transfer functions as described above are often too detailed. Important for good modeling, is to have a realistic time delay and a realistic noise level.

7.5.4 CONNECTIONS BETWEEN THE MUSCLE SENSORS AND THE CNS

In Figure 7.16, the connections between the Ia, Ib (Golgi) and II afferent sensory nerves and the CNS are shown. Multiple pathways of the sensory information through the CNS exist. The simplest path is the monosynaptic connection of the spindle information: The stretch reflex. If the muscle is stretched (e.g. by a hit on the knee tendon), the muscle spindle will fire and consequently the α -motor neuron will be excited and the muscle will contract: The well known knee tendon reflex. Less well known is the reciprocal inhibition. At the same time that the α -motor neuron of the agonist is excited, the antagonist is inhibited which will increase the effect of the stretch reflex. The stretch reflex is also called the short latency reflex. The latencies of this reflex loop are about 25 msec for shoulder muscles to about 50 msec for lower leg muscles.

The stretch reflex is a local reflex, only the muscles that are stretched are involved. In this respect, the muscle with monosynaptic reflex can be regarded as a 'reflexive muscle unit', in which much of the dynamic behavior results from the reflex. One important property is that the (apparent) stiffness and viscosity of the reflexive muscle unit increase far above the intrinsic muscle visco-elasticity that is beneficial especially for postural tasks. The input to the reflexive muscle unit is supra-spinal neural inputs originating from higher CNS levels.

In addition to the stretch reflex, reflexes that are more co-ordinated exist, involving higher levels of the CNS. Coordination at the joint level occurs presumably within one segment level in the spinal cord. At this level, an adequate response can be generated. For example, if the biceps muscle is stretched due to a pronation motion of the forearm, the stretch reflex will result in a supination motion, but also in an elbow flexion. However, a medium latency reflex (with latencies between 70 and 110 msec) will occur in the

biceps, but also in the triceps muscle. The triceps activity will generate an extending moment that counteracts the flexion moment of the biceps, and only the pronation motion will be counterbalanced by the biceps activity. The triceps was initially not stretched by the pronation motion, and received its sensory input from the muscle spindles of the biceps!

For coordination at a limb level, it is likely that more spinal levels are involved. These are called long latency reflexes, with latencies from 110 msec and up. Examples of these long latency reflexes are the withdrawing reflex when the hand touches a hot object. The sensory input originates from the skin sensors, not from muscle sensors, but a coordinated response will occur.

Sensory information is also important for adaptation of the internal representation of the environment. This internal representation, or internal model, is used as anticipation (feedforward control) to disturbance, which are going to occur. Using a feedforward control, faster and more appropriate reactions can be generated. An even more sophisticated use of sensory information is the learning of new motions.

7.6 The hearing

The hearing is important for humans, communication with other people and for orientation in the environment.

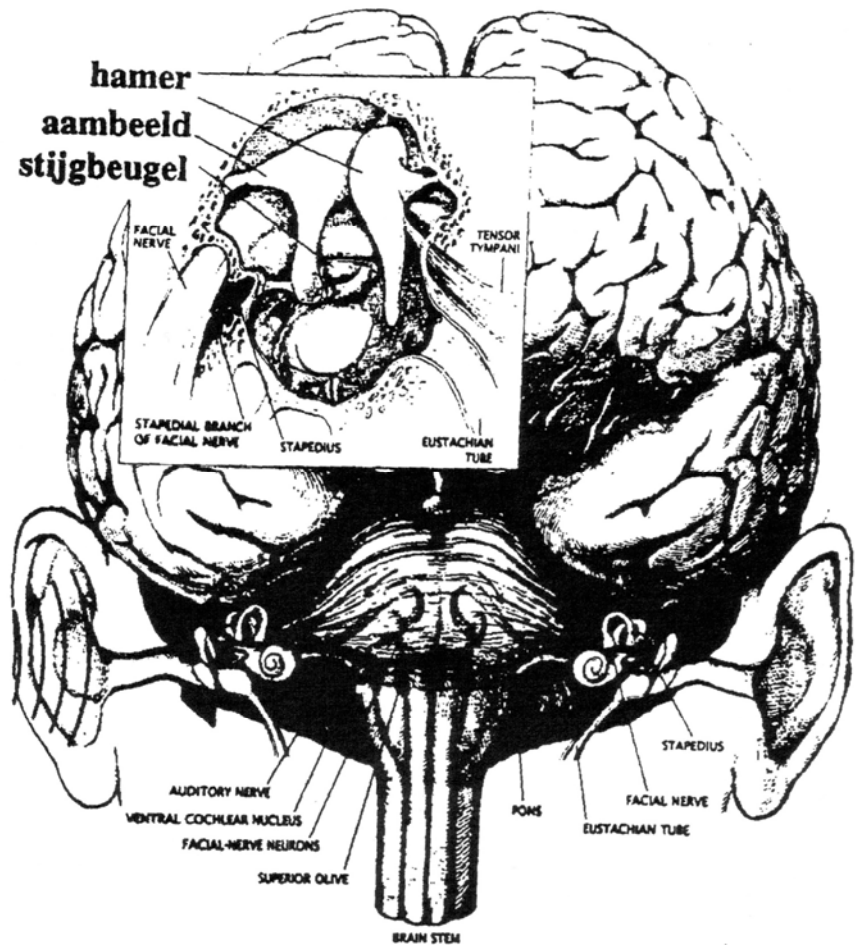


Figure 7.19: Anatomy of the human auditory organ

7.6.1 TONE AND INTENSITY

Figure 7.19 shows the position of the auditory organ in the head. The ear is a sensitive organ that transforms vibrations in the air (or another medium) into nerve pulses that are interpreted as sound. After passing through the ear shell and the outer auditory canal air vibrations do excite the eardrum. The eardrum is connected to three small bones, mallet (malleus), anvil (incus) and stirrup (stapes), which weigh 23, 27 and 2.5 grams respectively. The vibrations of the excited eardrum are transformed to a membrane in the oval window that is connected by the stirrup. By way of this mechanism vibrations with large amplitude and small pressure variation are converted into vibrations with small amplitude and large pressure variation. The leverage of the three bones causes the motions of the oval window to be about half of those of the eardrum. Besides this the area of the eardrum is about 50 to 90 mm² and that of the oval window about 3 to 4 mm². Without energy loss the pressure variations at the oval window would be about 30 to 50 times larger than that at the eardrum; in practice this is about 20 times for a great range of frequencies. The oval window causes a fluid to vibrate that flows through the cochlea, a snail-shell shaped organ. In the cochlea sensitive hair-cells are situated that are activated by the vibrations and send nerve pulses to the CNS.

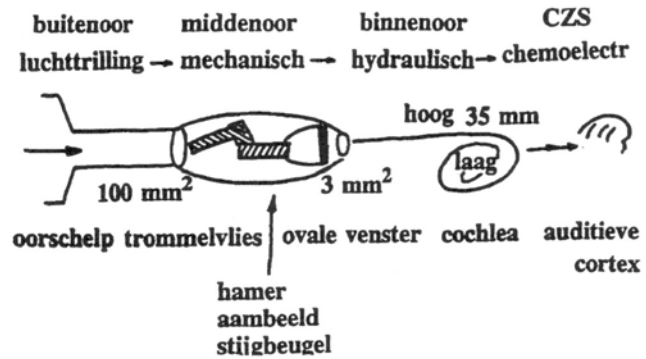


Figure 7.20: Transmission of vibrations in the ear

Summarized, the air vibrations are transformed to mechanical vibrations in the eardrum, mallet, anvil, stirrup and oval window. These mechanical vibrations cause hydraulic vibrations in the cochlea, which are transformed into nerve pulses by sensitive cells. The eardrum is stretched by a little muscle. If the amplitude of the air vibrations is large (loud sound), the muscle inhibits reflexively and the vibrations are transported weakened. With the same purpose the muscle pulls the stirrup a little loose from the oval window. Loud sounds are thus weakened (Figure 7.21). In order for the eardrum to function properly, the pressure at both sides should be the same. By way of the tube of Eustachius and the mouth cavity the inner ear is connected to the air outside. Swallowing causes the tube to open and makes the pressure in the inner and outer ear equal (again). If the tube of Eustachius is obstructed, this causes severe impairment to the hearing.

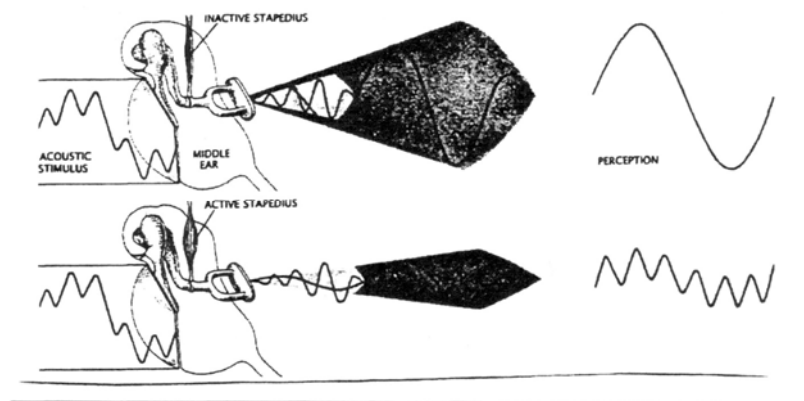


Figure 7.21: Protection of the ear against loud signals

In the cochlea an arriving and a departing tube are situated. Between these arriving and departing tube the basilar membrane is situated. The radius of the tube becomes smaller and smaller going in the direction of the center of the snail-shell (the apex). This construction causes high frequencies to be damped out faster than low frequencies. For this reason, close to the oval window the sensors are situated that mainly transmit information about high frequencies, while farther in the apex merely information about lower frequencies is present. In this way a kind of a frequency-analysis of incoming vibrations is performed,

and information is passed to the CNS about all components of the received sound. In the CNS these components are resembled, so that the sound is perceived as a whole. The different frequencies of the sound are perceived as pitches. The departing tube in the cochlea discharges into the middle ear, by way of the round window. Probably it serves to prevent reflection of the vibrations. The window width is determined by the frequencies that can still be perceived. The human ear can register frequencies in the range of 20 and 20,000 Hz. Aging leads to a decreased sensitivity for high tones. Often elderly people can only perceive frequencies up to 10,000 Hz. An optimum can be distinguished in the range of 150 and 8000 Hz. The range between 1000 and 3000 Hz is of major importance for the perception of speech.

Due to the large differences in intensity, it is usual to use a relative measure on a logarithmic scale, the decibel (dB). The decibel is defined as shown below:

$$NdB = 10 \log(E_2/E_1),$$

where

NdB = the number of decibels

E_2 = measured intensity of sound [W/m^2]

E_1 = standard intensity [W/m^2]

As reference intensity or standard intensity the sound threshold at 1000 Hz is chosen. On average this threshold lies at a sound pressure of $2 \cdot 10^{-5} W/m^2$ for well-hearing persons. In this way a logarithmic level scale is introduced, that uses the decibel as unit. In Table 7.3 the intensity is given of several sounds in daily life.

Table 7.3 Intensity of a number of sounds in daily life

Sound	dB
Whispering on 1 m distance	30
Conservation on 1 m distance	65
Drilling on 15 m distance	90
10 W sound installation on 1.2 m (max volume)	115
aeroplane on 50 m distance	120
pop concert	140
pain border	140

7.7 Tactile senses

7.7.1 TACTILE ORGANS

The skin forms the boundary between the human and his environment. The function of the skin is on the one hand to protect against influences from outside, like germs, unknown substances etc. On the other hand the skin also enables interaction between the inner part of the human and his direct environment.

A form of this interaction is the information exchange. In the skin sensoric nerve endings are situated, the receptors, that react to touch (mechanoreceptors), to cold and heat (thermo-receptors) and to pain (nociceptors). With regard to these receptors distinction is made between hairy and non-hairy skin.

The non-hairy skin

Like shown in Figure 7.23, the skin consists of two layers: the epidermis and the leathery skin (corium). The epidermis is the outer layer and protects the corium below it. The latter rather abruptly changes into the subcutaneous connective tissue on the inside (tela subcutanea). The receptive system is predominantly located in the corium.

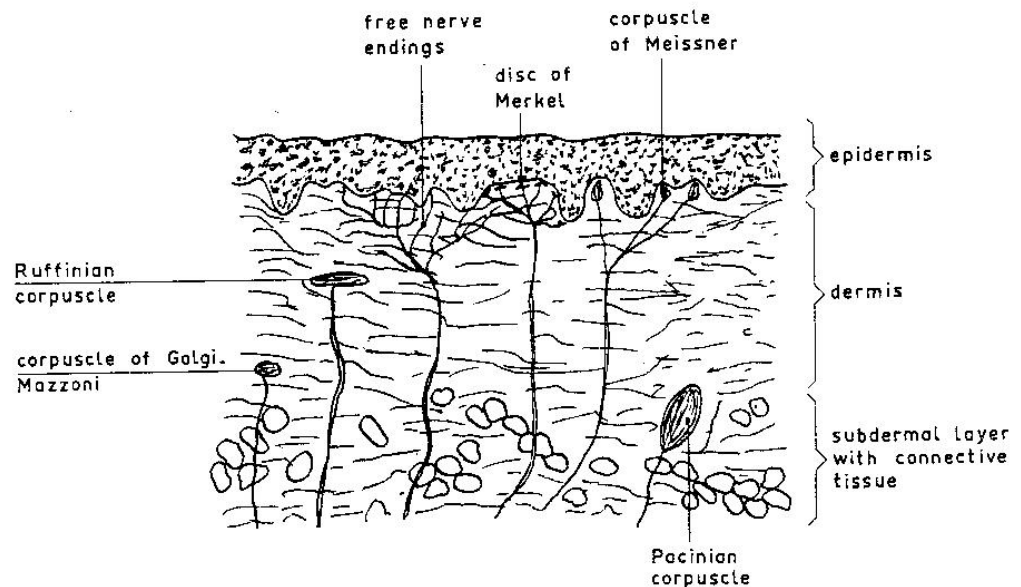


Figure 7.23: Cross-section of the non-hairy skin (Van Lunteren & Stassen, 1969)

In chronologic order of discovery the following receptors can be distinguished:

- The corpuscles of Pacini. These corpuscles are the largest; they have a length of about 2 to 3 mm. They are located rather deep in the skin; mostly in the transition of the corium into the subcutaneous connective tissue. It is assumed that these corpuscles react to light touch and small deformations (tactile sensory system).
- The corpuscles of Meissner. These corpuscles are located in small groups together just below the epidermis. As a result of this location they are outstanding tactile sensors.
- The corpuscles of Golgi-Mazzoni. These corpuscles usually are located at the boundary of the corium and the subcutaneous connective tissue. These mechano-receptors mainly react to large deformations and pressures (pressure sense).
- The disks of Merkel. These are located rather close below the surface of the skin and are therefore regarded as specific tactile receptors.
- The corpuscles of Ruffini. These corpuscles are usually located in the corium. Two kinds of these corpuscles can be distinguished, namely one that reacts to pressure stimuli and one that is sensitive to temperature.
- The free nerve-endings. These are the last branchings of the nerve fibers. They end completely free in the skin and are therefore not connected to some specific receptor. Their main task is probably the detection of pain. Besides that they also react to mechanical deformations and with this support the specific mechanoreceptors with the detection of deformations.

The receptor density is not equal at all sites of the body. Especially in the palm of the hand, in the finger tops and in the foot-sole they are numerous represented. This is understandable, because the hands and the feet are parts of the body with which man can find his way feeling. In the remaining parts of the non-hairy skin the receptors are present only scarcely. As an illustration the corpuscles of Meissner can be mentioned, of which the density in the finger top

is 23 per mm^2 , while on the lower arm on average only 1 per 36 mm^2 are situated; a proportion of 800:1. These areas with many sensors are represented in the cerebral cortex as relatively large areas where the incoming pulses are processed (Figure 7.24).

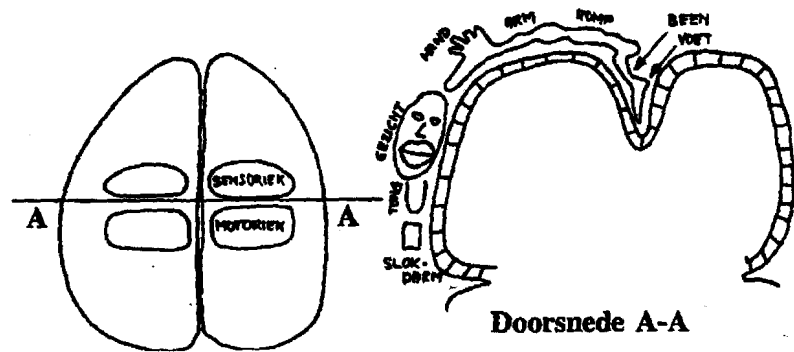
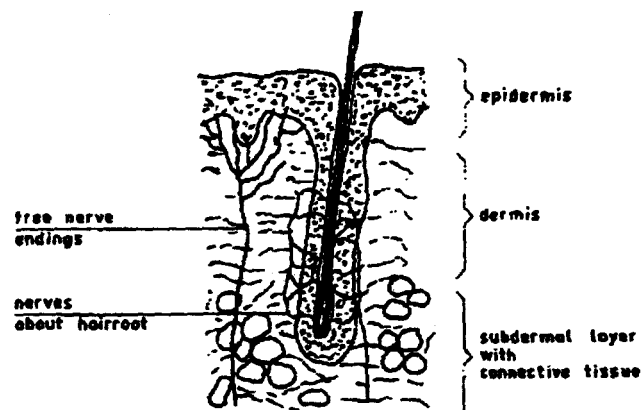


Figure 7.24: Representation of the sensors of the skin in the cerebral cortex

The hairy skin

Like shown in Figure 7.25, the hairy skin do have a similar structure as the non-hairy skin (Figure 7.23). The difference is in the underlying receptive system. Although the complete skin is basically sensitive to all stimuli, in the hairy skin (95% of our body surface) only tactile corpuscles of Merkel, free nerve-endings and nerves that rope off the hair roots like little baskets are present. This means that in combination these receptors can react to all stimuli.



7.25: Cross-section of the hairy skin (Van Lunteren & Stassen, 1969)

Although to each receptor a specific dominant feature is attributed, great uncertainty exists about the real influence of the different stimuli on these corpuscles. The nerve fibers that are connected to the receptors, can merge to one new fiber. This single fiber transports the signals from the different receptors at the same time and entangled. Then several receptors are connected to one afferent fiber. Also the opposite can occur: one receptor that is connected to several afferent fibers. As long as it is not possible to analyze the pattern of activity of all nerve fibers at the same time combined with psycho-physical perceptions, it is hardly possible to distinguish the specific features of the

different receptors. It can thus be put that with regard to the identity of the peripheral receptors for the sensibility of the skin not much is known (Van de Brink and Voorhoeve, 1984).

7.7.2 PERCEPTION WINDOWS

About the perception window of temperature sensors nothing is known. However, the perception window of tactile sensors is studied. In Figure 7.26 the frequency of a stimulus (window width) is plotted against the displacement of the skin caused by that stimulus (window height). It is remarkable that the threshold value behaves as an integrator. A certain power is necessary to cross the threshold value.

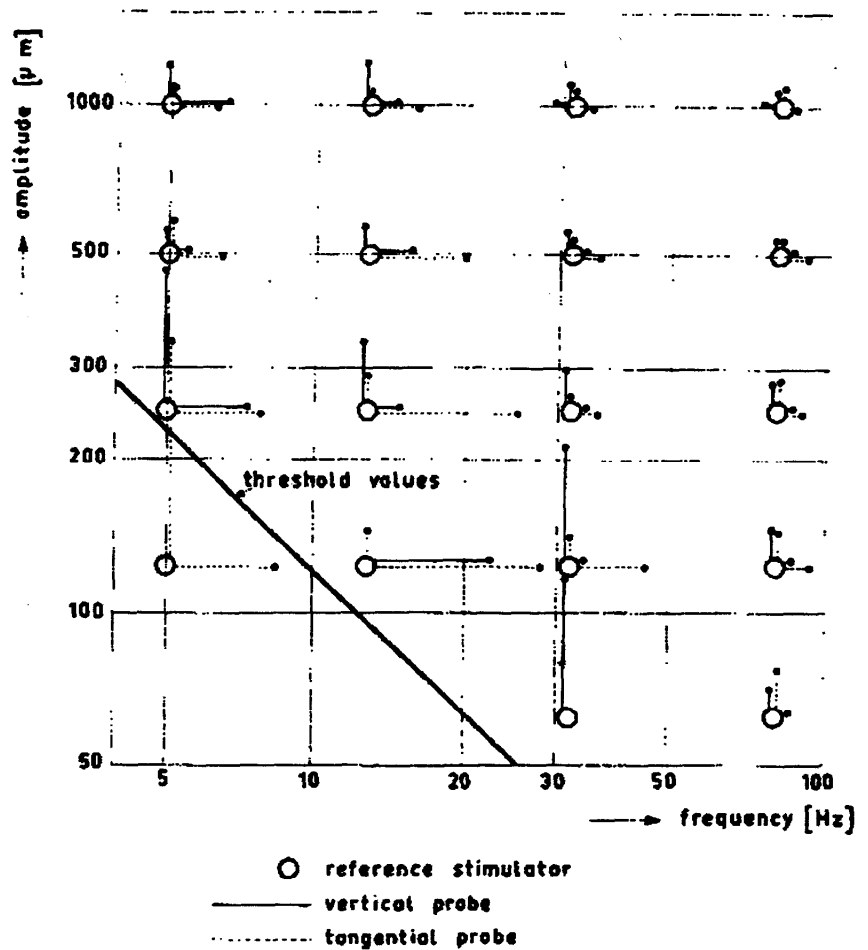


Figure 7.26: Perception window of the tactile sensors for mechanical vibrations on the inside of the lower arm (Van Lunteren & Stassen, 1969)

7.8 The visual system

The eye can be considered as the most versatile sensory system. Like no other sensory system man has the ability to voluntarily direct his attention with his eye. However, this ability of the eye to voluntarily direct attention (or focus point) only applies to the central field of view. The peripheral field of view mainly perceives visual information passively.

Active perception with other sensory systems is also possible, like for example with the tactile sense of our hands and the selectively direction sensitivity of listening.

The versatility of our visual system appears from the seeing of colors, the great ability to adapt to the intensity of light, the perception of movement of objects in our visual environment, the relative position of objects in space and the capacity to recognize patterns.

The eye itself is only a part of the visual system. The total visual system is made up of the eyeball, some parts of the brains and the oculomotor system.

In this chapter a number of the aspects of the visual system will be discussed that are of importance with regard to this course. Besides a general description of the eye attention will be paid to light sensitivity (wave length and intensity), sharpness of sight, color and sensitivity.

7.8.1 GENERAL DESCRIPTION

The eye ball lies loose in the eye socket and is supported by fat tissue. Six eye muscles keep the eye in its position and control the posture of the eye with relation to the eye socket. By means of the eye muscles rotations of the eye ball around three perpendicular axes are possible. The function of each of the three muscle pairs (consisting of a flexor and an extensor) in the rotation of the eye ball depends on the muscle pair and the position of the eye ball in the eye socket (Figure 7.27).

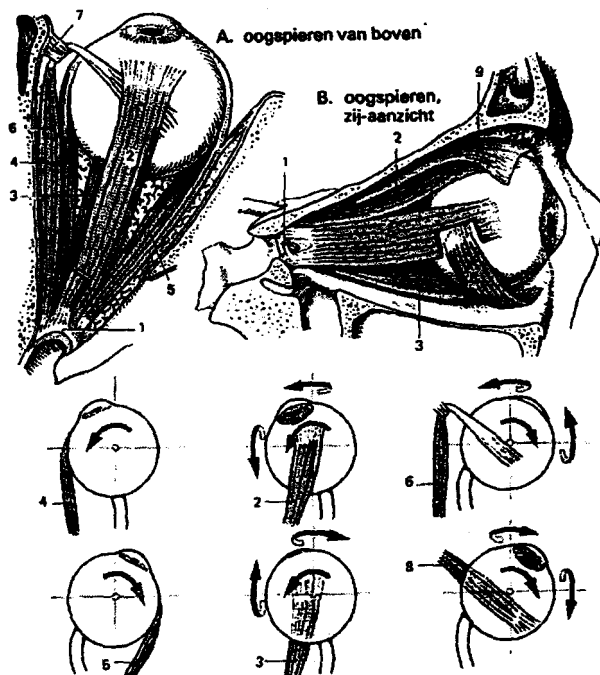


Figure 7.27: Eye socket and eye muscles

Five different eyeball movements are distinguished that strongly differ in origin and nature. The most important distinction is between eye movements for the tracking of a moving object (smooth pursuit) and reflexive eye movement for the stabilizing of the eyes during head movements. The saccadic eye movement, to point the attention fast from one object to another, is the fastest movement (max. 700 deg./sec). This high rotation velocity is possible because of the small

inertia of the eye and the relatively strong eye muscles. Different eye movements

When the light enters the eye, it passes successively the cornea, the anterior chamber (aqueous humor), the iris, the lens, the vitreous body (vitreous humor) and the retina (Figure 7.28). The cornea and the lens together take care of the refraction of the light, in order to get a sharp image on the retina. The cornea functions as the fixed lens and the deformable eye-lens, which functions as a variable lens.

The retina contains light-sensitive photoreceptors, the cones and the rods (Figure 7.29). The nerve fibers that connect the photoreceptors to the brain are situated on the inside of the retina and pass through the retina at the blind spot. In Figure 7.29 the light comes from above and has to pass through several layers of cells before it reaches the light-sensitive cells. The axis of symmetry off the eyeball differs slightly from the visual axis or the line that connects the fixation point with the fovea, the most sensitive central part of the retina.

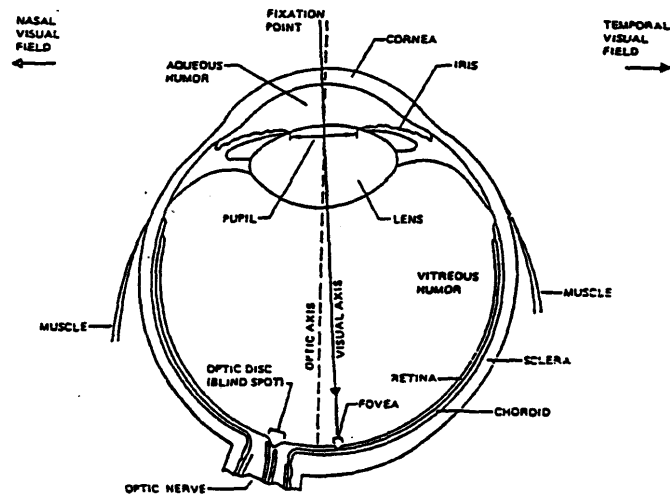


Figure 7.28: Horizontal cross-section of the right eye

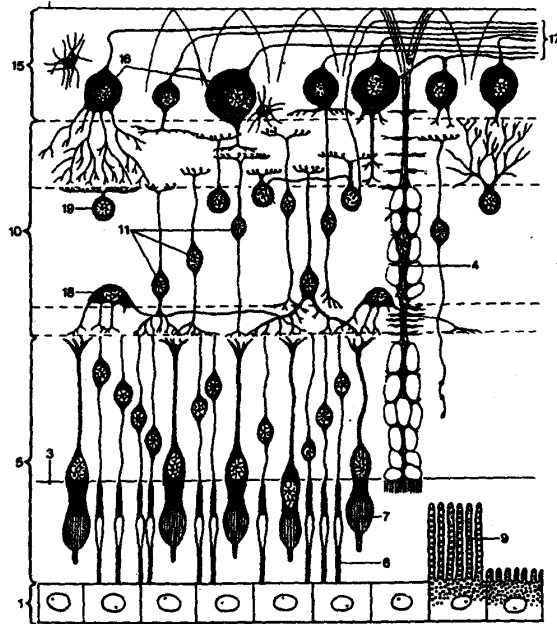


Figure 7.29: Scheme of the structure of the retina. The retina is constructed of several layers of nerve cells (neurons) and receptors: 16) the ganglion cells, 11) the bi-polar cells, 18) and 19) the horizontal and amacrine cells, 6) and 7) the light sensitive cells, the rods and the cones. The light comes from upside and has to penetrate the layers above the light sensitive cells

Optical stimuli from the left part of the field of view are projected in both eyes on the right half of the retina as a result of the optical properties of the lens. From the right part of the retina nerve fibers lead via the optic chiasm (chiasma opticum) to the right lateral geniculate nucleus (corpus geniculatum laterale). From the lateral geniculate nucleus the signals are transmitted to the visual cortex at the right dorsal side of the brains (Figure 7.30).

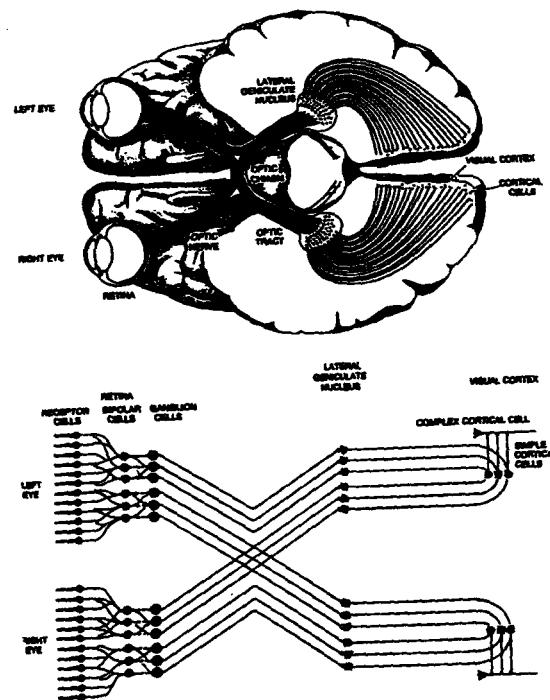


Figure 7.30: Anatomy of binocular vision

The transmission of signals from cell to cell takes place by means of the synapses. As a result of the properties of the different neurons, the structure of the connections, the activation of the synapses, etc. there exist a considerable number of vertical and transverse connections in the retina. This network is responsible for the first reduction of data and for the first phase of the processing of visual stimuli.

The cones are sensible to color while the rods are not. The cones primarily function in daylight and the rods in low light intensity conditions, like at night. In the fovea, the central part of the retina, only cones are present that lies very close together. Outside the fovea the density of cones decreases and that of the rods increases. The diameter of the fovea is approximately 0.3 mm, which corresponds to a view angle of one degree

At the fovea about as many nerve fibers leave the retina, as cones are present there. This does not mean that every cone corresponds to one specific fiber. In the periphery a much smaller number of fibers leaves the retina than rods or cones are present there. This means that a large reduction of data takes place in the retina. In total 130 million receptors converge to 1 million nerve fibers.

Besides the difference in location of cones and rods and the difference in colour sensitivity, there is a difference in sensitivity for the intensity of light. Rods are so sensitive that they are overburdened by daylight. Under normal daylight conditions the cones play the dominant role in seeing. Below the threshold value of the cones the vision is called scotopic. Above the saturation of the rods vision is called photopic. In the area in-between where both cones and rods are active the vision is called mesopic. A neural process controls the light sensitivity. The response time of this process is four times faster for the cones than for the rods. The opening of the iris, the pupil, plays a supplementary role in the control of the light intensity on the retina.

When we move from light to dark, the cones and rods will adapt to the new light

intensity. The first 7 to 8 minutes then the cones are more sensitive than the rods. After that the rods keep adapting for about 25 minutes by which the threshold value for light intensity is lowered even further.

7.8.2 SEEING COLOURS

The wavelength of visible light lies between 400 and 750 nanometer. Light with a larger wavelength, near infrared, is poorly absorbed by the color pigment in the light sensitive cells. Light with a shorter wavelength, near ultraviolet, can be absorbed by the color pigment, but does not reach the retina because it is absorbed by the cornea and the lens. The most sensitive wavelengths of the three kinds of cones are 430 (blue), 535 (green) and 570 (red) nanometer (Figure 7.31). Seeing color is accomplished by the interpretation of the combined effect of the reflected light by the object on the three different cone systems.

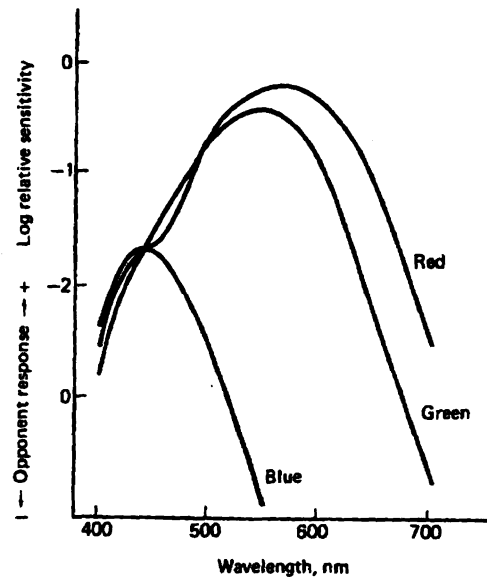


Figure 7.31: The absorption-spectra of the three color system of a test person with normal color perception

Why are three different types of light sensitive cells, with different sensitivity, needed for the perception of color? A colored object will partly absorb and partly reflect the light that falls on it. A red surface will reflect light with a wavelength of about 570 nm and absorb light with other wavelengths.

Imagine that only one type of light sensitive sensor would be present in the retina (Figure 7.32 A). Such a sensor will give the same neural output for different combinations of light intensity and wavelength. Such a system is for that reason color-blind, because it is not able to distinguish the different wavelengths (colors) of the detected light. This situation arises at night. At a low light intensity only the rods are able to detect variations in light intensity. Then only type of sensor is active. As a result we can only distinguish light intensity, gray-shades. When two objects reflect different wavelengths but result in the same receptor response, they cannot be distinguished from each other. Such a visual system we call achromatic.

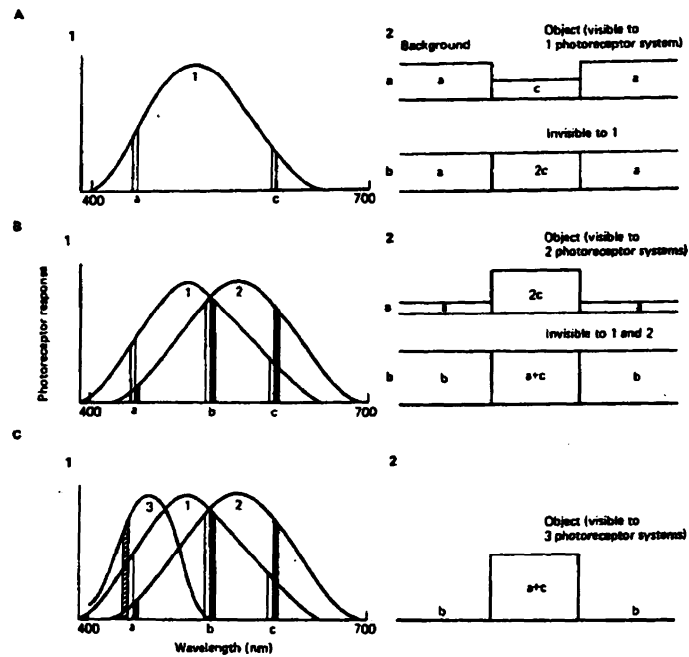


Figure 7.32: The response of an achromatic (A), dichromatic (B) and a trichromatic (C) system to objects with different color. An achromatic system is not able to distinguish combinations of light with different wavelengths (colors) that have a different intensity, like e.g. a and $2c$. No color can be perceived, only grayscales. A dichromatic system can not distinguish certain combinations of colors, e.g. $a + c$ and b : color can be distinguished to a restricted extent. A trichromatic system is able to perceive nearly every combination of colors.

The drawbacks of such a visual system can be removed for a considerable part by a system with two types of light sensitive sensors, sensible to two different wavelengths (Figure 7.32 B). Such a dichromatic visual system was possibly the first evolutionary step in seeing color. In most cases such a system will be able to discriminate an object from its background, because the responses of the two sensors, each with different light absorption properties, to the reflected light from the object and the background will differ. However, combinations of colors exist for which the detected light intensity by both sensors from the object and its background do show no difference. In this case the difference in color is not discriminated. In certain cases of color-blindness, dichromacy, the concerned person cannot discriminate between the colors red and green.

A visual system with three different types of light sensitive sensors, trichromatic, can considerably improve the detection capacity of a dichromatic system (Figure 7.32 C).

There exist a few kinds of birds with a tetrachromatic visual system. The evolution shows that this further expansion of the receptor system has not produced many extra advantages.

With the trichromatic visual system it is still possible that an isolated object with a certain color under lighting with a specific spectral density reflects the same light as an object with a different color under lighting with a different spectral density. In practice however, we do not see objects isolated, but in an

environment. In the processing of visual information the mutual proportions of the different colors of objects, are restored (color constancy), in spite of the spectral properties of the environmental light,.

7.8.3 A SIMPLIFIED MODEL OF MOTION PERCEPTION OF THE VISUAL SYSTEM

An important measure that is obtained by the visual system is the relative motion of gaze relative to the world. A schematic description of motion detection is given by Hosman. He uses the 'bilocal' motion detector to discuss some modeling features. This detector will be activated if a moving image stimulates two receptive fields F1 and F2 (Figure 7.33) by a time delay τ that coincides with the specific time delay τ_1 of the detector. In this way a detector is

only sensitive for the specific velocity V given by $V = \frac{S}{\tau_1}$, where S is the span

of the motion detector and V the stimulus velocity. The receptive fields on the retina are connected to a large number of these motion detectors, each sensitive for a specific direction and magnitude. In this way, perception of movement in the whole visual field is possible. Based on the conclusion of other authors, Hosman states that the time delay τ_1 has a constant value of approximately 65 ms for higher velocities and increases with the inverse of the velocity to a maximum of 1-5 seconds for lower velocities. The critical velocity that divides these two groups cannot be given precisely.

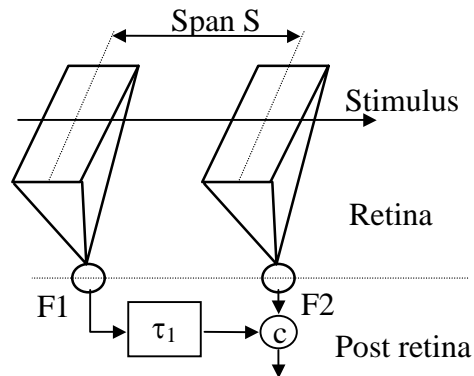


Figure 7.33: Motion detector [10]. The specific time delay τ_1 makes the detector only sensitive for one specific velocity.

When the visual information has passed the detectors, it is further delayed between the retina and the visual cortex and by the processing time needed for the perception of motion. This delay is denoted as τ_2 and provides together with τ_1 the transfer function for the stimulus velocity and perceived velocity. The gain, K , is normally assumed to be equal to 1 [10].

$$H_{velocity} = Ke^{-j\omega(\tau_1 + \tau_2)} \quad (7.4)$$

The time delay τ_2 cannot be measured directly.

Borah et al. [11] state that the visual self-motion sensation is roughly proportional to the velocity of the background peripheral visual field up to a saturation level. Circularvection and linearvection saturation levels are probably dependent on the characteristics of the visual field, but have been estimated at about 60 deg/sec and 1 m/sec, respectively'.

7.9 The vestibular organ

The organ of equilibrium, or the vestibular system, is situated in the inner ear and is sensitive to specific force and rotation acceleration, see Figure 7.34. The name “organ of equilibrium” already indicates the most important function of this organ; the maintaining of balance of our body during movement in the three-dimensional space. The maintaining of the equilibrium is essential for us humans, who are bipeds. A second, at least as important function of the organ of equilibrium is the stabilizing of the eyes during movement of the head.

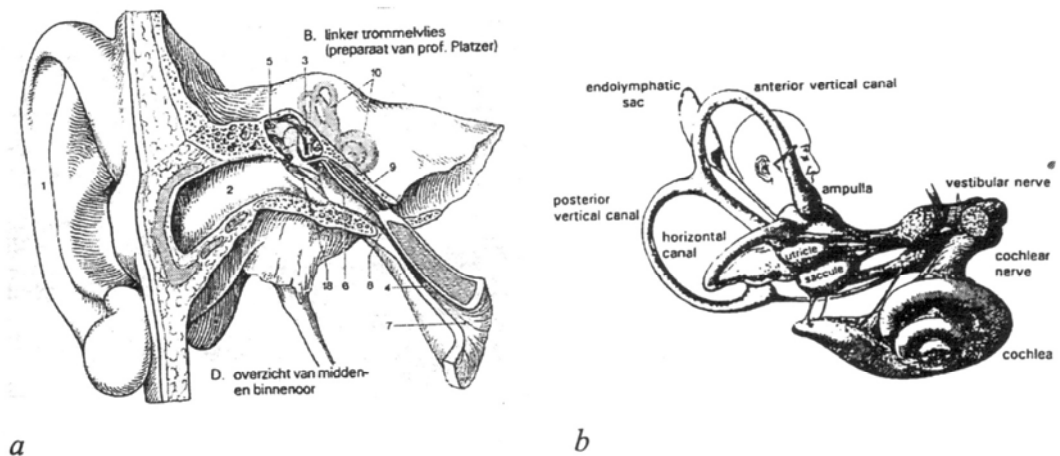


Figure 7.34: *a. overview of the middle and inner ear with the organ of equilibrium. b. The organ of equilibrium with the snail shell.*

For the discussion of the static and dynamical properties of the organ of equilibrium in this course a coordinate system will be used that has a fixed position in relation to the head, Figure 7.35. The origin lies in the plane of symmetry on the connection line between the start of both auditory canals. The X-axis lies in the symmetry plane of the head and is perpendicular to the vertical axis of the body, positive direction forward. The Y-axis is perpendicular to the plane of symmetry and has its positive direction to the right. The Z-axis is perpendicular to the XY-plane, with a positive direction downwards.

The organ of equilibrium consists of three semicircular shaped canals and the otoliths, the sacculus and the utricle. They are situated in the inner ear. The semicircular shaped canals are sensitive to rotational acceleration, while the otoliths are sensitive to specific force.

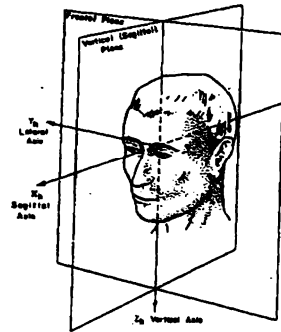


Figure 7.35: The coordinate system for the head

The specific force A is defined as the external force that acts onto an object per unit mass. Specific force has direction and magnitude and has the dimension of linear acceleration (m/s^2). In a gravitational field the acceleration a is determined by the vectorial sum of the measured specific force A and the gravitation g .

$$a = A + g \quad (7.5)$$

7.9.1 THE SEMICIRCULAR CANALS

The three semicircular canals are nearly perpendicular to each other and together constitutes measuring device that is sensitive to rotational acceleration with respect to the space. The canals themselves form about two-third of a circle and have as a collective basis, the utricle. The diameter of the canals is about 6 mm and the wall thickness of the canals is about 0.2 mm, Figure 7.36.

The canals are filled up with a liquid, the endo-lymph, and are sealed by the cupula in the ampulla, a local swelling of the canal, see Figure 7.37. The cupula consists of a jelly-like material and is founded on the crista. In the crista hair cells are located of which the hairs (ciliae) do extend into the cupula. The response of the endolymph to a rotational acceleration (vector of rotation perpendicular to the plane of the canal) will show a phase lag due to inertia. Since the canal is sealed with the cupula, a difference in pressure will arise over the cupula that causes it to bend. Thus, the deflection of the cupula is a direct result of the input angular acceleration.

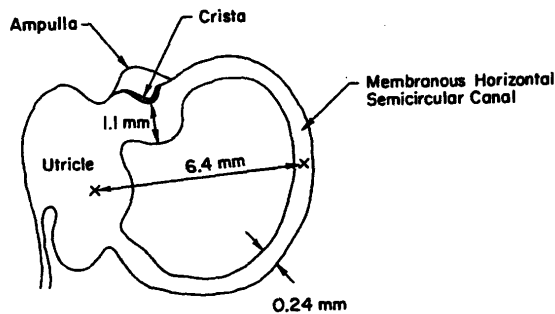


Figure 7.36: Sizes of the semicircular canal

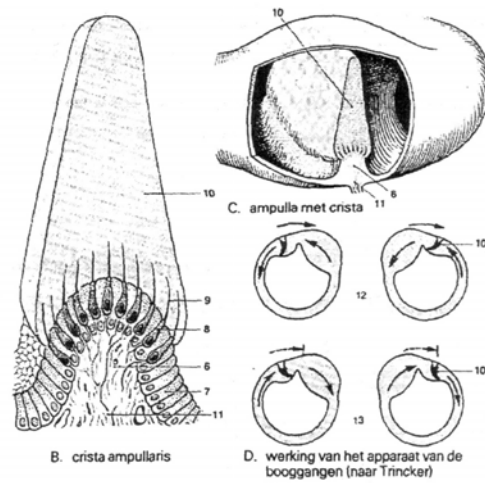


Figure 7.37: The ampulla and the crista

The hair cells in the crista, about 3000, are sensitive to the deflection of the cupula and the ciliae. The hair cells have two types of ciliae, the stereociliae and the kinociliae, see Figure 7.38. Every hair cell has several stereociliae (about 70), but only one kinocilium. The position of the kinocilium with respect to the stereociliae determines the sensitive direction of the haircell. Every hair cell transfers, using one or more synapses, information to an afferent neuron in the vestibular or eighth nerve. These afferent neurons are bipolar ganglion cells that transfer a stimulus of the hair cell to the brain stem. Bending of the stereociliae towards the kinocilium increases the impulse frequency of the afferent neuron and vice versa. The hair cells in the crista all have the same polarisation.

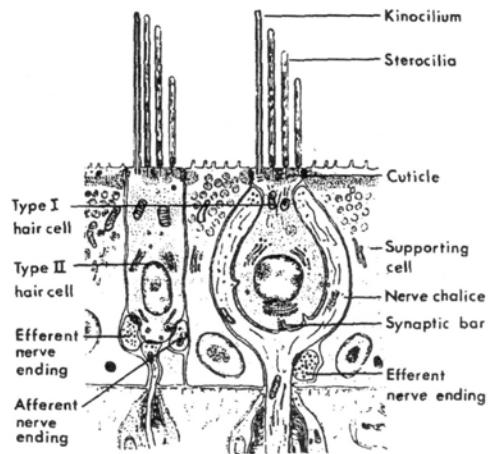


Figure 7.38: Type I and type II hair cells

Two types of hair cells do exist in the vestibular organ that essentially differ in construction and properties, the type I and the type II cell. The relation between the output signal of the afferent neuron and the deflection of the ciliae differ for the two types of hair cells.

Before the dynamical properties of the semicircular canals and the conversion of

the deflection of the cupula into an afferent signal will be discussed, we first discuss the otoliths.

7.9.2 THE OTOLITHS

In the utricle and the sacculus, cavities filled with endolymph, the otoliths are situated, which consist of a jelly-like layer with little calcium-carbonate stones in it. This layer is supported by the macula that contains sensitive hair cells or receptor cells, Figure 7.39. The hairs or ciliae of the receptor cells extend to this jelly-like layer. If a specific force occurs, parallel to the macula, then the otolith stones (specific mass about 2.7) will apply a shear force to the jelly-like layer. As a result the ciliae of the hair cells deflect. The hair cells in the macula each have their own sensitive direction. The polarization of the hair cells changes gradually over the surface of the macula.

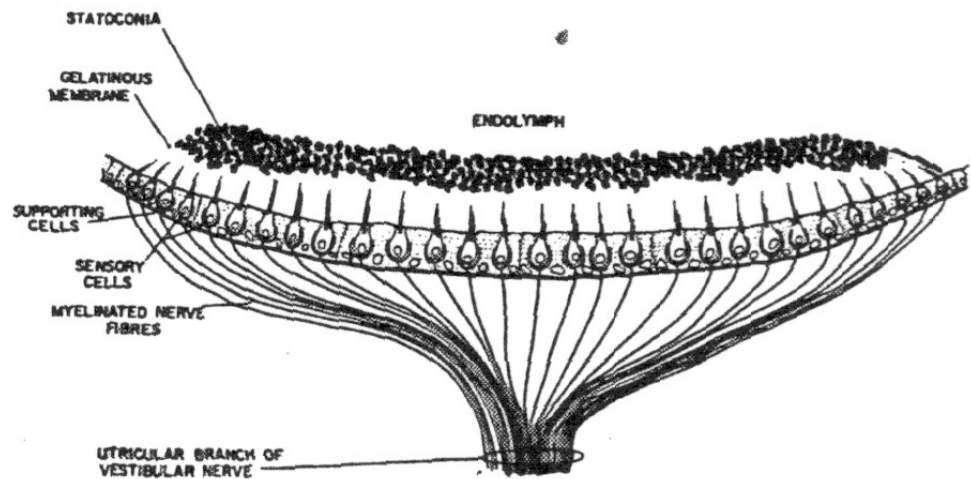


Figure 7.39 The macula with the hair cells and the otoliths

On the borderline, the striola, the polarization makes a 180 degree turn, Figure 7.40.

At both sides of the head the otoliths are situated in such a way that the sensitive directions of the receptor cells in the utriculi lie mainly in the horizontal plane and in the saculi they mainly lie in the vertical plane. In this way the specific force can be perceived in all three orthogonal axes. In the sensory epithelium of the macula the same types of hair cells as in the crista exist; i.e. type I and type II.

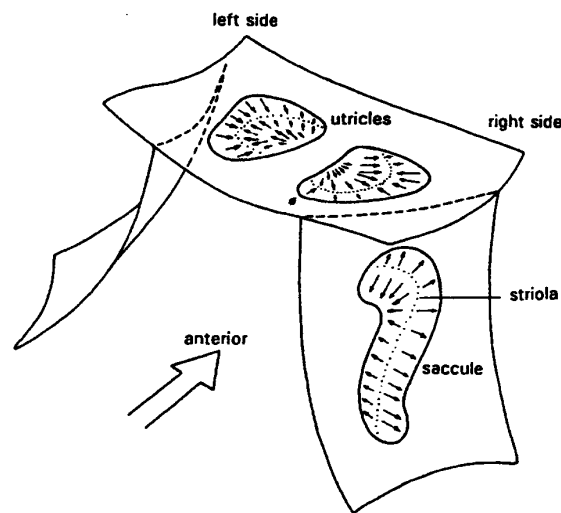


Figure 7.40 The sensitive direction of the hair cells in the utricle and saccule

7.9.3 TRANSITION OF THE STIMULUS INTO AFFERENT SIGNAL

As indicated above, in the crista and in the macula two types of hair cells occur. The cell body of these hair cells differs in shape and in the contact with the primary or afferent neuron. The cell body of the type I cell is spherical shaped, and is fully enclosed by one nerve cup that is made up of a thick nerve fiber. The upper part of this nerve cup can be considered as the actual synapse with the hair cell. The impulse frequency of the afferent neuron is irregular of character and is correlated to the deflection of the ciliae of the hair cell and the first derivative of the deflection. Cells that are sensitive to the first derivative of the deflection or displacement also occur in the muscle spindle and in the pressure receptors in the skin. The type II cell has a cylindrical shaped cell body that contacts the thin nerve fibers. The dendrites of afferent ganglion cells contact several type II cells by means of small synapses. This possibly causes the impulse frequency of these afferent cells to be regular of character. The change of impulse frequency is correlated only to the deflection of the ciliae of the hair cell.

7.9.4 MODELING OF THE DYNAMICAL BEHAVIOUR OF THE VESTIBULAR ORGAN

In the description of the dynamical behavior of a system usually a transfer function is used. To be able to determine the parameters of the transfer function, a model and measurements of the in- and output signal are needed. On the basis of the preceding description of the semicircular canals and the otoliths, several researchers formulated models. Depending on the equipment that was available to generate input signals for the vestibular organ and the available techniques to measure the output signal, the researchers succeeded in identifying the model parameters. The result of the parameter identification is mainly determined by the chosen method. This method strongly depends on which signal, related to the output signal of the organ of equilibrium, is used. The following four methods are important:

- Subjective response of the test person to carefully chosen vestibular input signals.
- Measurement of the slow nystagmus movement of the eyeball as a result of a vestibular input signal, see Chapter 9.

- Determination of the threshold value for motion perception as a function of the frequency of the input signal.
- Measurement of the response of afferent neurons in the vestibular nerve to vestibular input signals (not in humans but in monkeys).

The first three methods have as a major drawback that the output signal of the organ of equilibrium is not directly measured but only indirectly. An advantage is however that these methods can be performed with humans. The last method gives the most direct and reliable result, but can, until now, not be applied to a human or an animal without permanent damage to the vestibular organ. At the faculty of aerospace engineering (Hosman and Van der Vaart, 1978, De Boer, 1988) in the 1970's and 1980's the threshold values for stimulus angular acceleration around the X- and Y-axis and linear acceleration along the Z-axis are successfully determined using a flight simulator.

7.9.4.1 Dynamical model for the semicircular canal

As a result of the mass of the endolymph and the cupula, the viscous damping and the stiffness of the cupula, there is a dynamical relationship between the input rotational acceleration and the deflection of the cupula. A model for the dynamical properties of a well-damped torsion-pendulum model is first described by Steinhausen (1931). The parameters were first defined by Van Egmond et al. (1949) in Utrecht. The angular displacement of the endolymph $\xi(t)$ was related to the input angular acceleration $\alpha(t)$ by the differential equation:

$$\theta \frac{d^2 \xi(t)}{dt^2} + \pi \frac{d\xi(t)}{dt} + \Delta \xi(t) = \theta \alpha(t) \quad (7.6)$$

Where:

θ = the moment of inertia of the endolymph

π = the viscous damping of the endolymph in the canal

Δ = the stiffness of the cupula

Because the deflection of the cupula is approximately proportional to the angular displacement of the endolymph, the transfer ratio between the cupula deflection $\zeta(\omega)$ and the input angular acceleration $\alpha(\omega)$ can be formulated as:

$$\frac{\zeta(\omega)}{\alpha(\omega)} = \frac{K}{(1 + j\omega\tau_1)(1 + j\omega\tau_2)} \quad (7.7)$$

Here, $\tau_1 \approx 10$ s and $\tau_2 \approx 0.1$ s. These parameter values were determined on the basis of the subjective response of trained test persons to carefully chosen input signals with a turning chair and a torsion-pendulum. See for the Bode diagram Figure 7.41.

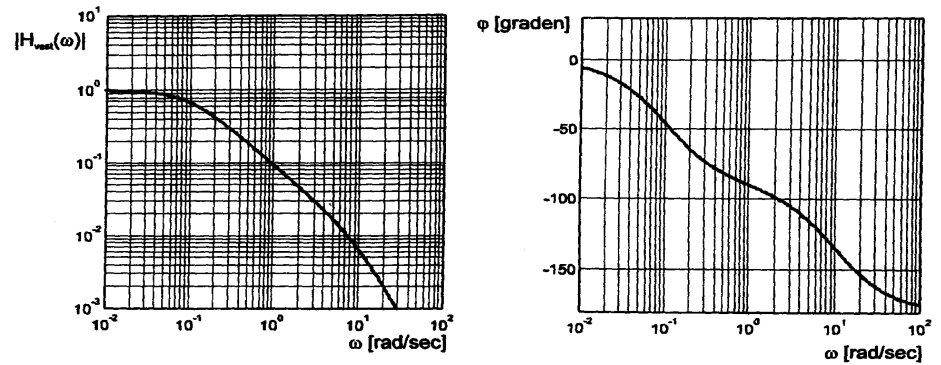


Figure 7.41: Transfer function between the input angular acceleration and the deflection of the cupula, Equation 7.7

After the improvement of the experimental techniques it appeared that the perception of rotation could no longer be described only by the deflection of the cupula. Adaptation was demonstrated as a result of prolonged rotational acceleration and was also found in research to the vestibulo-ocular reflex. Several researchers came to expand the model with the term:

$$H_a(\omega) = \frac{j\omega\tau_a}{(1 + j\omega\tau_a)} \quad (7.8)$$

Here the adaptation time constant $\tau_a = 80$ s.

Fernandez and Goldberg (1971) succeeded in measuring the response of primary neurons in the vestibular nerve of monkeys. They formulated a model that besides the dynamical properties of the semicircular canal also describes the collective influence of the type I and type II cells on the afferent response:

$$H_{SCC}(\omega) = \frac{j\omega\tau_a}{(1 + j\omega\tau_a)} \cdot \frac{K(1 + j\omega\tau_L)}{(1 + j\omega\tau_1)(1 + j\omega\tau_2)} \quad (7.9)$$

The transfer function $H_{SCC}(\omega)$ describes the relationship between the stimulus angular acceleration and the output in impulses per second. Here the time constant τ_L describes the influence of the type I cells that, after all, are sensitive to the first derivative of the deflection of the cupula. Fernandez and Goldberg estimated $\tau_L = 0.49$ s for the monkeys.

It appears that the break-point in the transfer function associated with τ_2 lies at such a high frequency that this time constant can not be determined from measurements. τ_2 has been estimated at 0.005 by Steer from the dimensions of the canals and the viscous properties of the endolymph. A good approximation for τ_L and τ_1 for humans could be obtained using the flight simulator of the faculty of Aerospace Engineering. The values are $\tau_L \approx 0.11$ s and $\tau_1 \approx 5.92$ s.

The Bode diagram of the transfer function is given in Figure 7.42. From this figure appears that the dynamical properties of canals for stimulus rotational acceleration over a wide range of frequencies (0.1 – 10 rad/s) globally equal that of an integrator. The output signal in the mentioned frequency range is most correlated to the rotational velocity. However, from the Bode diagram appears that the output signal leads the rotational acceleration. The rotational velocity lags the rotational acceleration by 90° , while the afferent signal lags by a

maximum of 70° . Outside the mentioned frequency area, at low and high frequencies, the afferent signal has a different meaning. More attention will be paid to this in the discussion of the visual-vestibular interactions.

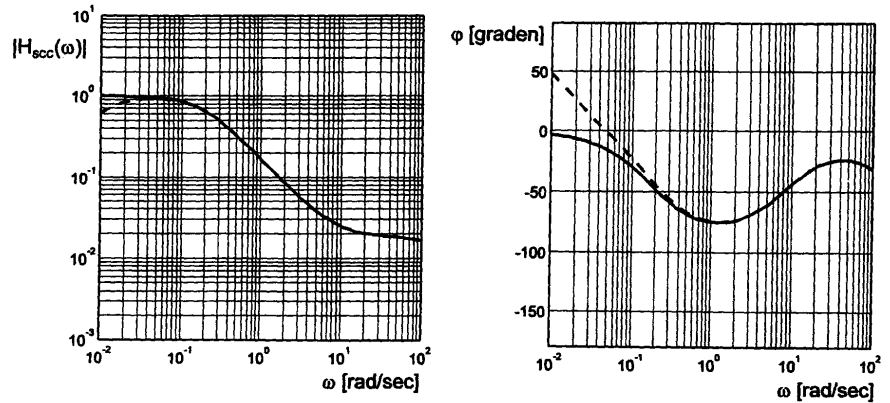


Figure 7.42: Bode diagram of the transfer ratio of the semicircular canals, Equation 7.9. The dotted line includes the adaptation term

7.9.4.2 Dynamical model of the otoliths

On the basis of the construction of the otoliths the dynamical model is an acceleration meter or mass spring damper system, which can be described by the differential equation:

$$m\ddot{x}_o(t) + r\dot{x}_o(t) + kx_o(t) = \ddot{x}_h(t) \quad (7.10)$$

where:

m = the mass of the otoliths

r = the viscous damping

k = the spring stiffness

x_o = the displacement of the otoliths with respect to the macula

x_h = the displacement of the head

Such a system has a transfer function equal to that of the Steinhausen model:

$$H_{oto}(\omega) = \frac{K}{(1 + j\omega\tau_1)(1 + j\omega\tau_2)} \quad (7.11)$$

Researchers have had great difficulties to identify the parameters of this model. The major reason for this is the lack of appropriate equipment to generate the necessary stimulus, linear acceleration. The counterparts of the torsion pendulum and the turning chair are the parallel swing and the sled (platform that is moved along a high quality transmission with a controlled acceleration). Of great importance in such installations is a very low level of acceleration noise and a sufficiently large stroke of the sled.

Because of different reasons several researchers conclude that the numerator of Equation 7.18 should be expanded with a first order term that describes the neural process of the type I cells. About the magnitude of the time constants the researchers were not able to reach an agreement. In 1976 Goldberg and Fernandez published a research about the otoliths of the monkeys, where they

applied the same technique as in the research about the semicircular canals. The form they chose for the transfer function gave the best agreement with the measured transfer ratio and gives the relationship between the input specific force and the output impulse frequency:

$$H(\omega) = K \frac{(1 + j\omega K_a \tau_a)}{(1 + j\omega \tau_a)} \cdot \frac{(1 + K_v (j\omega \tau_v)^{K_v})}{(1 + j\omega \tau_m)} \quad (7.12)$$

Here the first term is the adaptation term and the denominator of the second term is a simplification of the second order description of the mass spring damper system. The numerator of the second term is a velocity dependent term that is caused by the type I cells in the transition of the deflection of the ciliae of the receptor cells. How the fractioned power in the numerator of the second term of Equation 7.19 should be explained physically is still unclear. Goldberg and Fernandez present the time constants and the gains for the type I as well as for the type II cells, Table 7.4. A transfer ratio that is practical to work with and gives a good approximation is:

$$H(\omega) = K \frac{(1 + j\omega \tau_n)}{(1 + j\omega \tau_1)(1 + j\omega \tau_2)} \quad (7.13)$$

where: $\tau_n = 1$ s, $\tau_1 = 0.5$ s, and $\tau_2 = 0.016$ s. The Bode diagram of this transfer function is presented in Figure 7.43.

Table 7.4 Time constants and gains of the transfer functions of the otoliths resulting from the type I and type II cells

Cell type	K	K_a	τ_a (s)	K_v	τ_v (s)	τ_m (s)
I	20.5	1.9	101	0.44	40	0.009
II	25.6	1.12	69	0.188	40	0.016

Goldberg and Fernandez also have measured the static output of the afferent cells as a function of the stimulus specific force. From Figure 7.44 the non-linear course of this relation appears clearly. At a negative specific force of -1 à -2 g as well as at a positive force of 3 à 4 g saturation occurs.

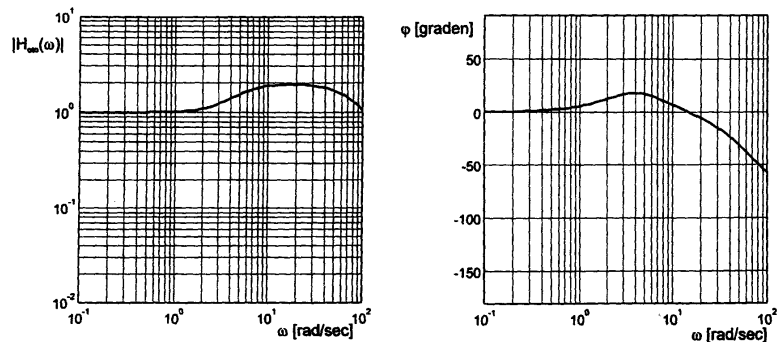


Figure 7.43 Transfer ratio of the otoliths, Equation 7.13

7.9.5 THE PERCEPTION WINDOW OF THE VESTIBULAR ORGAN

The perception window of the organ of equilibrium is determined by the lower limit of the perceivable stimulus rotation or linear acceleration and the upper

limit of the maximum perceivable acceleration.

The lower limit is the threshold value. This is found by determining the amplitude of a sine-shaped stimulus acceleration that is just perceivable, using test persons. As a result of the dynamical properties of the semicircular canals and the otoliths the threshold value depends on the frequency of the stimulus. The threshold value is similar to the minimum perceivable contrast in the visual system. Also the minimal contrast and the contrast sensitivity $S = 1/C$ for the visual system appeared to depend on the stimulus frequency in the time domain and the spatial domain. In Figure 7.45 the threshold values are given for the linear acceleration along the vertical axis, Z-axis of the main coordinate system and the rotational acceleration around the Y-axis as a function of the stimulus frequency in the time domain.

The upper limit is determined by the range of the afferent ganglion cells. Fernandez and Goldberg determined the maximum range for the linear acceleration along the vertical axis in monkeys between -15 and 50 m/s^2 , Figure 7.44. Outside these ranges the output signal of the vestibular system does not change anymore. For the rotational acceleration the range is difficult to measure, but lies above approximately 150 degrees/s^2 . The values of the linear and rotational acceleration at which damage of the organ of equilibrium occurs lie much higher. They can only be determined using destructive tests and are for that reason not determined.

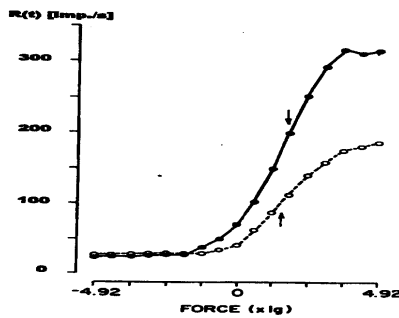


Figure 7.44: Static relationship between the input specific force and the output impulse frequency of two afferent cells

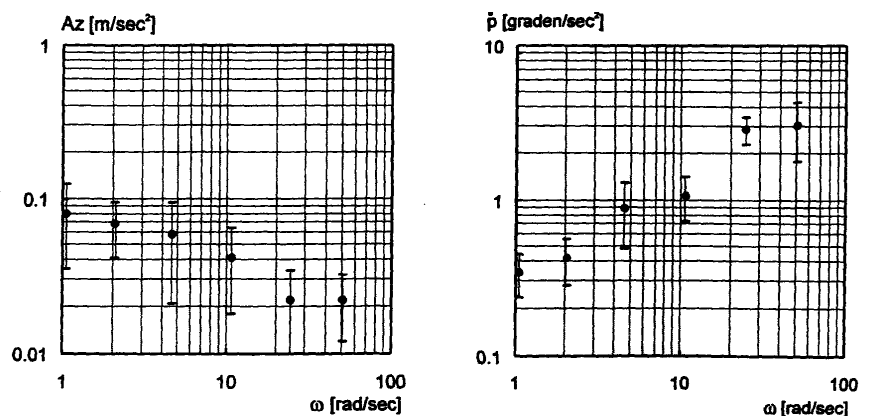


Figure 7.45: The threshold values for motion perception. The linear acceleration along the vertical axis and the rotational acceleration around the perpendicular axis as a function of the sine stimulus frequency

REFERENCES

- De Boer (1988)
- Fernandez C, Goldberg JM (1971). Physiology of peripheral neurons innervating semicircular canals of the squirrel monkey. II. Response to sinusoidal stimulation and dynamics of peripheral vestibular system. *J Neurophysiol.* 34(4):661-75
- Hosman RJAW (1996) Pilot's perception and control of aircraft. PhD-Thesis. Delft University of Technology, The Netherlands
- Hosman RJ, Van der Vaart JC (1981). Effects of vestibular and visual motion perception on task performance. *Acta Psychol (Amst).* 48(1-3):271-87
- Hosman RJ, Van der Vaart JC (1978)
- Poppele RE, Bowman RJ (1970). Quantitative description of linear behavior of mammalian muscle spindles. *J Neurophysiol*, 33(1):59-72
- Steinhausen (1931)
- Van de Brink, Voorhoeve (1984)
- Van Egmond AA, Groen JJ, Jongkees LB (1949). The mechanics of the semicircular canal. *J Physiol.* 110(1-2):1-17
- Van Lunteren, Stassen (1969)

Stability and Admittance

INTRODUCTION

Human beings are capable of moving their extremities in an environment with many unpredictable perturbations. These perturbations will bring the limb to another position than the desired one. Therefore, a system must be functional to correct for these unwanted perturbations: A feedback system. In any position stability is required. Stability is defined as the property that the limb will return to its original position or trajectory after a perturbation. Admittance (inverse impedance) is defined as the actual behavior of the limb after a perturbation, i.e. the way the limb is returning to the original position. The admittance depends on the inertia, viscosity and stiffness, but also on the feedback loops like the reflexive feedback.

The goal of this chapter is to explain the contribution of the muscle visco-elasticity and the proprioceptive reflexes for the feedback control of human motions. In this chapter a block scheme of the motor control system will be explained (see Figure 8.1). In this scheme all building blocks from the previous chapters will be combined: Inertial and geometrical properties of the musculoskeletal system, muscle dynamics and sensor dynamics. The block scheme describes the feedback properties of the motor control system, so it starts with a desired reference position or motions, and shows how the neuromusculoskeletal system can attain this reference despite the effect of perturbation forces.

OBJECTIVES

This chapter addresses:

- The definitions of stability and admittance (inverse impedance).
- Interpretation and use of the feedback control scheme of Figure 8.1.
- The role of intrinsic feedback (muscle stiffness and viscosity) and reflexive feedback (muscle spindles and Golgi tendon organs) in the impedance.
- The contribution of length and velocity feedback from the muscle spindles and force feedback from the Golgi tendon organs for position control.
- Identification of the gains of reflex loops in perturbation experiments.

8.1 Introduction

The Central Nervous System (CNS) is unique in its capacity to control a wide variety of tasks ranging from standing, walking, jumping to fine motor tasks as grasping and manipulating. Instantaneously, the human can switch from accurate positioning tasks to contact tasks. The neuromusculoskeletal system consists of many non-linear components, which has nicely distributed properties enabling these difficult control tasks. Many researchers have focused on separate components of the system, but thereby they are overlooking the interaction of the components and the relative importance of each.

In many tasks humans have to deal with all types of perturbations. For example, while walking with a cup of coffee, the perturbations of the trunk must be neutralized by very compliant behavior of the arm. On the contrary, while using a drill, the drill must be kept from slipping, while exerting a force in the drilling

direction. Two strategies are used by humans to resist perturbations. On the one hand, by co-contraction of antagonistic muscles the joints are stiffened. This strategy will work against all sorts of perturbations, though it is highly energy consuming. On the other hand, by using proprioceptive feedback the perturbations will be detected and the muscles will generate a restoring force. This strategy is energy-efficient, because muscles are only activated when perturbations are present. Due to the time-delays in the feedback caused by neural transportation and processing, this strategy will only be effective against low frequency perturbations.

In this chapter a model will be presented for postural tasks against force perturbations. In this model the linkage system (skeleton), the actuator system (muscles), the sensory system (muscle spindles and Golgi tendon organs) and controller system (CNS) are present. Simulations will show the interactions between the various components. Finally, an experimental method will be presented to identify the proprioceptive feedback gains.

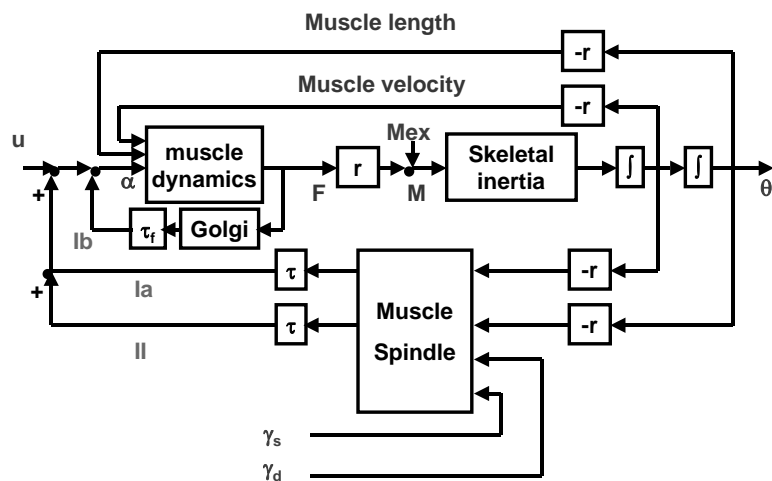


Figure 8.1: Block scheme of the neuromusculoskeletal system. In the forward path neural input u activates muscles and a force is generated. This force is multiplied by moment arm r and results in acceleration through the skeletal inertia. Twice integrating the acceleration will result in position θ . The intrinsic feedback is due to the length and velocity dependency of the muscle contraction dynamics, i.e. the muscle stiffness and viscosity. Muscle force feedback results from the Golgi Tendon Organ, with output I_b afferent signals, and length and velocity feedback results from the muscle spindle, with output I_a and II afferent signals and with additional inputs γ_d and γ_s . Time-delays τ are due to neural transportation and processing time. Control behavior is the change of position θ as a result of neural input u . Admittance behavior (or disturbance behavior) is characterized by the changes in position θ due to external moment perturbations M_{ex} .

8.2 The neuromusculoskeletal model

8.2.1 NON-LINEAR MODEL DESCRIPTION

In Figure 8.1 a block scheme is shown of a neuromusculoskeletal system. The

Central Nervous System (CNS) activates muscles (α -activation). The muscles also receive length and velocity input due to the motions of the skeletal system. The muscles generate (translational) forces, and through a lever arm r muscle moments are generated. These muscle moments result in angular accelerations at the joints. After a double integration of the accelerations the actual joint angle θ will result. Two feedback loops exist: The ‘intrinsic’ feedback loop due to the intrinsic visco-elastic properties of the muscles, and the proprioceptive feedback loop due to the muscle force feedback in the GTO, and the length and contraction velocity feedback in the muscle spindles.

In the intrinsic feedback loop, the joint angles and angular velocities will result in muscle length and lengthening velocities, through multiplying with the lever arm $-r$. This length change and lengthening velocity will give rise to an increase of force (or in certain circumstances in a decrease). This is a common way to show stiffness or viscosity in a block scheme: A force change due to a change of position is exactly the stiffness, and a force change due to a change of velocity is the viscosity.

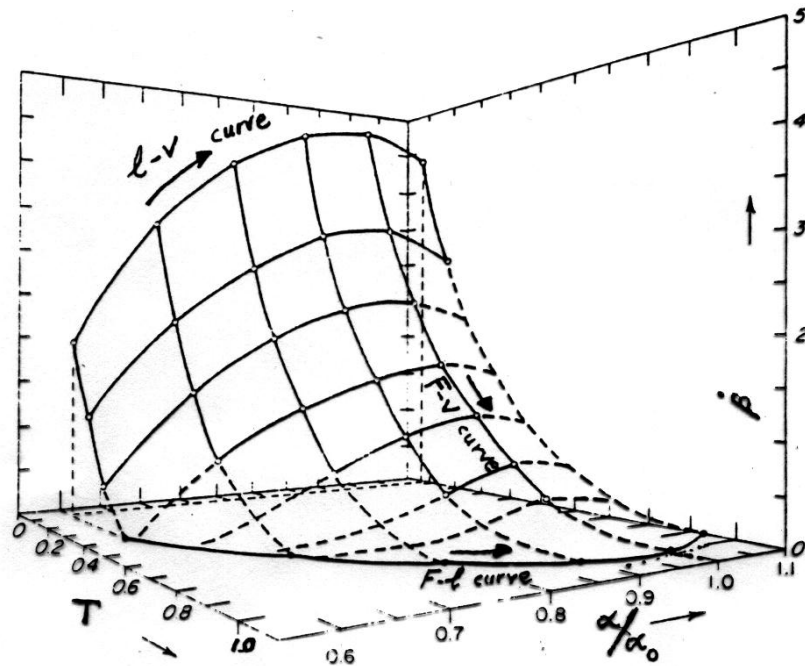
The force generated by a muscle depends for a great deal on the muscle length and velocity, as can be seen in the force-length-velocity graph in Figure 8.2. Simple, Hill-type muscle models are descriptive models in which the length and velocity dependency is incorporated in the Contractile Element (CE), see Chapter 4. In these models, the resulting intrinsic muscle stiffness and viscosity is simply the partial derivative of the force-length and force-velocity curve, $\partial F/\partial l$ and $\partial F/\partial v$ respectively. In the real muscle, this length and velocity dependency results from a complex dynamic cross-bridge behavior, and the modeled stiffness and viscosity are generally an underestimation of the real values.

Position perturbations due to the external perturbing moment will give rise to proprioceptive signals, coming from the muscle spindles. These proprioceptive signals are fed back to the spinal cord, and give rise to an increase or decrease of the α -motor neuron activation. This will result in an increase or decrease of the muscle force. This can be regarded as a kind of stiffness and viscosity as well: A change in length (or lengthening velocity) will result in a change of force. However, due to the limited transportation velocity of the neural signals through the peripheral and central nervous system, there will be important time-delays in the system. Hence, the muscle spindle feedback can be seen as a spring with a time-clock. The spring is stretched, and after a small time-period the force increases.

8.2.2 FORCE VERSUS POSITION PERTURBATIONS

The block scheme in Figure 8.1 shows the correct causal relation between perturbations and position: An external force perturbation is causing a position deviation, because the mass is accelerated. This acceleration is twice integrated in order to obtain the position. In the strict sense, position perturbations do not even exist: A robot can impose a position by exerting a force to the system. Through a very fast control algorithm the force is quickly adapted to bring the system to the desired position. Such a position control algorithm can be seen as a (very stiff) spring. If the controller is a PD (proportional-differential) control, the proportional action is comparable with the stiffness, and the differential action is comparable with the viscosity. However, often the controllers are PID controllers, where the I stands for the integrative action. If a robot hits a wall, and the desired position is just behind the wall, the integrative action will accumulate the robot force until the maximum of the actuators. This integrative action can be regarded as a very high stiffness, since a static offset (frequency is zero) will be corrected by the integrative action.

Humans are superior to robots since they can switch in a very short instance



from position control to force control. If a wall is hit, the force will not increase infinitely, but will be feedback and adjusted such that a desired force will result.

Figure 8.2: Three-dimensional representation of force-length and force-velocity curves. In a Hill-type muscle model, the stiffness and viscosity are obtained as the derivatives of the force-length and force-velocity curves, respectively.

8.2.3 STABILITY AND ADMITTANCE

Notice that there are four types of independent inputs in the system. A theoretical neural input signal u (which might be highly multivariable and complex in nature) is supposed to originate from higher supraspinal regions. There is also a force (or moment) perturbation signal M_e entering at the skeletal system. There are two additional inputs in the system, the dynamic and static γ -signals, which determine the sensory gains in the muscle spindles. Presumably, additional gain setting will take place in the spinal cord in the interneural processing from input sensory signals to output motor neuron signals. There is one output (in a positioning task), i.e. the joint angle (or endpoint position). The transfer function from u to position θ is the control behavior:

$$H_{u\theta}(\omega) = \frac{\theta(\omega)}{u(\omega)}$$

the transfer function from external moments M_e to position θ is the disturbance behavior, or the admittance (inverse impedance) $H_a(\omega)$ the system:

$$H_a(\omega) = H_{M\theta}(\omega) = \frac{\theta(\omega)}{M_{ex}(\omega)}$$

Note that the admittance is a dynamic transfer function (i.e. the gain and phase

changes with the frequency ω), comprising the (muscle) stiffness and viscosity, inertial terms, but also the proprioceptive feedback. In Figure 8.1 both the intrinsic muscle stiffness and viscosity as well as the reflexive feedback are shown as feedback loops. The forward path together with the feedback pathways are called the open-loop transfer function. The loop gain of the open-loop transfer function is important for the dynamic behavior of the system. If the loop gain becomes high, the system will start to oscillate. If the gain becomes even higher, the system can become unstable and will not return to the desired position (see also the definition of stability!).

A mechanical system as shown in Figure 8.1 is subject to force perturbations, which will have an effect on its position. Therefore, the transfer function $H_a(\omega)$ from force to position is denoted in the frequency domain as the admittance:

$$H_a(\omega) = \frac{\theta(\omega)}{M_e(\omega)} \quad (8.1)$$

This transfer function has units of degrees/Nm (or in translational units m/N). In contrast, the impedance denotes the change in moment due to a position disturbance, and has units Nm/degree. However, in real life position perturbations do not exist: A mechanical system is always moved by forces acting on it. Only in the typical case of a very rapid position servo-control loop, with high power, the perturbations appear as position perturbations.

8.3 Linearization of the neuromusculoskeletal model

The highly non-linear and adaptive model in Figure 8.1 lends itself not very good for an analysis of its behavior. Therefore, it is convenient to linearize the model in a certain equilibrium point (Figure 8.3). If we assume a static neural input signal u_0 , and only small amplitudes of perturbations M_e , the limb will hardly move and the linearization is warranted.

Muscle dynamics consists of activation dynamics (non-linear first order calcium inflow/outflow dynamics) and contraction dynamics (the contractile machinery having cross-bridges connecting and disconnecting), see also Chapter 4. For small perturbations, the length and velocity dependency can be separated from the activation dynamics, and be added to the joint stiffness and viscosity of passive structures. The muscle stiffness and viscosity are a monotonous increasing function of the constant neural input u_0 . The activation dynamics are represented by a linear first-order system, in which the different time-constants for inflow and outflow are averaged. However, strictly a model with a hard non-linearity like this can not be linearized. For convenience matters, the maximal force output F_{max} is added to the activation dynamics (not shown in Figure 8.3). The muscle spindle dynamics can be simplified by assuming that the CNS is able to derive the length and velocity contributions out of the Ia and II afferent signals. In addition, one might assume that the dynamics could be described by a static gain and a time-delay (about 25 msec for e.g. shoulder muscles). Including these assumptions in order to linearize the system, the block scheme in Figure 8.3 is obtained. In this chapter we will focus on the impedance behavior of the system, i.e. the transfer function of M_e to θ . Therefore, we will analyze the behavior of some of the subsystems (Rozendaal, 1997).

8.3.1 INTRINSIC MUSCLE STIFFNESS AND VISCOSITY

The straight path from input $M_{ex}(\omega)$ to output $\theta(\omega)$ for the admittance $H_a(\omega)$ is

$$H_a(\omega) = \frac{1}{J_\theta} \cdot \frac{1}{j\omega} \cdot \frac{1}{j\omega} \quad (8.2)$$

i.e. the inertia transferring force to acceleration and a double integration to acquire the position signal.

The intrinsic muscle stiffness is represented by $K_m(\omega)$ and the viscosity by $B_m(\omega)$. Both are shown in a feedback pathway:

$$H_{ff}(\omega) = (B_m \cdot r^2) \cdot j\omega + K_m \cdot r^2$$

If we derive the forward path divided by one plus the open-loop, the following equation result:

$$\begin{aligned} H_a(\omega) &= \frac{\theta(\omega)}{M_e(\omega)} = \frac{1}{J_\theta \cdot (j\omega)^2} \\ &= \frac{1}{J_\theta \cdot (j\omega)^2 + (B_m \cdot r^2) \cdot j\omega + (K_m \cdot r^2)} \\ &= \frac{1}{J_\theta \cdot (j\omega)^2 + B_\theta \cdot j\omega + K_\theta} \end{aligned} \quad (8.3)$$

In which $B_\theta(\omega)$ and $K_\theta(\omega)$ are the joint viscosity and stiffness, respectively. It is obvious that this is a second order mass-spring-damper system, with the spring ($K_m(\omega)$) and damper ($B_m(\omega)$) properties inherited from the muscle properties.

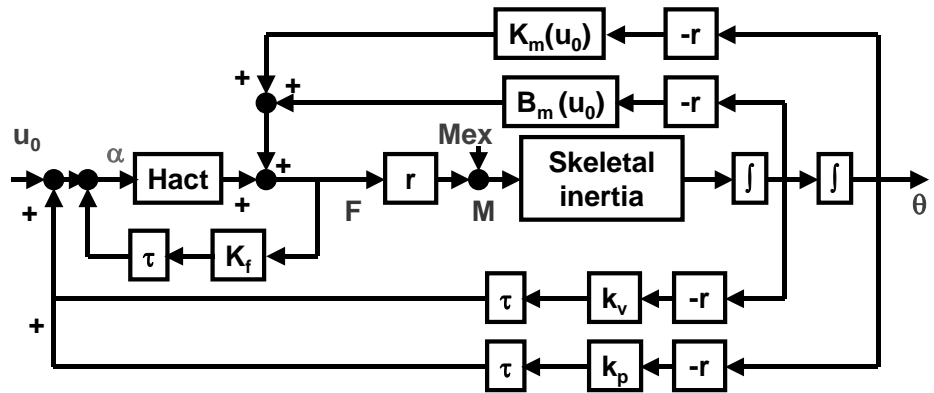


Figure 8.3: Linearized model representation of the system in figure 4. Input u_0 is assumed constant. Muscle stiffness and viscosity is represented by K_m and B_m , as a function of u_0 , respectively. The force, velocity and length proprioceptive feedback are represented by a static gain (k_f , k_v and k_p respectively) and a time-delay τ .

8.3.2 FORCE FEEDBACK LOOP

Secondly, we will focus on the force feedback. As can be seen in Figure 8.3, a subsystem can be discerned, in which the activation dynamics H_{act} has a force feedback loop added. The activation dynamics H_{act} can be described as:

$$H_{act} = \left(\frac{1}{\tau_{act} \cdot j\omega + 1} \right) \cdot F_{max} \quad (8.4)$$

in which τ_{act} is the linearized time-constant to describe the calcium in/output to the sarcoplasmic reticulum (one of the activation dynamic processes) and F_{max} is the maximal muscle force. Then, the following transfer functions can be derived:

$$H_{act}^* = \frac{H_{act}}{1 + H_{act} \cdot k_f \cdot e^{-j\omega\tau}} \quad (8.5)$$

for the transfer function from neural input u to force F . The transfer function is the forward path divided by one plus the open-loop transfer function. The transfer function is shown in Figure 8.4, for several values of force feedback gain k_f . It can be seen that the increase of k_f results less phase lag for frequencies up to 6 Hz, but that the gain for low frequencies decreases. The stability of the length and velocity feedback loop (originating from the muscle spindles) is determined by the open-loop transfer function. The system will become unstable if the gain of the open-loop transfer function is higher than one while the phase is -180 degrees. The stability is described by either the phase margin (the difference in phase with -180 degrees while the gain of the open-loop transfer function is one) or by the amplitude margin (the difference in gain with one, while the phase lag is -180 degrees). Hence, for the overall phase lag in the system, the decreased phase lag of $H_{act}^*(\omega)$ due to increased k_f is important. The decrease in gain can easily be compensated by higher proprioceptive feedback gains k_p and k_v . The proprioceptive feedback loop will benefit from higher force feedback gains! But also the muscle stiffness and viscosity contribution to the muscle force are filtered by the force feedback loop:

$$H_{act}^{**}(\omega) = \frac{F(\omega)}{F_{BK}(\omega)} \frac{1}{1 + H_{act}(\omega) \cdot k_f \cdot e^{-j\omega\tau}} \quad (8.6)$$

in which $F(\omega)$ is the muscle force (output) and $F_{BK}(\omega)$ are the visco-elastic forces (input). This transfer function is shown in Figure 8.5. Here, also increasing k_f decreases the gain for low frequencies. Physically, this means that stretching muscle results in an increased muscle (and tendon) force. This tendon force is fed back to the CNS and lower muscle activation and lower muscle force result! Increasing the force feedback gain k_f is not beneficial for the intrinsic feedback loop.

Summarizing, increasing k_f has a two-fold effect: Decreasing the phase lag of the activation dynamics, and decreasing the effect of muscle stiffness and viscosity. It can be shown that these effect exactly cancel each other out, so at this moment it is not clear what the rationale is for the settings of the force feedback k_f . For some tasks the increase of bandwidth might be more important than the reduction of intrinsic stiffness and viscosity, in which case an open-loop gain $K_f = k_f \cdot F_{max} = 1.27$ results in an acceptable behavior, i.e. an oscillation peak of two times the steady state gain.

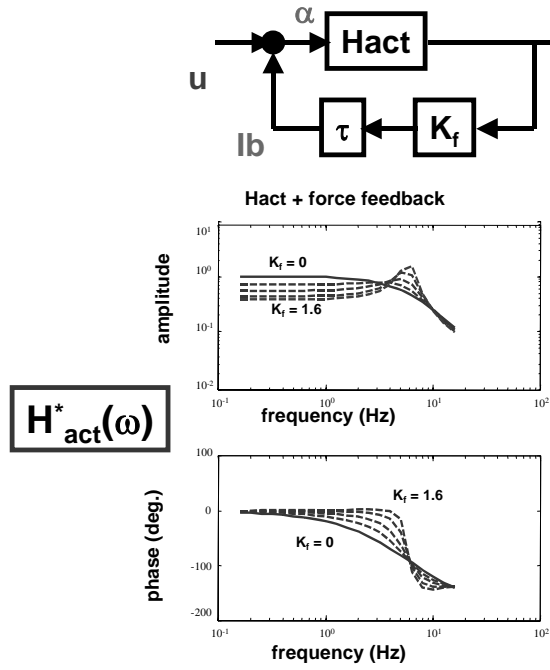


Figure 8.4: Block scheme and bode plot of transfer function H_{act}^* , from neural input u to force F , for increasing values of open-loop gain $K_f = k_f F_{max}$. It is seen that increasing K_f results in less phase lag of the transfer function for frequencies up to 6 Hz, but also a lower gain for these frequencies result.

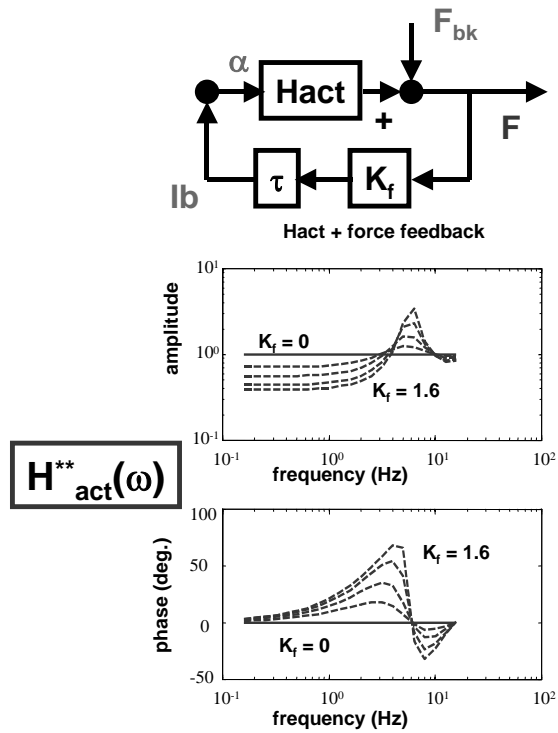


Figure 8.5: Block scheme and bode plot of transfer function of H_{act}^{**} from stiffness and viscosity force contribution F_{bk} , to muscle force. Increasing open-loop gain $K_f = k_f \cdot F_{max}$ results in a decreased gain for lower frequencies, i.e. the stiffness and viscosity is effectively decreased.

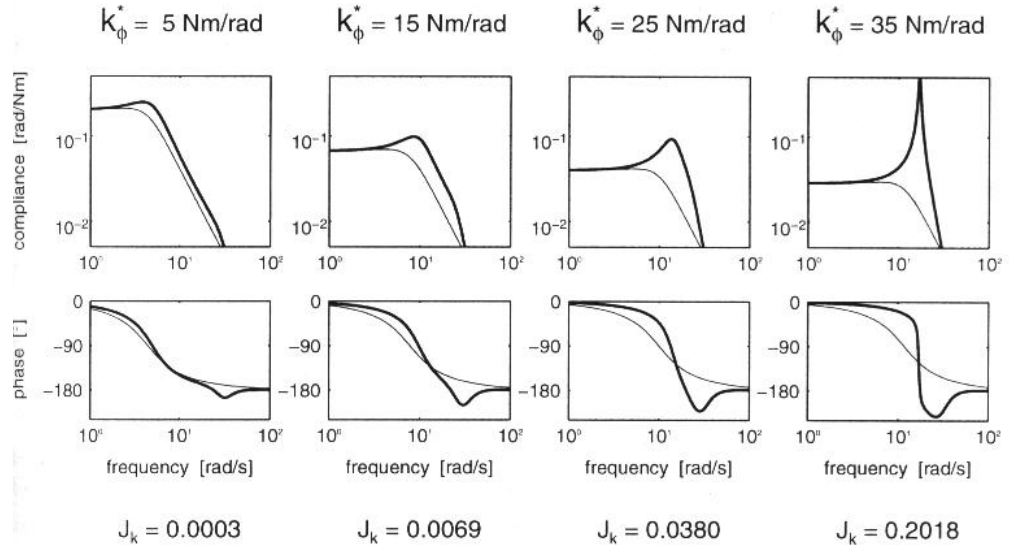
8.3.3 LENGTH AND VELOCITY FEEDBACK LOOP

The proprioceptive length and velocity feedback from muscle spindles is represented by proportional feedback gains k_p and k_v , respectively. Now, the overall compliance (the inverse transfer function of the impedance) can be described by:

$$H_a(\omega) = \frac{\theta(\omega)}{M_e(\omega)} = \frac{1}{J \cdot (j\omega)^2 + (H_{act}^{**} B_m \cdot r^2 + k_v H_{act}^* e^{-j\omega\tau}) j\omega + (H_{act}^{**} K_m \cdot r^2 + k_p H_{act}^* e^{-j\omega\tau})} \quad (8.7)$$

in which we can recognize the inertia J , the ‘viscous’ contributions from the intrinsic feedback ($H_{act}^{**}(\omega) \cdot B_m \cdot r^2$) and the proprioceptive feedback ($k_v \cdot H_{act}^*(\omega) \cdot e^{-j\omega\tau}$), and the ‘stiffness’ contributions from the intrinsic feedback ($H_{act}^{**}(\omega) \cdot K_m \cdot r^2$) and the proprioceptive feedback ($k_p \cdot H_{act}^*(\omega) \cdot e^{-j\omega\tau}$). Obviously, this transfer function is not a simple second order transfer function, but contains higher order dynamics due to the force feedback and the time-delays. In Figure 8.6 some realizations of the transfer function $H_a(\omega)$ are shown, in order to obtain different combinations of a certain desired steady state stiffness and damping by adjusting k_p and k_v . For higher stiffness values it can be seen that it is difficult to achieve with length feedback, because the time-delay of the proprioceptive feedback loop result in an oscillatory behavior of the system. This is due to a lack of damping in the system (in this realization without co-contraction the intrinsic damping and stiffness is low). In the

admittance $H_a(\omega)$ the increased bandwidth of the activation dynamics through an increased force feedback gain k_f (inner loop) does allow for higher velocity feedback gain (next outer loop), which in turn allows for a higher length



feedback gain (most outer loop). Also, higher intrinsic feedback values K_m and B_m , e.g. due to co-contraction, would allow for higher velocity and length feedback gains.

Figure 8.6: Some realizations of admittance transfer function $H_a(\omega)$, shown with thick line, by changing k_p and k_v in order to obtain a desired steady state stiffness K^* (normalized for inertia), drawn with fine line. It can be seen especially in the phase lag that $H_a(\omega)$ does not resemble a second order system, and that there is a lack of damping for higher stiffness values.

8.4 Experimental validation

For experimental validation it is necessary to measure certain variables of the system, in order to estimate the transfer functions. If the transfer functions are properly estimated e.g. in the frequency domain, parameters like the length and velocity feedback gains k_p and k_v can be estimated. As mentioned before, the variables, which can be measured in the system, are very limited. Practically, only the position and external forces can be measured, and the EMG signal (ElectroMyoGram: the electrical activity of the muscles).

The EMG signal can be picked up by surface electrodes on the skin, or by wire electrodes inserted in the muscles. The EMG signal is typically in the order of a few millivolts, and needs to be adequately pre-amplified near the electrodes in order to reduce the noise. Subsequently, the signal is high-pass filtered (cut-off frequency around 15 Hz) to remove movement artefacts, and low-pass filtered in order to remove high frequencies in order to prevent aliasing. The sample frequency of the EMG signal must be at least two times the cut-off frequency of the low-pass filter. Then the EMG is rectified (negative peaks are taken positive), through which process low frequencies return into the signal. Then the EMG can be low-pass filtered and is often as such interpreted as the activation signal to the muscles.

EMG is very often used to investigate the nature of the reflexes. The procedure is apparently simple: A perturbation is imposed, and from the onset and

amplitude of the EMG the time-delay and the reflexive feedback gain can be estimated. Unfortunately, due to the noisy character of the EMG signal and the unknown filtering characteristics of the soft tissue between muscle and electrodes, no good estimates of k_p and k_v can be obtained.

Using only mechanical variables as position and force is another approach. The objective is to estimate the admittance of the system. As an example, if one would like to estimate the stiffness of a spring, a force can be applied and the position measured (resulting in the compliance of the spring), or the position can be imposed and the force can be measured (resulting in the stiffness of the spring). In a linear system the compliance is exactly the inverse of the stiffness. However, the human neuromusculoskeletal system is not a linear system, and even worse, the system rapidly adapts to the type of perturbations imposed.

There are two major problems in identifying the feedback gains:

1. The system is a *closed-loop system*. In a closed-loop system the noise affects all variables measured inside the closed-loop. A transfer function estimated using these variables always contains the forward path characteristics as well as the open-loop characteristics, and the relative contribution of both depends on the noise amplitudes. Hence, special closed-loop identification algorithms are needed to estimate the transfer functions, using an external signal that is independent of noise present in the closed-loop, e.g. a force or position perturbation imposed on the subject. Preferably this external signal consists of force perturbations, since this is the natural task for the subjects.
2. There are basically *two types of feedback loops* present in the system, i.e. intrinsic feedback and proprioceptive feedback. These feedback contributions should be separated in order to be able to estimate the reflexive feedback gains.

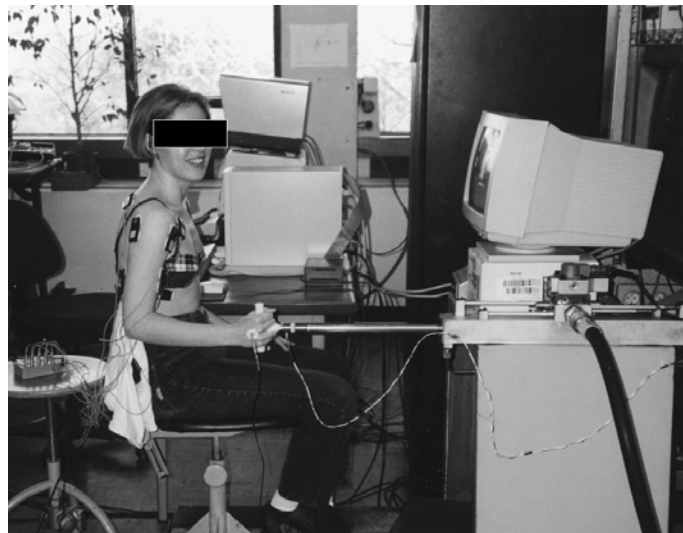


Figure 8.7: A one Degree-of-Freedom robotic manipulator is used to impose force perturbations on the arm. The subject is requested to minimize position deviations.

In the laboratory of the Man-Machine Systems & Control group (Delft University of Technology), experiments have been performed to identify the proprioceptive length and velocity feedback gains under varying conditions (Broun, 2000). For this, a one DOF (translational) robotic manipulator has

been used (see Figure 8.7). The subject holds a handle, which can move backwards and forwards. The position of the handle, as well as the force applied on the handle, is recorded. The robotic manipulator can impose external forces (comparable to the external moments M_e) to the subject. Hence, a closed-loop identification algorithm is used with the external force as independent input (see Figure 8.8). Then, the following transfer function can be estimated by the cross-spectral densities $S_{wf}(\omega)$ and $S_{wx}(\omega)$ of the measured signals position $X(\omega)$, hand force $F(\omega)$ and external force perturbation $W(\omega)$:

$$\hat{S}_{wf} = \frac{-\hat{H}_a(f) \cdot H_p(f)}{1 + \hat{H}_a(f) \cdot H_p(f)} \cdot \hat{S}_{ww} \quad (8.8)$$

$$\hat{S}_{wx} = \frac{H_p(f)}{1 + \hat{H}_a(f) \cdot H_p(f)} \cdot \hat{S}_{ww} \quad (8.9)$$

$$\hat{H}_a(f) = -\frac{\hat{S}_{wf}(f)}{\hat{S}_{wx}(f)} \quad (8.10)$$

with the coherence function

$$\hat{\Gamma}(f) = \sqrt{\frac{|\hat{S}_{wf}(f)|}{\hat{S}_{ss}(f) \cdot \hat{S}_{xx}(f)}} \quad (8.11)$$

in which $H_a(f)$ is an estimate of the arm impedance ($f = \omega/2\pi$) and $H_p(f)$ is the transfer function of the robotic manipulator. The coherence function $\Gamma(f)$ is a measure for the signal to noise ratio and thus for the linearity of the dynamic process, and ranges from zero in the worst case to one when a perfect linear estimate can be obtained. Note that the estimate of $H_a(f)$ is independent of $H_p(f)$, i.e. the dynamic properties of the robotic manipulator do not affect the estimate of the arm impedance.

The perturbation signal is very important for the task performance. If a deterministic signal would be used, e.g. a sinusoid, a human is able to predict the signal, and exactly counteract to the sinusoid. The perturbation signal should be unpredictable, in order to excite the feedback properties of the system.

Stochastic signals are a particular type of unpredictable signals. In this experiment, three conditions have been imposed on the subject: White noise (WB) ranging from 0.05 Hz to 20 Hz, Narrow Band noise (NB1) ranging from lowest frequency 0.05 Hz to highest frequency f_h , and Narrow Band noise (NB2) having a range of 0.3 Hz around center frequency f_c .

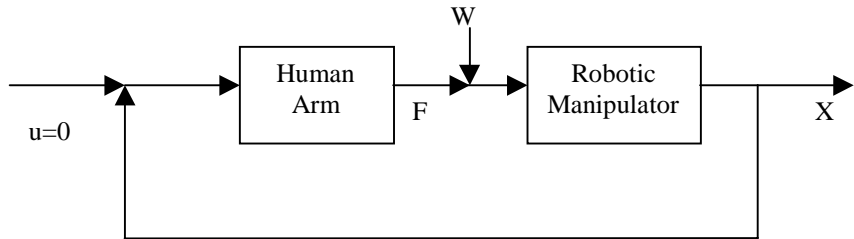


Figure 8.8: Block scheme of the experimental set-up of the experiment shown in Figure 8.7. An external force signal $W(\omega)$ is input to a robotic manipulator with known impedance $H_p(\omega)$, and results in position $X(\omega)$. This position X is imposed to the arm of the subject, who will respond with a hand force $F(\omega)$. The impedance of the human arm $H_a(\omega)$ can be estimated by a close-loop identification algorithm with independent external input $W(\omega)$.

The results showed that when the highest frequency bandwidth f_h became smaller, that the subjects increased their impedance (see Figure 8.9). If we consider the impedance at frequency $f=0$, i.e. the stiffness, it can be seen that the stiffness is about a factor 5 higher for low frequent disturbances (recognizable by the fact that the graphs do not extend beyond their highest frequency) than for disturbances containing high frequencies (WB noise). This increase in impedance is explained by the effect of proprioceptive feedback. In other words, due to the proprioceptive feedback the stiffness increases by a factor 5 compared to a *maximally co-contracted* arm! It is clear that the proprioceptive feedback is very important for the dynamic behavior of the human arm.

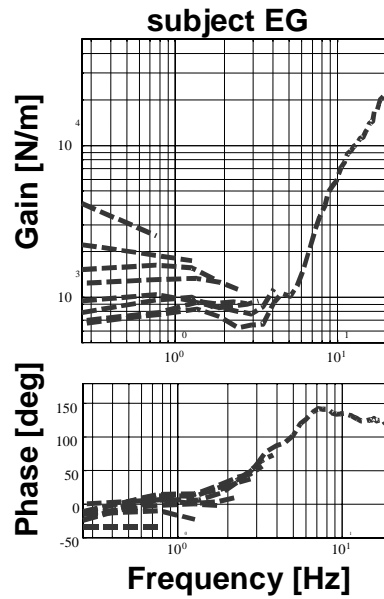


Figure 8.9: Bode plot of the estimated impedance transfer function $H_i(f)$, for narrow band noise (NBI) with increasing highest frequency f_h . Only the part of the transfer function, which could be estimated (i.e. for which frequencies there was a perturbation), is shown. It can be seen that when the highest frequency in the perturbation signal decreases, the amplitude of the impedance increases. This is due to the increasing contribution of the proprioceptive length and velocity feedback.

Using the transfer function $H_a(f)$, the parameters k_p and k_v can be fitted for all conditions. k_p and k_v are zero for white noise (WB), otherwise there would be a large oscillation peak around the eigen frequency of the system. If the perturbation frequencies are lower than the eigen frequency, then the feedback gains k_p and k_v will increase. In Figures 8.10 and 8.11 the results are shown for NB1 and NB2 noise. It is concluded that the feedback gains are rapidly adapted to the changing conditions, and that virtually any combination is possible. Humans have a very flexible feedback system in order to co-operate with a changing environment! Recently it was shown that the measured feedback gains indeed approached the optimal feedback gains of the system. Physically, one may assume that the feedback gains k_p and k_v can be changed by the γ -stimulation to the muscle spindles, or by supraspinal gain settings of interneurons in the spinal cord. The results in Figure 8.11 show that also negative feedback gains are possible, when the perturbation signal has a small bandwidth (0.3 Hz, almost a pure sine wave). Normally, negative feedback gains would result in an unstable system. Here, the stability is due to the intrinsic feedback contribution, and the proprioceptive feedback contribution is optimal to compensate for the time-delays in the system! These negative feedback gains can only be obtained by supraspinal gain settings, since the muscle spindle itself can not send negative neural signals. In case of white noise (WB) the proprioceptive feedback gains are virtually zero. In the white noise case, the proprioceptive feedback gains would result in an oscillation peak around the eigen frequency of the system, which would amplify certain frequencies in the spectrum. Only when the perturbation

frequencies are below the eigen frequencies of the system (more or less determined by the inertia, intrinsic stiffness and viscosity), then increasing the proprioceptive feedback gains results in a improved performance (= disturbance rejection). The unavoidable oscillation peak is then not important, since the spectrum of the perturbation signal does not contain frequencies in that region (Figure 8.12).

It is concluded that the human proprioceptive feedback system is a very flexible system, and that we have obtained thus far only a small window to peek into the enormous capacities of the Central Nervous System to get optimal performance.

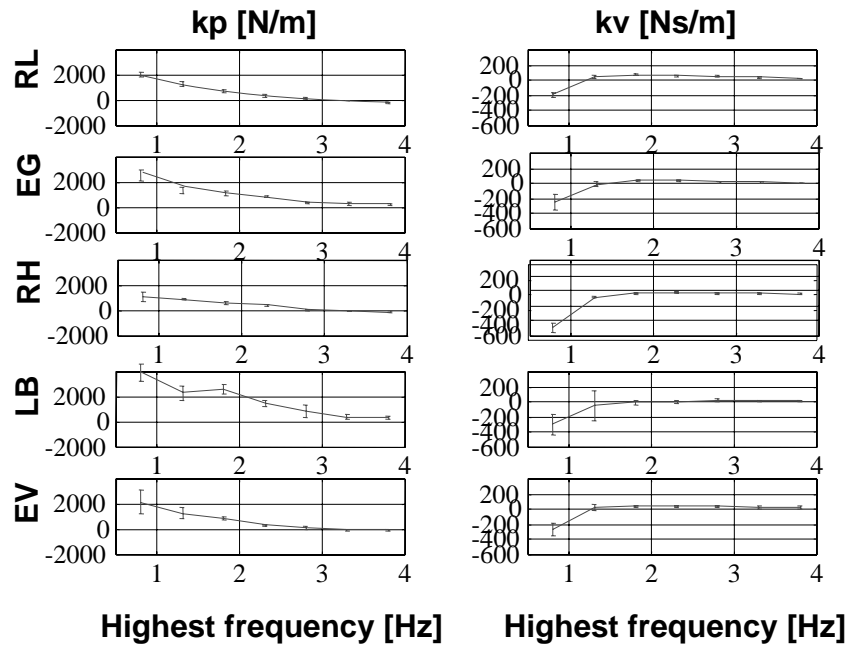


Figure 8.10: Length feedback gain k_p and velocity feedback gain k_v shown versus the highest frequency in the perturbation signal (NB1). Results are very similar for five subjects (RL, EG, RH, LB, EV). Mean and standard deviations are shown for four repetitions (Brouwn, 2000).

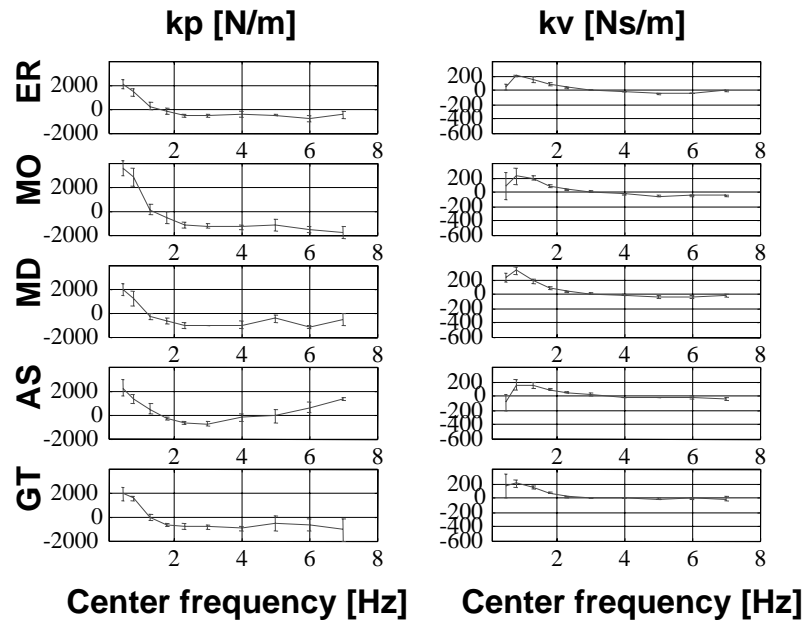


Figure 8.11: Length feedback gain k_p and velocity feedback gain k_v shown versus the center frequency (NB2) of the perturbation signal. Results are shown for five subjects. Mean and standard deviations are shown for four repetitions (Brouwn, 2000). Negative feedback gains indicate supraspinal gain settings.

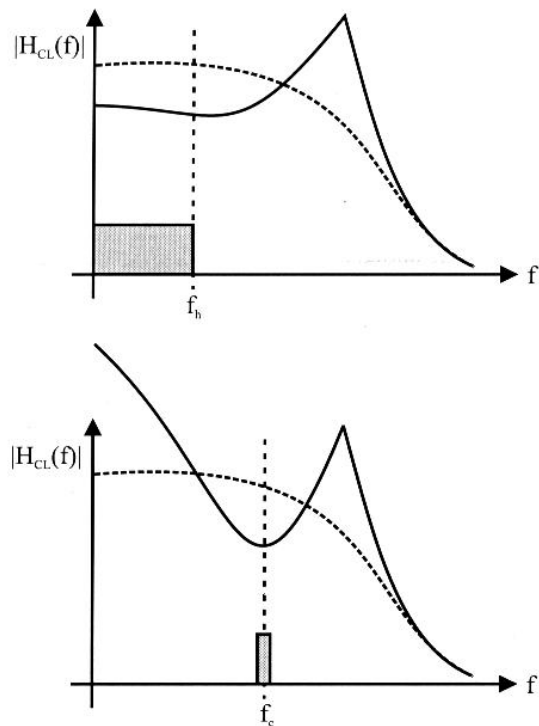


Figure 8.12: The optimal admittance depends on the frequency characteristics of the perturbation signal. In case of narrow bandwidth perturbations NB1 (top figure) the optimal admittance is as small as possible in those frequencies where the perturbation is present, from 0.05 Hz to f_h . For the narrow bandwidth perturbation NB2 the admittance is low at the center frequency of the perturbation signal imposed on the subject. The occurrence of an oscillation peak around the eigenfrequency is less important since almost no perturbations are present in that frequency range.

REFERENCES

- Brouwn GG (2000). Identification of intrinsic and reflexive components of human arm dynamics during postural control. PhD thesis, Delft University of Technology, The Netherlands.
- Rozendaal LA (1997). Stability of the shoulder, intrinsic muscle properties and reflexive control. PhD thesis, Delft University of Technology, The Netherlands.

(Models of) Human perception

INTRODUCTION

In the previous chapter the sensory signals from the muscle spindles and golgi tendon organs could be used as feedback signals to modulate the dynamic characteristics of the arm (e.g. admittance, stability etc). However, in other tasks humans have to control variables that cannot be derived from single or parallel sensory output flows in a direct way. For example in the control of balance, the orientation of the body with respect to the earth vertical has to be controlled. Humans do have not a single sensor that detects this spatial orientation. The visual and the proprioceptive signals do provide us with information relative to an external reference frame (e.g. a stationary or moving visual scene, or a stationary or fixed support base). Also the vestibular signals from the otoliths and semicircular canals do not detect spatial orientation directly. In order to perceive our orientation with respect to gravity (or subjective vertical) we have to integrate or fuse multiple sensory signals.

In this chapter we will first discuss some experimental observations of sensory interactions (Section 9.1) with special attention to the oculomotor system (Section 9.1.1), the perception of ego motion (Section 9.1.2) and balance control (Section 9.1.3). In Section 9.2 we will discuss hypothetical models of sensory integration that we developed. Many other models of human perception, balance control and the oculomotor system have been developed but will not be discussed in this chapter.

OBJECTIVES

This chapter addresses:

- Experimentally found sensory interactions in the oculo-motor system.
- The problems associated with perceiving the orientation with respect to the earth vertical ('subjective vertical').
- In what situation sensory illusions occur and how these illusion can be explained from the dynamic properties of the human senses.
- How in balance control the contribution of different sensory systems can be experimentally assessed.
- The structure and rationale of a presented model of human perception; i.e. the adaptive Kalman filter.
- How vestibular related threshold effect can be explained with this model.
- How visual induced postural can be explained.
- Why the vestibular system is crucial in the distinction of ego motion and motion of the environment.

9.1 Sensory interactions

As a result of the interaction between the organ of equilibrium and the visual system several effects occur of which some are experienced as a positive property, while others are seen as less positive or sometimes even annoying. From the scheme in Figure 9.1 appears that the vestibular and the visual system both influence:

- The oculomotor system
- The perception of motion and orientation
- Balance control

In all three cases it can concern a simultaneous contribution of both senses.

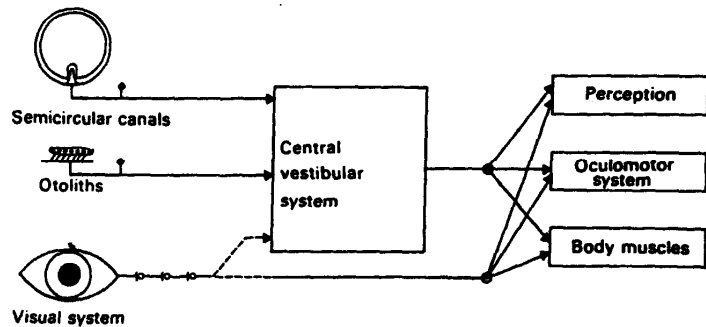


Figure 9.1: Schematic representation of the relation between the visual and the vestibular system and the perception, the oculomotor system and postural control

How exactly the processing of the output signals of the visual-vestibular system works is not completely clear yet. Under different conditions apparently different rules apply. To indicate which factors play a role, below several important facts are mentioned.

For the perception of motion it is important to make a distinction between the absence of a signal and the null signal. Considering the fact that the vestibular system always gives an output signal when the head is kept still, the vestibular system can not be turned off to study only the influence of visual input. Oppositely, by closing the eyes or in a dark environment every visual output can be excluded.

From research appeared that if only visually a movement stimulus is presented, optokinetic stimulation, the afferent neurons in the vestibular nerve are stimulated. Besides that the output of the organ of equilibrium is used to stabilize the eyes during head movement, to help the visual system in this way to fixate the eye on the desired object.

9.1.1 OCULOMOTOR SYSTEM

9.1.1.1 saccadic eye movements

The rapid versional (conjugate) eye movements are under both voluntary and reflex control. Examples of voluntary saccades are willed refixations and those in response to command, e.g. "Look to the right"; "Look up". The sudden appearance of a peripheral object or an eccentric sound may evoke a reflex saccade in the direction of the stimulus. In the usual situation these saccades are accompanied by head movements in the same direction. However, in both clinical examinations and most physiologic experiments, the head is stabilized.

The visual stimulus for a saccade is target (object) displacement. Following an instantaneous change in target position, the human ocular motor system will respond with a saccade after a latency (delay) of 200 to 250 msec. Both the peak velocity and the duration of the saccade are dependent upon the size (amplitude)

of eye movement, varying from 30 degrees to 700 degrees/second respectively, for movements from 0.5 degrees to 40 degrees in amplitude. Saccades are conjugate and ballistic. The physiological control system responsible for their generation is discrete, that is, at discrete instants in time, control decisions are made based upon the continuous inflow of visual information from the retina; these decisions are essentially irrevocable: once the eyes are in motion their trajectory cannot be altered. The control signal is retinal position error, which is reduced to zero by the negative feedback nature of this subsystem.

After an appropriate latency, the saccadic response to target displacement consists of a period of acceleration to peak velocity and deceleration of the eyes onto the new target position. The muscular activity in the agonist-antagonist pair is characterized by a burst of maximal facilitation in the agonist, and total inhibition in the antagonist during the movement deceleration is not consequent to active braking by the antagonist muscle. Rather, the two muscles merely assume the relative tensions necessary to hold the new target position. This is sufficient to accomplish the rapid deceleration because of the braking effect (damping) of the "ocular motor plant" (ie, globe, muscles, check ligaments, and fatty supporting tissues of the orbit).

9.1.1.2 Pursuit

The major stimulus for a pursuit eye movement is a fixated target which moves; this evokes a following eye movement after latency of 125 msec. The maximum pursuit velocities are only 30 degrees to 50 degrees per second. Pursuit eye movements are conjugate, smooth and under control system capable of continuous modification of motor output in response to visual input (in contrast to discrete saccadic control). The input signal is retinal error ("slip") velocity which is reduced to zero when eye velocity matches target velocity. Recent work suggests that the velocity of the target moving across the retina is used by the brain to create an internal cerebral target velocity signal and it is this "perceived target velocity" which drives the pursuit system. This would provide an explanation for many of the "pursuit" eye movement responses to non-moving targets such as after images. Under most conditions a moving target is required to move the eyes smoothly; attempts to voluntarily move the eyes smoothly without actual target motion result in a series of small saccades, so called "cog-wheel" pursuit.

9.1.1.3 Vergence

The stimuli for vergence eye movements are target displacement or motion along the visual z-axis (toward or away from the observer). The latency for vergence eye movements is approximately 160 msec; maximum velocities are in the range of 20 degrees per second, and the movements are generally faster than divergence movements and the system is unique in being able to generate uniocular eye movements. For example, if a target were placed exactly in front of the right eye and slowly brought closer to the observer, the right eye would remain stationary but the left eye would converge.

9.1.1.4 Vestibulo-ocular interactions

Head movement is the stimulus for the compensatory eye movements elicited by the vestibular system. The latency between the onset of head movement and the resultant slow vestibular movement has been reported to vary from 10 to 100 msec. The peak velocities of vestibular induced eye movements is also variable and may be as fast as 300 degrees/s. The eyes move in an opposite direction in

the head in response to head movements in the dark. With a visible target the ocular counter-rotation may exactly match or compensate the head movement. This indicates a major visual-vestibular interaction. These interactions are called the vestibular ocular reflex or VOR. Visual stimuli can modify the VOR. The eye movements in the vestibulo-ocular system are conjugate and smooth, but then interrupted by saccades which recenter the eyes toward a midposition in the orbit. This repetitive pattern of slow and fast eye movements is an example of one type of nystagmus.

9.1.1.5 Nystagmus

Nystagmus is an ocular oscillation with repetitive to and from movements, usually composed of a slow component and a fast or saccadic component. An other type of nystagmus occurs in case of rotations of the head for example around the Z-axis over large angles when it is not possible to keep the eye fixed on a fixed object in the space. Nystagmus occurs then. In that case the eye fixes temporarily on an arbitrary point and thus turns in the opposite direction compared to the head, the slow phase (pursuit) of the nystagmus. If the fixation point deviates too much from the X-axis, the head turns fast (saccade) in the same direction as the head until a new fixation point at the other side of the X-axis, the fast phase of the nystagmus. Nystagmus may be induced by normal physiologic stimuli or may be an expression of disease or drugs altering the normal control of eye movements.

The nystagmus can be aroused by a visual stimulus, optokinetic reflex (OKR) as well as by a vestibular stimulus, vestibulo-ocular reflex (VOR), Figure 9.2. The nystagmus resulting from a vestibular stimulus occurs following to a rotation in the dark. Figure 9.2 gives a registration of the EOG (Electro Oculogram) and the derivative of the slow phase eye velocity during a sine-shaped rotation velocity variation. The stroke of slow and fast phase of the nystagmus movement of the eyeball lies between 30 and 50 degrees.

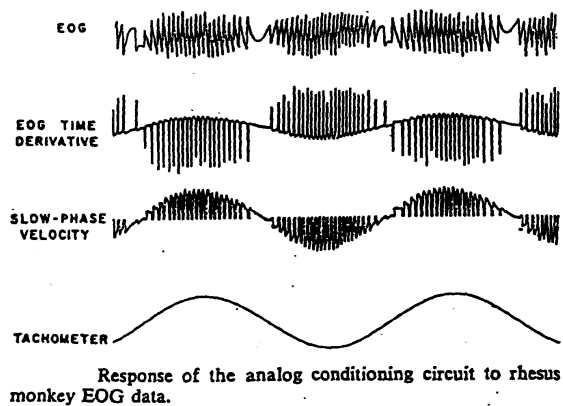


Figure 9.2: Measured nystagmus with the EOG as a function of the input rotational velocity

By measuring the rotation velocity of the eye during the slow phase of the nystagmus resulting from a vestibular input, it is possible to determine the relationship between the input acceleration and the output eye rotation. This relationship contains the dynamical properties of the organ of equilibrium and the oculomotor system.

If the eye is fixated consciously onto an object that turns along with the head, like for example the interior of a car during driving in a bend, the nystagmus is suppressed under normal conditions.

9.1.2 PERCEPTION OF MOTION AND ORIENTATION (LARGE PART OF THE TEXT IS ADOPTED FROM BOS AND BLES, 2002)

From the discussion of the transfer function of the semicircular canals (Chapter 7) appeared that at low ($\omega < 0.1$ rad/s) and high ($\omega > 10$ rad/s) frequencies of the input rotational acceleration the afferent signal is no longer directly correlated to the rotational velocity. Especially at low frequencies (long lasting movements) this gives problems. We are then not able to, only with the organ of equilibrium, make a normal perception of the rotational velocity and from there determine our position with relation to the environment. Moreover, for the determination of the position in space the rotation signal should be integrated. Integration over a longer time will lead to a growing error and uncertainty of the thus determined position.

From Figure 9.1 it appears however that for the perception of motion the visual as well as the vestibular system contribute. Under normal circumstances, using visual information, our position in space can be determined. Moreover, velocity detectors in the visual system give an approximation of the linear and rotational velocities.

The collective properties of the visual and vestibular system are in a way that they supply each other and over a very broad range of circumstances guarantee a reliable perception of position and velocity. However, under special circumstances it is possible to disturb or incorrectly influence the motion perception, which leads to disorientation, also called sensory illusions. Examples of sensory illusions are the Ferris Wheel effect, linear and circularvection, somatogravic illusion and illusions caused by constant linear accelerations.

9.1.2.1 The Gif Resolution

To be able to move about on earth in a controlled manner requires knowledge of self-motion. This holds for linear as well as angular motion, both with three Cartesian components. On earth we are also faced with gravity, and a total of nine variables must therefore be considered. Physically, however, accelerations due to motion and due to gravity are indistinguishable, a fact also referred to as Einstein's equivalence principle, or the GIF-resolution problem (cf. Merfeld 1995).

Intermezzo: Motion and gravity. By Newton's second law we know that a mass m moved with an acceleration $a = d^2x/dt^2$ (with x representing position) is subject to a force $\underline{F} = m\underline{a}$, or any mass m to which a force F is applied tends to move with an acceleration a (and hence, the ratio F/a is a constant m). If two masses are involved (e.g. one being yourself and the other being the huge mass of earth), these will attract each other with a force proportional to both these masses (Newton's gravitational law). As before, this force provokes an acceleration specifically denoted by g . So, when moving on earth we only "feel" the resultant of these accelerations, $\underline{f} = \underline{a} + \underline{g}$, where the specific force f is also called the gravito-inertial acceleration (GIA). To distinguish between \underline{a} and \underline{g} , angular information is essential too, because head tilt may result in a condition with an equal head-referenced GIA as compared to one of pure linear acceleration.

By path integration we may calculate position from acceleration. If we would then not discern gravity as such we might feel like an astronaut within five minutes, ($\Delta x = \int \int g dt^2 = \frac{1}{2} g t^2 \approx 440 \text{ km}$), with $g = 9.81 \text{ m/s}^2$ and $\Delta t = 300$

s). Of course this is not the case, indicating that our CNS employs some algorithm to filter out gravity. An example regarding this peculiarity that is often overlooked in the literature on spatial orientation is given by the somatogravic effect. The semicircular canals (SCC) are the part of the labyrinth in the inner ear that detects angular velocity (ω), and the otoliths are sensitive to the GIA. The otoliths alone cannot make the distinction between rotation and linear acceleration, as is shown in Figure 9.3. Moreover, because motion in the three-dimensional space should be described by six degrees of freedom (three rotational and three translational), both canal and otolith afferents are needed. For the CNS, the GIA is head referenced (the otoliths are head fixed), while gravity is earth fixed. Hence, the acceleration \underline{a} needed for proper path integration should be calculated by

$$\underline{a} = R_{\omega}(\underline{f}) - \underline{g}$$

Here, R_{ω} represents the matrix determined by canal afferents (ω) to rotate the head-referenced GIA into an earth-referenced vector. It is essential that the rotation R is accurate (Vieville and Faurgas 1990; Mergner and Glasauer 1999), and perhaps more importantly, that gravity is known a priori.

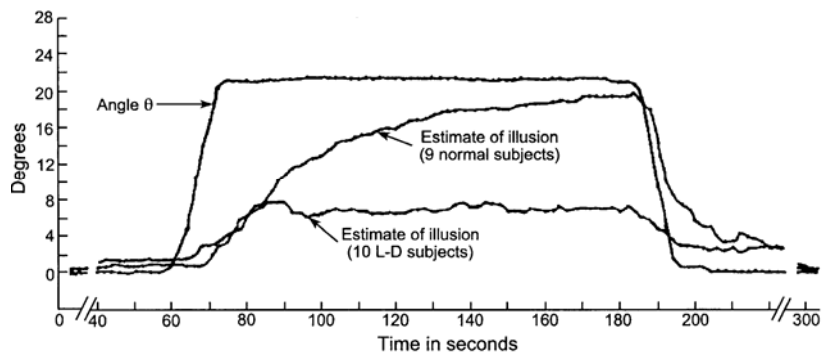


Figure 9.3: Average estimated angle of tilt (θ) as observed by nine normal subjects and ten labyrinthine-defective subjects (L-D subjects), experiencing a centripetal acceleration of approximately $0,4 g$ from $t = -60 s$ to $t = +185 s$ (after Graybiel and Clark). (Source: Bos and Bles, 2002)

Under natural conditions, i.e. of self-propelled (loco) motion, our vestibular system as a whole functions near perfection: we can control our body motion well (we rarely fall over), we can realize a satisfactory visual fixation and we do not get sick from motion. To this end we are equipped with sensors such as the eyes and a somatosensory and a vestibular system. It is only under artificial conditions such as being moved by a ship, or with incongruent vestibular and visual motion in a simulator, for example, that the system is driven beyond its range of near perfection and troubles with balance, gait, vision or sickness may occur.

With advancing technology we are faced more and more with such unnatural conditions, therefore knowledge on canal-otolith interactions becomes even more relevant. In elaborating this interaction while focusing on the vestibular cues, often under unnatural conditions the following imperfections are at stake. First, angular velocity is not sensed without errors by the SCC, e.g. there is no difference in the firing rate of SCC afferents between zero and constant angular velocity (see Chapter 7, and the Ferris wheel illusion in this section). Second, the assumption that our CNS "knows" \underline{g} a priori is inappropriate. Both its magnitude and its orientation with respect to earth should then either be (genetically) predetermined or (more likely) set at conception, for example.

Because sequences of DNA probably do not track orientation, an exclusive genetic origin can be ruled out. An initialization at conception is also unlikely, since then it should be known by the impregnated cell that it is not moving with respect to earth, while its attitude has to be known. Hence knowledge (in a perceptual, and not in a cognitive sense) about gravity can only be gained during life, and due to the equivalence principle, filtering out gravity is a matter of inference, and not of physics. As a consequence, any model that relies on initial settings for motion and gravity therefore cannot represent the true function of our vestibular system.

The somatogravic effect and the Ferris wheel illusion may help better understand the way our CNS solves this GIF-resolution problem. Both effects concern our sense of verticality, or subjective vertical (SV), when only somatosensory and vestibular cues are at stake. We will therefore first consider the SV below.

Subjective vertical

Most if not all-living beings seem to experience a sense of verticality. Humans are fully aware of what is "up" and what is "down", even with the eyes closed (Bourdon 1906). It is not known why this is so and why the outer world is not perceived tilted or even inverted (Stratton 1896). We do know that several senses are involved. Vision is important, because trees and houses are naturally oriented vertically and their substrates are mostly horizontal, for example. Our vestibular system senses how we move and how we are oriented with respect to gravity. Somatosensory cues (e.g. ankle joints, abdominal graviceptors, neck muscle afferents and "seat of the pants"; see also Mittelstaedt and Fricke 1988; Mittelstaedt 1992) all typically point at the direction of the GIF. Depending on how it manifests itself, the perceived vertical (percept of \underline{g}) has been given various adjectives such as visual, kinaesthetic, postural, subjective, apparent or gravitational (Graybiel and Brown 1951; Gibson and Mowrer 1938; Gibson 1952, Mittelstaedt 1983, 1988). Here, we will use the term "sensed vertical" (denoted by \tilde{g}) for the estimation of gravity as determined by our senses and "subjective vertical" (denoted by \hat{g}) when specifically the output of further processing by an internal model is meant. The abbreviation SV refers to any derivative of either the sensed or subjective vertical. Unfortunately, only these derivatives can be measured by verbal responses, joystick manipulations or adjustments of a visual line for example.

9.1.2.2 Sensory illusions

Somatogravic illusion

The past two centuries have revealed many observations on how the SV behaves. Purkinje (1820) perceived a tilt during "centrifugation" in a merry-go-round, and Mach (1898) used a dedicated centrifuge and first observed a tilt asymmetry in response to acceleration and deceleration. Helmholtz (1866) also noticed that aboard a ship the cabin is seen stationary at first with a suspended barometer appearing to sway, whereas after a while the perceived vertical is "anchored to gravity" again. Wertheimer (1912) examined the tilt of this vertical induced by a tilted mirror image of the surroundings, indicating that vertically is attracted towards visual verticality within a period of minutes. Gibson and Mowrer (1938) lucidly reviewed a number of these examples. Temporal aspects became more clear with the advent of jet-aircraft (Graybiel et al. 1947; Clark and Graybiel 1949) and the subsequent construction of high-G human centrifuges (Graybiel and Brown 1951; Clark and Graybiel 1963, 1966; Graybiel and Clark 1965). When a subject is fixed to the end of a centrifuge arm

(a distance r from the centre) and he is rapidly brought to constant angular velocity (ω) about an earth vertical axis, he will experience a centripetal acceleration ($\omega^2 r$) which is perpendicular to the gravitational acceleration. The resultant GIA hence tilts ramp-wise with respect to the subject. It is observed that the SV only approaches the GIA asymptotically within a period of (tens of) seconds. This apparent tilt during centrifugation was termed the somatogravic (Graybiel et al. 1947) or oculogravic illusion, depending on whether it is perceived proprioceptively or visually (Graybiel and Clark 1965). Figure 9.4 shows some results of Graybiel and Clark (1965) on both healthy and labyrinthine defective subjects, indicating the significance of the vestibular apparatus regarding this effect. Observed time constants of the exponential increase from 5 s to 20 s (Graybiel and Brown 1951; Clark and Graybiel 1963; 1966; Young and Meiry 1968; Stockwell and Guedry 1970; Guedry 1974; de Graaf et al. 1996; Seidman et al. 1998). Since Graybiel et al. (1947), some models on vestibular perception do employ these data (Mayne 1974; Glasauer 1992a,b; Dies and de Graaf 1993), and others do not (Merfeld et al. 1993; Angelaki et al. 1999; Droulez and Darlot 1989; Vieville and Fugeras 1990; Holly 1997). The somatogravic effect hence illustrates that we do not employ a veridical "sense" of verticality, but adapt to the GIA instead.

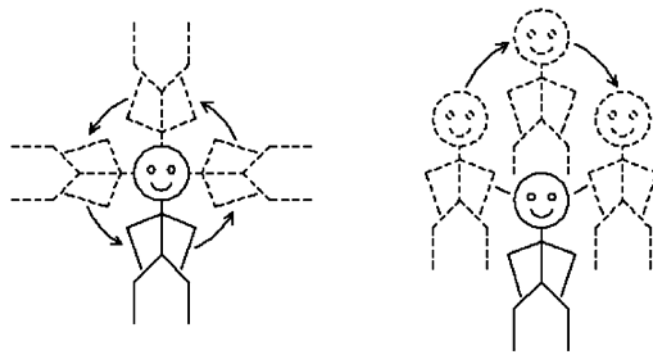


Figure 9.4: Ferris wheel illusion. A subject rotation with a constant angular velocity about an earth-horizontal axis (left) perceives a motion like a gondola of a Ferris wheel after his canal signals have returned to their rest values (right). Source (Bos and Bles, 2002)

Ferris wheel illusion.

When a subject is rotated with a constant angular velocity about an earth-horizontal axis, he will first perceive the veridical motion. But when his canal afferents have returned to their resting value (see Appendix A), normally corresponding to zero angular velocity, he will only feel a linear acceleration (Figure 9.4). Because the horizontal component of this linear acceleration is 90° out-of-phase with the vertical component, and there is no canal angular velocity signal, this is interpreted as a circular motion with some fixed orientation (Mayne 1974; Mittelstaedt et al. 1989). This latter orientation is dependent upon path integration of canal afferents, the idiotropic vector (Mittelstaedt 1983) and somatosensory cues. For example, pressure applied to the feet will result in an upward orientation, while pressure applied to the head will result in an inverted orientation (I. E. Bos, W. Dies, Personal observation, 1988; Lackner and Graybiel 1978; Mittelstaedt et al. 1989). This illusion nicely shows the deficient functioning of our canal system under unnatural circumstances.

Vection

In Figure 9.5 the results are given of a study in which the test person was fixated in relation to the earth, while a rotation room, in the form of a drum with a vertical black and white stripe pattern, was rotated around the test person. Because the rotating room is the only reference for the test person, after a while he gets the sensation of himself turning and the room standing still.

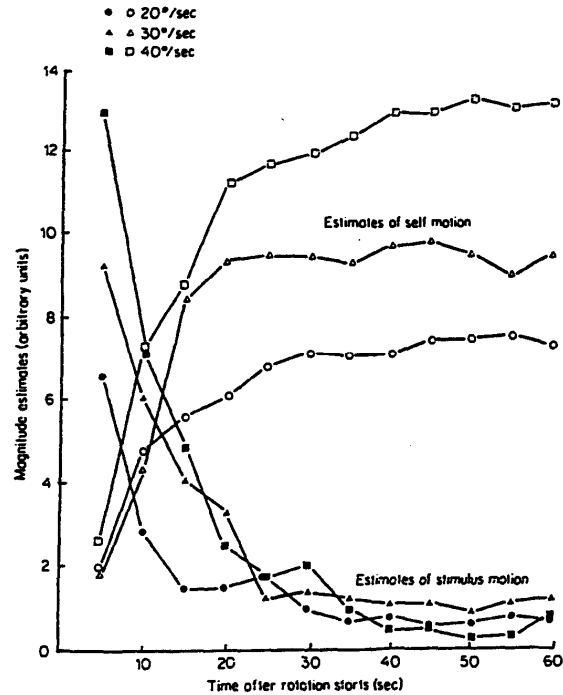


Figure 9.5: Perceived self-motion and stimulus motion in a rotating room (Circular vection)

In Figure 9.6 it can be clearly seen the occurrence of vection depend on how the subject look at the visual scene. Two situations are considered. The first in case subjects gaze though the visual pattern and the second contrast for the situation where subjects try to follow the pattern with their eyes. For first situation the perception of ego motion depends on the frequency content of the stimulus. This frequency dependency of ego-motion perception can also be clearly seen for different combinations vestibular and visual stimuli (Figure 9.7)

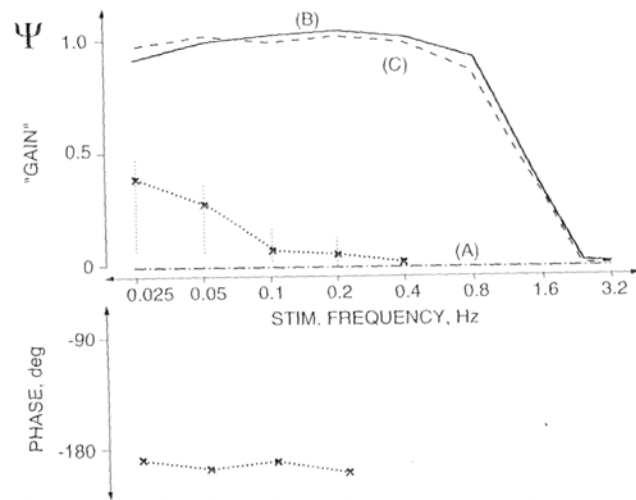


Figure 9.6: Ego-motion perception during pure visual stimulation (visual pattern rotated about stationary subject). Median 'gain' and phase values are plotted as a function of stimulus frequency. Dotted curve for the situation in which subject had to stare through the visual pattern (median pointer indications, 95 % confidence intervals). Dash-dot-dashed and continuous curves are data from the situation in which in normal subjects did follow the visual pattern instead of staring through this pattern, experiencing either no Circular Vection (A) or full vection (B) and patients with bilateral vestibular loss (C), respectively (pattern displacement ± 8 degrees) (source Mergner et al, 1995 in *Multisensory control of posture*, pp 160)

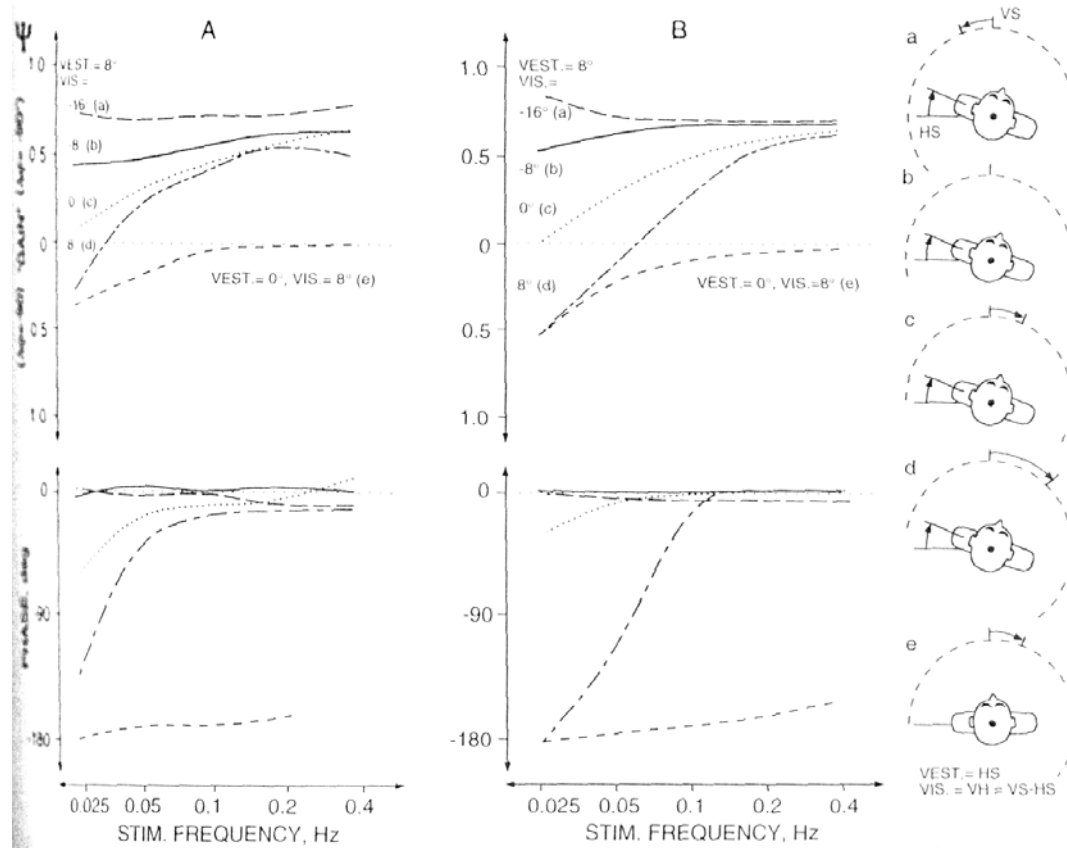


Figure 9.7: Ego motion perception during visual-vestibular stimulus combinations. Smoothed median gain and phase values are plotted as a function of stimulus frequency. A vestibular stimulus (peak displacement, 8 degrees) was combined with inphase and counter-phase visual stimuli of different amplitudes as indicated (see also insets on the right side for physical stimulus condition). Curve e is a repetition of the previous figure with gain values mirrored about the x-axis to be consistent with the gain conventions of this figure. A is experimental data; B is model of Mergner et al (not explained here) (source Mergner et al, 1995 in *Multisensory control of posture*, pp 161)

Illusions caused by constant linear acceleration

During an accelerated flight the pilot gets the sensation that he is rotated backward and that the plane is ascending, see Figure 9.8 and 9.9. This sensation has at first led to accidents with the catapult start of fighter planes from aircraft carriers, where very large accelerations occur. Here the flyers steered against the supposed ascending and ended up in the sea.

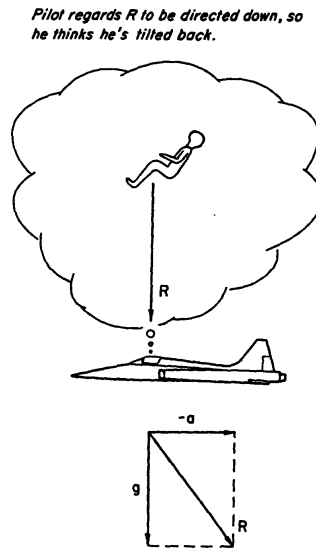


Figure 9.8: Influence of the resultant of the specific force on the position perception

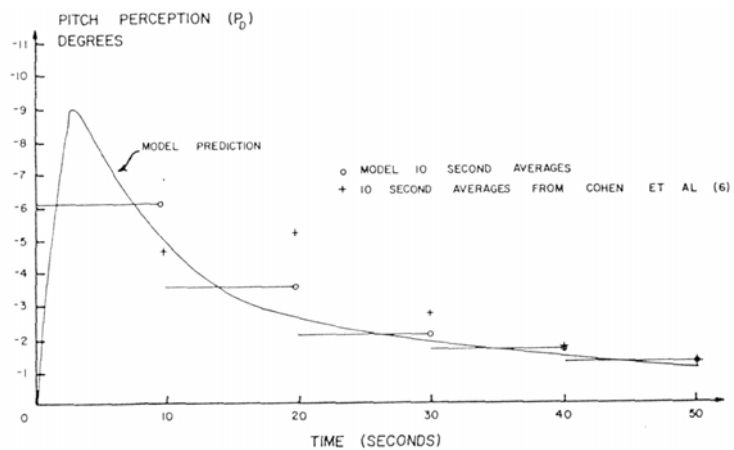


Figure 9.9: Pitch perception for catapult launch simulation (source Ormsby and Young)

9.1.2.3 Human perception in human-machine control

However, the visual and the vestibular system can also cooperate well. If with a flight simulator the dynamics of an inverted pendulum are simulated, it can be investigated how the test person performs the stabilization task with only visual information or with both visual and vestibular information. The position of the pendulum is then presented using a display or the position of the simulator or both. In Figure 9.10 RMS of the position of the pendulum are plotted against the unstable eigenfrequency of the pendulum. The measurements are performed under two conditions. The first with a display that presented the position of the pendulum in the central field of view, and the second with the central display supplied by the simulated motion of the pendulum.

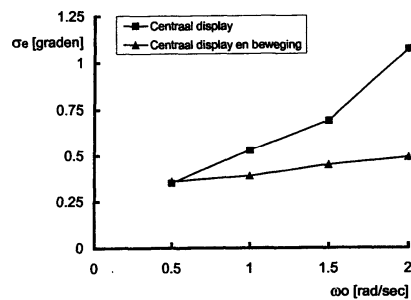


Figure 9.10: The influence of the visually and vestibular perceived movement on the stabilization of an inverted pendulum as a function of the eigenfrequency ω_0 .

The positive influence of the simulated movement on the steering performance is clear. The cause of this positive influence lies in the dynamical properties of the organ of equilibrium. Like shown in Chapter 7, the phase of the output signal of the semicircular canals leads the rotational velocity. Hosman (1996) demonstrated that this lead can be determined using measurements and has a value of at least 150 ms.

9.1.3 POSTURAL CONTROL

Postural control is a complex process of integrating sensory information and selecting muscle actions based on this information, in order to maintain standing in specific environmental conditions. Although we can measure outside signals such as reaction forces, kinematics etc. directly, we do not have direct access to inside signals and processes responsible for postural control. Combining experimental data with a model approach offers the possibility to gain insight in processes and the influence of constraints, which are hidden in experimental data. Observed postural sway and stability is highly context dependent and sensitive to the availability and precision of sensory information (see overview [Horak et al, 1996]). This dependency is demonstrated by numerous elegant experiments where the support base was rotated or translated, where vision was blocked, with patients with vestibular loss or somatosensory deficits. In figure 9.11 the six different experimental conditions of the Sensory organization test are shown. The idea behind sway referencing the platform or the visual scene is to remove proprioceptive and/or visual clues about postural orientation (with respect to the earth vertical) and to study postural responses in order to study the contribution of the different sensory systems in postural control. The problems with available data are the large inter and intra individual differences and a lack of a verified theoretical framework to interpret the complex postural responses.

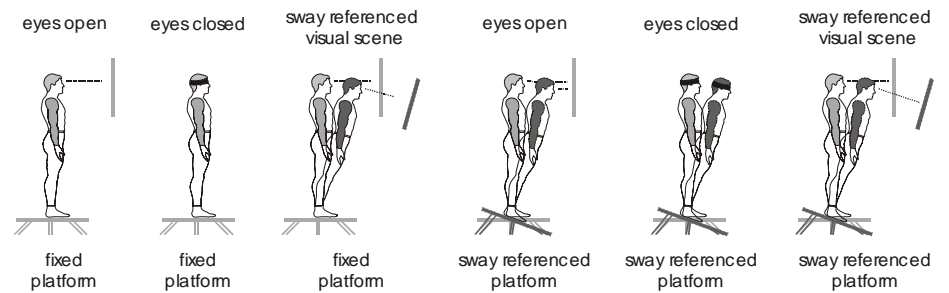


Figure 9.11: Six sensory conditions are used to evaluate postural control: (1) Eyes open and fixed platform; (2) Eyes closed and fixed platform; (3) Sway referenced visual scene and fixed platform; (4) Eyes open and sway referenced platform; (5) Eyes closed and sway referenced platform (6) Sway referenced visual scene and platform. Sway referencing the visual scene or the platform is a technique that ‘clamps’ the visual scene or the platform to the body, respectively. When the visual scene is sway referenced the distance between the eyes and the visual scene remains constant. In this condition the visual clues no longer provide any information about postural orientation with respect to the earth vertical. When the platform is sway referenced, the ankle joint angle remains constant. In this condition muscle spindles around the ankle no longer provide any information about postural orientation with respect to the earth vertical

Artificial stimulation of sensory systems also shows that in the control of posture different sensory systems are involved (Figure 9.12). Although artificial stimulation give a qualitatively insight in how the different senses contribute to postural control it is very difficult to obtain quantitative relations between sensory inputs and postural responses since the sensory inputs are not very well defined in case of artificial stimulation of these senses.

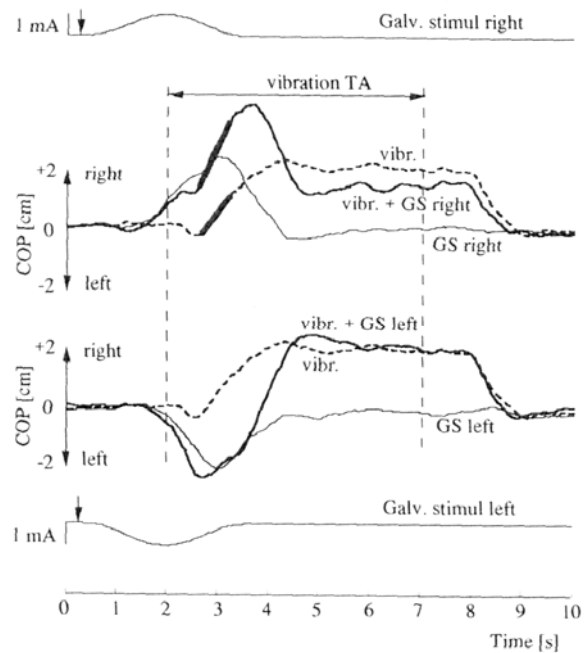


Figure 9.12: Left right of Centre of Pressure (COP) as a function of time for vestibular (GS rights or GS left-thin line), vibratory (vibr. Dashed line, TA-m.tibialis ant.) and for paired stimulation (vibr.+GS-heavy line). Arrows on the galvanic stimulus curves indicate the onset of vestibular stimulation. Vertical dashed lines indicate the onset and determination of muscle vibration. Curves are formed by averaging the results from 10 subjects. (source Hlavacka and Krizkova et al, 1995 in *Multisensory control of posture*, pp 160)

9.2 An adaptive model of sensory integration in a dynamic environment (modified from van der Kooij et al., 2002)

9.2.1 INTRODUCTION

To control posture, postural orientation has to be known. Humans utilise multiple sources of sensory information to orient themselves in space. When the visual scene or support base is fixed, visual or proprioceptive information is sufficient to define postural orientation with respect to the gravitational axis and both can stabilize posture (e.g. Akimase et al., 1997; Peterka and Benolken, 1995). However, when the support base is rotating or the visual scene is moving, they destabilize posture (e.g. Bolha et al., 1999; Berthoz et al., 1979). Proprioceptive and visual clues alone are insufficient to distinguish ego-motion, visual scene and support base motion from each other. In that case the vestibular system appears to be crucial to distinguish ego-motion from environmental motion (see also Mergner et al., 1991.; Mergner et al. , 1992.; Mergner et al., 1995). This is demonstrated by experiments, where for large movements of the visual scene (Peterka and Benolken, 1995) or large platform rotations (Maurer and Mergner, 1999), vestibular loss patients were not able to maintain balance in contrast to controls. By the nature of the vestibular system, it is impossible to get an ideal estimate of orientation of head in space, especially for low frequency movements (Mergner and Glasauer., 1999; Cohen

et al., 1973). In most models of the vestibular system this non-ideal low frequency behavior is included as a physical threshold (e.g. Nashner et al. 1989; Borah et al., 1988; Hosman, 1996). However, these thresholds are based on perceptual thresholds for ego-motion obtained from psychophysical studies (e.g. Clark and Stewart, 1969). There is evidence that vestibular related thresholds are from central origin and depend on other sensory clues (Mergner et al., 1995).

Among others (Borah et al., 1988; Wolpert et al. 1995; Gerdes et al. , 1994), we have described the complex process of human spatial orientation with the use of optimal estimation theory (Van der Kooij, 1999a). According to this view the control model has a kind of internal representation (IR) which includes 'knowledge' of the body and sensor dynamics and the external environment. Using this representation the control model makes an estimate of spatial orientation using both the motor and sensory output signals. These sensory and motor signals are integrated in such a way that a minimum variance estimate of postural orientation is obtained. Spatial orientation under various illusory sensations (Borah et al., 1988) and specific multivariate changes of postural sway due to altered visual or platform perturbation conditions (Van der Kooij, 1999b) can be predicted using optimal estimation theory. Optimal estimation theory, however, does not fully explain how humans integrate multisensory information. By using optimal estimation theory some 'knowledge' is required of the precision of the different sensory systems and of the external environment acting upon the body and the sensory system. This 'knowledge' is usually specified by power spectral density matrices of the sensor noise and of the disturbances acting on the body. These matrices are defined by the designer of the optimal estimator (Kalman filter) and are usually used as design variables. It is easy and tempting to use these power spectral matrices to match model predictions with experimental results. In models using a Kalman filter to model spatial orientation, the system and sensor noise statistics are used as 'tune parameters' to mimic model with experimental results (Borah et al., 1988; Wolpert et al., 1995; Gerdes et al. 1994). The statistical properties of external forces, support base translations and rotation and visual scene motion have to be specified in the human stance control model to obtain a minimum variance estimate of spatial orientation. The intriguing question of how humans solve the problem of distinguishing ego-motion from motion of the environment can not be understood within the concept of a non-adaptive observer like the (extended) Kalman filter; when using a Kalman filter the statistical properties of environmental motion are specified by the model designer.

Therefore, in this paper an adaptive estimator model of human spatial orientation is presented where, besides spatial orientation, 'knowledge' of the external environment is estimated from the sensory output signals instead of being specified by the designer. Only the sensor noise characteristics have to be specified by the model designer. We believe that the modified model is biologically more realistic.

The model is used to investigate:

1. Whether it is possible to estimate postural orientation based on sensory information only and use this estimate to stabilize posture, without specifying environmental conditions as is done in existing models of spatial orientation;
2. Whether sensor noise properties can be found by matching model predictions with experimental results;
3. Whether the model produces vestibular related thresholds without including physical thresholds;
4. Whether vestibular related thresholds can be understood by the noisy properties of the sensory signals;

5. How sensory loss affects postural control and orientation under different environmental conditions; and
6. Whether experience/ cognitive resources can be modeled within this model and how they influence postural orientation and control.

9.2.2 METHODS

Optimal estimator models of spatial orientation are usually realized by including a Kalman Filter (KF). The working of the KF is a combination of two processes. The first process uses the current estimate of spatial orientation and motor outflow to predict the next estimate of spatial orientation by simulating the dynamics using an Internal Model (IM) of the body and environment. The second process uses an IM of the sensory dynamics to predict the sensory output corresponding with this predicted next estimate. The sensory error, the difference between actual and predicted sensory output, is weighted by the Kalman gain to drive the estimate of spatial orientation, resulting from the first process, to its true value. The elements of the Kalman gain are determined by the uncertainty in the predicted next estimate (e.g. caused by an imperfect IM or uncertainties of environmental conditions) and the uncertainty in a sensory output signal. These uncertainties are specified by the designer of the KF as power spectral density matrices of the sensor noise and of the external environmental variables acting on the body. We modified our human stance control model (Van der Kooij, 1999a) by replacing the KF with an adaptive KF. In the original model the statistical properties of mechanical disturbances, platform rotation and accelerations and visual scene motion had to be specified by the model designer. In the modified model these statistical properties of the environment acting on the body are estimated by the adaptive KF simultaneously with the estimate of spatial orientation based on sensory and motor output signals only. Only the sensory noise levels have to be specified by the model designer and they are assumed to be stationary.

Besides replacing the extended with an adaptive KF, the following modifications to the model were made (Figure 9.12):

1. Since, in this paper, we do not focus on inter-segmental co-ordination but on postural orientation in space, the segment was reduced to an inverted pendulum model to save computational power;
2. The model was linearized and converted to a discrete-time system with a sample time of 10 ms. The predictor, which compensates for neural time delays is realized as a tapped delay line (Appendix A);
3. In the original model the visual scene was defined fixed in space or relative to the support base. The visual scene is now allowed to move. As a consequence visual scene motion is defined in the IM of the environment as a state variable;
4. Vertical platform motion was excluded; and
5. Other tactile afferents than the one sensing shear forces were not included in the model.

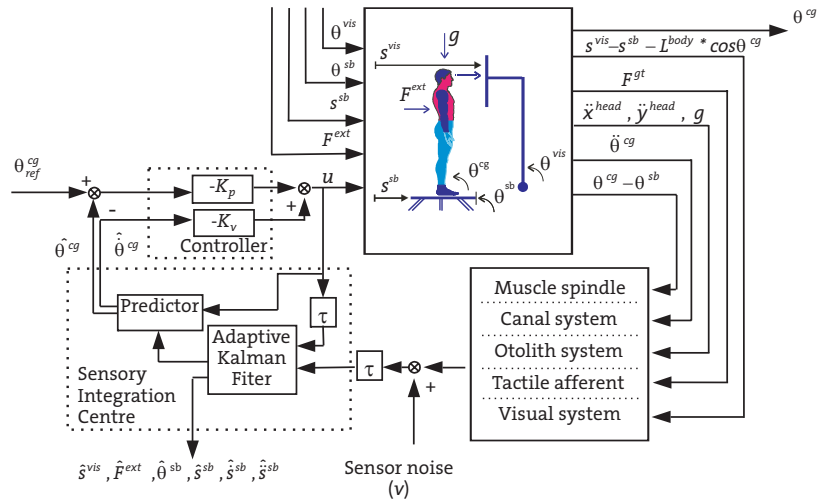


Figure 9.12: Schematic view of modified human stance control model. Standing person is modeled as an inverted pendulum exposed to environmental variables. The person stands on a support base, which can translate (s^{sb}) and rotate (θ^{sb}). External forces acting on the body are support base accelerations, external forces (F^{ext}) and gravity (g). The modeled person looks at a visual scene at distance s^{vis} . The visual scene can rotate around an axis (θ^{vis}). Different sensor systems are modeled. Input to the muscle spindle is ankle joint angle. Input to the canal systems is angular acceleration of the head. Inputs to the otolith system are gravitational and linear accelerations of the head. Input to the visual system is the distance between the head and the visual scene. Input to the tactile afferents is shear force at the sole. Based on delayed sensory output signals and synchronized control inputs, an adaptive Kalman filter estimates postural orientation and environmental conditions for $t-\tau$. A predictor compensates for the neural time delays ($\tau=100$ ms). The controller to stabilize posture with respect to the desired orientation uses the resulting estimate of spatial orientation.

9.2.2.1 Adaptive sensory integration centre

To obtain an optimal estimate of spatial orientation, the environmental dynamics has to be included in the IM used by the KF (Van der Kooij et al., 1999a). After the above-mentioned modifications the IM is defined in discrete state-space format by:

$$\begin{bmatrix} \underline{x}_k^{body} \\ \underline{x}_k^{env} \end{bmatrix} = \begin{bmatrix} A^{body} & A^{env2body} \\ 0 & A^{env} \end{bmatrix} \begin{bmatrix} \underline{x}_{k-1}^{body} \\ \underline{x}_{k-1}^{env} \end{bmatrix} + \begin{bmatrix} B \\ 0 \end{bmatrix} u_{k-1} + \begin{bmatrix} 0 \\ G \end{bmatrix} w_{k-1}^{env} \quad (9.1a)$$

$$\underline{y}_k = \begin{bmatrix} H^{body} & H^{env} \end{bmatrix} \begin{bmatrix} \underline{x}_k^{body} \\ \underline{x}_k^{env} \end{bmatrix} + D u_{k-1} + \underline{v}_k \quad (9.1b)$$

where,

\underline{x}_k^{body} is the state vector of body and sensor dynamics; including the states of the sensor dynamics (\underline{x}^{sen}) and the orientation and velocity of the body with respect to the earth vertical axis ($\theta^{cg}, \dot{\theta}^{cg}$). The sensor dynamics are obtained from literature (Borah et al., 1988; Appendix B);
 \underline{x}_k^{env} is the state vector of the environment including the orientation of the support base with respect to the earth vertical (θ^{sb}), external forces acting on the body (F^{ext}), horizontal support base displacement, velocity and acceleration of the support base ($s^{sb}, \dot{s}^{sb}, \ddot{s}^{sb}$) and the position of the visual scene (s^{vis});

u_{k-1} is the control moment to stabilize the body generated by a PD controller;

w_{k-1}^{env} are the random forcing functions of the environmental variables;

v_k is the sensory output;

v_k is the sensory output noise;

A^{body} is the representation of the body and sensor dynamics;

$A^{env2body}$ is the representation of the effect of the environment on body and sensor dynamics;

A^{env} is the representation of environmental dynamics;

B is the control input distribution matrix;

G is the noise input matrix;

H^{body} is the mapping of the body states on the sensory output vector;

H^{env} is the mapping of the environmental states on the output vector;

D is the mapping of the control inputs on the sensory output vector.

In compact form Equation 9.1 is given by:

$$\underline{x}_k = A\underline{x}_{k-1} + B u_{k-1} + w_{k-1} \quad (9.2a)$$

$$\underline{y}_k = H \underline{x}_k + D u_{k-1} + v_k \quad (9.2b)$$

The random vectors w_{k-1} and v_k are treated as independent, non stationary, Gaussian, white noise sequences with the properties

$$E[w_i] = 0, E[w_i w_j] = Q_i \delta_{ij} \quad (9.3a)$$

$$E[v_i] = 0, E[v_i v_j] = R_i \delta_{ij} \quad (9.3b)$$

where Q_i and R_i are true moments about the mean of the state and sensory output noise sequences respectively. Since changes in the external world are a priori not known, these possible changes are included in the IM as random walks; i.e. a differential equation with stochastic inputs (\underline{w}) (Van der Kooij et al. 1999a; Appendix C). In our model, the strength of the state noise, \underline{w} , is related to the first derivatives of support base rotations, external disturbances, horizontal support base accelerations and visual scene motion (Appendix C). So, in our model the state noise is directly related to the physics of the external world. The state noise only exists in the IM to model the external world but is not put into the model of the standing person (Figure 9.12, \underline{w} is not put into the model). Since in this paper only finite motions of the environment are considered, the assumption that \underline{w} is zero mean distributed (Equation 9.3a) is not restricting.

An optimal estimate for the system defined by Equation 9.2 is obtained with the standard KF:

$$\begin{aligned} \text{State propagation} \quad \underline{\bar{x}}_k &= A\hat{\underline{x}}_{k-1} + Bu_{k-1} \\ \underline{\bar{P}}_k &= A\hat{P}_{k-1}A^T + Q_{k-1} \end{aligned} \quad (9.4a)$$

$$\text{Observation residual} \quad \underline{z}_k = \underline{y}_k - H\underline{\bar{x}}_k \quad (9.4b)$$

$$\text{Kalman gain} \quad K_k = \underline{\bar{P}}_k H^T [H\underline{\bar{P}}_k H^T + R_k]^{-1} \quad (9.4c)$$

$$\begin{aligned} \text{State estimation} \quad \hat{\underline{x}}_k &= \underline{\bar{x}}_k + K_k \underline{z}_k \\ \hat{P}_k &= \underline{\bar{P}}_k - K_k H \underline{\bar{P}}_k \end{aligned} \quad (9.4d)$$

where $\underline{\bar{x}}_k$ and $\underline{\bar{P}}_k$ are the propagated state and error covariance conditioned on observations prior to time t_k . $\hat{\underline{x}}_k$ and \hat{P}_k are the estimated values after the new sensory output vector \underline{y}_k has been processed. When the statistics of state noise and sensor noise are known as a function of time the KF supplies an optimal estimate. In many applications these statistics are however not known a priori. In most applications these statistics are assumed constant and chosen a priori based on experimental data or design criteria.

An optimal filter for state estimation under unknown noise statistics does not exist (Myers and Taply, 1976). Many suboptimal schemes have been derived. All methods can be classified into two approaches: (1) the direct approach identifying the KF gain from data directly (e.g. Juan et al., 1993) ; and (2) the indirect approach estimating the noise statistics first and then using them to compute the Kalman filter gain (Equation 9.4). We followed the second approach. We modified the method of Myers and Taply (1976), to sequentially estimate the state noise statistics. We assume that the sensor noise statistics (R) are constant and known. Myers and Taply derived an unbiased estimator for Q given by (Appendix D):

$$\hat{Q} = \frac{1}{N-1} \sum_{j=1}^N \left\{ (\underline{q}_j - \hat{\underline{q}})(\underline{q}_j - \hat{\underline{q}})^T - \left(\frac{N-1}{N} \right) [A\hat{P}_{j-1}A^T - \hat{P}_j] \right\} \quad (9.5a)$$

$$\hat{\underline{q}} = \frac{1}{N} \sum_{j=1}^N \underline{q}_j \quad (9.5b)$$

$$\underline{q}_j \equiv \hat{\underline{x}}_j - A\hat{\underline{x}}_{j-1} - Bu_{k-1} \quad (9.5c)$$

After the state estimation (Equation 9.4d), Q_k is estimated based upon the last N noise samples \underline{q}_j ($j=k-N+1, \dots, k$) at time t_k . The diagonal elements of \hat{Q} are always reset to the absolute values of their estimates. For first N time-steps of the simulation, Q is set to the initial value $Q_0 = GQ_0^{env}$ and \hat{Q} is estimated for $k > N$.

9.2.2.2 Evaluation of the adaptive sensory integration model

First, the minimal set of sensory systems was determined for which it is possible to obtain a stable estimate of postural orientation without specifying environment conditions. External disturbances (F^{ext}) and support base displacements (s^{sb}) were applied to the model. Sensory output signals were assumed to be ideal, i.e. not distorted with noise ($R \sim 0$). Next, the effect of imperfect sensory signals was investigated by adding white noise to the sensory output signals. Model responses to sinusoidal⁹ movements of the visual scene were compared with experimental results of visual induced sway. Finally, model responses to sinusoidal support base rotations were calculated and qualitatively compared with experimental findings.

For all simulations the mass of the pendulum was 80 kg, the length 1.8 m, the height of CoM 1.1 m and the moment of inertia around CoM 24.8 kgm². For all simulations the controller was implemented as a Proportional Derivative controller with $K_p=1815$ and $K_v=560$. The number of samples used to estimate Q was $N=16$. The initial value of Q was $Q_0=GQ_o^{env}$ with $Q_o^{env}=I * 1e-9$, where I is a 4x4 unity matrix. To initialize the filter for the first 14 seconds only sensory noise was put into the model.

Minimal set of sensory systems

At first, the modeled sensory systems were assumed to be ideal; sensory output signals were not distorted with noise ($R \sim 0$). Disturbances applied to the model were either a combination of sinusoidal external disturbances (F^{ext}) applied at a height of 1 m, and support displacements (s^{sb}) or external disturbances only. The frequency of F^{ext} was 1 Hz and the amplitude 10 N. The frequency of s^{sb} was 0.5 Hz and its amplitude 10 cm. The ability to maintain standing was examined for different scenarios: (1) non rotating support base and fixed visual scene; (2) sway referencing¹⁰ the support base, keeping the ankle joint constant; (3) sway referencing the visual scene, keeping visual input constant; and (4) simultaneously sway referencing the support base and visual scene.

Sway referencing the visual scene and support base was initiated at the start of applied perturbations. To obtain minimal sets of sensory systems for the four different scenarios, sensory loss was simulated, by removing the corresponding sensory system from the model. Normalized peak to peak amplitudes of the Centre of Gravity sway angle ($\theta_{cg}(t)$) are used to quantify the effect of sensory loss for the four different scenarios. Peak to peak amplitudes of postural sway were normalized to the condition for which the visual scene was fixed, the support base was not rotating and no sensory loss was modeled.

Model responses to sinusoidal visual scene displacements

The effect of imperfect sensory signals was studied by adding white noise to the sensory output signals. Sensory noise was applied to the model for the: (1) muscle spindle; (2) canals; (3) otoliths; (4) visual system; and (5) tactile afferents (Figure 9.12). The strength of the noise for the five different sensory

⁹ We are aware that it is better to use stochastic inputs instead of sinusoidal inputs to obtain the frequency response function of a closed loop system. However in order to compare model responses with reported experimental results sinusoidal inputs were applied to the model.

¹⁰ Sway referencing the support base/ visual scene is a technique to position the support base/ visual scene in such a way that the orientation/ distance of the support base/ visual scene relative to the body remains constant, thereby eliminating proprioceptive and visual clues about postural orientation with respect to the earth vertical.

systems was determined by trying to mimic the experimental results of visual induced sway (Peterka and Benolken, 1995). Appropriate noise levels were found by trial and error. Different sinusoidal visual scene displacements were applied to the model. The following specifications of the simulations are adapted in agreement with the experiments of Peterka and Benolken (1995). The visual scene rotated around an axis, which was colinear with the ankle joint axis and was located about 10 cm above the ankle (Fig 9.12, $s^{\text{vis}}=0.65-(1.80-0.1) \cdot \sin(\theta^{\text{vis}}-\pi/2)$). The visual scene was located about 65 cm from the eyes. The model was evaluated for fixed and for sway referenced support base conditions. Removing the vestibular organ from the model simulated the performance of vestibular loss patients. The visual scene was rotated using sinusoids of two different frequencies (0.1 Hz and 0.2 Hz) and with six different amplitudes (0.2°, 0.5°, 1°, 2°, 5° and 10°). All combinations were applied for 60 seconds. All trials were repeated 30 times with the same initial settings to average the effect of sensor noise. Sway referencing was initiated at the start of the sinusoidal visual scene motion. The Centre of Gravity sway angle ($\theta_{cg}(t)$) was used to evaluate the model response. Fourier analyses of the Centre of Gravity (CG) angle and the visual scene angle time series were used to calculate the amplitude of the CG sway relative to visual scene motion. The discrete-time Fourier transform of sampled CG sway angle and the visual scene angle time series evaluated at frequency f are defined as:

$$\theta^{cg}(f) = F[\theta^{cg}(i)] \quad (9.6a)$$

$$\theta^v(f) = F[\theta^v(i)] \quad (9.6b)$$

where $\theta^{cg}(i)$ is the sampled CG sway angle and $\theta^v(i)$ is the sampled visual scene angle time series from the simulations.

The frequency response function¹¹, $H_{v2cg}(f)$, between the visual stimulus and CG sway is defined as:

$$H_{v2cg}(f) = \frac{\theta^{cg}(f)}{\theta^v(f)} \quad (9.7)$$

The first cycle of CG angle and visual scene angle time series were excluded from the Fourier analysis. Fourier analysis was performed over a range of frequencies to test whether the model showed a clear response to the visual stimuli. Amplitudes of the CG sway and of the frequency response function were calculated at the frequency of the visual stimulus.

9.2.3 RESULTS

9.2.3.1 Minimal set of sensory systems

The model is able to resist external forces in case of ideal sensory output signals from muscle spindles, the vestibular organ, the visual system and tactile afferents sensing shear forces from the sole (Table 1, A). Even for sensory conflict conditions, like sway referencing the support base and/or the visual

¹¹ In general it is better to use the cross-spectral density to calculate the frequency response function. However, since the data of Peterka (1995) is used, his approach is adopted and the quotient of the Fourier transform of input and output signals is used to calculate the frequency response function.

scene, the model predicts a stable posture. Loss of somatosensory or visual information hardly affects posture, even when both the visual scene and the support base are sway referenced (Table 9.1, B; D and E). Without vestibular function the model predicts stable standing if the visual scene and support base are fixed (Table 9.1, C1). However, in case of sensory conflicts the vestibular organ seems to be crucial. Without a vestibular system, the model is not able to obtain a stable estimate of posture and falls are predicted for those cases where sensory conflicts occur in combination with small external disturbances (Table 9.1, C2-C4). Surprisingly the model predicts a decrease in CG sway when proprioception is excluded. Although the relative differences are considerable, the absolute differences are very small (maximal 0.05°). The differences are difficult to interpret, since only one specific stimulus was applied to the model.

These results are in agreement with the experimental results of the Sensory Organization Test (SOT) for controls and vestibular loss patients (Black et al., 1988). Controls were able to maintain standing during the SOT, even when the support base and/ or the visual scene was sway referenced. Vestibular loss patients were able to maintain standing when sensory conflicts were absent. However, in case of sway referencing the support base and/or the visual scene the majority was unstable for these sensory conflict situations.

				
Sensory loss	1	2	3	4
A: No Loss	1	0.7	1	0.7
B: Muscle spindle	0.8	0.9	1	1
C: vestibular	1*	X*	X	X
D: vision	1	0.7	-	-
E: Tactile	0.8	1*	1	1*

Table 9.1: Effect of sensory loss in the presence of external disturbances

($F^{ext}(t) = 10 \cdot \sin(2\pi \cdot 1 \cdot t)[N]$); four different scenarios are considered: (1) fixed support base and visual scene; (2) sway referencing the support base; (3) sway referencing the visual scene; and (4) sway referencing the support base and visual scene. The effect of sensory loss was modelled by removing different sensory systems. Shown are the amplitudes of the CG sway angles, normalized to condition A1: fixed visual scene, non rotating support base and no sensory loss. In some conditions the model predicted instability (denoted by crosses). Stars indicate excessive initial responses at the onset of the disturbance.

When all sensory systems are included the model is able to resist a combination of external forces and support base displacements, (Table 9.2, A). The effect of somatosensory loss is different compared to the situation without support base displacements (Table 9.1). Removing the muscle spindles or tactile afferents from the model results in an increase in CG sway by a factor 4 (Table 9.2, B and E). For additional sinusoidal support displacements, the effect of vestibular loss is even worse compared to the case of external forces only. After removal of the vestibular system the model is not able to maintain standing even when the support base is not rotating and the visual scene is fixed (Table 9.2, C).

Not much is known about the contribution of skin afferents in postural control.

However, after anaesthesia of both feet and ankles subjects altered their postural responses to sudden support base displacements resulting in excessive body sway (Horak et al., 1990). This experimental finding is in agreement with the predicted increase in CG sway during platform translations due to loss of tactile afferents (Table 9.2, E) or loss of muscle spindles (Table 9.2, B). However, also in this case we should be careful since only one specific stimulus was applied to the model.

The inability of the model to stabilize posture without vestibular function but with reliable visual and muscle spindle input (Table 9.2, C1) is at first glance surprising. Vestibular loss patients are able to maintain standing when exposed to sudden support displacements even with eyes closed (Runge et al., 1998). The difference with the model simulations is that these experiments studied the effect of short support translations of a few centimeters. However, vestibular loss patients will fall when exposed to continuous sinusoidal translations of the support base even with eyes open (Buchanan and Horak, 1998).

				
Sensory loss	1	2	3	4
A: No Loss	1	1	1	1
B: Muscle spindle	4	4	4	4
C: vestibular	X	X	X	X
D: vision	1	1	-	-
E: Tactile	4	4*	4*	4

Table 9.2: Effect of sensory loss in the presence of simultaneously external disturbances ($F^{ext}(t) = 10 \cdot \sin(2\pi \cdot 1 \cdot t)[N]$) and support base translations ($s^{sb}(t) = 0.1 \cdot \sin(2\pi \cdot 0.5 \cdot t)[m]$); four different scenarios are considered: (1) fixed support base and visual scene; (2) sway referencing the support base; (3) sway referencing the visual scene; and (4) sway referencing the support base and visual scene. The effect of sensory loss was modelled by removing different sensory systems. Shown are the amplitudes of the CG sway angles, normalized to condition A1: fixed visual scene, non rotating support base and no sensory loss. In some conditions the model predicted instability (denoted by crosses). Stars indicate excessive initial responses at the onset of the disturbance.

9.2.3.2 Model responses to sinusoidal visual scene displacements

The variance of signal noise for muscle spindles is: $V_{spin}=1.1e-6$; for sole afferents, $V_{sole}=33$; for semicircular canals, $V_{sem}=0.21$; for otoliths, $V_{oto}=65$ and for vision $V_{vis}=1.2e-5$. For these noise intensities, the model predictions match with the experiment results (Figure 9.13). The amplitude of model predicted visual induced sway in controls depends on stimulus frequency, stimulus amplitude and support face condition (Figure 9.13). The amplitude of CG sway for sway referenced conditions is larger than for fixed support base conditions, for any stimulus frequency and amplitude. The amplitude of CG sway increases with stimulus amplitude until a saturation level is reached. For sway referenced conditions the saturation level is four times higher than for fixed support base conditions. The saturation level decreases with increasing stimulus frequency.

The instant at which saturation occurs also depends on stimulus frequency and support base condition. For sway referenced conditions and for faster stimulus frequencies the CG sway saturates at larger stimulus amplitudes.

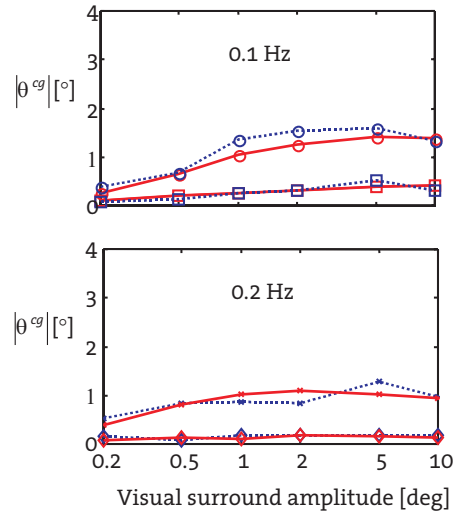


Figure 9.13: Mean CG sway amplitude induced by visual scene motion as a function of stimulus amplitude. Model prediction (solid lines) and experimental results (dotted; Pertka and Benolken 1995) in normal subjects. Top panel, stimulus frequency 0.1 Hz; bottom panel, stimulus frequency 0.2 Hz. Support base was fixed (boxes and diamonds) or sway referenced (circles and crosses).

In fixed support base conditions the gain for normal subjects is always less than unity (Figure 9.14). For sway referenced support base conditions, the gain is larger than unity for small stimulus amplitudes. The gain decreases in proportion with the logarithm of stimulus amplitude until the saturation effect occurs. Again, model simulations are similar to the experimental results. In Figure 9.14 the non-linear input-output behavior is clearly seen; for linear systems, the gain would not be dependent on the amplitude of the input stimulus.

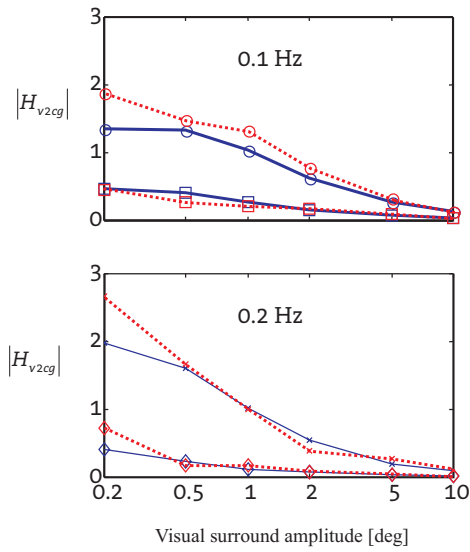


Figure 9.14: Gain of mean CG sway amplitude induced by visual scene motion as a function of stimulus amplitude. Model prediction (solid lines) and experimental results (dotted; Pertka and Benolken 1995) in normal subjects. Top panel, stimulus frequency 0.1 Hz; bottom panel, stimulus frequency 0.2 Hz. The support base was fixed (boxes and diamonds) or sway referenced (circles and crosses).

Sensory errors arise due to sensory output noise, external forces and motion of environment. It can be clearly seen that for the smallest amplitude of visual scene motion the sensory errors are dominated by sensory output noise (Figure 9.15, left and middle). For the largest amplitude of visual scene motion, the visual scene motion can be clearly seen in the sensory errors (Figure 9.15, right). From Figure 9.15 it can also be understood why the sensory output noises of the different systems dramatically differ. Due to different sensor dynamics (Appendix B), the sensitivity of the sensory organs differs as reflected in the sensory errors (Figure 9.15, right). The found sensory output noises are in proportion to the changes in sensory output signal due to ego-motion or motion of the environment.

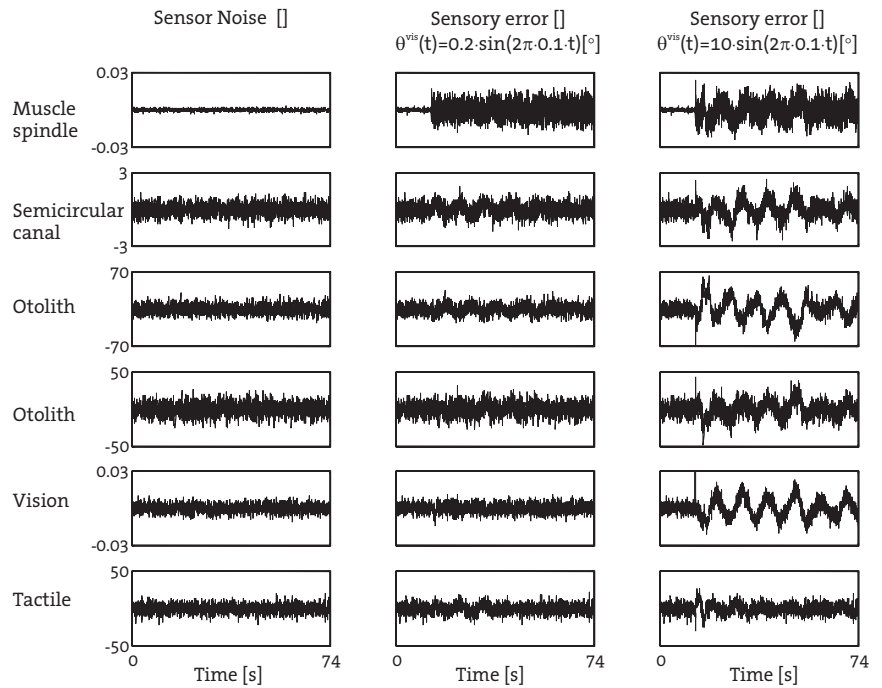


Figure 9.15: Noise properties of sensor related signals. Left panel, typical example of sensory output noise v_k of the different sensory systems; middle panel, typical example of sensory errors (Equation 4b) in case of visual induced sway with a small stimulus amplitude ($\theta^{\text{vis}}(t) = 0.2 \cdot \sin(2\pi \cdot 0.1 \cdot t)$ [°]) and a sway referenced support base; right panel, typical example of sensory errors in case of visual induced sway with a large stimulus amplitude ($\theta^{\text{vis}}(t) = 10 \cdot \sin(2\pi \cdot 0.1 \cdot t)$ [°]) and a sway referenced support base. Note that the stimuli were applied after 14 s.

Simulation results of CG sway of vestibular loss patients compared to the CG sway of controls for fixed support base conditions are shown in Figure 9.16. For low stimuli amplitudes model predictions for controls and vestibular loss patients are similar. However, at larger stimuli amplitudes, the saturation effect does not occur for vestibular loss patients. The model results of vestibular loss patients diverge from controls at higher stimuli amplitudes. The amplitude where the results diverge depends on stimulus frequency. For faster stimuli, the results diverge at lower stimulus amplitudes. For large stimulus amplitudes the model predicts the falling of patients, mainly caused by excessive transient response at the onset of the stimulus (results not shown). These results for vestibular loss patients agree well with experimentally found results (Pertka and Benolken, 1995). Whereas in the experiment vestibular loss patients were able to maintain standing for small stimuli amplitudes while the support base was sway referenced, the model was not able to estimate a stable posture for these conditions.

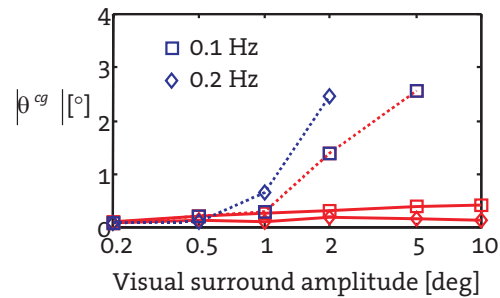


Figure 9.16: Gain of mean CG sway amplitude induced by visual scene motion as a function of stimulus amplitude. Model prediction of controls (solid lines) and vestibular loss patients (dotted lines). Boxes, stimulus frequency 0.1 Hz; diamonds, stimulus frequency 0.2 Hz. The support base was fixed.

9.2.4 DISCUSSION

Previous work (Van der Kooij et al., 1999a) demonstrated that to obtain a minimum variance estimate of spatial orientation, humans should have:

- An internal representation of the dynamics of the body, the sensory systems and the environment;
- Knowledge of the precision of the different sensory systems; and
- Knowledge of the amount of changes in visual scene motion, motion of the support base and external forces acting on the body.

When the dynamics are linear this minimum variance estimate is an optimal estimate. Spatial orientation can only be estimated optimally if these three conditions are satisfied. In our previous work, we assumed that these three conditions were fulfilled. It is reasonable to assume that due to a learning process humans have a kind of knowledge of the dynamic properties of their own body and their environment and of the reliability of their sensory organs. However, the assumption that humans have a (correct) knowledge of the amount of changes in environmental conditions is non-trivial. This is demonstrated by common illusionary sensations where ego-motion and motion of the environment are misinterpreted. A well-known illusionary ego-motion perception is the illusion that the train you are in is moving, whereas actually the train on the other track is moving.

In the modified model we do not have to quantify the amount of changes in environmental conditions as in the optimal model. These properties are now directly estimated from sensory output signals, resulting in a dynamically weighting of sensory error signals, depending on environmental conditions. The modified model was applied to human stance control. With only five model parameters, specifying the precision of the sensory systems, experimental results of a visual induced sway experiment (Pertka and Benolken, 1995) could be reproduced. The model predicted far more than five data points, suggesting a strong predictive capacity. Moreover, the model predictions for slow platform rotations qualitatively resembled experimental results presented by Bolha (1999). Model predictions show that:

1. Vestibular function is necessary to solve sensory conflicts;
2. Vestibular function is not crucial when sensory conflicts are absent;
3. Tactile afferents in the feet play an important role when the support base is translating; and

4. Responses to motion of the visual scene and to support base rotation are highly non-linear. The gain depends on stimulus amplitude and frequency, and on support base condition (fixed or sway referenced).

All these model predictions are consistent with experimental results. The presented adaptive model of sensory integration is more realistic than the previous developed model (Van der Kooij, 1999a) and other models of spatial orientation. It requires less assumptions and model input parameters. Moreover, model predictions and experimental results of visual induced sway suggest that postural orientation can not always be estimated optimally. Intuitively, visual scene motion should be ignored when standing on a fixed support to obtain an optimal estimate of postural orientation, since visual clues in this particular case cause an illusory perception of ego-motion. Model simulations of visual induced sway with the optimal model confirm this intuitive finding. In contrast with the adaptive model the optimal model predicts almost no response to visual scene motion, especially for larger stimuli amplitudes (Figure 9.17).

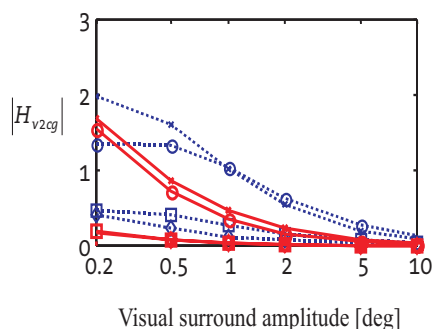


Figure 9.17: Gain of mean CG sway amplitude induced by visual scene motion as a function of stimulus amplitude. Model predictions of the optimal (solid lines) and the adaptive (dotted lines) model. Boxes, the support base was fixed, stimulus frequency 0.1 Hz; diamonds, the support base was fixed, stimulus frequency 0.2 Hz; circles, the support base was sway referenced, stimulus frequency 0.1 Hz; crosses, the support base was sway referenced, stimulus frequency 0.2 Hz.

The vestibular organ is needed to distinguish ego-motion from the motion of the environment. Especially for slow and small movements humans are not able to distinct ego from environmental motion as demonstrated by experiments and model predictions. In most models of spatial orientation this non-ideal or not-optimal behavior is included as a physical threshold related to vestibular output signals. The existence of a perceptual threshold is proven (e.g. Hosman, 1996). However, there is no evidence for a physical threshold. Interestingly, the modified model predicted a vestibular related threshold: the saturation of visual induced CG sway for sway reference condition is related to a vestibular threshold (Pertka and Benolken, 1995).

In addition, the model gives insight in the origin of vestibular related thresholds. Noisy sensory error signals - the difference between expected and actual sensory output signals - are used to obtain an estimate of spatial orientation of posture and environment. Sensor noise and changes in the external world (visual scene, support base, forces) cause sensory errors. In case of slow and small motion of the environment the error signals related to the vestibular system are dominated by vestibular output signal noise (e.g. Figure 9.15). Therefore, these error

signals are almost useless to update the estimate of spatial orientation and the amount of movement of the environment, causing sensory illusions. This does not imply, however, the existence of high biological noise levels of vestibular output signals. Prediction of high noise levels for a particular sensory output signal should be interpreted in such a way that the signal of that corresponding sensory system is modeled unreliably.

Although a simple inverted pendulum model was used for body dynamics, there are no fundamental limitations to include more segments, dimensions or muscle models etc.

In the presented model it is hypothesized that humans have a kind of internal representation of the dynamics of the body, the sensors and the external world and have knowledge of the precision of different sensory systems. There is much debate about the existence and location of internal presentations in the brain that mimic the behavior of the sensorimotor system and the external world. Only indirect evidence (e.g. Figure 9.18) of the existence of these internal representations is available (e.g. Kawato and Wolpert, 1998; Merfeld et al., 1999; Angelaki et al., 1999; Wolpert et al. 1998, Imamizu et al., 2000). An interesting question is to what level of detail these internal representations should correspond with reality. Should these internal representations capture only the kinematics or should they capture both the kinematics and the dynamics? In the present paper, the internal model was an exact copy of the actual dynamics of the body, the sensors and the external world. In the future we will study the effect of imperfect internal models by adding additional state noise or simplifying the internal models. In this paper the internal models are explicitly modeled. In some models of sensorimotor integration these internal models are implicitly modeled. For example, by assuming that the joint angles are known it is implicitly assumed that there exist an inverse model of muscle attachments around a joint and of the muscle spindle dynamics (e.g. Mergner and Rosemeier, 1998).

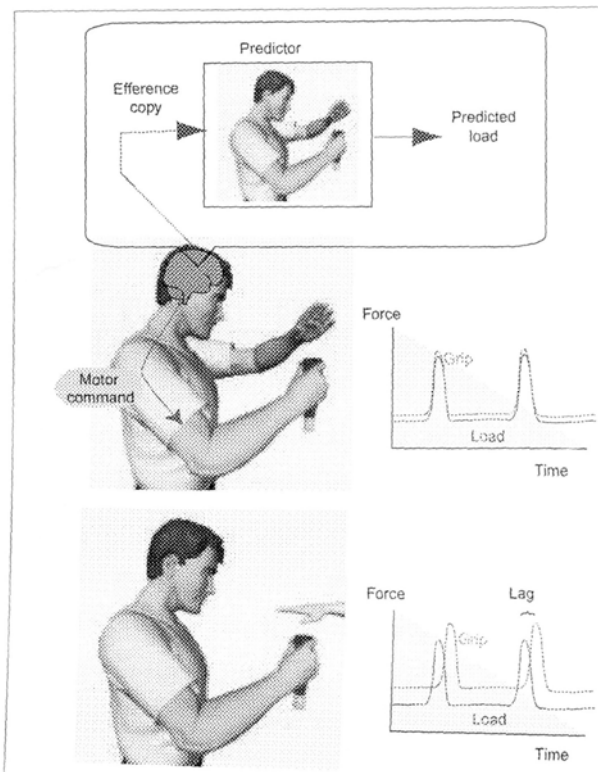


*Figure 9.18: Example of indirect evidence that humans utilize internal models in motor control. To prevent a ketchup bottle from slipping, sufficient grip force must be exerted to counteract the load. When the load is increased in a self-generated manner (left hand strikes the ketchup bottle, top), a predictor can use an efferent copy of the motor command to anticipate the upcoming load force and thereby generate grip that parallels load force with no delay. However, when the load is externally generated (another person strikes the bottle, bottom), then it cannot be accurately predicted. As a consequence, the grip force lags behind the load force and the baseline grip force is increased to compensate and prevent slippage. (Source Wolpert and Flanagan, *Current Biology*, 11(18)).*

In the presented model, the estimated or internal states can be equated to the perception of external forces acting on the body, support base displacements and rotations, motion of the visual scene and orientation of the body in space. Perception of these states can be accessed by psychophysical experiments, by recording of eye movements or by neural recordings. Predictions of an optimal estimator model for human spatial orientation of angular velocity and tilt perception correspond well to animal neural recordings and human psychophysical data (Borah et al., 1988)

An intriguing question is how an internal representation is obtained. Theoretically it is possible to derive an internal representation from motor outflow and sensory output signals (e.g. Mehra, 1971) and also to estimate the precision of different sensory systems from these signals (e.g. Myers and Taply, 1976).

Further experiments will have to be done, to validate the model for a wide variety of experimental settings. Special attention should be drawn to the design of the experiment, since model predictions suggest that postural responses are history dependent. In the future, the adaptive sensory integration model will also be used to model the perception of ego-motion and object motion, trying to reproduce well documented experimental results (Mergner et al., 1991; Mergner et al., 1992). The model will be used in combination with experiments to identify and quantify different balance disorders and their causes.

REFERENCES

- Akimase I, Imai S, Fukuoka Y (1997) Analysis of the posture control system under fixed and sway-referenced support conditions. *IEEE Trans Biomed Eng* 44:333-336
- Angelaki DE, McHenry MQ, Dickman JD, Newlands SD, Hess BJ (1999) Computation of inertial motion: neural strategies to resolve ambiguous otolith information. *J Neurosci* 19:316-327
- Berthoz A, Lacour M, Soechting JF, Vidal PP (1979) The role of vision in the control of posture during linear motion. *Prog Brain Res* 50:197-209
- Black FO, Shupert CL, Horak FB, Nashner LM (1988) Abnormal postural control associated with peripheral vestibular disorders. *Prog Brain Res* 76:263-275
- Bolha B, Hlavacka F, Maurer C, Mergner T (1999) Sensory interaction in postural responses to sinusoidal platform rotation. *Gait & Posture* 9 Suppl. 1: S38
- Borah J, Young LR, Curry RE (1988) Optimal estimator model for human spatial orientation. *Ann NY Acad Sci* 545: 51-73
- Buchanan JJ, Horak FB (1998) Control of head and trunk position in space in a postural coordination task: the role of the vestibular and visual systems. Proceedings Identifying control mechanisms for postural behaviours, A satellite meeting to the society for neuroscience meeting, Los Angeles USA.
- Clark B, Stewart JK (1969) Effects of angular accelerations on man: Threshold for perception of rotations and the oculogyral illusion. *Aerospace Med* 40:952-956
- Cohen MM, Crosbie RJ, Blackburn LH (1973) Disorienting effects of aircraft catapult launchings. *Aerospace Med.* 44: 37-39
- Fernandez C, Goldberg JM (1971) Physiology of peripheral neurons innervating semicircular canals of the squirrel monkey. II. Response to sinusoidal stimulation and dynamics of peripheral vestibular system. *J. Neurophysiol.* 34:661-675
- Gelb A (1974) Applied optimal estimation. The MIT Press, Cambridge England
- Gerdes VG, Happee R (1994). The use of an internal representation in fast goal-directed movements: a modelling approach. *Biol Cyb* 70:513-524
- Horak FB, Nashner LM, Diener HC (1990) Postural strategies associated with somatosensory and vestibular loss. *Exp Brain Res* 82:167-177
- Hosman RJAW (1996) Pilot's perception and control of aircraft. PhD-Thesis. Delft University of Technology, The Netherlands
- Imamizu H, Miyauchi S, Tamada T, Sasaki Y, Takino R, Putz B, Yoshioka T, Kawato M (2000) Human cerebellar activity reflecting an acquired internal model of a new tool. *Nature* 403:192-195
- Jacobs R, van der Kooij H, Burleigh-Jacobs A (1997) Modelling a new

- definition of the goal of postural control. Proceedings Multisensory Control of Posture and Gait, 13th International Symposium. Paris, France.
- Juang JN, Chen CW, Phan M (1993) Estimation of Kalman filter gain from output residuals. *Journal of Guidance and control* 16:903-908
 - Kawato M, Wolpert D (1998) Internal models for motor control. *Novartis Found Symp* 218:291-304
 - Kleinman DL (1969) Optimal control of linear systems with time-delay and observation noise. *IEEE Trans Automat. Contr* 15:524-527
 - Maurer C, Mergner T (1999) Postural reaction to platform tilt in normal and subjects and patients with vestibular loss. *Gait & Posture* 9 Suppl. 1: S35
 - Mehra RK (1971) On-line identification of linear dynamic systems with applications to Kalman filtering. *IEEE Trans Autom Control* 16:12-21
 - Merfeld DM, Zupan L, Peterka RJ (1999) Humans use internal models to estimate gravity and linear acceleration. *Nature* 398:615-618
 - Mergner T, Siebold C, Schweigart G, Becker W (1991) Human perception of horizontal head and trunk rotation in space during vestibular and neck stimulation. *Exp Brain Res* 85:389-404
 - Mergner T, Rottler G, Kimmig H, Becker W (1992) Role of vestibular and neck inputs for the perception of object motion in space. *Exp Brain Res* 89:655-668
 - Mergner T, Schweigart G, Kolev O, Hlavacka F, Becker W (1995). Visual-vestibular interaction for human ego-motion perception. In: Mergner T, Hlavacka F, editors. *Multisensory control of posture*. New York: Plenum Press: 157-168
 - Mergner T, Rosemeier T (1998) Interaction of vestibular, somatosensory and visual signals for postural control and motion perception under terrestrial and microgravity conditions-a conceptual model. *Brain Res Reviews* 28:118-135
 - Mergner T, Glasauer S. (1999) A simple model of vestibular canal-otolith signal fusion. *Ann N Y Acad Sci.* 871:430-434
 - Myers KA, Taply BD (1976). Adaptive Sequential Estimation with Unknown Noise Statistics. *IEEE Trans. Automat Contr* 22: 520-523
 - Nashner LM, Shupert CL, Horak FB, Black FO (1989) Organisation of posture control: an analysis of sensory and mechanical constraints. *Prog Brain Res* 80:411-418
 - Peterka RJ, Benolken MS (1995), Role of somatosensory and vestibular cues in attenuating visually induced human postural sway. *Exp Brain Res* 105:101-110
 - Runge CF, Shupert CL, Horak FB, Zajac FE (1998) Role of vestibular information in initiation of rapid postural responses. *Exp Brain Res* 122:403-412
 - Van der Kooij H, Jacobs R, Koopman B, Grootenboer H (1999a) A Multisensory integration model of human stance control. *Biol Cyb* 80:299-308
 - Van der Kooij H, Koopman B, Jacobs R, Mergner T, Grootenboer H (1999b) Interpretation of multivariate swaydescriptors. Proceedings Biomechanics Workshop, University of Twente, Enschede, Netherlands.
 - Wolpert DM, Ghahramani Z, Jordan MI (1995) An Internal Model for Sensorimotor Integration. *Science* 269: 1880-1882
 - Wolpert DM, Goodbody SJ, Husain M (1998) Maintaining internal representations: the role of the human superior parietal lobe. *Nat Neurosci* 1:529-533

APPENDIX A: TAPPED DELAY LINE AS PREDICTOR FOR TIME DELAYS

An optimal estimator for a linear system including time delays is the cascade combination of a Kalman Filter and a predictor (Kleinman 1969). A discrete optimal predictor is a tapped delay line (Figure 9.19). The tapped delay line used in this paper is a forward simulation of the discretized dynamics ($A^*=A^{pend}$, $B^*=B^{pend}$) of the pendulum, using known previous control input (u_k) from the delayed estimate made by the adaptive Kalman Filter at t_{k-N} , to the current time t_k . $N=10$, is determined by the modelled neural time delay ($\tau=100$ ms) and sample time of the discrete model ($1/z=10$ ms).

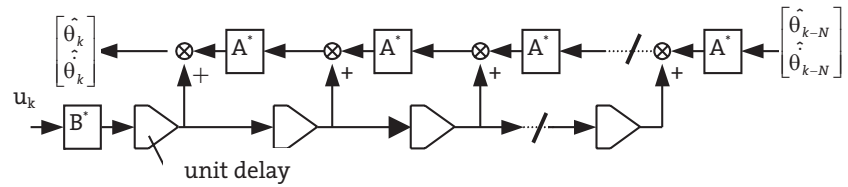


Figure 9.19: A tapped delay line to make an optimal prediction of the current spatial orientation from the delayed estimate of spatial orientation as obtained by the adaptive Kalman Filter at t_{k-N} , to the current time t_k . It is a forward simulation of discretized dynamics ($A^*=A^{pend}$, $B^*=B^{pend}$) of the pendulum, using known previous control input (u_k), N is number of forward simulation steps and $1/z$ is sample time of the discrete model.

APPENDIX B: SENSOR DYNAMICS

The sensor dynamics are approximated by linear transfer functions (Borah et al., 1988).

$$\text{Muscle spindle model: } \frac{\text{afferent fire rate}}{\text{joint angle}} = \frac{5(s+4)}{s+20}$$

$$\text{Semicircular model: } \frac{\text{afferent fire rate}}{\text{angular acceleration}} = \frac{0.574s(s+100)}{(s+0.1)(s+0.033)}$$

$$\text{Otolith model: } \frac{\text{afferent fire rate}}{\text{specific force}} = \frac{90(s+0.1)}{s+0.2}$$

$$\text{Vision Model: } \frac{\text{afferent fire rate}}{\text{distance head - visual scene}} = 1$$

$$\text{Tactile Model: } \frac{\text{afferent fire rate}}{\text{force}} = \frac{s+0.01}{s+0.1}$$

APPENDIX C:

$$\begin{bmatrix} \theta_k^{sb} \\ F_k^{ext} \\ s_k^{sb} \\ \dot{s}_k^{sb} \\ \ddot{s}_k^{sb} \\ s_k^{vis} \end{bmatrix} = \begin{bmatrix} 1 & 0 & 0 & 0 & 0 & 0 \\ 0 & 1 & 0 & 0 & 0 & 0 \\ 0 & 0 & 1 & T_s & \frac{1}{2}T_s^2 & 0 \\ 0 & 0 & 0 & 1 & T_s & 0 \\ 0 & 0 & 0 & 0 & 1 & 0 \\ 0 & 0 & 0 & 0 & 0 & 1 \end{bmatrix} \begin{bmatrix} \theta_{k-1}^{sb} \\ F_{k-1}^{ext} \\ s_{k-1}^{sb} \\ \dot{s}_{k-1}^{sb} \\ \ddot{s}_{k-1}^{sb} \\ s_{k-1}^{vis} \end{bmatrix} + \begin{bmatrix} 1 & 0 & 0 & 0 \\ 0 & 1 & 0 & 0 \\ 0 & 0 & 0 & 0 \\ 0 & 0 & 0 & 0 \\ 0 & 0 & 1 & 0 \\ 0 & 0 & 0 & 1 \end{bmatrix} \begin{bmatrix} w_{k-1}^{\theta sb} \\ w_{k-1}^{F ext} \\ w_{k-1}^{sb} \\ w_{k-1}^{vis} \end{bmatrix} \Leftrightarrow \underline{x}_k^{env} = A^{env} \underline{x}_{k-1}^{env} + G \underline{w}_{k-1}^{env} \quad (9.8)$$

where T_s is the sample time

$$\begin{bmatrix} w_{k-1}^{\theta sb} \\ w_{k-1}^{F ext} \\ w_{k-1}^{sb} \\ w_{k-1}^{vis} \end{bmatrix} = \begin{bmatrix} \theta_k^{sb} \\ F_k^{ext} \\ \ddot{s}_k^{sb} \\ w_k^{vis} \end{bmatrix} - \begin{bmatrix} \theta_{k-1}^{sb} \\ F_{k-1}^{ext} \\ \ddot{s}_{k-1}^{sb} \\ w_{k-1}^{vis} \end{bmatrix} \Rightarrow \frac{1}{T_s} \begin{bmatrix} w_{k-1}^{\theta sb} \\ w_{k-1}^{F ext} \\ w_{k-1}^{sb} \\ w_{k-1}^{vis} \end{bmatrix} \approx \begin{bmatrix} \dot{\theta}_k^{sb} \\ \dot{F}_k^{ext} \\ \ddot{s}_k^{sb} \\ \dot{s}_k^{vis} \end{bmatrix} \quad (9.9)$$

Combining Equation 9.8 and 9.9,

$$E \left\{ \underline{w}^{env} (\underline{w}^{env})^T \right\} \approx T_s^2 E \left\{ \begin{bmatrix} \dot{\theta}^{sb} & \dot{F}^{ext} & \ddot{s}^{sb} & \dot{s}^{vis} \end{bmatrix}^T \begin{bmatrix} \dot{\theta}^{sb} & \dot{F}^{ext} & \ddot{s}^{sb} & \dot{s}^{vis} \end{bmatrix} \right\} \quad (9.10)$$

APPENDIX D:

For the sake of convenience, the derivation of the estimator for Q is literally cited (Myers et al, 1976). Consider the linear dynamical state relation at a given time t_j , given by $\underline{x}_j = A\underline{x}_{j-1} + B\underline{u}_{j-1} + \underline{w}_{j-1}$, where \underline{x}_j is an n -vector and $\underline{w}_{j-1} \sim N(\underline{q}, Q)$. The true states \underline{x}_j and \underline{x}_{j-1} are unknown so \underline{w}_{j-1} cannot be determined, but an intuitive approximation \underline{q}_{j-1} is

$$\underline{q}_j \equiv \hat{\underline{x}}_j - A\hat{\underline{x}}_{j-1} - B\underline{u}_{j-1} \quad (9.11)$$

Where \underline{q}_j is defined as the state noise sample at time t_j . Note that the subscript j contrasts the noise sample from the true unknown mean \underline{q} . By hypothesis, the \underline{w}_{j-1} for $j=1 \rightarrow N$ are independent, and the parameters \underline{q} and Q are constant. If the \underline{q}_j is assumed to be representative of the \underline{w}_{j-1} , they may be considered as independent and identically distributed. Defining a parameter estimation problem, let \mathfrak{R} be a random variable on the sample space Ω_2 from which is obtained the data \underline{q}_j , $j=1 \rightarrow N$. Based on the measurements, the unknown distribution of \mathfrak{R} , characterised by \underline{q} and C_q is to be estimated. An unbiased estimator for \underline{q} is the sample mean

$$\hat{\underline{q}} = \frac{1}{N} \sum_{j=1}^N \underline{q}_j \quad (9.12)$$

An unbiased estimator for Q is obtained by constructing the estimator for C_q , the covariance of \mathfrak{R} ,

$$\hat{C}_q = \frac{1}{N-1} \sum_{j=1}^N (\underline{q}_j - \hat{\underline{q}})(\underline{q}_j - \hat{\underline{q}})^T \quad (9.13)$$

The expected value of this quantity is:

$$E[\hat{C}_q] = \frac{1}{N} \sum_{j=1}^N A\hat{P}_{j-1}A^T - \hat{P}_j + Q \quad (9.14)$$

An unbiased estimate of Q , after substitution of Equation 9.13 is given by

$$\hat{Q} = \frac{1}{N-1} \sum_{j=1}^N \left\{ (\underline{q}_j - \hat{\underline{q}})(\underline{q}_j - \hat{\underline{q}})^T - \left(\frac{N-1}{N} \right) [A\hat{P}_{j-1}A^T - \hat{P}_j] \right\} \quad (9.15)$$